Conversion of Carbon Dioxide and Crude Glycerine into Value-Added Products

by

Yanet Rodriguez Herrero

A thesis submitted in partial fulfillment of the requirements for the degree of

Doctor of Philosophy

in

Bioresource and Food Engineering

Department of Agricultural, Food and Nutritional Science
University of Alberta

Abstract

Modern civilization has become dependent on fossil fuels as a source of energy and chemicals. As a result, the rapid industrial development and growing energy demand are pushing toward two imminent problems, the depletion of fossil fuel reserves and the negative impact on global climate. Subsequently, the lookout for renewable alternatives as energy sources and chemical feedstock has mobilized the academic community and the industry to adapt existing technologies and develop new methodologies. Biomass is currently the most widespread alternative feedstock due to its availability and relatively short regeneration cycle, yet its valorization has to deal with the waste that results from biomass processing. For instance, the biodiesel industry, the second larger biofuel manufacturer, generates approximately 10 wt.% of crude glycerol from the transesterification of vegetable oil, and 0.71 kg of CO_2 is released into the atmosphere per liter of biodiesel combusted as vehicle fuel.

Thus, this thesis focuses on valorization routes for the major by-products from the biodiesel industry. We investigated the catalytic conversion of carbon dioxide (CO_2) to methanol, and a microwave-assisted metal-free catalytic route for glycerol transformation to allyl monomers and polymers. The general background is presented in the literature review, and the results are discussed in three data chapters as follows:

In the first study, CO_2 was reduced to methanol in mini-batch reactors using a Cu/ZnO as an active phase supported in a novel hydrophobic material, phenyl polyhedral oligomeric silsesquioxane (POSS). Two types of POSS nanoparticles, octaphenyl POSS (O-POSS) and dodecaphenyl POSS (D-POSS) were compared to evaluate the influence of the cage size and the number of ligands in the CO_2 conversion and methanol yield. The nanoparticles had an average

size of 7 nm (CuO/ZnO/O-POSS) and 15 nm (CuO/ZnO/D-POSS). The structural characterization of the as-synthetized materials revealed that CuO/ZnO were electron withdrawers from POSS. Furthermore, the increased number of phenyls attached to the siloxane cage augmented the catalytic system's hydrophobic character, resulting in higher CO_2 conversion and methanol yield under the conditions studied.

Furthermore, we identified that the hydrophobic nature of the supports plays a decisive role in driving the reaction to completion. These conclusions emerged after comparing the results with Cu/ZnO supported on reduced graphene oxide (RGO). Although RGO had a higher surface area due to its hydrophilic character but yielded 0% of methanol under the conditions studied. Finally, the thermal gravimetric analysis in a nitrogen atmosphere revealed the thermal stability of the new catalytic systems under the interest temperature range (200 °C – 270 °C).

The second study deepened the thermal stability of the catalytic system CuO/ZnO/POSS. We identified irreversible thermal events with low transition energy associated with the supports' molecular relaxation and crystalline arrangements. The impregnation, followed by mild calcination of the metal oxides CuO/ZnO, did not interfere with the thermal stability of supports until about 450 °C. Nevertheless, as temperature increased above 450 °C, the metal oxides accelerated the support degradation rate.

In the third study, glycerol was converted to allyl alcohol through a formic acid-mediated metal-free deoxydehydration reaction under microwaves. The produced allyl alcohol was also converted to allyl formate and allyl phthalate. The synthesized monomers (allyl alcohol, allyl formate, and allyl phthalate) were polymerized using microwave-assisted polymerizations. The microwave-assisted method resulted in faster conversions and higher energy efficiency (>16 times

less energy consumption) compared to the conventional heating method to produce allyl alcohol. Furthermore, a three-factor, three-level Box-Behnken response surface design was performed to investigate the influence of time, temperature, and molar ratio on the yield of allyl alcohol and allyl formate. The results showed that temperature and molar ratio between formic acid to glycerol had a more significant effect on the reaction, whereas the reaction time did not impact the yield of allyl alcohol.

In summary, this thesis developed two approaches for utilizing two waste-biomass resources to value-added products using friendly technologies such as microwaves, which helped to reduce reaction time and minimize energy consumption. Overall, this research would benefit the biodiesel industry to utilize glycerol and petrochemical industries to deepen the know-how to improve CO_2 catalytic conversion.

Preface

This thesis contains original work Ms. Yanet Rodriguez Herrero performed and written according to the Faculty of Graduate Studies and Research guidelines at the University of Alberta.

The thesis consisted of six chapters. Chapter One provides a general introduction to the context, the hypothesis, and the objectives of the different studies. Chapter Two consists of a literature review on several topics relevant to the thesis.

Chapter Three has been submitted to a peer-reviewed journal as *"Hydrophobic Polyhedral Oligomeric Silsesquioxane Support Enhanced Methanol Production from CO_2 Hydrogenation."* The initial conceptualization of using oligomeric silsesquioxane belongs to Dr. Aman Ullah. As the fundamental understanding of the research advanced, I contributed to the conceptualization and selection of the hydrophobic supports. In addition, I was responsible for experimental design, laboratory analyses, data interpretation, and manuscript preparation. Dr. Ullah is the corresponding author and is responsible for manuscript review, data interpretation, editing, and submission.

Chapter Four has been prepared as a manuscript for submission to a peer-reviewed journal as *"Thermal Stability Study of Catalyst (CuO/ZnO) Supported on Phenyl Polyhedral Oligomeric Silsesquioxanes (POSS)."* I am responsible for conceptualization, experimental design, laboratory analyses, data interpretation, and manuscript writing. Dr. Ullah is the corresponding author, manuscript review, editing, and submission.

Chapter Five of this thesis has been published as *"Herrero YR, Ullah A. Rapid, Metal-free, Catalytic Conversion of Glycerol to Allyl Monomers and Polymers. ACS Sustainable Chemistry & Engineering. 2021 Jul 2;9(28):9474-85."* This chapter resulted in a patent published as *"Ullah A, Herrero YR, inventors; University of Alberta, assignee. Methods for Converting Glycerol to Allyl Compounds. United States patent US 10,633,316. 2020 Apr 28."* I contributed to the conceptualization and experimental design and performed all laboratory analyses, data interpretation, and manuscript writing. Dr. Ullah, the corresponding author, contributed to the conceptualization, manuscript review, editing, and manuscript submission.

Chapter Six presents the concluding remarks and future directions of the studies discussed.

Specially dedicated

to my beloved mother, husband, and children for always believing in me.

Acknowledgments

Firstly, I would like to express my sincere gratitude to my supervisor Dr. Aman Ullah for giving me the opportunity to be part of his research group and for his continuous support throughout my Ph.D. study and related research. His patience, motivation, and endless guidance helped me throughout this journey.

I want to thank the members of my thesis committee: Dr. Arno De Klerk and Dr. Rajender Gupta, for their insightful comments and encouragement, but also for the challenging questions which motivated me to broaden my critical thinking and, at the same time, help me focus the research questions. It has been such an honor to work with you.

I would also like to acknowledge Dr. Arno de Klerk for opening his lab and introducing me to his amazing research group. I met excellent professionals such as Dr. Cibele Halmenschlager, Lina Maria Yanez, Dr. Felix Link, Dr. Garima Chauhan, Priscila Nascimento, Shirley Fong, Cloribel Santiago Flores, and many others. I learned so much from you, from assembling a batch reactor to operating a Gas GC. Thank you, colleagues! Each of you inspired me to be a better person and a more critical scientist today. Finally, I have a special thanks to Dr. Natalia Montoya Sánchez. You are a special gift I found in the Engineering department. The way you approach a scientific problem has been an inspiration for me. I sincerely thank you for being such a fantastic friend and advisor, without your motivation and support, this journey would have been even harder.

I want to thank all my lab mates in Dr. Ullah's research group, special to Karen López Camas, Huiqi Wang (Kiki), and Siti Amirah Binti Haji Yussof, for all the laughs and encouragement. Thank you, Dr. Reza Ahmadi, for all the help in getting started with my Ph.D.;

your tidiness and organizational skills will never be forgotten. Special thanks to Ereddad Kharraz for assisting in the training of various lab equipment. I am grateful to Dr. Irum Zahara and Dr. Muhammad Faisal Irfan for their thoughtful advice and encouragement.

I want to acknowledge the staff from the Fabrication & Characterization Centre (nanoFab) at the University of Alberta, Dr. Nancy Zhang and Dr. Shihong Xu, for the training and support using complex equipment. I also want to acknowledge the Chemistry NMR Laboratory, Dr. Mark Miskolzie and Nupur Dabral, for your help in NMR spectroscopy.

I would like to extend my gratitude to many friends and family that were always attentive to my progress and a special note to my beloved godmother Amita, for all your prayers and love.

This journey has been long and intense. I started as a Master's student and then transferred to the Ph.D. program. When I thought I was getting somewhere, COVID-19 hit, and I had to take an absence of leave to care for my family. I encountered many challenges, and some were solved, others, I had to drive away and start from zero again. However, I knew I was not alone, in every challenge along the way, I always felt care and support. Since day zero, my husband, Eickerman, and my mother, Hilda, have been by my side and cheering me up unconditionally. To both of you, thank you, without your love and support, I would not be here today. Thank you for being patient during my family absences, late nights, and early mornings. Thank you for all your love and care.

To my children, Tiago and Diego, you have been my light in the darkest days, my inspiration to persist and not give up. Thank you for your patience when you had to stay home instead of having fun because mom had to finish the lab work. Thank you for the time you had to be quiet because mom was writing. Thank you for your kisses every morning and your encouragement to get closer to the finish line. Now that time has come, it is my turn to see you conquer the stars.

Table of Contents

List of Tables

List of Figures

Chapter 1. Introduction

For more than 150 years, mankind has relied on fossil fuels, such as oil, gas, and coal, as a significant energy source to meet their needs. Technological inventions can explain this dependence [1]. For instance, the beginning of the steam engine brought growth in food production, cheaper and faster transportation, and industrial development. Moreover, a critical problem in modern civilization with this reliance on fossil fuels is that these reserves are finite in quantity and rapidly depleting. On the other hand, global fossil fuels are associated with climate change as the most significant contributor to the greenhouse (GHG), around three-quarters of global emissions [2], leading to a sharp rise in the lookout for sustainable and long-term solutions for fossil fuel substitution [3,4].

Renewable resources offer an attractive replacement, as they are considered clean, safe, and obtained from natural processes [5]. In addition, they can restock at a rate equivalent to or faster than the rate at which they are exhausted [6]. The common energy sources are sun, wind, hydroelectric, geothermic, ocean thermic, biogas, liquid biofuels, and solid biomass (Fig. 1-1).

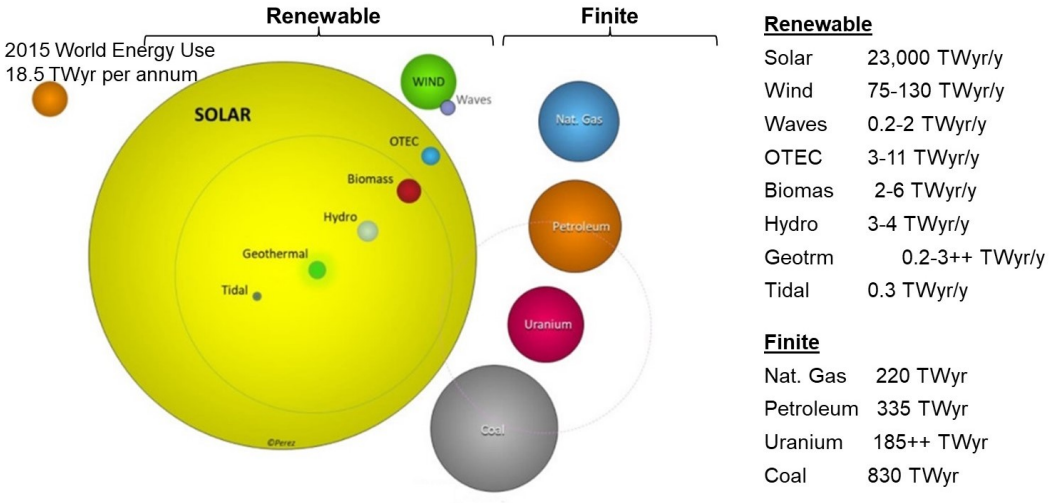

Figure 1-1 2015 estimated finite and renewable planetary energy reserves (Terawatt-years). Annual yield is shown for the renewable resources. Total recoverable reserves are shown for the finite resources. Yearly potential is shown for the renewables (the volume of each sphere is proportional to the corresponding reserve) (adapted from Perez-Perez [5]).

For instance, solar energy represents the most prominent energy supply and combined with wind energy, could provide the world's total energy demand. Nevertheless, wind and solar energies fluctuate and hinge on the season, time of the day, and weather. Therefore, developing storage energy solutions with other available feedstock could ease the transition to renewable resources while balancing energy production and demand [7].

Biomass-based routes have great potential as energy sources and feedstock for new and existing processes [8]. Biomass covers an accumulation of plant and animal resources and their waste [9]. Notably, this resurging feedstock is available around the globe and can be easily stored and transported. However, even though biomass is already the feedstock of numerous biomaterials and biochemicals [10], it has low energy density and decentralized production, making it a relatively inefficient starting material [11]. Moreover, the adoption of biomass has to address many other challenges, such as dealing with the waste generated in the conversion process [12]. A clear example is the development of technologies to manufacture biodiesel from vegetable oils to power vehicle engines, which is considered promising from an economic and environmental perspective, however, this process produces crude glycerol as waste, and CO_2 is emitted from the combustion engine (Fig. 1-2). Consequently, the further valorization of crude glycerol and CO_2 is an alternative route of carbon source and to treat the waste [13].

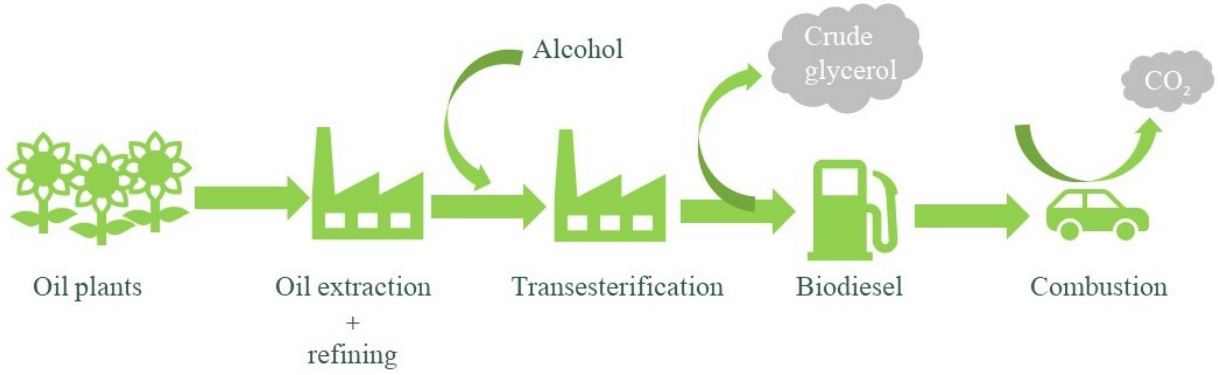

Figure 1-2 Simplified representation of main wastes produced in biodiesel production and utilization.

Keeping in mind the stated issues, this Ph.D. research aims to investigate two routes to utilize CO_2 and glycerol as potential sustainable feedstocks for valuable materials. For instance, CO_2 is produced in nature as part of the carbon cycle and human activities from the combustion of fuels for electricity, heat, and transportation. Ideally, CO_2 could be converted to methanol that could be employed as energy storage, used directly as fuel, or as the precursor for other value-added products. Nevertheless, this chemical conversion is limited on account of the stability of CO_2, which requires high energy to drive the transformation, besides an active, selective, and stable catalytic system. On the other hand, conventional crude glycerol applications are limited in terms of purity and cost, so exploring directly used as the feedstock of fine chemicals is of great interest.

1.1 Research Aim and Objectives

1.1.1 Aim of the Research

This study has been divided into two parts:

1. The first part of the research explores an alternative catalytic system, water resistance, and thermal stability for CO_2 hydrogenation to methanol.
2. The second part of the research investigates an energy-efficient and fast alternative method to convert glycerol to value-added products.

1.1.2 Specific Objectives

1. To investigate the use of novel hydrophobic support with CuO/ZnO on reducing CO_2 with H_2 to methanol.
2. To examine the influence of CuO/ZnO on the thermal stability of the hydrophobic support and compare how a change in the size of the support molecule and the number of ligands influence the thermal stability of the catalytic system.
3. To develop a rapid and energy-efficient method for converting glycerol to allyl monomers and polymers.

1.1.3 Research Questions and Hypothesis

i- Do hydrophobic supports promote CO_2 hydrogenation to methanol?

Hypothesis (*i*): catalyst (support) activation against water production (by product during reaction) and its thermal stability could be enhanced by homogeneously dispersing active metals on hydrophobic material.

ii- How do interactions of metal oxide-support affect the structure and thermal stability of the hydrophobic material?

Hypothesis (*ii*): the support's thermal stability and chemical structure may be changed as a result of the interactions of metal oxide with support.

iii- Does microwave assist glycerol conversion to the other value-added products?

Hypothesis (*iii*): glycerol is a polar compound with a high dielectric constant, the use of microwave radiation may decrease the glycerol's activation energy towards any precursor.

1.1.4 Research Approach

To answer the research questions, the following analyses were conducted:

i- Preliminary screened for hydrophobic supports directed us to select two types of phenyls polyhedral oligomeric silsesquioxane. The selection was based on the molecule size and number of phenyls to control the changes in the results. In addition, hydrophilic support with a larger surface area was also selected, reduced graphene oxide, to assess the influence of the surface area in the conversion of CO_2.

ii- The influence on the thermal stability of the hydrophobic polyhedral oligomeric silsesquioxane was studied with thermal analysis in an inert and oxidizer atmosphere followed by spectroscopy analysis.

iii- Develop the microwave-assisted method for the conversion of glycerol to allyl monomers. Optimize the main parameters: time, temperature, and reactants ratio. Next, the conversion time and energy consumption were compared with conventional methods

1.1.5 Thesis Outline

This thesis is divided into six chapters, starting with Chapter One (Introduction), which includes a general background information. A short description of the work conducted from Chapter Two to Chapter Six is presented in the following:

Chapter Two: ***Literature Review***

This chapter is divided in the two parts to understand the sources of carbon dioxide and glycerol. Furthermore, the current methodologies to utilize these materials are explored as well as their potentials as prospective renewable feedstocks,

Chapter Three: ***Hydrophobic Polyhedral Oligomeric Silsesquioxane support enhanced methanol production from CO_2 hydrogenation***

The literature indicates the harmful effect of water formed during reverse water gas shift reaction during CO_2 hydrogenation to methanol to the traditional catalyst and the rate of reaction. This chapter evaluated two novel hydrophobic supports for hydrogenating CO_2 to methanol. A comparison with hydrophilic support is explored.

Chapter Four: ***Thermal Stability Study of Catalyst (CuO/ZnO) supported on Phenyl Oligomeric Silsesquioxanes (POSS)***

Thermal degradation is a common cause of catalyst deactivation as the properties of the catalytic system could irreversibly change. This chapter evaluates the metal oxide catalysts' stability on the hydrophobic supports over a temperature increase in inert and oxidative atmospheres.

Chapter Five: ***Rapid, Metal-Free, Catalytic Conversion of Glycerol to Allyl Monomers and Polymers***

Efficient methods are required to utilize industrial waste. This chapter explores and optimizes microwave-assisted glycerol conversion to value-added products. In addition, a comparison with a conventional method is established regarding energy consumption.

Chapter Six: ***Conclusions***

In this chapter, the main conclusions of CO_2 and glycerol utilization as renewable feedstock are highlighted, as well as the insights that will contribute to the field of catalysis.

1.2 References

[1] Budzianowski WM. Negative carbon intensity of renewable energy technologies involving biomass or carbon dioxide as inputs. Renew Sustain Energy Rev 2012;16:6507–21.

[2] IEA (2021), Greenhouse Gas Emissions from Energy Data Explorer, IEA, Paris 2021. https://www.iea.org/data-and-statistics/data-tools/greenhouse-gas-emissions-from-energy-data-explorer (accessed October 27, 2022).

[3] Saygin D, Gielen DJ, Draeck M, Worrell E, Patel MK. Assessment of the technical and economic potentials of biomass use for the production of steam, chemicals and polymers. Renew Sustain Energy Rev 2014;40:1153–67.

[4] Gerssen-Gondelach SJ, Saygin D, Wicke B, Patel MK, Faaij APC. Competing uses of biomass: Assessment and comparison of the performance of bio-based heat, power, fuels and materials. Renew Sustain Energy Rev 2014;40:964–98.

[5] Perez M, Perez R. Update 2022 – A fundamental look at supply side energy reserves for the planet. Sol Energy Adv 2022;2:100014.

[6] About Renewable Energy n.d. https://www.nrcan.gc.ca/our-natural-resources/energy-sources-distribution/renewable-energy/about-renewable-energy/7295.

[7] Holechek JL, Geli HME, Sawalhah MN, Valdez R. A global assessment: can renewable energy replace fossil fuels by 2050? Sustainability 2022;14:4792.

[8] Yogalakshmi KN, Poornima Devi T, Sivashanmugam P, Kavitha S, Yukesh Kannah R, Varjani S, et al. Lignocellulosic biomass-based pyrolysis: a comprehensive review. Chemosphere 2022;286:131824.

[9] Popp J, Kovács S, Oláh J, Divéki Z, Balázs E. Bioeconomy: biomass and biomass-based energy supply and demand. N Biotechnol 2021;60:76–84.

[10] Williams CL, Westover TL, Emerson RM, Tumuluru JS, Li C. Sources of biomass feedstock variability and the potential impact on biofuels production. BioEnergy Res 2016;9:1–14.

[11] Montoya Sánchez N, Link F, Chauhan G, Halmenschlager C, El-Sayed HEM, Sehdev R, et al. Conversion of waste to sustainable aviation fuel via Fischer–Tropsch synthesis: front-end design decisions. Energy Sci Eng 2022;10:1763–89.

[12] Nzihou A. Toward the valorization of waste and biomass. Waste and Biomass Valorization 2010;1:3–7.

[13] Kumar LR, Kaur R, Tyagi RD, Drogui P. Identifying economical route for crude glycerol valorization: Biodiesel versus polyhydroxy-butyrate (PHB). Bioresour Technol 2021;323:124565.

Chapter 2. Literature Review

One of the main challenges for academia and industry is finding sustainable replacements for fossil fuel energy and chemical sources due to environmental concerns and fossil fuel depletion [1]. To tackle these problems, the utilization of biomass and petrochemical waste has been evaluated [2,3]. Hence, this chapter reviews carbon dioxide (CO_2) and glycerol, two abundant chemicals from natural and synthetic processes. In the following sessions, we explore the industrial origins of these compounds and rationalize the reasons to utilize them as feedstock for value-added chemicals, for instance, their immediate availability and their chemistry as a source of carbon. Furthermore, we look into the challenges of using these materials as precursors, such as the purification grade, the adaptation of current technologies, and the development of new methods.

2.1 Carbon Dioxide (CO_2) as a Renewable Feedstock

CO_2 is a controversial compound as the most abundant substance produced by human activity and is simultaneously one of the main contributors to fossil fuel pollution [4]. Nevertheless, CO_2 may play a decisive role in a sustainable future as a readily available material if utilized effectively. Furthermore, CO_2 is environmentally friendly, non-toxic, non-flammable, and the cheapest source of carbon on the planet Earth. As a result, chemical approaches to CO_2 conversion have increased in the last decades to identify alternative routes for producing chemicals, such as methanol, methane, or synthetic fuel, which could become the primary energy source [5]. Despite the benefits of CO_2 as cheap biomass, its chemical conversion into other chemicals remains a challenge. CO_2 is a thermodynamically stable molecule ($\Delta_f H°$=-393.52 $kJmol^{-1}$) [6] that requires intensive energy processes to overcome the high activation barriers in a typical reaction [7].

2.1.1 Sources of CO_2 Emissions

CO_2 emissions occur *naturally* as part of an active natural carbon cycle that circulates carbon between the atmosphere, ocean, and terrestrial biosphere daily for thousands of years due to animal and plant respiration, decomposition of organic matter, forest fires, and emissions from volcanic eruptions [8]. The next type of carbon emissions is *anthropogenic* sources, which result from emissions related to human activities, such as fossil fuel combustion, transportation, industrial activities, chemical production, and agricultural practices [9]. For example, fossil combustion results when fossil carbon compounds are broken down via combustion or other oxidation processes to produce CO_2, carbon monoxide (CO), sulfur oxides (SO_x), nitrogen oxides (NO_x), and hydrocarbons. Furthermore, fossil carbonates such as calcium and magnesium carbonate produce large quantities of CO_2 when used in essential chemical processes such as cement production.

Before the pre-industrial Era, deforestation and other land-use change[1] activities were the principal causes of the release of carbon into the atmosphere [10]. However, after the First Industrial Revolution, burning fossil fuels became the dominant anthropogenic source of emissions from the 1950s, continuously increasing until the present (Fig. 2-1). For instance, global fossil CO_2 emissions from energy combustion and industrial processes have increased from 8.7 gigatonnes (Gt CO_2) in 1960 to 36.3 Gt CO_2 in 2021, distributed among coal (40%), oil (29%), and natural gas (21%), and non-combustion sources (10%) [11]. Furthermore, CO_2 emissions from industrial sectors account for 43% of energy-related CO_2 emissions [4], where *direct emissions* involve burning fuel for power or heat through chemical reactions and leaks from industrial processes or equipment. In contrast, *indirect emissions* are produced by burning fuel at a power plant to produce electricity, which is further used to power industrial buildings and machinery [12].

Land use overall affects the CO_2 levels on Earth, as trees act as natural *carbon sinks*, which are considered when more carbon is absorbed from soil, plants, and oceans from the atmosphere than released [9,13]. Therefore, land use, land-use change, and forestry are considered substantial

[1] "Land-use change" is any way in which humans modified the natural landscape e.g., urban expansion, cropland abandonment, and forest restoration.

sources of anthropogenic CO_2, accounting for 14% of CO_2 emissions in 2010-2019 from deforestation, afforestation, logging, and forest degradation [14].

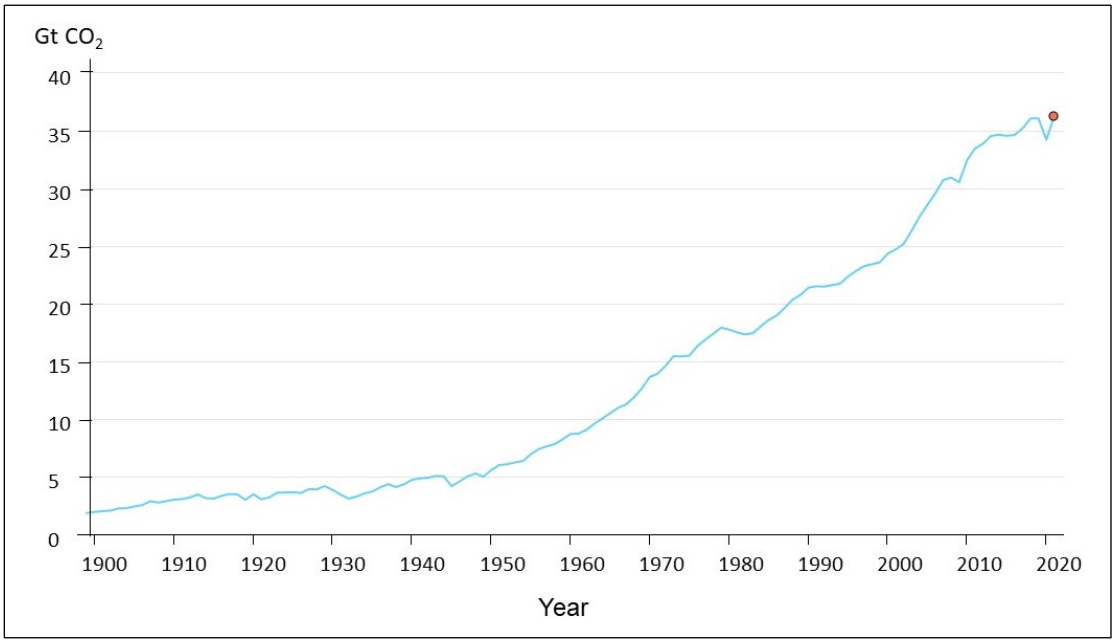

Figure 2-1 Fossil CO_2 emissions from energy combustion and industrial processes, 1900-2021 (adapted from IEA [11]).

2.1.2 CO_2 Emission Mitigation and Utilization

Scientists have linked the rapid increase of atmospheric CO_2 due to human activities with global climate change, and mitigating CO_2 has become a pressing matter. As a result, three main streams have been adopted to tackle the abundance of CO_2: *i*-carbon sequestration; *ii*-capture and storage (CCS); and *iii*- carbon capture utilization (CCU). Below we will review each of these streams.

2.1.2.1 Carbon Sequestration

Carbon sequestration consists of removing atmospheric CO_2 or from the emission source to prolong the storage of CO_2. Currently, there are four main strategies: *i*-oceanic carbon

sequestration (OCS), *ii*-geological carbon sequestration (GCS), and *iii*-biological carbon sequestration (BCS), and *iv*-mineral carbonation (MC) as shown in Fig. 2-2.

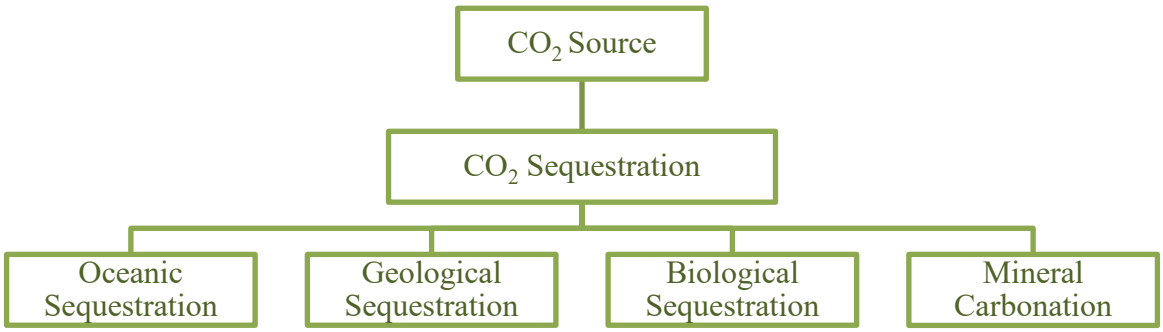

Figure 2-2 Main methods for carbon sequestration.

i- In the OCS, the carbon dioxide is captured from significant emission sources and injected into the ocean. Oceans absorb up to a third of the carbon released by human activity, somewhere around 2.6 GtC/yr [9]. OCS is one of the promising methods to sequester carbon due to the amount of CO_2 that oceans can absorb. Oceans cover approximately 70% of the surface of the Earth, with an average depth of about 3.7 km. The main drawback of this method is the ocean's pH change. CO_2 is a weak acidic gas, and the pH of the sea is reported to be around 8.1, which is alkaline, but if the ocean continues to absorb more CO_2, the pH decreases and will become more acidic. Ocean acidification could negatively affect marine species and alter the food chains [15].

ii- GCS is the process of storing CO_2 in deep geologic formations or rocks to reduce the atmospheric CO_2 level [16]. CO_2 is captured from primary emitter sources, transported by a pipeline, and injected into porous rock formations in geological basins. The CO_2 is mixed with water and pressurized until it becomes a liquid; once it enters the underground water, CO_2 is retained or trapped as carbonate [17]. Shortcomings of this method include the limitation of suitable type of reservoirs needed to sequester the CO_2, high economic cost, and environmental risks such as the impact on ecosystems, return to the atmosphere, trigger earthquakes, potential contamination of both soil and groundwater in the surrounding areas of the storage site [18,19].

iii- BCS involves the removal of CO_2 from the atmosphere by plants and microorganisms and its storage through soil, vegetation, woody products, and wetlands [20]. The beauty

of this method is that it is a natural path, and it may be economically feasible to reduce the atmospheric levels of CO_2. Plants sequester the soil's carbon through photosynthesis, which can be stored as soil organic carbon. Soil can also store carbon as carbonates. Furthermore, carbonates are inorganic materials with a carbon storage capacity of more than 70,000 years, while soil organic matter typically stores carbon for several decades.

iv- The MC process stores CO_2 from the atmosphere or direct emitters through the reaction of CO_2 with magnesium (Mg) or calcium (Ca) based minerals, where insoluble and thermodynamically stable carbonates are formed [21]. When the CO_2 produced from power plants and industrial processes is captured, compressed, and injected into alkaline rock to form solid carbonate species is called *carbon in situ mineralization* [22]. When the sequestration occurs above ground, using engineering processes, is known as *ex situ mineralization* [23]. The captured CO_2 can be recovered and recycled in numerous industrial processes for further applications. However, this method is associated with high costs and large energy consumption, thus, is limited to small emitters (>2.5 Mt CO_2) [24].

2.1.2.2 Carbon Capture and Storage

Carbon capture and storage (CCS) is a process that involves CO_2 separation from industrial and energy-related sources, transport to a storage location, and prolonged CO_2 escape to the atmosphere [25]. There are four significant methodologies for CCS: *i*- post-combustion capture, *ii*-pre-combustion capture, and *iii*-oxyfuel process as shown in Fig. 2-3.

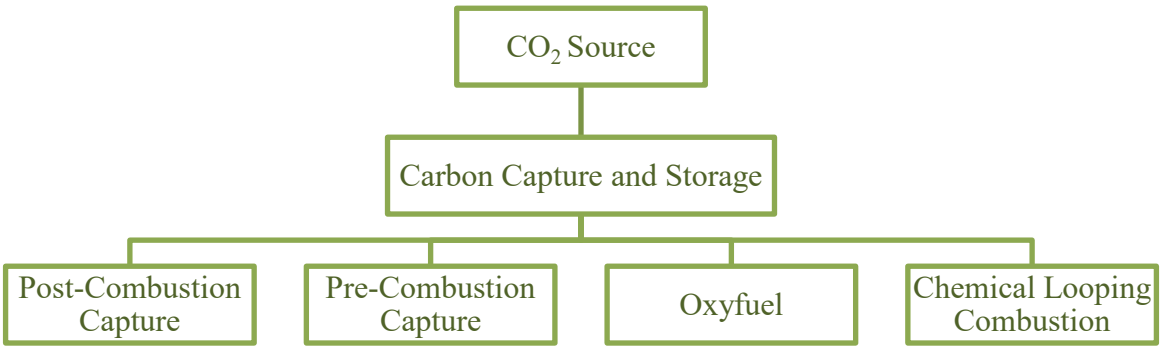

Figure 2-3 Main methods for carbon capture and storage.

i- Post-Combustions Carbon Capture

Post-combustions carbon capture and storage refers to separating CO_2 from flue gas derived from burning fossil fuels, namely oil, coal, and natural gas. Flue gas is a mixture of CO_2, N_2, some oxygenated compounds (SO_x, NO_x, H_2O, and O_2), and heavy metals. Currently, the most robust technology is amine scrubbing with several alkylamines in an aqueous solution to remove CO_2 from the flue gas [26]. The first significant large-scale CO_2 capture plant in the United States started at the Searles Valley Minerals Plant in Trona, California, in 1978, which is still active [27]. They adopted an amine scrubbing process to recover CO_2 from flue gas in the coal-fired plant. However, as a drawback, amine scrubbing is costly as large absorbers, extensive heat exchange requiring multiple parallel exchangers, and expensive compressor trains are needed. Besides, amines are lost through evaporation due to the high regeneration temperatures. Furthermore, the formation of corrosive species causes deterioration in the operating units [28].

ii- Pre-Combustion Capture

In pre-combustion capture, the fossil fuel is partially oxidized with oxygen, air, or steam to give mainly a synthesis gas (syngas) or fuel gas composed primarily of carbon monoxide (CO) and hydrogen (H_2) [29]. The CO is further reacted with steam in a catalytic reactor to produce CO_2 and more H_2. Finally, H_2 is further separated from CO_2 by a physical or chemical absorption process, resulting in a hydrogen-rich fuel with several applications, such as boilers, furnaces, gas turbines, engines, and fuel cells [30]. Pre-combustion capture is a well-established process with high CO_2 absorption efficiency. The operating pressure is 20–30 bar at high temperatures. Even though it is used in several chemical processes, including syngas production, this method lies in a complex and costly CO_2/H_2 separation [31].

iii- Oxyfuels

In oxyfuel combustion capture, the fuel is burned with nearly pure oxygen (typically between 95% and 97% O_2) mixed with recycled flue gas to enrich the concentration of CO_2 in the stream. For instance, in a conventional combustion process with air as a comburent, the resulting concentration of CO_2 is typically 12−16%v. dry basis, whereas in the oxyfuel process, the resulting concentration of CO_2 increases to 65−85%v dry basis [32]. Once flue gas is cooled and compressed to remove water leaves almost pure CO_2 [33]. This technology is well-established and can be

applied with slight modifications to existing power plants. The main drawback to oxyfuel combustion is the cost associated with producing large quantities of oxygen, including capital and energy costs [34].

iv- Chemical Looping Combustion

In the chemical looping combustion process, combustion or partial combustion uses a metal/metal oxide as an oxygen carrier to transfer oxygen from the air to fuel [35]. The process consists of two interconnected reactors: an air reactor and a fuel reactor. Air is introduced in the first reactor, and the oxygen carrier completes a cyclic loop between the two reactors. Thus, the fuel reacts with the oxygen carrier and produces CO_2 and H_2O. The reduced metal oxide is transported back to the air reactor for reoxidation. Pure CO_2 is recovered by condensing water vapor, removing the additional energy requirement for CO_2 separation. The main advantage of this method consists of the inherent separation of the N_2 from the produced CO_2 and the oxidizing air without additional separation costs. An essential aspect of this method is the mechanical and chemical stability of the oxygen carrier particles to endure repeated oxidation and reduction cycles [36].

2.1.2.3 Carbon Capture and Utilization

Using CO_2 as a valuable feedstock is attractive for two reasons: developing fuels and chemicals and mitigating CO_2 emissions. However, if all chemicals were based on CO_2 as feedstock, the CO_2 emissions would only be reduced by about 1% [37]. Around 200 $MtCO_2/y$ are used worldwide to produce chemicals and other non-chemicals [38].

CO_2 is the final product from all combustion processes of fossil fuels. Today, the amount of CO_2 produced by industrial sources is significantly higher than the current CO_2 demand. CO_2 can be captured and supplied from fossil fuel power plants and other production plants such as cement, iron and steel, refineries, pulp and paper, and chemical plants to produce energy and chemicals. Another source of CO_2 is to capture it from the atmosphere, which currently contains about 3000 Gt CO_2 [39]. In addition, direct air capture (DAC) allows capturing of indirect CO_2 emissions from mobile CO_2 sources [40].

Some industrial processes generate almost pure CO_2 streams, such as the synthesis of ammonia [41] and ethylene oxide [42], while the majority of sources produce CO_2 levels between 3 to 15% in the gas stream [30]. Hence, CO_2 is an abundant carbon feedstock accessible at a reasonable price. However, to exploit the carbon atom in CO_2 for value-added products, the reduction agent requires enough energy to overcome the thermodynamic and kinetic stability of CO_2. The principal reduction routes are shown in Fig. 2-4 and described below. Furthermore, for these reactions to be economically feasible, require that hydrogen comes from cheap renewable energy sources like solar energy (water electrolysis), biomass fermentation, or nuclear energy [43].

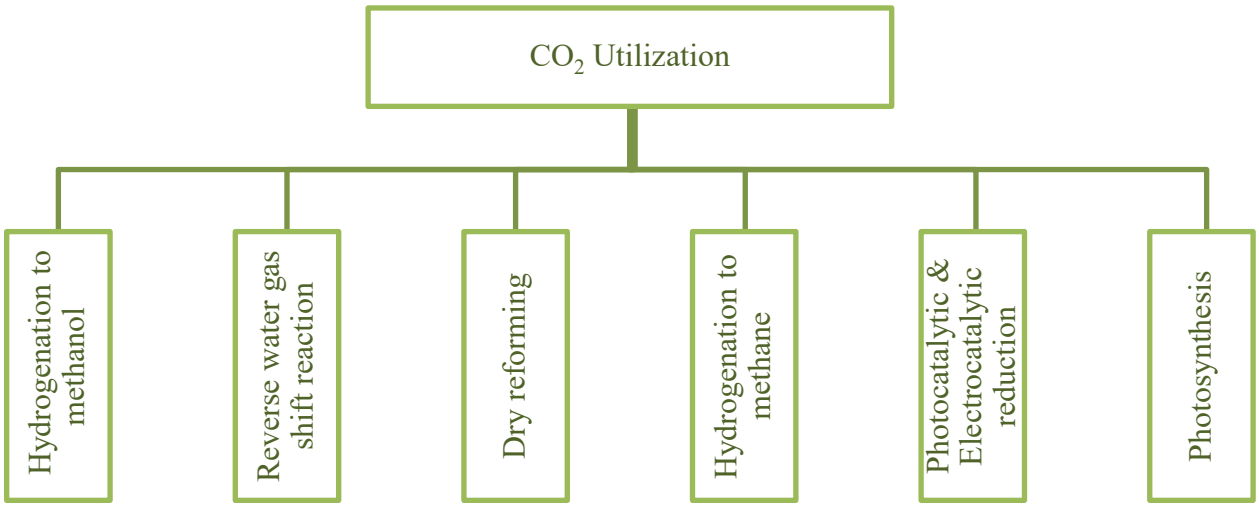

Figure 2-4 Main reduction routes for CO_2 valorization.

i- CO_2 Hydrogenation to Methanol

The methanol production from CO_2 requires a pure source of hydrogen as a reduction agent and a catalyst to overcome the thermodynamic stability of CO_2 [44]. In conventional methanol production, methanol is produced from fossil fuel (synthesis gas) via hydrogenation [45]. There are mainly two processes: high-pressure methanol synthesis and low-pressure methanol synthesis. The first process was employed in the 1920s to convert syngas at 25-35 MPa and 300-450 °C, using zinc oxide supported on chromium oxide [46]. This catalyst combination was stable to the sulfur and chlorine compounds in the syngas. In the 1950s, syngas was available at a higher purity,

and the catalytic system was replaced by copper catalysts, resulting in higher activity and selectivity [47].

The low-pressure catalyst for industrial application was developed and commercialized by Imperial Chemical Industries (ICI) (today: Johnson Matthey) in the 1960s, who discovered the technology to synthesize a more stable and active catalyst [48]. Currently, this technology is used worldwide to produce methanol from syngas. The catalyst is a composite of copper oxide, and zinc oxide supported on alumina, employed to produce methanol from syngas at 220-230 °C and 5 MPa. The high selectivity of the catalyst could provide a methanol purity of >99.5%. In addition, the low operating temperature reduced the formation of byproducts (e.g., methane, carbonyls, dimethyl ether, and alcohol). Furthermore, researchers discovered that a mixture of CO with 2-5 % of CO_2 not only enhanced the yield of methanol but also reduced the activation energy of the reaction [49].

Using the previous catalytic systems, many researchers started investigating the direct conversion of CO_2 to methanol. Lurgi reported the first CO_2 conversion to methanol at the 207th American Chemical Society national meeting in 1994 [37]. In 1996, Japan reported a pilot plant for CO_2 conversion [50–53]. Since 2012, Iceland has operated the first commercial plant to convert methanol from geogenic CO_2 at Carbon Recycle International (CRI) [7,54]. The plant's production capacity is 5 million liters of methanol, recycling about 5500 tons of CO_2 annually.

The CO_2 hydrogenation reaction to methanol (Eq. 2.1) is similar to the classic syngas conversion to methanol (Eq. 2.2). Both syntheses also have the water gas shift reaction (WGSR, Eq. 2.3).

$$CO_2 + 3H_2 \rightleftharpoons CH_3OH + H_2O \qquad \Delta H_{R\,(298K)} = -49\ kJmol^{-1} \qquad \text{Eq. 2.1}$$

$$CO + 2H_2 \rightleftharpoons CH_3OH \qquad \Delta H_{R\,(298K)} = -91\ kJmol^{-1} \qquad \text{Eq. 2.2}$$

$$CO + H_2O \rightleftharpoons CO_2 + H_2 \quad \text{(WGSR)} \qquad \Delta H_{R\,(298K)} = +41\ kJmol^{-1} \qquad \text{Eq. 2.3}$$

Reactions Eq. 2.1 and Eq. 2.2 are exothermic with a reduction in volume. Theoretically, methanol synthesis is favored by increasing pressure and decreasing temperature, with the

maximum conversion at the equilibrium composition. The WGSR is reversible, with the catalyst active in both directions and water formation.

From a practical point of view, replacing syngas with a pure CO_2 stream is attractive but not economically feasible. Although small amounts of CO_2 in the syngas hydrogenation improve methanol yield, when the syngas feed is replaced with pure CO_2 results in lower reaction rates because of the large amount of water formed as a byproduct [55]. With a high CO-to-CO_2 ratio, water formation decreases, and the catalyst activation rate increases. On the contrary, using pure CO_2 favors the formation of water, which causes significant catalyst deactivation and reduces the rate of methanol yield. Furthermore, the presence of water and CO in the feed increases the selectivity of other byproducts, such as dimethyl ether, methyl formate, methane, and alcohol [37].

Many catalysts have been examined regarding selectivity, long-term stability, and activity to improve the methanol selectivity and conversion rate. Cu catalysts were the basis for further catalyst development. Most of them consist of noble metals such as Cu, Pt, Pd, Ag, Re, and Au for hydrogen activation in combination with less noble metal oxides for carbon activation such as ZnO, Al_2O_3, and ZrO_2. Recently, materials such as SiO_2, metal oxides, carbon nanotubes, reduced graphene oxide, zeolite, metal-organic framework, or organic/inorganic hybrid materials have been used to support the active phase.

The methanol economy has a promising future among the technical routes for CO_2 reduction. Methanol is extensively used as a remarkably versatile chemical in different industries [56]. First, methanol can be mixed with conventional gasoline without requiring any technical modification in the vehicle [57]. Second, methanol can be used as a convenient energy carrier for hydrogen storage and transportation, as it is a suitable fuel. Furthermore, methanol is the feedstock of acetic acid and formaldehyde, which are used to make adhesives, foams, solvents, and windshield washer fluid. However, methanol can be an alternative platform for producing basic chemicals like C_2–C_4 olefins and aromatics. For example, in 2010, the world's first Methanol-to-olefins (MTO) commercial unit was constructed in Baotou, North China, by the Shenhua group with a unit capacity to produce 0.6 Mt polyethylene and polypropylene per year [58,59].

Methanol can also serve as the raw material to generate energy via fuel cells [60]. It can be used either in direct methanol fuel cells (DMFC) or indirectly as high-temperature proton exchange

membrane fuel cells (HT-PEMFC) [60]. The first technology uses liquid methanol and water to generate electricity via electrochemical reactions. DMFC is suitable for portable power generation due to its power range and rapid refueling properties [61]. In the second technology, HT-PEMFC, methanol is steam reformed into a hydrogen-rich gas mixture. Reformed methanol fuel cells are an efficient alternative to produce energy, with up to 50% efficiency [62].

Methanol could be the platform for other chemicals, such as dimethyl ether (DME), dimethyl carbonate (DMC), and methyl tert-butyl ether (MTBE), with fuel perspectives. DMC can be produced from methanol using the oxycarbonylation reaction [63]. DMC substitutes solvents such as toluene, ethyl acetate, butyl acetate, or acetone. Another part of DMC is employed in the pesticides and pharmaceutical industries. MTBE results from the reaction between methanol and isobutene on acidic exchange resins at moderate conditions. MTBE is a blending component for gasoline fuels due to its high octane number. MTBE is a requirement in the catalytic converters in passenger cars [64].

Lastly, methanol could be used as energy storage. For example, hydrogen could be generated from extra electric power from renewable sources via water splitting. Nevertheless, as a gas, hydrogen is very limited by the volumetric energy density and is challenging to store. So, an alternative consists of further reacting the hydrogen with CO_2 to form methane or methanol. On the other hand, methanol is a liquid that can easily be stored, transported, and dispensed under ambient conditions [65].

About 90% of methanol is produced from natural gas [37] involving three steps: *i*-production of synthesis gas (syngas), *ii*-conversion of the syngas into crude methanol, and *iii*-the distillation of the crude methanol to achieve the desired purity [56]. The methanol conversion requires high temperature and pressure (250–300 °C and 5–15 MPa) in the presence of a $Cu/ZnO/Al_2O_3$ catalyst [7].

Methanol can be produced from feedstocks such as biomass, biogas, and municipal waste [66,67]. Nevertheless, a fascinating alternative to fossil fuels would be the direct conversion of CO_2 to methanol (Eq. 2.1) with cheap renewable hydrogen. This solution would offer abundant feedstock and, to some extent, alleviate CO_2 emissions [7].

Nowadays, CO_2 conversion to methanol is in a research state, and others are at the pilot stage. Therefore, finding an optimal catalytic system and efficient technology that utilizes CO_2 as a renewable feedstock for chemicals and fuels is a daunting but exciting and necessary task.

ii- Reverse Water Gas Shift Reaction

A different approach for CO_2 utilization consists of the reverse water gas shift (RWGS) reaction (Eq. 2.4), which produces syngas, an essential building block of the chemical industry and the energy sector. CO and H_2, known as "synthesis gas or syngas," are the main products of the RWGS *via* CO_2 reduction. Syngas is mainly obtained from non-renewable sources such as coal, oil, and natural gas, but a transition to renewable sources such as biomass and organic waste is forthcoming.

$$CO_2 + H_2 \rightleftharpoons CO + H_2O \qquad \text{(RWGS)} \qquad \Delta H_{R\,(298K)} = -41\ kJmol^{-1} \qquad \text{Eq. 2.4}$$

RWGS reaction occurs as an independent or intermediate reaction of many other processes, such as CO_2 hydrogenation to methanol over a wide range of catalytic systems [68]. Moreover, RWGS is an equilibrium reaction with an endothermic character, thus thermodynamically favored at high temperatures. For instance, between 100 °C and 170 °C, methane is produced as an undesired product *via* the Sabatier reaction (Eq. 2.9), whereas CO becomes the primary product above 700 °C [69]. However, the high temperatures reduce the catalyst activity mainly through sintering and the reactor life by mechanical corrosion.

The RWGS reaction is frequently used with the Fischer –Tropsch (FT) synthesis to produce hydrocarbon fuels from syngas. The FT-Hydrocarbon Synthesis mainly produced linear alkane and alkene, both employed as liquid fuels and precursors for other valuable chemicals, and could be expressed as Eq. 2.5 and Eq. 2.6 [70,71]. Additionally, FT can form some oxygenate compounds such as methanol and ethanol (Eq. 2.7) [72]. The FT conversion reactions are typically catalyzed by metals (iron, cobalt, and sometime ruthenium) often supported on oxides such as silica or alumina. The reaction conditions selected for the FT reaction (typically 200-375 °C) will determine the final products, lower temperatures for long-chain alkanes and higher temperatures for shorter [73]. Hence, special attention has been placed on selecting the catalysts for the RWGS

reaction at a lower temperature range to avoid additional heat to the FT process, considering that RWGS requires higher temperatures to attain an acceptable degree of activity [74].

$(2n + 1)\ H_2 + n\ CO \rightarrow C_nH_{2n+2} + n\ H_2O$ (synthesis of alkanes) Eq. 2.5

$2n\ H_2 + n\ CO \rightarrow C_nH_{2n} + n\ H_2O$ (synthesis of alkenes) Eq. 2.6

$n\ CO + (2n + 1)\ H_2 = C_nH_{2n+1}OH + nH_2O$ (synthesis of alcohols) Eq. 2.7

Syngas has other relevant industrial applications apart from FT synthesis, including CO hydrogenation to methanol, one of the top five products sold in the world, and its synthesis and applications have been described here and elsewhere [60]. Other products of interest include ethanol, which is currently produced from fossil fuels via the hydration of ethene [75], or renewable sources by fermentation biomass-derived sugars [76]. Although extensive research for the direct conversion of syngas to ethanol, no commercial process is currently in place.

iii- CO_2-Reforming with Methane

Conventionally, methane is converted to syngas via the steam methane reforming process, as shown in Eq. 2.3 and Eq. 2.8 and:

$CO + H_2O \rightleftharpoons CO_2 + H_2$ (WGSR) $\Delta H_{R\ (298K)} = +41\ kJmol^{-1}$ Eq. 2.3

$CH_4 + H_2O \rightarrow CO + 3H_2$ (SRM) $\Delta H_{R\ (298K)} = +206\ kJmol^{-1}$ Eq. 2.8

$CO_2 + CH_4 \rightleftharpoons 2CO + 2H_2$ (Dry reforming) $\Delta H_{R\ (298K)} = +247\ kJmol^{-1}$ Eq. 2.9

When CO_2 replaces steam, the process is known as CO_2-reforming with methane or dry reforming, as shown in Eq. 2.9. This reaction offers valuable environmental advantages, including removal of greenhouse gases (methane and CO_2), biogas application [77], and conversion of natural gas to syngas using high concentrations of CO_2 [78]. The syngas from methane dry reforming results in a lower H_2/CO ratio, which is convenient for manufacturing oxygenated compounds and hydrocarbons from the FT synthesis [79]. Furthermore, syngas mixture from dry reforming has been considered energy storage for solar and nuclear sources [80]. For example, solar energy could convert methane and CO_2 to syngas, and syngas could be easily transported to places where energy sources are limited [81].

iv- CO_2 Methanation

The CO_2 methanation, also known as the Sabatier reaction (Eq. 2.10), is an essential route to CO_2 utilization. Using the power-to-gas[2] approach, CO_2 emissions could be recycled in conjunction with a large amount of renewable energy to produce methane [82]. The methanation process results in synthetic natural gas (SNG) comparable to non-renewable natural gas and compatible with the current infrastructure of natural gas distribution. Moreover, the methanation process could be incorporated into power-to-methane biogas plants, upgrading biogas to biomethane [83]. Furthermore, methanation reaction has been recognized as a vital process in assisting long-standing space exploration missions by space agencies [84].

The CO_2 methanation can be performed chemically or biologically. The chemical route is reversible and exothermic, and from a thermodynamic perspective, low temperature, and high-pressure favor methane formation. Typically, the process operates between 200 and 550 °C and pressures up to 100 bar, depending on the catalysts' activity and thermal stability [85]. However, the reduction of CO_2 to methane is kinetically limited and requires a catalyst to accomplish acceptable efficiency. For instance, various transition metals have been proven to catalyze CO_2, including Ru, Fe, Ni, Co, Rh, Pd, Pt, and Ir [86].

The CO_2 methanation's mechanism is still under debate, and more research is needed to identify the intermediate involved in the rate-determining step [86]. In the CO_2 methanation process, four important reactions take place: CO_2 methanation (Eq. 2.10), RWGS reaction (Eq. 2.4), CO methanation (Eq. 2.11), and reverse dry reforming (Eq. 2.12). Other side reactions produce coke and higher hydrocarbons, leading to catalyst fouling, blockage of catalyst pores, and collapse [87]. Another limitation of chemical methanation is the need for high-purity feedstocks to avoid catalyst deactivation due to impurities in the stream, such as hydrogen sulfide [88].

$$CO_2 + 4H_2 \rightleftharpoons CH_4 + 2H_2O \quad \text{(Sabatier reaction)} \quad \Delta H_{R\,(298K)} = -165\ kJmol^{-1} \qquad \text{Eq. 2.10}$$

$$CO + 3H_2 \rightleftharpoons CH_4 + H_2O \quad \text{(CO methanation)} \quad \Delta H_{R\,(298K)} = -206\ kJmol^{-1} \qquad \text{Eq. 2.11}$$

$$2CO + 2H_2 \rightleftharpoons CH_4 + CO_2 \quad \text{(Reverse dry reforming)} \quad \Delta H_{R\,(298K)} = -247\ kJmol^{-1} \qquad \text{Eq. 2.12}$$

[2] Power-to-gas refers to the process of converting renewable energy to gaseous energy carriers such hydrogen or methane via electrochemical water splitting.

The biological route uses biological catalysts through microorganisms to catalyze the methanation reaction [89]. Therefore, the reaction temperatures are between 37 and 65 °C and pressures from 1 – 15 bars to meet the optimum growth conditions of the microorganisms. The methanogens, a methane-producing bacterium, are the more robust microorganism to fluctuations in reactant gas supply and contaminants such as hydrogen sulfide. The main drawback of the biological process is the poor hydrogen gas-to-liquid mass transfer, resulting in lower space-time yield and a need for larger reactors [90].

v- Photocatalytic/Electrocatalytic CO_2 Reduction

Photocatalytic reduction of CO_2 was inspired by the natural process of photosynthesis, where most plants, algae, and even some microorganisms convert CO_2 and H_2O to carbohydrates and O_2 under sunlight at room temperature [91]. Many research groups have studied how to replicate the reduction of CO_2 with H_2O to organic compounds and CO. Fujishima, and Honda discovered the splitting of water into H_2 and O_2 using UV light-induced electrocatalysis in the presence of titanium dioxide (TiO_2) as photoanode in an electrochemical cell in 1972 [92]. Later on, their group reported the photocatalytic reduction of CO_2 in the presence of heterogeneous semiconductor powders suspended in an aqueous solution [93]. Since then, many semiconductors such as TiO_2, $SrTiO_3$, $Sr_2Nb_2O_7$, Zn_2GeO_4, Zn_2GaO_4, and Zn_2SnO_4 have been described to accomplish the activation of CO_2 with H_2O through photoreduction [94–98].

Electrocatalytic reduction of CO_2 is an additional pathway for the valorization of CO_2 to chemicals and fuels (Eq. 2.13). Promising results have been attained for the electrochemical reduction to CO, formate, hydrocarbons (*e.g.*, methane, ethene), and oxygenated compounds (e.g., methanol, ethanol), which can be used as feedstock and fuels, as well as serve as energy storage [99]. Nevertheless, the catalyst stability, catalytic activity, and product distribution are yet distant from commercialization without even considering the large amount of electricity required to overcome the high overpotentials for CO_2 reduction.[3]

$$CO_2 + H_2O \xrightleftharpoons{h\cdot\gamma} CO + H_2 + O_2 \qquad \Delta H_{R\,(298K)} = -41\ kJmol^{-1} \qquad \text{Eq. 2.13}$$

[3] "The "overpotential" corresponds to the difference between the applied potential at the working electrode and the equilibrium potential of the net redox reaction" [159].

Another innovative approach for CO_2 reduction consists in the photoelectrocatalytic route, which combines photocatalysis with electrocatalysis with some notorious benefits listed below:

(a) Using solar energy can reduce the applied voltage, decreasing electricity consumption.
(b) Using external voltage can enhance the separation and transfer of photogenerated carriers and obtain a higher density of photogenerated electrons for CO_2 reduction.
(c) Using split half cells can avoid the reoxidation of reactive products such as methanol.

vi- Photosynthesis

The biological CO_2 fixation via photosynthesis of all terrestrial plants and many photosynthetic microorganisms has received much attention [8]. Photosynthesis only requires sunlight, CO_2, and water to produce glucose (Eq. 2.14), which plants use to produce energy and other valuable chemicals such as cellulose, starch, and lipids. However, plants are predicted to contribute only with a 3-6% reduction of global CO_2 emissions [100]. Thus, the research has been centered on evaluating microalgae and cyanobacteria, owing to their faster growth rate and higher CO_2-fixation efficiency rate than terrestrial plants [101,102].

$$CO_2 + H_2O \rightleftharpoons \text{-CHO} + H_2O \qquad \Delta H_{R\,(298K)} = -2824\ kJmol^{-1} \qquad \text{Eq. 2.14}^4$$

Microalgae can employ one or more of their three main metabolic modes (photoautotrophy, heterotrophy, and mixotrophy) to incorporate captured carbon into various macromolecules and biochemical compounds [103]. These products can be upgraded and used as alternative fuels, organic drugs, ecological polymers, or livestock feed. For instance, the lipid content of microalgae is usually between 20-50% of the cell's dry weight and can be as high as 80% under certain conditions [104]. Furthermore, microalgal lipids with saturated and mono-saturated C_{14}–C_{20} fatty acids are used for renewable biofuel production, while polyunsaturated fatty acids with more than 20 carbon atoms are used as health food supplements [105].

Microalgae represent a promising source of valuable bio-based products, but the process still requires optimized cultivation technologies to boost growth rates and cell densities to improve efficiency [103]. Furthermore, when algae are produced on a large scale undergo a progressive

[4] ΔH_R value is taken for glucose as the fermentation product [160].

drop in productivity attributed to nonuniform light distribution. Algae's surface layer quickly reaches photosynthesis saturation, while the inner layers are light-limited. Thus, the cultivation of microalgae is still far from being commercially viable.

2.2 Glycerol as Value-Added Waste

Glycerol is a biomass-derived oxygenated hydrocarbon, recognized as a convenient and sustainable chemical platform found in all-natural fats and oils as fatty esters. Glycerol has many applications in cosmetics, food and beverages, and pharmaceuticals as a solvent and additive as a result of its particular physical and chemical properties [106]. The glycerol market value in 2021 was USD 2.5 billion and is projected to increase a 6.4% until 2027 [107].

2.2.1 Glycerol Physicochemical Properties

Glycerol, chemical formula $C_3H_8O_3$, is the simplest triol known as glycerine, propane-1,2,3-triol, 1,2,3-propanetriol, 1,2,3-trihydroxypropane, propanetriol, and glycyl alcohol. Natural or native glycerol is produced from natural feedstock, whereas synthetic glycerol is made from the petrochemical industry [108] (Table 2-1).

The hygroscopic property and complete miscibility with water and other organic compounds (Table 2-1) are attributed to the glycerol structure's three hydrophilic alcoholic hydroxyl groups [109]. These, along with the outstanding chemical and physical stability, non-toxic, sweet taste, and compatibility with many materials, rationalize the more than 1500 commercial end uses of glycerol listed in the literature from the field since 1945 [110,111].

Table 2-1 Main physicochemical properties of glycerol at 20 °C.

Chemical formula	$C_3H_8O_3$
Molecular mass	92.09382 g/mol
Density	1.261 g cm^{-3}
Viscosity	1.5 Pa.s
Boiling point	290 °C
Melting point	18.2 °C
Flash point	160 °C (closed up)
Surface tension	64.00 mN/m
Miscible	Water, methanol, ethanol, phenol, ethylene, propylene, trialkyl glycols, and the isomers of propanol, butanol, and pentanol
Partial miscible	Ethyl ether, ethyl acetate

The elasticity of the molecule favors the formation of both intra- and intermolecular hydrogen bonds, leading to a highly branched network resulting in high viscosity and boiling point [112]. Theoretical calculations indicate that the hydroxyl groups form a cyclic structure with three internal hydrogen bonds in the lowest energy state. At the same time, in the aqueous phase, the molecule stability depends on a combination of intramolecular hydrogen bonds and intermolecular hydration of hydroxyls (Fig. 2-5) [113]. Another molecular dynamic study on glycerol reported the relationship between temperature and viscosity. As a result, the intermolecular interactions weaken when temperature increases, decreasing viscosity [114].

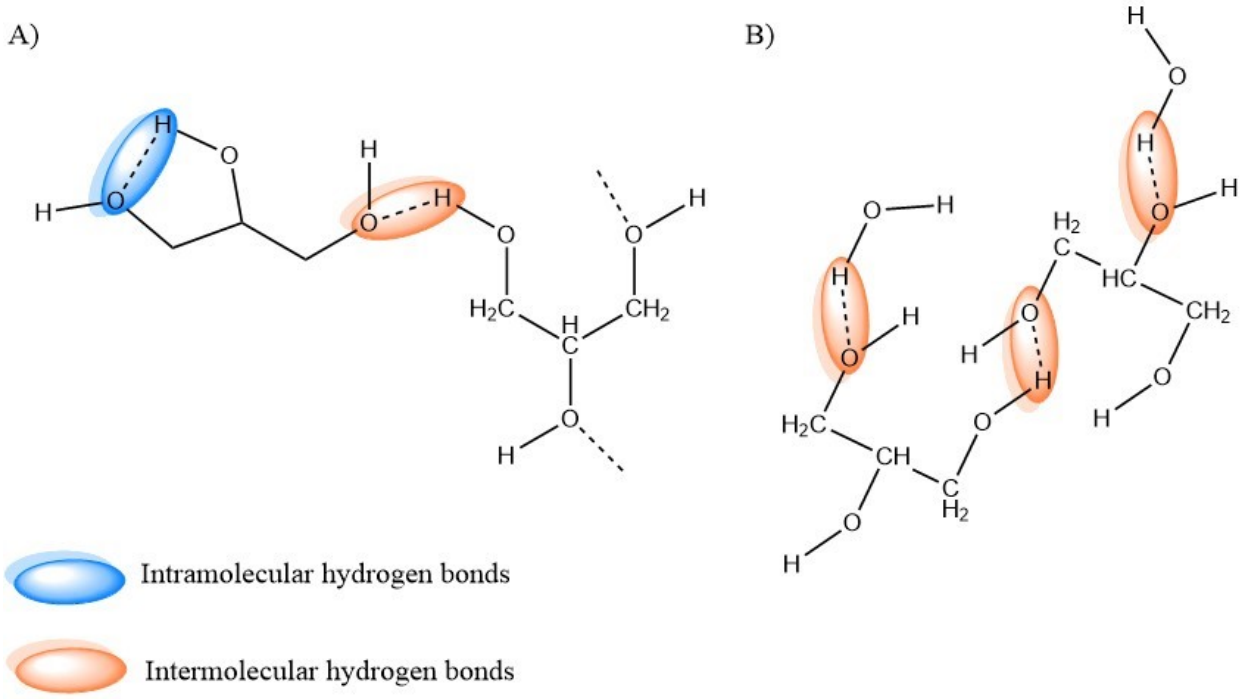

Figure 2-5 Schematic representation of intramolecular (blue) and intermolecular (orange) hydrogen bonds in (**a**) glycerol and (**b**) aqueous solution of glycerol**.**

The chemical structure of glycerol makes a highly versatile molecule, owing to the three hydroxyl groups, that can undergo many reactions and produces many value-added products such as ether, ester, carbonates, aldehyde, ketones, and polymerization (Fig. 2-6). The two terminal hydroxyl groups are more reactive than the internal secondary hydroxyl group and can undergo oxidation to aldehyde or carboxyl groups, nevertheless the secondary hydroxyl to carbonyl groups [115].

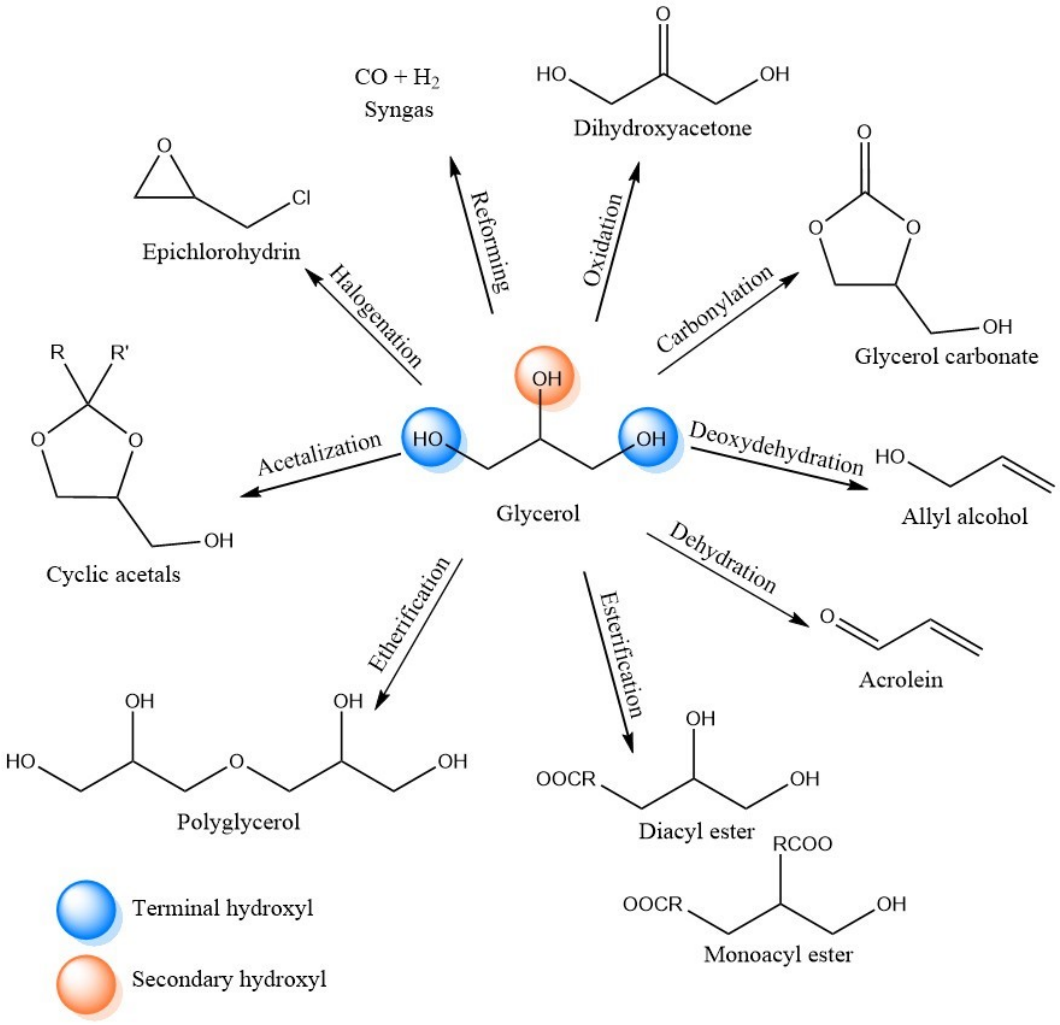

Figure 2-6 Different chemical transformations of glycerol to value-added products.

2.2.2 Synthetic Glycerol

Glycerol production has evolved since Carl Scheele's discovery in 1779 [116]. After Alfred Nobel invented the dynamite in 1866, glycerol was in great demand as raw material for nitroglycerin during World War I. At that time, glycerol produced by the soap industry failed to reach the market. Hence new factories were established in Europe, Russia, and the United States where synthetic glycerol was made through a microbial, low-yield sugar fermentation process. Afterward, synthetic glycerol was invented in Germany from petroleum feedstock adding chlorine to the propane molecule, which appears as a top fraction during crude oil distillation [117].

Synthetic glycerol has a high purity (99.7%), making it very suitable for use in the pharmaceutical industry.

During the 1990s, due to political changes and environmental concerns, biodiesel production grew significantly worldwide, which flooded the market with glycerol, causing glycerol market prices to enter a downward trend. As a result, the synthetic glycerol industry was hard hit, and many facilities closed down or reduced their production to meet the demand for specific pharma and food-grade products. On the bright side, the oversupply stimulated the research into new opportunities to utilize glycerol and develop methods to improve its quality.

2.2.3 Glycerol from Renewable Feedstocks

In nature, one molecule of glycerol appears attached, as the backbone, with three fatty acids to form a triglyceride. Triglycerides are a type of lipids present in plant cell walls, bacteria, algae, fish, and animal fats. The separation of fatty acids and glycerol is essential in many industries to obtain value products such as fatty acid methyl ester (FAME) in the biodiesel industry, where glycerol is the main byproduct. Other examples are the fatty acid industry through the hydrolysis of fats and soap production in a process known as saponification. In the following, these processes will be reviewed.

i- Transesterification Reaction of Lipids

FAME, also known as biodiesel, is a fuel substitute made from renewable materials and used in diesel engines. Potential biodiesel sources come from oil crops such as canola, palm or soybean, animal fats, and waste cooking oil, making it a sustainable alternative to diesel from fossil fuels [118]. The triglycerides present in the feedstock react with a molecule of alcohol, generally methanol, activated by a catalyst to produce biodiesel and glycerol in a transesterification process (Fig. 2-7). The most common catalysts used in biodiesel production are strong alkali catalysts, including sodium hydroxide (NaOH), potassium hydroxide (KOH), and sodium methoxide (CH_3ONa), and acid catalysts, such as sulfuric acid (H_2SO_4) and hydrochloride acid (HCl). As the reaction progress, there is a separation of two layers, the top layer, rich in biodiesel, and the bottom layer, rich in glycerol, due to density and polarities differences [119]. Throughout this process, about 100 kg of glycerol is generated as a byproduct for each ton of biodiesel.

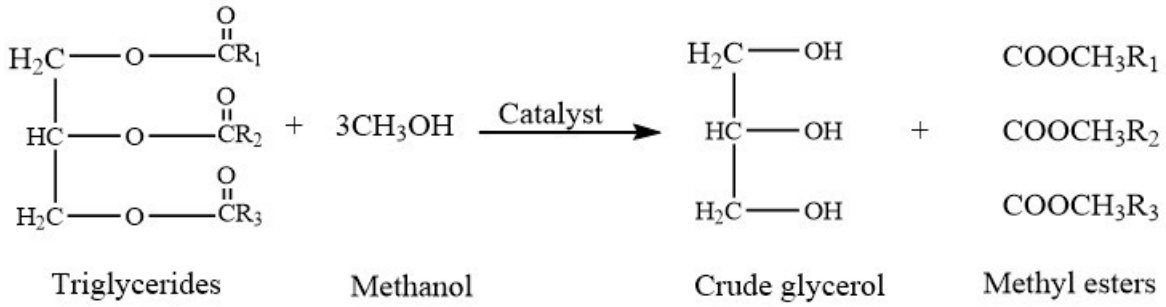

Figure 2-7 Transesterification reaction of triglycerides to biodiesel and crude glycerol.

After the separation process, the glycerol produced is labeled as "crude glycerol" because it is contaminated with the other compounds in biodiesel production, inhibiting its direct usage in industries. However, this crude glycerol may find some limited applications, for instance, as fuels [120], fuel additives [121], and animal diet additives [122]. Another method to enable its use is the purification of glycerol, as various purification methods and technologies are available today.

Nowadays, the biodiesel industry competes for almost all available natural and renewable feedstock; in 2000, it used roughly 14.5% of global fat and oil production, and in 2017, this number reached 26.3% [123]. In 2019, the global production of biodiesel reached 48 billion L generating 4.8 billion L of crude glycerol (Fig. 2-8) [124].

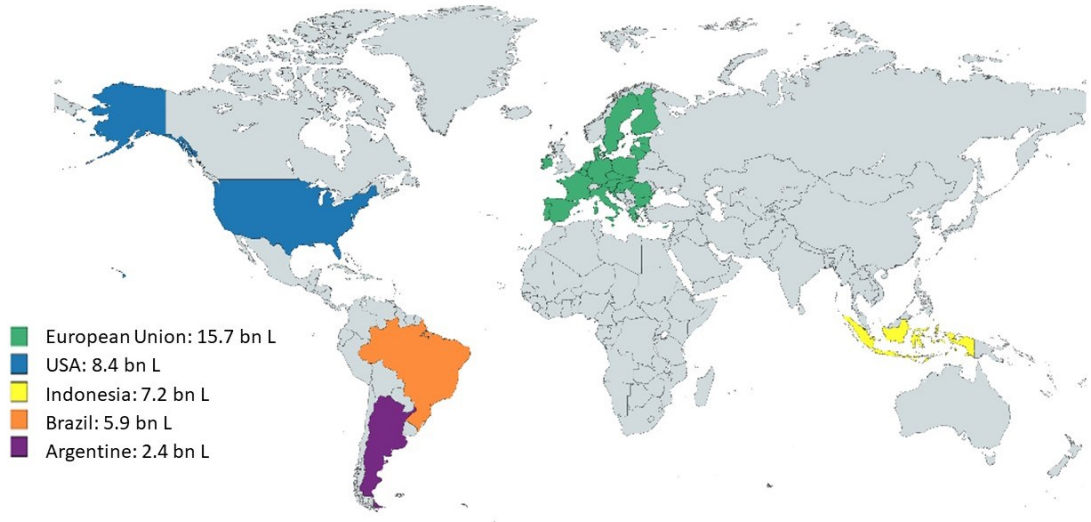

Figure 2-8 Global biodiesel and glycerol production in 2019 (Source: IEA 2020) [124].

ii- Saponification

Triglycerides can undergo alkaline saponification (Fig. 2-9), which is the process foundation of the soap-making industry. During saponification, the sodium hydroxide or potassium hydroxide breaks the ester bonds, via hydrolysis, between the fatty acids and glycerol of the triglyceride, resulting in a soap of alkali metal and glycerol [125]. Three molecules of soap are formed, and the interaction between one molecule of triglyceride and three molecules of alkali liberates one molecule of glycerol. Finally, the soap is filtered, and the filtrate contains 35% glycerol, free alkali, soluble soap, and some NaCl with suspended impurities.

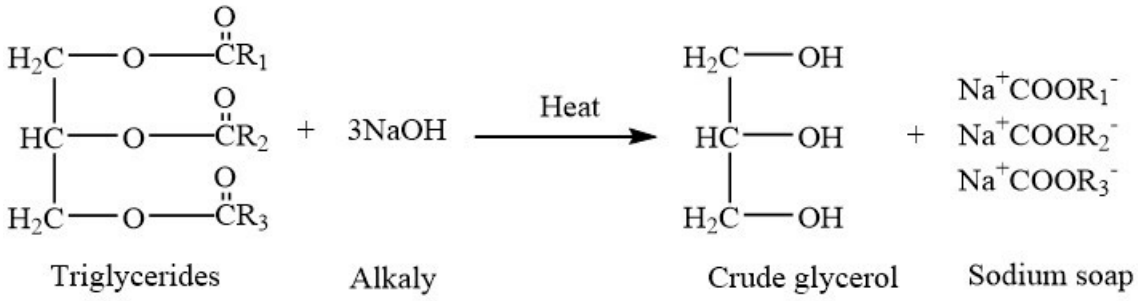

Figure 2-9 Saponification of triglyceride.

iii- Hydrolysis

The hydrolysis of fat and oils is used in the oleochemical industry to yield the corresponding fatty acids and glycerol as a byproduct. Hydrolysis is a reversible process where a hot water molecule breaks free the glycerol from the fatty acids (Fig. 2-10), and glycerol must be withdrawn continuously to drive the reaction to completion. Therefore, a high temperature (245 – 255 °C) and high pressure (2 – 6 MPa) are required to improve the solubility of the water phase into the fat and favor the reaction [123,126]. During the process, the final mixture contains a light fraction of fatty acids and a heavy fraction of glycerol and water (16% to 18%), called sweet water due to the natural sweetness of glycerol [123]. Thus, getting high-purity glycerol requires the removal of contaminants from the final hydrolysates through purification techniques.

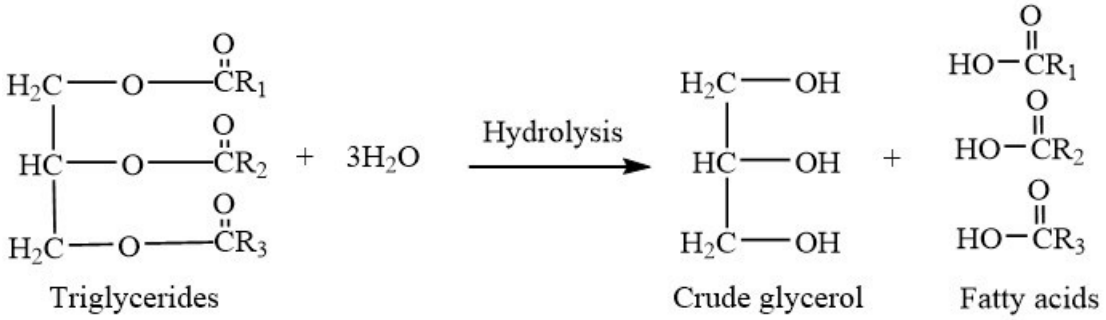

Figure 2-10 Hydrolysis of triglyceride used in the oleochemical industry.

2.2.4 Purification of Crude Glycerol

Crude glycerol composition may vary from source to source and depends on the industrial process. Next, Table 2-2 shows the main impurities of the glycerol-rich solution obtained by different methods. For example, the biodiesel industry produces between 60 wt.% and 70 wt.% refined glycerol from crude glycerol. On the other hand, the saponification process can make around 35 wt.% of pure glycerol, and the hydrolysis in the oleochemical industry, approximately 15 wt.% of glycerol could be purified to an 80 wt.% purity [127].

Table 2-2 Composition of the crude glycerol from various processes [127,128].

Component	**Transesterification (wt.%)**	**Saponification (wt. %)**	**Hydrolysis (wt. %)**
Glycerol	50-87	80	88-90
Ash	10	8.8	0.7-1.0
Water	10	6-7	8-9
MONG[a]	5	3-4	0.7-1.0
Trimethylene glycol	1	0.1	0.2

[a] MONG: matter organic non-glycerol.

So crude glycerol cannot be used in food, cosmetics, or pharmaceutical industries as they require a highly purified feedstock. Hence, some biodiesel producers refine glycerol to an acceptable purity level in dedicated refineries to sell it at a low price as technical grade (95,5%) or further refined to USP grade[5] or kosher/halal certified grade [129].[6] Various methods are used to purify crude glycerol, such as distillation, filtration, chemical treatment, ion-exchange, adsorption, extraction, and crystallization. Each purification technique uses various properties of crude glycerol. Table 2-3 compares the advantages and limitations of each of them.

According to different compositions of crude glycerol feedstock, many purification processes have been studied. Numerous techniques are combined sequentially to achieve high recovery and purification efficiency. For example, a combination of three purification steps, specifically neutralization, microfiltration, and ion-exchange resin, ungraded crude glycerol to a technical grade [130]. In a different study, purified glycerol was recovered at an average of 52 wt.% purity by the combination of acidification with sulfuric acid, filtration, decantation, neutralization, solvent extraction, and evaporation [131]. A non-distillation method resulted in purified glycerol with 86 wt.% by using chemical and physical treatments such as neutralization, saponification, and filtration [132]. Furthermore, crude glycerol was purified to a 93.3 wt.% purity at a laboratory scale by combining repeating cycles of acidification, phase separation, neutralization, and ethanol extraction [133]. A similar laboratory scale experiment combined acidification, polar solvent extraction, and activated carbon adsorption produced 95.7 wt.% glycerol purity at optimal conditions[134]. Depending on the composition of the crude glycerol and to obtain ultrahigh purity, adsorption by ion-exchange resin is included to remove salt traces. Usually, vacuum distillation at high temperatures (150-200 °C) must be employed as the final step to obtaining refined grade (>99.5 wt.%) glycerol. However, this step introduced enormous capital costs, making the process less economically feasible and more technologically demanding [135].

[5] USP grade: A chemical grade of sufficient purity (≥99.5 wt%) to meet or exceed requirements of the United States Pharmacopeia (USP).

[6] Kosher/halal certified grade: vegetable glycerol has to be prepared and maintained in compliance with the customs of the Jewish or Islamic religion.

Table 2-3 Crude glycerol purification methods.

Method	Advantage	Limitations	Reference
Distillation	• Easy and effective to remove methanol and water • Useful to separate high contents of salts and MONG	• Energy-intensive for vaporization • Causes thermal degradation	[136]
Vacuum distillation	• Conventional method • High-quality glycerol	• Energy-intensive • Non-economical for small and medium size manufacturing • Requires high maintenance • Sensitive to feed stream variations	[137–139]
Membrane filtration	• Low energy intensive • Easy to operate • Easy to scale-up • Flexible operation	• Not fully optimized for industrial scale	[140,141]
Chemical treatment	• Used as a neutralization step • High-quality fatty acids • Removal of soaps	• Low glycerol yield • Requires coupling with other methods to produce high-quality glycerol	[134,142,143]
Adsorption (Activated carbon)	• Reduces color • Inexpensive • Low energy intensive	• Limited to remove other impurities	[134,140]
Ion-exchange	• Low cost • Easy to scale-up • Simple process	• Further treatment for washing waters • High salt content requires resin chemical regeneration	[136,144,145]

		• Challenged for crude with high salt content	
Decantation	• Simple process • High purity glycerol	• Requires in combination with other methods • Too many steps • Not optimized	[146]
Crystallization	• High purity glycerol	• Require high-purity starting materials • It takes a long time • Phase equilibria limit yield	[147–149]

2.2.5 Glycerol to Value-Added Products

Glycerol is a highly functionalized molecule compared to hydrocarbons produced by the petroleum industry. Therefore, the purification process of crude glycerol is costly for small and medium-scale biodiesel plants [143]. However, due to its availability, crude glycerol has become very attractive to use as a carbon source to produce value-added products, providing a solution to the abundance of raw glycerol and serving as a renewable feedstock.

Several strategies based on biological and chemical conversions are being explored to utilize the surplus glycerol. Biological routes use microorganisms and enzymes either under aerobic or anaerobic conditions. For instance, ethanol and hydrogen have been obtained from crude glycerol using *Enterobacter aerogenes* through anaerobic fermentation [150]. Furthermore, lactic acid, which is employed in the food industry as a food preservative, fermentation agent, and flavor enhancer, is obtained from glycerol via fermentation using several microorganisms [151]. Besides, anaerobic digestion of glycerol also produced biogas [152]. On the other hand, challenges in the biological routes rest on the negative effect of the impurities of crude glycerol on the growth of cells and product formation. For example, an excess of salts or soap increases the yield of byproducts such as carbohydrates and lipids [153], and the presence of methanol changes the membrane fluidity and enzymatic activity [143].

Chemical routes for glycerol conversion are the most explored method, as the versatility of glycerol makes it possible to convert it to many useful intermediates or end-use products (Fig. 2-6) [154]. For instance, glycerol polymerization produces polyglycerols used in the food, detergent, and cosmetic -industries [155]. The acetalization or condensation of glycerol produces solketal, an oxygenated fuel additive, surfactant, and flavoring stabilizer [156]. In addition, the esterification of glycerol provides oxygenated fuel additives such as polyglycerol ester, acylated esters, glyceryl diacetate, and glyceryl triacetate [157]. Another example is the synthesis of allyl alcohols produced from the deoxydehydration of glycerol via a metal-catalyzed or metal-free route. Allyl alcohol is an additive in flame-resistant materials, drying oils, and plasticizers [158].

In conclusion, new sources of renewable energy and materials are needed in the short and long terms for a sustainable economy and climate change fight. There are several possibilities with technologies at different phases of commercial development, and other options are still in their infancy. Researchers, businesspeople, and governments are in a race to find feasible solutions to mitigate global warming and the possible shortage of the world's oil reserves. Nevertheless, these solutions require near-zero greenhouse gas (GHG) emissions that use Earth-available non-toxic materials. In addition, these materials could be the byproducts of new and established technologies, which should be investigated and utilized to reduce the overall cost and the carbon footprint.

2.3 References

[1] Soeder DJ. Fossil fuels and climate change. Fracking Environ. A Sci. Assess. Environ. risks from Hydraul. Fract. Foss. fuels, Cham: Springer International Publishing; 2021, p. 155–85.

[2] Bohmer N, Roussiere T, Kuba M, A Schunk S. Valorisation of glycerol as renewable feedstock: comparison of the exploration of chemical transformation methods aided by high hroughput Experimentation. Comb Chem High Throughput Screen 2012;15:123–35.

[3] Vu TTN, Desgagnés A, Iliuta MC. Efficient approaches to overcome challenges in material development for conventional and intensified CO2 catalytic hydrogenation to CO, methanol, and DME. Appl Catal A Gen 2021;617:118119.

[4] IEA. Global Energy Review: CO2 Emissions in 2021. https://www.iea.org/reports/global-energy-review-co2-emissions-in-2021-2.

[5] Amouroux J, Siffert P. Carbon dioxide: a raw material and a future chemical fuel for a sustainable energy industry. IOP Conf. Ser. Mater. Sci. Eng., vol. 19, 2011, p. 012001.

[6] Chase MW, (US) NISO. NIST-JANAF thermochemical tables. American Chemical Society Washington, DC; 1998.

[7] Olah GA. Beyond oil and gas: the methanol economy. Angew Chemie Int Ed 2005;44:2636–9.

[8] Gonzalez-Meler MA. Plant respiration and elevated atmospheric CO2 concentration: cellular responses and global significance. Ann Bot 2004;94:647–56.

[9] Friedlingstein P, O'Sullivan M, Jones MW, Andrew RM, Hauck J, Olsen A, et al. Global carbon budget 2020. Earth Syst Sci Data 2020;12:3269–340.

[10] Stocker TF, Qin D, Plattner G-K, Tignor M, Allen SK, Boschung J, et al. Climate change 2013: the physical science basis. Contribution of working group I to the fifth assessment report of the Intergovernmental Panel on climate change. Cambridge University Press, Cambridge, United Kingdom and New York, NY, USA: 2013.

[11] IEA (2022), Global energy review: CO2 emissions in 2021, IEA, Paris 2022.

[12] US EPA. Sources of greenhouse gas emissions 2022. https://www.epa.gov/ghgemissions/sources-greenhouse-gas-emissions (accessed October 16, 2022).

[13] Arneth A, Sitch S, Pongratz J, Stocker BD, Ciais P, Poulter B, et al. Historical carbon dioxide emissions caused by land-use changes are possibly larger than assumed. Nat Geosci 2017;10:79–84.

[14] O'Neill BC, Tebaldi C, van Vuuren DP, Eyring V, Friedlingstein P, Hurtt G, et al. The scenario model intercomparison project (scenario MIP) for CMIP6. Geosci Model Dev 2016;9:3461–82.

[15] Archer D, Eby M, Brovkin V, Ridgwell A, Cao L, Mikolajewicz U, et al. Atmospheric lifetime of fossil fuel carbon dioxide. Annu Rev Earth Planet Sci 2009;37:117–34.

[16] Zhang D, Song J. Mechanisms for geological carbon sequestration. Procedia IUTAM 2014;10:319–27.

[17] Fagorite VI, Onyekuru SO, Opara AI, Oguzie EE. The major techniques, advantages, and pitfalls of various methods used in geological carbon sequestration. Int J Environ Sci Technol 2022:1–30.

[18] Pruess K. Leakage of CO2 from geologic storage: Role of secondary accumulation at shallow depth. Int J Greenh Gas Control 2008;2:37–46.

[19] Xie X, Economides MJ. The impact of carbon geological sequestration. All Days, SPE Americas E&P Envrironmenatl and Safety Conference; 2009.

[20] Farrelly DJ, Everard CD, Fagan CC, McDonnell KP. Carbon sequestration and the role of biological carbon mitigation: A review. Renew Sustain Energy Rev 2013;21:712–27.

[21] Thonemann N, Zacharopoulos L, Fromme F, Nühlen J. Environmental impacts of carbon capture and utilization by mineral carbonation: A systematic literature review and meta life cycle assessment. J Clean Prod 2022;332:130067.

[22] Gadikota G. Carbon mineralization pathways for carbon capture, storage and utilization. Commun Chem 2021;4:1–5.

[23] Gerdemann SJ, O'Connor WK, Dahlin DC, Penner LR, Rush H. Ex situ aqueous mineral carbonation. Environ Sci Technol 2007;41:2587–93.

[24] Neeraj, Yadav S. Carbon storage by mineral carbonation and industrial applications of CO2. Mater Sci Energy Technol 2020;3:494–500.

[25] Metz, Bert and Davidson, Ogunlade and De Coninck, H and Loos, M and Meyer L. Intergovernmental panel on climate change special report on carbon dioxide capture and storage. Cambridge, UK New York, USA 2005.

[26] Rochelle GT. Amine scrubbing for CO2 capture. Science (80-) 2009;325:1652–4.

[27] Barchas R, Davis R. The Kerr-McGee/ABB Lummus Crest technology for the recovery of CO2 from stack gases. Energy Convers Manag 1992;33:333–40.

[28] Guo B, Ghalambor A. Dehydration. Nat Gas Eng Handb 2005:143–71.

[29] Jansen D, Gazzani M, Manzolini G, Dijk E van, Carbo M. Pre-combustion CO2 capture. Int J Greenh Gas Control 2015;40:167–87.

[30] Metz, B., Davidson, O. De Coninck, H.C. Loos, M., Meyer L. IPCC special report on carbon dioxide capture and storage. 2005.

[31] Olabi AG, Obaideen K, Elsaid K, Wilberforce T, Sayed ET, Maghrabie HM, et al. Assessment of the pre-combustion carbon capture contribution into sustainable development goals SDGs using novel indicators. Renew Sustain Energy Rev 2022;153:111710.

[32] Stanger R, Wall T, Spörl R, Paneru M, Grathwohl S, Weidmann M, et al. Oxyfuel combustion for CO2 capture in power plants. Int J Greenh Gas Control 2015;40:55–125.

[33] Nemitallah MA, Habib MA, Badr HM, Said SA, Jamal A, Ben-Mansour R, et al. Oxy-fuel combustion technology: current status, applications, and trends. Int J Energy Res 2017;41:1670–708.

[34] Miller BG. Carbon dioxide emissions reduction and storage. Clean Coal Eng. Technol., Elsevier; 2017, p. 609–68.

[35] Lyngfelt A. Chemical looping combustion: status and development challenges. Energy & Fuels 2020;34:9077–93.

[36] Nandy A, Loha C, Gu S, Sarkar P, Karmakar MK, Chatterjee PK. Present status and overview of chemical looping combustion technology. Renew Sustain Energy Rev 2016;59:597–619.

[37] Bertau M, Offermanns H, Plass L, Schmidt F, Wernicke H-J. Methanol: the basic chemical and energy feedstock of the future. Springer; 2014.

[38] Aresta M, Dibenedetto A, Angelini A. The changing paradigm in CO2 utilization. J CO2 Util 2013;3:65–73.

[39] von der Assen N, Müller LJ, Steingrube A, Voll P, Bardow A. Selecting CO2 sources for CO2 utilization by environmental-Merit-Order curves. Environ Sci Technol 2016;50:1093–101.

[40] Kumar A, Madden DG, Lusi M, Chen K, Daniels EA, Curtin T, et al. Direct air capture of CO2 by physisorbent materials. Angew Chemie Int Ed 2015;54:14372–7.

[41] Liu X, Elgowainy A, Wang M. Life cycle energy use and greenhouse gas emissions of ammonia production from renewable resources and industrial by-products. Green Chem 2020;22:5751–61.

[42] Bains P, Psarras P, Wilcox J. CO2 capture from the industry sector. Prog Energy Combust Sci 2017;63:146–72.

[43] Crabtree GW, Dresselhaus MS, Buchanan M V. The hydrogen economy. Phys Today 2004;57:39–44.

[44] Ganesh I. Conversion of carbon dioxide into methanol – a potential liquid fuel: Fundamental challenges and opportunities (a review). Renew Sustain Energy Rev 2014;31:221–57.

[45] Lange J-P. Methanol synthesis: a short review of technology improvements. Catal Today 2001;64:3–8.

[46] Lloyd L. Hanbook of industrial catalysts. Springer Science & Business Media; 2011.

[47] Höppener RH, Doesburg EBM, Scholten JJF. Preparation and characterization of stable copper/zinc oxide/alumina catalysts for methanol systhesis. Appl Catal 1986;25:109–19.

[48] Rogerson PL. Imperial chemical industries' low pressure methanol plant. Proc. Chem. Eng. Prog. Symp. Ser., vol. 66, 1970, p. 28–34.

[49] Liu X-M, Lu GQ, Yan Z-F, Beltramini J. Recent advances in catalysts for methanol synthesis via hydrogenation of CO and CO2. Ind Eng Chem Res 2003;42:6518–30.

[50] Ushikoshi K, Mori K, Kubota T, Watanabe T, Saito M. Methanol synthesis from CO2 and H2 in a bench-scale test plant. Appl Organomet Chem 2000;14:819–25.

[51] Saito M, Takeuchi M, Fujitani T, Toyir J, Luo S, Wu J, et al. Advances in joint research between NIRE and RITE for developing a novel technology for methanol synthesis from CO2 and H2. Appl Organomet Chem 2000;14:763–72.

[52] Toyir J, Miloua R, Elkadri NE, Nawdali M, Toufik H, Miloua F, et al. Sustainable process for the production of methanol from CO2 and H2 using Cu/ZnO-based multicomponent catalyst. Phys Procedia 2009;2:1075–9.

[53] Saito M. R&D activities in Japan on methanol synthesis from CO2 and H2. Catal Surv from Asia 1998;2:175–84.

[54] Kourkoumpas DS, Papadimou E, Atsonios K, Karellas S, Grammelis P, Kakaras E. Implementation of the power to methanol concept by using CO2 from lignite power plants: Techno-economic investigation. Int J Hydrogen Energy 2016;41:16674–87.

[55] Sahibzada M, Metcalfe IS, Chadwick D. Methanol synthesis from CO/CO2/H2 over Cu/ZnO/Al2O3 at differential and finite conversions. J Catal 1998;174:111–8.

[56] Dalena F, Senatore A, Marino A, Gordano A, Basile M, Basile A. Methanol production and applications: an overview. Methanol, Elsevier; 2018, p. 3–28.

[57] Galindo Cifre P, Badr O. Renewable hydrogen utilisation for the production of methanol. Energy Convers Manag 2007;48:519–27.

[58] Yang M, Fan D, Wei Y, Tian P, Liu Z. Recent progress in methanol-to-olefins (MTO) catalysts. Adv Mater 2019;31:1902181.

[59] Tian P, Wei Y, Ye M, Liu Z. Methanol to olefins (MTO): from fundamentals to commercialization. ACS Catal 2015;5:1922–38.

[60] Simon Araya S, Liso V, Cui X, Li N, Zhu J, Sahlin SL, et al. A review of the methanol economy: the fuel cell route. Energies 2020;13.

[61] Mekhilef S, Saidur R, Safari A. Comparative study of different fuel cell technologies. Renew Sustain Energy Rev 2012;16:981–9.

[62] Zhang J, Xie Z, Zhang J, Tang Y, Song C, Navessin T, et al. High temperature PEM fuel cells. J Power Sources 2006;160:872–91.

[63] Keller N, Rebmann G, Keller V. Catalysts, mechanisms and industrial processes for the dimethylcarbonate synthesis. J Mol Catal A Chem 2010;317:1–18.

[64] Ziyang Z, Hidajat K, Ray AK. Determination of adsorption and kinetic parameters for methyl tert-butyl ether synthesis from tert-butyl alcohol and methanol. J Catal 2001;200:209–21.

[65] Räuchle K, Plass L, Wernicke H-J, Bertau M. Methanol for renewable energy storage and utilization. Energy Technol 2016;4:193–200.

[66] Roode-Gutzmer QI, Kaiser D, Bertau M. Renewable methanol synthesis. ChemBioEng Rev 2019;6:209–36.

[67] Deka TJ, Osman AI, Baruah DC, Rooney DW. Methanol fuel production, utilization, and techno-economy: a review. Environ Chem Lett 2022.

[68] Fujitani T, Nakamura I, Uchijima T, Nakamura J. The kinetics and mechanism of methanol synthesis by hydrogenation of CO2 over a Zn-deposited Cu (111) surface. Surf Sci 1997;383:285–98.

[69] González-Castaño M, Dorneanu B, Arellano-García H. The reverse water gas shift reaction: a process systems engineering perspective. React Chem Eng 2021;6:954–76.

[70] Riedel T, Claeys M, Schulz H, Schaub G, Nam S-S, Jun K-W, et al. Comparative study of Fischer–Tropsch synthesis with H2/CO and H2/CO2 syngas using Fe- and Co-based catalysts. Appl Catal A Gen 1999;186:201–13.

[71] Zhang Q, Cheng K, Kang J, Deng W, Wang Y. Fischer-Tropsch catalysts for the production of hydrocarbon fuels with high selectivity. ChemSusChem 2014;7:1251–64.

[72] Krylova AY. Products of the Fischer-Tropsch synthesis (A Review). Solid Fuel Chem 2014;48:22–35.

[73] Pastor-Pérez L, Baibars F, Le Sache E, Arellano-García H, Gu S, Reina TR. CO2 valorisation via Reverse Water-Gas Shift reaction using advanced Cs doped Fe-Cu/Al2O3 catalysts. J CO2 Util 2017;21:423–8.

[74] de Klerk A, Maitlis PM. Greener Fischer-Tropsch processes for fuels and feedstocks. Wiley; 2013.

[75] Katada N, Iseki Y, Shichi A, Fujita N, Ishino I, Osaki K, et al. Production of ethanol by vapor phase hydration of ethene over tungsta monolayer catalyst loaded on titania. Appl Catal A Gen 2008;349:55–61.

[76] Saha BC, Nichols NN, Qureshi N, Kennedy GJ, Iten LB, Cotta MA. Pilot scale conversion of wheat straw to ethanol via simultaneous saccharification and fermentation. Bioresour Technol 2015;175:17–22.

[77] Pham Minh D, Siang TJ, Vo D-VN, Phan TS, Ridart C, Nzihou A, et al. Hydrogen production from biogas reforming: an overview of steam reforming, dry reforming, dual reforming, and tri-reforming of methane. Hydrog. Supply Chain., Elsevier; 2018, p. 111–66.

[78] Boretti A, Banik BK. Advances in hydrogen production from natural gas reforming. Adv Energy Sustain Res 2021;2:2100097.

[79] Wurzel T, Malcus S, Mleczko L. Reaction engineering investigations of CO2 reforming in a fluidized-bed reactor. Chem Eng Sci 2000;55:3955–66.

[80] Agrafiotis C, von Storch H, Roeb M, Sattler C. Hydrogen production by solar thermal methane reforming. Transit. to Renew. Energy Syst., Weinheim, Germany: Wiley-VCH Verlag GmbH & Co. KGaA; 2013, p. 451–82.

[81] Wang F, Ouyang D, Zhou Z, Page SJ, Liu D, Zhao X. Lignocellulosic biomass as sustainable feedstock and materials for power generation and energy storage. J Energy Chem 2021;57:247–80.

[82] Vogt C, Monai M, Kramer GJ, Weckhuysen BM. The renaissance of the Sabatier reaction and its applications on Earth and in space. Nat Catal 2019;2:188–97.

[83] Mhadmhan S, Ngamcharussrivichai C, Hinchiranan N, Kuchonthara P, Li Y, Wang S, et al. Direct biogas upgrading via CO2 methanation to high-quality biomethane over NiMg/CNT-SiO2 fiber catalysts. Fuel 2022;310:122289.

[84] Murdoch K, Goldblatt L, Carrasquillo R, Harris D. Sabatier methanation reactor for space exploration. 1st Sp. Explor. Conf. Contin. Voyag. Discov., Reston, Virigina: American Institute of Aeronautics and Astronautics; 2005.

[85] Rönsch S, Schneider J, Matthischke S, Schlüter M, Götz M, Lefebvre J, et al. Review on methanation – From fundamentals to current projects. Fuel 2016;166:276–96.

[86] Frontera P, Macario A, Ferraro M, Antonucci P. Supported catalysts for CO2 methanation: a review. Catalysts 2017;7:59.

[87] Strucks P, Failing L, Kaluza S. A short review on Ni-catalyzed methanation of CO2: reaction mechanism, catalyst deactivation, dynamic operation. Chemie Ing Tech 2021;93:1526–36.

[88] Götz M, Lefebvre J, Mörs F, McDaniel Koch A, Graf F, Bajohr S, et al. Renewable Power-to-Gas: A technological and economic review. Renew Energy 2016;85:1371–90.

[89] Enzmann F, Mayer F, Rother M, Holtmann D. Methanogens: biochemical background and biotechnological applications. AMB Express 2018;8:1.

[90] Bailera M, Lisbona P, Romeo LM, Espatolero S. Power to gas projects review: lab, pilot and demo plants for storing renewable energy and CO2. Renew Sustain Energy Rev 2017;69:292–312.

[91] Butburee T, Chakthranont P, Phawa C, Faungnawakij K. Beyond artificial photosynthesis: prospects on photobiorefinery. ChemCatChem 2020;12:1873–90.

[92] Fujishima A, Honda K. Electrochemical photolysis of water at a semiconductor electrode. Nature 1972;238:37–8.

[93] Inoue T, Fujishima A, Konishi S, Honda K. Photoelectrocatalytic reduction of carbon dioxide in aqueous suspensions of semiconductor powders. Nature 1979;277:637–8.

[94] Kou J, Gao J, Li Z, Yu H, Zhou Y, Zou Z. Construction of visible-light-responsive SrTiO3 with enhanced CO2 adsorption ability: highly efficient photocatalysts for artifical photosynthesis. Catal Letters 2015;145:640–6.

[95] Kodera M, Moriya Y, Katayama M, Hisatomi T, Minegishi T, Domen K. Investigation on nitridation processes of Sr2Nb2O7 and SrNbO3 to SrNbO2N for photoelectrochemical water splitting. Sci Rep 2018;8:15849.

[96] Yan S, Wang J, Gao H, Wang N, Yu H, Li Z, et al. Zinc gallogermanate solid solution: a novel photocatalyst for efficiently converting CO2 into solar fuels. Adv Funct Mater 2013;23:1839–45.

[97] Li X, Sun Y, Xu J, Shao Y, Wu J, Xu X, et al. Selective visible-light-driven photocatalytic CO2 reduction to CH4 mediated by atomically thin CuIn5S8 layers. Nat Energy 2019;4:690–9.

[98] Yan S, He Z, Zhou G, Yu Y, Cao Y. Hexagonal Zn2SnO4 nanoplates self-doped with Sn4+ ions towards efficient photoreduction of CO2 into CH4. Mater Sci Semicond Process 2021;130:105818.

[99] Hou S, Dong J, Zhao B. Formation of C-X Bonds in CO2 chemical fixation catalyzed by metal−organic frameworks. Adv Mater 2020;32:1806163.

[100] Cuellar-Bermudez SP, Garcia-Perez JS, Rittmann BE, Parra-Saldivar R. Photosynthetic bioenergy utilizing CO2: an approach on flue gases utilization for third generation biofuels. J Clean Prod 2015;98:53–65.

[101] Costa JAV, Linde GA, Atala DIP, Mibielli GM, Krüger RT. Modelling of growth conditions for cyanobacterium Spirulina platensis in microcosms. World J Microbiol Biotechnol 2000;16:15–8.

[102] Daneshvar E, Wicker RJ, Show P-L, Bhatnagar A. Biologically-mediated carbon capture and utilization by microalgae towards sustainable CO2 biofixation and biomass valorization – A review. Chem Eng J 2022;427:130884.

[103] Abreu AP, Morais RC, Teixeira JA, Nunes J. A comparison between microalgal autotrophic growth and metabolite accumulation with heterotrophic, mixotrophic and photoheterotrophic cultivation modes. Renew Sustain Energy Rev 2022;159:112247.

[104] Chisti Y. Biodiesel from microalgae. Biotechnol Adv 2007;25:294–306.

[105] Maltsev Y, Maltseva K. Fatty acids of microalgae: diversity and applications. Rev Environ Sci Bio/Technology 2021;20:515–47.

[106] Luo X, Ge X, Cui S, Li Y. Value-added processing of crude glycerol into chemicals and polymers. Bioresour Technol 2016;215:144–54.

[107] Glycerol Market Size, Share & Trends Analysis Report By Source (Biodiesel, Fatty Alcohol, Fatty Acids, Soaps), By Type (Crude, Refined), By End Use, By Region, And Segment Forecasts, 2021 - 2027 n.d. https://www.grandviewresearch.com/industry-analysis/glycerol-market# (accessed July 5, 2022).

[108] Ciriminna R, Pina C Della, Rossi M, Pagliaro M. Understanding the glycerol market. Eur J Lipid Sci Technol 2014;116:1432–9.

[109] Gregory SR. Physical properties of glycerine. Glycerine, CRC Press; 2018, p. 113–56.

[110] Leffingwell G, Lesser MA. Glycerin, its industrial and commercial applications. Chemical publishing, New York; 1945.

[111] Pagliaro M, Rossi M. The future of glycerol. 2008.

[112] Chelli R, Procacci P, Cardini G, Della Valle RG, Califano S. Glycerol condensed phases Part I. A molecular dynamics study. Phys Chem Chem Phys 1999;1:871–7.

[113] Callam CS, Singer SJ, Lowary TL, Hadad CM. Computational analysis of the potential energy surfaces of glycerol in the gas and aqueous phases: effects of level of theory, basis set, and solvation on strongly intramolecularly hydrogen-bonded systems. J Am Chem Soc 2001;123:11743–54.

[114] Moghaddam MB, Goharshadi EK, Moosavi F. Glycerol revisited molecular dynamic simulations of structural, dynamical, and thermodynamic properties. J Iran Chem Soc 2017;14:1–7.

[115] Pagliaro M, Ciriminna R, Kimura H, Rossi M, Della Pina C. From glycerol to value-added products. Angew Chemie Int Ed 2007;46:4434–40.

[116] Chilakamarry CR, Sakinah AMM, Zularisam AW, Sirohi R, Khilji IA, Reddy VJ, et al. Bioconversion of glycerol into biofuels—Opportunities and challenges. BioEnergy Res 2022;15:46–61.

[117] Martin A, Richter M. Oligomerization of glycerol –A critical review. Eur J Lipid Sci Technol 2011;113:100–17.

[118] BCC Research, Report Code EGY171A, Published March 2020. 2020.

[119] Sdrula N. A study using classical or membrane separation in the biodiesel process. Desalination 2010;250:1070–2.

[120] Yang F, Hanna MA, Sun R. Value-added uses for crude glycerol--a byproduct of biodiesel production. Biotechnol Biofuels 2012;5:13.

[121] Leng L, Yuan X, Zeng G, Chen X, Wang H, Li H, et al. Rhamnolipid based glycerol-in-diesel microemulsion fuel: formation and characterization. Fuel 2015;147:76–81.

[122] Carvalho VB, Leite RF, Almeida MTC, Paschoaloto JR, Carvalho EB, Lanna DPD, et al. Carcass characteristics and meat quality of lambs fed high concentrations of crude glycerin in low-starch diets. Meat Sci 2015;110:285–92.

[123] BCC Research, Report Code CHM062E, Published January 2019. 2019.

[124] IEA (2020). Renewables 2020, IEA, Paris 2020. https://www.iea.org/reports/renewables-2020 (accessed October 17, 2022).

[125] Prabu SL, Suriya Prakash TNK, Thirumurugan R. Cleaning validation and its regulatory aspects in the pharmaceutical industry. Dev Surf Contam Clean 2015:129–86.

[126] Zarli A. Oleochemicals: all time players of green chemistry, 2020, p. 77–95.

[127] Tan HW, Abdul Aziz AR, Aroua MK. Glycerol production and its applications as a raw material: A review. Renew Sustain Energy Rev 2013;27:118–27.

[128] Dobrowolski A, Mituła P, Rymowicz W, Mirończuk AM. Efficient conversion of crude glycerol from various industrial wastes into single cell oil by yeast Yarrowia lipolytica. Bioresour Technol 2016;207:237–43.

[129] Pagliaro M. Glycerol: the renewable platform chemical. Elsevier; 2017.

[130] Isahak WNRW, Ismail M, Yarmo MA, Jahim JM, Salimon J. Purification of crude glycerol from transesterification RBD palm oil over homogeneous and heterogeneous catalysts for the biolubricant preparation. J Appl Sci 2010;10:2590–5.

[131] Ooi T, Yong K, Dzulkefly K, Wan Yunus W, Hazimah A. Crude glycerine recovery from glycerol residue waste from a palm kernel oil methyl ester plant. J Oil Palm Res 2001;13:16–22.

[132] Hájek M, Skopal F. Treatment of glycerol phase formed by biodiesel production. Bioresour Technol 2010;101:3242–5.

[133] Kongjao S, Damronglerd S, Hunsom M. Purification of crude glycerol derived from waste used-oil methyl ester plant. Korean J Chem Eng 2010;27:944–9.

[134] Manosak R, Limpattayanate S, Hunsom M. Sequential-refining of crude glycerol derived from waste used-oil methyl ester plant via a combined process of chemical and adsorption. Fuel Process Technol 2011;92:92–9.

[135] Potthast R, Chung CP, Mathur I. Purification of glycerin obtained as a bioproduct from the transesterification of triglycerides in the synthesis of biofuel. US Patent 7,718,833, 2010.

[136] Raman A, Abdul A, Tan HW, Buthiyappan A. Two-step purification of glycerol as a value added by product from the biodiesel production process. Front Chem 2019;7:774.

[137] Javani A, Hasheminejad M, Tahvildari K, Tabatabaei M. High quality potassium phosphate production through step-by-step glycerol purification: A strategy to economize biodiesel production. Bioresour Technol 2012;104:788–90.

[138] Van Gerpen J. Biodiesel processing and production. Fuel Process Technol 2005;86:1097–107.

[139] Chongkhong S, Tongurai C, Chetpattananondh P. Continuous esterification for biodiesel production from palm fatty acid distillate using economical process. Renew Energy 2009;34:1059–63.

[140] Dhabhai R, Ahmadifeijani E, Dalai AK, Reaney M. Purification of crude glycerol using a sequential physico-chemical treatment, membrane filtration, and activated charcoal adsorption. Sep Purif Technol 2016;168:101–6.

[141] Baker RW. Membrane technology and applications. John Wiley & Sons; 2012.

[142] Nanda, MR and Yuan, Z and Qin, W and Poirier, MA and Chunbao X. Purification of crude glycerol using acidification: effects of acid types and product characterization. Austin J Chem Eng 2014;1:1–7.

[143] Kumar LR, Yellapu SK, Tyagi RD, Zhang X. A review on variation in crude glycerol composition, bio-valorization of crude and purified glycerol as carbon source for lipid production. Bioresour Technol 2019;293:122155.

[144] Carmona M, Valverde JL, Pérez A, Warchol J, Rodriguez JF. Purification of glycerol/water solutions from biodiesel synthesis by ion exchange: sodium removal Part I. J Chem Technol Biotechnol 2009;84:738–44.

[145] Isahak WNRW, Ramli ZAC, Ismail M, Jahim JM, Yarmo MA. Recovery and Purification of Crude Glycerol from Vegetable Oil Transesterification. Sep \& Purif Rev 2015;44:250–67.

[146] Muniru OS, Ezeanyanaso CS, Akubueze EU, Igwe CC, Elemo GN. Review of different purification techniques for crude glycerol from biodiesel production. J Energy Res Rev 2018;2:1–6.

[147] Eisenbart FJ, Angermeier N, Ulrich J. Production of highly dry glycerol by solvent-aided melt layer crystallization. J Cryst Growth 2017;469:191–6.

[148] Hass H, Patterson J. Purification of glycerol by crystallization. Ind Eng Chem 1941;33:615–6.

[149] Meenan PA, Anderson SR, Klug DL. The influence of impurities and solvents on crystallization. Handb Ind Cryst 2002:67–100.

[150] Ito T, Nakashimada Y, Senba K, Matsui T, Nishio N. Hydrogen and ethanol production from glycerol-containing wastes discharged after biodiesel manufacturing process. J Biosci Bioeng 2005;100:260–5.

[151] Hong A-A, Cheng K-K, Peng F, Zhou S, Sun Y, Liu C-M, et al. Strain isolation and optimization of process parameters for bioconversion of glycerol to lactic acid. J Chem Technol Biotechnol 2009;84:1576–81.

[152] Anitha M, Kamarudin SK, Kofli NT. The potential of glycerol as a value-added commodity. Chem Eng J 2016;295:119–30.

[153] Xu J, Banerjee A, Pan SH, Li ZJ. Galactose can be an inducer for production of therapeutic proteins by auto-induction using E. coli BL21 strains. Protein Expr Purif 2012;83:30–6.

[154] Kaur L, Gupta GD. A review on microwave assisted grafting of polymers. Int J Pharm Sci Res 2017;8:422.

[155] Gholami Z, Abdullah AZ, Lee KT. Dealing with the surplus of glycerol production from biodiesel industry through catalytic upgrading to polyglycerols and other value-added products. Renew Sustain Energy Rev 2014;39:327–41.

[156] Vannucci JA, Gatti MN, Cardaci N, Nichio NN. Economic feasibility of a solketal production process from glycerol at small industrial scale. Renew Energy 2022;190:540–7.

[157] Okoye PU, Abdullah AZ, Hameed BH. Synthesis of oxygenated fuel additives via glycerol esterification with acetic acid over bio-derived carbon catalyst. Fuel 2017;209:538–44.

[158] Rodriguez Herrero Y, Ullah A. Rapid, Metal-Free, Catalytic Conversion of Glycerol to Allyl Monomers and Polymers. ACS Sustain Chem Eng n.d.;9:9474–85.

[159] Nutting JE, Gerken JB, Stamoulis AG, Bruns DL, Stahl SS. “How Should I Think about Voltage? What Is Overpotential?”: Establishing an Organic Chemistry Intuition for Electrochemistry. J Org Chem 2021;86:15875–85.

[160] Aiba S. Growth kinetics of photosynthetic microorganisms. Microb. React., Berlin, Heidelberg: Springer Berlin Heidelberg; 1982, p. 85–156.

Chapter 3. Hydrophobic Polyhedral Oligomeric Silsesquioxane Support Enhanced Methanol Production from CO_2 Hydrogenation

Abstract

The abundance of CO_2 from the cement industry, power generation, petroleum production, and combustion of biomass, makes it a readily available feedstock to produce chemicals and materials, though it has yet to achieve optimal development. Even though syngas ($CO + H_2$) hydrogenation to methanol is an established industrial process, when the same catalytic system based on $Cu/ZnO/Al_2O_3$ is employed with CO_2, the water formed as a byproduct reduces the activity, stability, and selectivity of the process. Here, we explored the potential of phenyl polyhedral oligomeric silsesquioxane (POSS) as hydrophobic support of Cu/ZnO for direct CO_2 hydrogenation to methanol. Mild calcination of the copper-zinc-impregnated POSS material affords the formation of CuZn-POSS nanoparticles able to reach a 3.8% yield of methanol with a 4.4% of CO_2 conversion and with selectivity as high as 87.5% within 18 hours. The structural investigation of the catalytic system reveals that CuO/ZnO are electron withdrawers in the presence of the siloxane cage of POSS. The catalytic system metal-POSS is stable and recyclable under H_2 reduction and CO_2/H_2 conditions. The increased number of phenyls in the structure of POSS results in an increased hydrophobic character that plays a decisive role in the methanol formation after comparison with CuO/ZnO supported on reduced graphene oxide (RGO) with 0% selectivity to methanol under the study conditions. The materials were characterized using SEM, TEM, ATR FT-IR, XPS, powder XRD, FTIR, BET, contact angle, and TGA. The gaseous products were characterized by GC coupled with TCD/FID.

Keywords: carbon dioxide; methanol; heterogeneous catalysis; hydrophobicity; silsesquioxane; hydrogenation

3.1 Introduction

Carbon dioxide (CO_2) is a widely available greenhouse gas that is produced from natural and anthropogenic sources and is a major driver in current climate change. Its conversion to chemicals, fuels, and energy is very appealing as an alternative to fight the global warming caused by the accumulation of CO_2 in the atmosphere, as well as an alternative to replace fossil fuels. Hydrogenation of CO_2 has been one of the major approaches to chemically converting CO_2 into oxygenated compounds such as methanol, formic acid, and dimethyl ether. The hydrogenation of CO_2 to methanol has been the center of investigations due to the low number of hydrogens needed and the growing demand for methanol as fuel and energy storage.

The commercial path for the production of methanol employs a syngas feed catalyzed by $Cu/ZnO/Al_2O_3$ at 493−573 K and a pressure of 5−10 MPa [1]. When the syngas feed is replaced by CO_2 (Eq. 3.1 and Eq. 3.2), the water produced as a byproduct, acts as an inhibitor when it binds to the active metal site, reducing the surface area and the reaction rate. Further, the strong hydrophilic property of the Al_2O_3 favor the formation of $ZnAl_2O_4$ disrupting the synergistic effect of Cu/ZnO and promoting the rapid Cu sintering, resulting in severe catalyst deactivation. Thus, the repellence of the water from the reaction turns out to be an essential issue to improve the system efficiency [2]. Therefore, despite substantial improvement in the catalytic activity for the hydrogenation of CO_2, the catalytic stability has been a major challenge.

$$CO_2 + 3H_2 \rightleftarrows CH_3OH + H_2O \qquad \Delta H°=-49.5\ kJmol^{-1} \qquad \text{Eq. 3.1}$$

$$CO_2 + H_2 \rightleftarrows CO + H_2 \qquad \Delta H°=+41.2\ kJmol^{-1} \qquad \text{Eq. 3.2}$$

To address these activity and stability issues, a wide range of catalysts have been investigated containing Cu and Zn as the main components together with modifiers (Zr, Ga, Si, Al, B, Cr, Ce, V, Ti) [3,4] in order to solve Cu sintering and increase the dispersion. Recently, carbon materials [5] have been used as effective supports of CuO [6] and CuO/ZnO [7]. Among the carbon materials, graphene has many characteristics that make it suitable for developing new catalysts. The high theoretical specific surface area, the low cost of starting materials, the easy

electron mobility, the high chemical, thermal optical and electrochemical stabilities are among the properties of graphene to enhance catalyst stability.

Another alternative to overcome the deactivation of the catalyst is dispersing the metallic nanoparticles on porous three-dimensional inorganic solids with hydrophobic properties. The use of polyhedral oligomeric silsesquioxane (POSS) has received a lot of attention in research for its well-defined organic/inorganic hybrid constituents and its unique rigid cage-like molecular structure connected by Si-O-Si bonds. POSS are characterized by high thermal stability (>350 °C) and fully tunable solubility. The irregularity of molecular shapes of certain POSS molecules inhibits crystallization by preventing good packing. The siloxane cage provides hydrophobic regions which do not favor the water adsorption to the surface. Furthermore, hydrophobic groups attached to the cage increase the hydrophobic character of POSS to potentially prevent catalyst deactivation by water effect [8].

The phenyl polyhedral oligosilsesquioxanes exhibit remarkable thermal stability and in many instances can be prepared in high yields from phenyl trichlorosilane [9]. Some researchers have proved that the modifications by using POSS molecules can effectively improve the hydrophobic properties of materials. For instance, POSS cages have been combined with graphene oxide (GO) to prepare hydrophilic-hydrophobic hybrid membrane for ethanol dehydration [10]. In a different study, three hydrophobic POSS molecules with phenyl, isobutyl, and isooctyl as functional groups, were successfully exploited as surface coating to increase the hydrophobicity of phosphate glass (Pglass) [11]. After the Pglass was dipped coated on the hydrophobic POSS solution followed by condensation reaction, the contact angle between Pglass and water gradually increased from 81.6° to 91.3°. Similarly, Deng *et al*. used a functionalized octavinyl-POSS to modify cotton fabric and increased the hydrophobicity with a contact angle higher than 142° [12].

Furthermore, the organic-inorganic synergy of POSS molecules has been explored as catalyst support. Thus, POSS molecules have been used as stabilizing support for metal nanoparticles as heterogeneous catalysts for hydrogenation reactions. More specifically Saab *et al*. prepared palladium nanoparticles stabilized with octa(propylammonium)-POSS for the direct hydrogenation of 1,4-diphenylbutadiyne [13]. Similarly, Yan *et al.* synthesized metal colloids of palladium, platinum, and ruthenium nanoparticles using octa(diacetic aminophenyl)

silsesquioxane as stabilizer and $NaBH_4$ as reducing agent for the catalytic hydrogenation of some phenyl aldehydes [14,15]. Styryl-linked POSS polymers were used as platinum supports via π-coordination interaction taking advantage of the π-electron environment provided by the styryl linkages. The system was tested for the hydrosilylation of styrene with dimethylphenylsilane with similar results to the commercial Pt catalyst [16].

Computational studies has demonstrated that octaphenyl-POSS (O-POSS) and dodecaphenyl-POSS (D-POSS) can form stable endohedral and exohedral metal coordination with ions and transition metals [17,18]. The fluoride anion have been confirmed within the cage by X-crystal diffraction after its introduction using tetraalkylammonium fluoride (*n*-Bu_4NF) via hydrolysis and condensation reactions [19,20]. Atomic hydrogen has been successfully encapsulated using γ-irradiation of $T_8(OSiMe_3)_8$ in air [21] and later was encapsulated by glow discharged [22].

CO_2 hydrogenation to methanol is recognized to be structure sensitive and the catalytic properties are strongly associated with the size and composition of the metal oxide-interface [23]. Beside a hydrophobic support with high thermal stability is required to prevent Cu/ZnO deactivation by sintering. Hence, nPhenyl-POSS are advantageous in this regard for the three-dimensional cage that could accommodate the active metal either inside the cage and/or around. We speculate that ionic metals can form stable complexes through ionic bonding or charge transfer with the core siloxane cage and the phenyl groups and repel the water while promoting the CO_2 hydrogenation.

In this research, we investigated the Cu/ZnO dispersion onto the hydrophobic n-phenyl POSS ($(PhSiO_{1.5})_n$ n=8 and 12 represent the number of phenyl groups attached to the siloxane cage) via incipient wetness impregnation. Their catalytic performance on direct hydrogenation of CO_2 to methanol under mild conditions was studied. For comparison purpose, the reaction was also conducted over Cu/ZnO dispersed on RGO. We compared the activity of the catalysts at 10% metal loading on O-POSS, D-POSS, and RGO. To the best of our knowledge, this is the first report for CO_2 hydrogenation to methanol on Cu/ZnO over n-phenyl POSS (n=8,12).

3.2 Material and Methods

3.2.1 Materials

The chemicals used in this study were octaphenyl POSS (O-POSS, MS0840) and dodecaphenyl POSS (D-POSS, MS0802) from Hybrid Plastics and were used as received. Copper nitrate trihydrate (99.5%, $Cu(NO_3)_2 \cdot 3H_2O$, Sigma-Aldrich) and zinc nitrate hexahydrate (98%, $Zn(NO_3)_2 \cdot 6H_2O$, Sigma-Aldrich), graphite powder (<20μm, Sigma-Aldrich), sulphuric acid (95-98%, H_2SO_4, ACP Chemicals), phosphoric acid (85%, H_3PO_4, Fisher), potassium permanganate (≥99.0%, $KMnO_4$, ACS), hydrogen peroxide (30%w/w, H_2O_2, Sigma-Aldrich), hydrochloric acid (36.5-38 %, HCl, Fisher), hydrazine monohydrate (64-65% N_2H_4, Sigma-Aldrich) and anhydrous ethyl alcohol from Supelco were used as received. The gases N_2, H_2, CO_2:H_2 (1:3) were purchased from Praxair with purity >99.9995%.

3.2.2 Synthesis of Cu/ZnO/POSS

The catalysts were prepared with different weight percentages of 10, 20, and 30% Cu-Zn metals, with equivalent Cu:Zn molar ratio with POSS support via an incipient wetness impregnation using anhydrous ethyl alcohol as solvent. The catalysts were dried at 90 °C for 24 h and calcined in a muffle at 270 °C for 7 h with a heating rate of 2 °Cmin^{-1}. The catalysts were coded based on the % of POSS used. Catalysts supported on octaphenyl POSS (n=8) and dodecaphenyl POSS (n=12) were labelled O-POSS and D-POSS, respectively. Herein, catalysts loaded with 10, 20, and 30% are denoted as follows: CuZnX-Y-POSSZ, where X is the weight percentage of CuZn, Y is the type of POSS, and Z is the % weight of POSS. A model compound CuO/ZnO was synthesized with equivalent Cu:Zn molar ratio following the same procedure previously described.

3.2.3 Synthesis of RGO

CAUTION! The synthesis was performed according to the reported procedure with some modifications [24]. Concentrated H_2SO4 and H_3PO_4 (360:40 mL) were mixed in a 2 L funnel. Then, graphite oxide (3 g) was slowly added under stirring. Next, $KMnO_4$ (18 g) was slowly added to the reaction increasing the temperature to 40 °C. Follow, the temperature was increased to 50 °C

and the reaction continued for 12 h. After the reaction, contents were cooled to room temperature and then poured into a 1 L beaker containing 400 mL of ice water and 10 mL of H_2O_2. The color changed from brown to yellow. The reaction was left overnight for sedimentation. Then, the upper layer was removed, and 800 mL of deionized water was added to the sediments and left for 12 h. After the top layer was removed, the solids were washed twice with water, 30% HCl and ethanol in a ratio 1:1:1. After sedimentation, the GO was purified with a dialysis membrane (MWC of 6000-8000 g/mol) for 48 h. The GO was centrifuge at 4000xg for 10 min at room temperature in Avanti JE centrifuge with JLA 16.250 rotor. Finally, the GO was freeze dried.

3.2.4 Synthesis of Cu/ZnO/RGO

GO (1 g) in water (300 mL) was sonicated for 3 h at room temperature to exfoliate the GO layers. Then, hydrazine (30 mL) was added while stirring at 200 rpm for 5 h at 98 °C in a silicon bath to reduce the GO. The RGO was vacuum filtered, washed with copious amounts of water, and oven dried at 105 °C for 24 h.

The RGO was pulverized and sieved. The particle size ranged between 180 and 425 µm. The 10 wt.% Cu-Zn (equimolar amounts of Cu & Zn) was impregnated on RGO support via an incipient wetness impregnation method. The impregnated catalyst was dried overnight at 90 °C and calcined at 350 °C for 7 h with a heating rate of 2 °Cmin^{-1}. The sample was labelled CuZn10-RGO90.

3.2.5 Catalyst Characterization

Attenuated Total Reflectance - Fourier-transform infrared spectroscopy (ATR-FTIR) spectra were recorded in triplicate at room temperature in the region of 400-4000 cm^{-1} at 16 scans and resolution of 4 cm^{-1} with a Bruker Alpha FTIR spectrophotometer (Bruker Optics, Esslingen, Germany) equipped with a single-bounce diamond ATR crystal. The manipulations of the spectra and baseline corrections were done using Nicolet Omnic software (version 8).

Metal content was determined by X-ray fluorescence (XRF) using a Bruker AXS (Bruker S2 Ranger, Karlsruhe, Germany). Measurements were performed in triplicate without previous preparation.

X-ray Photoelectron Spectroscopy (XPS) was used to study the chemical composition of the catalysts. The XPS measurements were performed on ULTRA spectrometer (Kratos Analytical Limited, Manchester, UK). The analytical chamber has a base pressure lower than $3x10^{-8}$ Pa. The spectrometer was equipped with a monochromatic Al Ka (*hv* =1486.6 eV) source operated at a power of 140 W. The resolution of the instrument is 0.55 eV for Ag 3d and 0.70 eV for Au 4f peaks. The survey scans were taken in the range of 0–1100 eV with analyzer pass energy of 160 eV and a step of 0.4 eV. For the high-resolution spectra, the pass-energy was 20 eV with a step of 0.1 eV. The sample charging if any was compensated by an electron flood gun. The data were processed using the Vision 2 Processing Software. The binding energy of each photopeak was referenced to the C 1s level at 284.7 eV. Compositions were calculated from the high-resolution spectra using Tougaard background and sensitivity factors provided by the instrument database.

Wide angle X-ray scattering on the bulk sample was performed on a D8 Discover Bruker equipped with Cu Kα radiation (λ=0.154 nm) source operated at 40 kV and high LynxEYE 1-dimensional detector. Samples were scanned between 4° and 80° of 2θ at 2 ° min^{-1} with a step of 0.03°. Material crystallinity (%) was determined by integrating the diffraction peaks in the 2θ= 18°– 35° range.

The surface area, nitrogen adsorption isotherms, pore size distribution, and pore volume of the calcined catalysts were determined by adsorption/desorption at 77 K using an Autosorb-1MP (Quantachrome, USA). Before analysis, all the samples were outgassed at 393 K under vacuum for 2 h. The isotherms were prepared following BET method for surface area calculation and the DFT method was used for micropore and mesopore evaluation.

The morphology of the samples as well as the elemental information was studied with scanning electron microscopy with energy dispersive X-ray spectroscopy (SEM-EDX) using the Sigma FESEM with a GEMINI column (SIGMA Zeiss, Germany). It is configured with in-lens secondary electron (SE) detector and a backscatter (BSD) detector. The POSS samples were coated with carbon 2 nm deep and the RGO samples were coated with gold 2 nm deep.

TEM imaging was performed using a JEOL-2010 electron microscope (JEOL, USA) equipped with a cold field emission gun operated at 200 kV voltage. Specimens were prepared by drop-casting isopropyl alcohol suspensions of samples onto carbon-coated copper grids.

The thermal stability of the supported catalysts was studied by thermogravimetric analysis (TGA) (TGA/DSC1, Mettler Toledo, Switzerland) with MX5 microbalance and GC 10 gas controller was employed in a nitrogen environment with 50 $mLmin^{-1}$. Approximately 10 mg of sample was placed in an alumina crucible and heated from 25 °C to 900 °C at heating rate of 10 ºC min^{-1}.

The contact angle was used to evaluate the surface hydrophobicity of the neat supports and the catalysts. The samples were compressed to tablets using a Carver Press at room temperature and pressure of 1000 psi for 5 min. The measurements were made using the sessile drop method with a dynamic contact angle analyzer, FTA 200 (First Ten Angstroms, Portsmouth, VA, USA). A small droplet of 5 µL was put on the surface using a needle with diameter equal 1 mm. The measures were made in triplicate with an accuracy < ±2° [25].

3.2.6 Catalytic Activity Test

The catalytic activity of the synthesized material was carried out in Swagelok stainless steel micro-batch reactors (Fig. 3-1a). The catalyst was placed (50 mg) in a clear glass vessel inside the reactor to avoid contact between the catalyst and the reactor wall. Then, it was closed and pressurized with nitrogen to 3 MPa to perform leak test. Next, the reactor was purged with nitrogen three times, and 0.2 MPa of nitrogen was left inside to keep an inert atmosphere. 0.6 MPa of H_2 were added to the reactor to achieve catalyst reduction. The final pressure was of 0.8 MPa before reaction. The reactor was heated at 220 °C and kept at this temperature for 30 min, and then, the pressure reached 1 MPa. After the completion of the catalyst reduction, the system was cooled down using pressurized air, then was partially emptied to 0.2 MPa, and purged twice with nitrogen. To tune the catalyst activation, the methodology was repeated 1, 3, and 6 times to identify the optimum repetition number to remove water produced during the reduction. The results indicated three consecutives reduction steps produced the optimal results.

Following the catalyst activation, the reactor was partially emptied (up to 0.1 MPa) and flushed three times with N_2. The hydrogenation of the CO_2 was performed by filling the reactor with H_2/CO_2 in 3:1 ratio until reaching 2 MPa. The pressure increased to 2.2 MPa at reaction temperature (200 – 270 °C). The experiments were performed under isothermal conditions for the duration of 18 h. The batch reactor was not equipped with any form of agitation.

Heating was achieved by placing the pressurized reactor inside an Omega fluidized sand bath heater set at the corresponding experimental temperature (Fig. 3-1b). The reaction temperature was monitored with an installed thermocouple in the reactor. Reaction time reported corresponds to the time period starting at the reactor reached temperature set point.

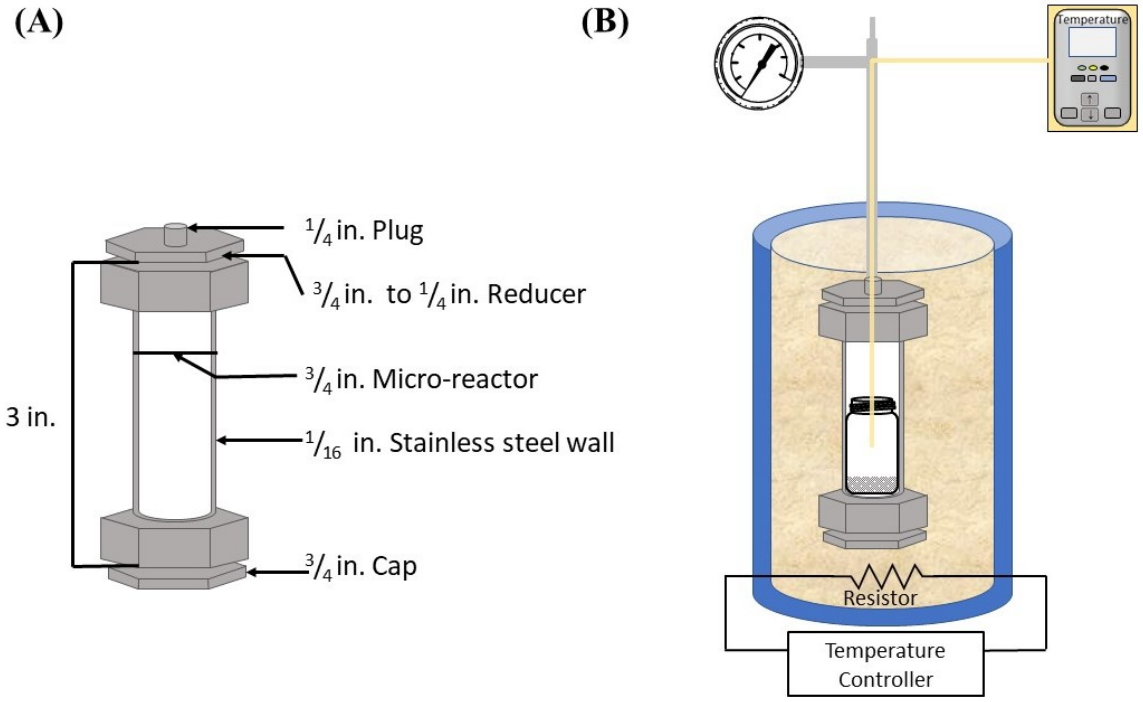

Figure 3-1 (**a**) Schematic representation of the stainless steel micro-batch reactor used for catalyst activity test, and (**b**) heating set-up system.

3.2.7 Characterization of Gaseous Products

The gaseous products from the hydrogenation of CO_2 were collected in a gas bag after the reactor was cooled down to 40 °C. The gas products were analyzed in a gas chromatograph (Agilent GC 7890A, USA) equipped with a HayeSep R80/100 packed column (1.83 m x 25.4 mm

x 2 mm) for hydrocarbon separation and a Molecular Sieve 13X packed column (for permanent gas separation) additionally a thermal conductivity detector and a flame ionization detector.

The selectivity, CO_2 conversion (X_{CO2}), and yield was determined using the formulas below:

$$Selectivity\ of\ R = \frac{moles\ of\ R\ produced}{moles\ of\ all\ products} \quad \text{Eq. 3.3}$$

$$X_{CO_2} = \frac{(moles\ (CO_2)_{initial} - moles\ (CO_2)_{non\ reacted})}{moles\ (CO_2)_{initial}} \quad \text{Eq. 3.4}$$

$$\%\ Yield\ (CH_3OH) = Selectivity\ (CH_3OH) \times X_{CO_2} \times 100 \quad \text{Eq. 3.5}$$

3.3 Results and Discussion

3.3.1 Catalytic Characterization

In order to protect Cu/ZnO from water deactivation during the CO_2 hydrogenation, we selected POSS with 8 and 12 phenyl ligands attached to the silanol cages for their hydrophobic character. The hydrogenation of CO_2 produces undesirable water which can be repelled from the hydrophobic and bulky phenyl ligands, protecting the active sites dispersed along the surface of the supports. We used incipient wetness impregnation to disperse the metals over the surface of POSS. An ethanol solution containing the desired % of metals were deposited dropwise in the support and allowed to dry overnight at 50 °C followed by calcination. Table 3-1 shows the chemical composition of the supported catalysts.

The structure of O-POSS (Fig. 3-2a) may be described- as a cube-shaped arrangement of Si atoms with interstitial cuboctahedron of connecting O atoms [26]. The D-POSS has been reported with a hexagonal-prismatic arrangement consisting of fused eight-and ten-membered silicon-oxygen rings (Fig. 3-2b) [27].

Table 3-1 Chemical composition of CuZn/POSS.

Sample	XRF				
	Cu (wt%)[a]		Zn (wt%)[a]		Cu + Zn
	x	*s*	*x*	*s*	(wt%)
CuZn10-O-POSS90	5.402	0.024	5.739	0.039	11.141
CuZn20-O-POSS80	9.325	0.081	9.634	0.124	18.959
CuZn30-O-POSS70	14.212	0.175	16.203	0.301	30.415
CuZn10-D-POSS90	4.820	0.003	5.212	0.012	10.032
CuZn20-D-POSS80	8.821	0.330	10.204	0.174	19.025
CuZn30-D-POSS70	15.188	0.807	17.508	0.431	32.696
CuZn10-RGO90	5.102	0.054	4.965	0.107	10.067
CuO/ZnO	48.932	0.021	49.611	0.201	98.543

[a] Average (*x*) and sample standard deviation (*s*) of analyses in triplicate are reported.

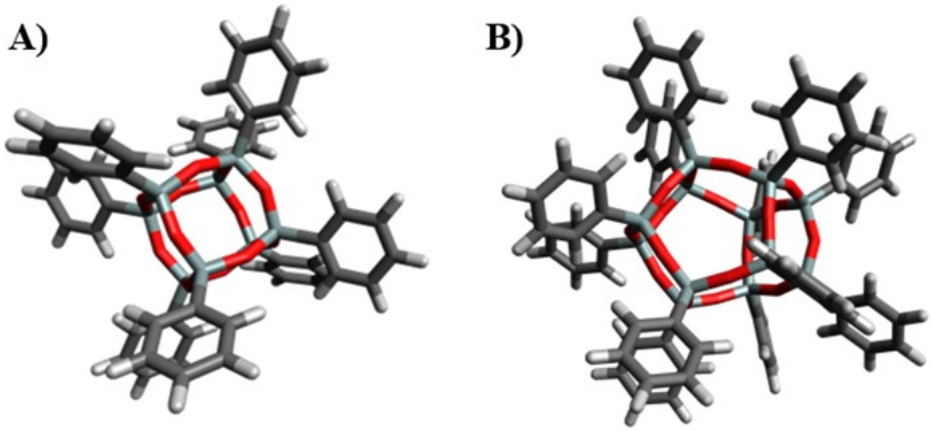

Figure 3-2 Structural model of (**a**) Octaphenyl polyhedral oligomeric silsesquioxane (O-POSS) and (**b**) Dodecaphenyl polyhedral oligomeric silsesquioxane (D-POSS). Blue, red, grey, and white represent for Si, O, C, and H atoms, respectively.

The crystalline structure of the catalysts was studied by powder XRD. Fig. 3-3 shows the XRD patterns of the neat O-POSS, D-POSS, CuO/ZnO and a series of CuZnX-Y-POSSZ catalysts with different CuZn:POSS ratio after calcination at 270 °C. The supported catalysts show diffraction peaks at 2θ = 32.5°, 35.5°, 38.7°, 48.8°, 61.6°, 67.9°, 72.5°, and 75.1 that can be attributed to CuO phase (PDF #98-000-0429). The peaks at 2θ = 31.7°, 34.4°, 36.2°, 47.5°, 56.5°, 62.8°, 66.3°, and 69.1° can be attributed to ZnO phase (PDF # 98-000-0483). The characteristic diffraction peaks of O-POSS occur at 2θ value of 8.2° (d=1.1 nm), 18.5° (d=0.48 nm), and 24.5° (d=0.36 nm) associated to the overall dimension of POSS molecules, body diagonal of the POSS cage, and the distance between opposite Si_4O_4 faces of the silsesquioxane cube plane, respectively [28,29]. The 2θ position, the intensity, and d space of O-POSS did not change after the dispersion of the metal oxides, meaning the overall molecule size and cage dimensions did not change with the metals or with the calcination temperature over the catalyst preparation (Table A-1, Fig. A-1a, Supplementary Information, SI). The diffraction peak corresponding to the overall size of the molecule of D-POSS suffered a shift from 7.7° to 8.0° with a broaden of the signal (Table A-1, Fig. A-1b, SI). This could be an indication of new linkages between the metal oxides and the support and a change in the crystal lattice as a function of composition. The other distinctive change was a shift from 24.6° (d=0.36 nm) to 23.9° (d=0.37nm) of the diffraction peak associated to the distance between opposite Si_4O_4 faces of the silsesquioxane cube plane of D-POSS that confirmed a change in the overall molecule size and cage due to the metals in the system.

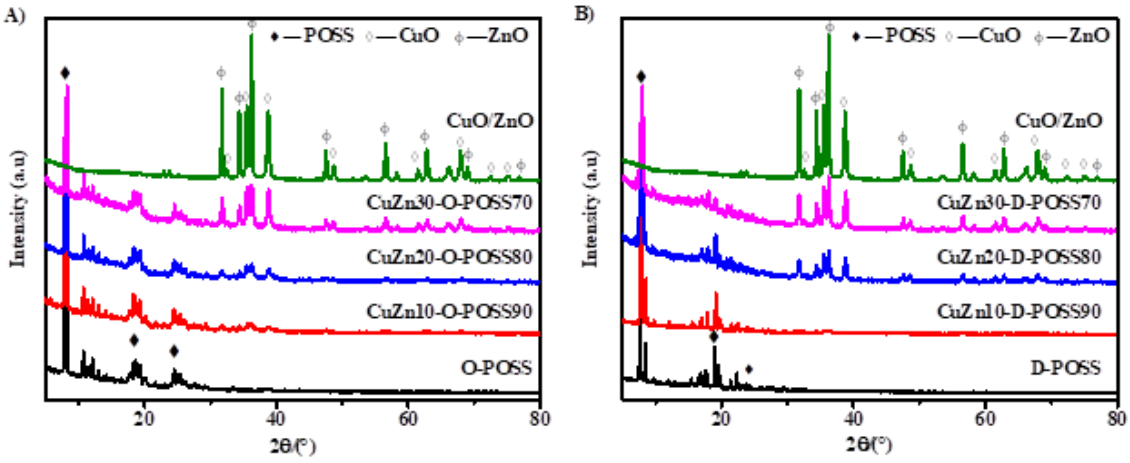

Figure 3-3 XRD patterns of (**a**) O-POSS and their supported catalysts and (**b**) D-POSS and their supported catalysts**.**

The XRD pattern of the GO, RGO, CuZn10-RGO90 are shown in Fig. A-2, (SI). The graphene oxide (GO) shows a wide diffraction peak that is 2θ= 10.6° corresponding to an interlayer spacing of d=0.83 nm. The reduced graphene oxide shows a broad peak at 2θ= 25.5° (d=0.34 nm) indexed to the graphitic planes (002) of graphene nanosheets. The shifted from GO 2θ= 10.6° to 25.5° indicates that GO has been converted into RGO with sonication and hydrazine treatment [30]. Once the metals have been loaded into the graphene layers, the new peaks from the diffraction pattern correspond to the crystal phase of CuO and ZnO. Despite the metal oxides are detectable in the X-ray diffractogram, the CuZn10-RGO90 has an amorphous structure [31].

When a 10 wt.% of CuO/ZnO was dispersed on both POSS, the diffraction peaks corresponding to the oxides were barely noticeable. These is an indication of a homogeneous dispersion of the metals over the supports and the interaction metal oxide/POSS gives place to an amorphous material. The later could be confirmed with the calculation of the crystallinity index in the range from 18° to 35°, which revealed that the presence of CuO and ZnO reduce the crystallinity of O-POSS and D-POSS from 94.95% to 34.72% and from 58.52% to 45.63%, respectively (Table 3-2). As the concentration of the metals oxides increases, gradually increases the sharpness and intensity of the diffraction peaks of CuO and ZnO, increasing the crystallinity of the samples.

The grain sizes of CuO (D_{CuO}) and ZnO (D_{ZnO}) for the catalysts calculated by Scherrer's equation are listed in Table 3-2. In general, the grain size of ZnO phase is greater than CuO phase, signifying the relationship between both phases. Previous reports considered the grain size of ZnO larger than CuO due to the fact that ZnO can dissolve well the CuO particles inhibiting Cu aggregation [32]. As a result, the activity of the catalysts will increase with a homogenised dispersion of the active phase [33].

Table 3-2 Physicochemical properties of the composites CuZn/POSS and CuZn/RGO.

Catalysts	Crystallinity Index (%)	D_{CuO} [a] (-1 1 1) (nm)	D_{ZnO} [a] (1 0 0) (nm)	S_{BET} ($m^2 g^{-1}$)	Pore volume ($cm^3 g^{-1}$)	Pore width (nm)
O-POSS	94.95	-	-	1.7	0.014	30.5
CuZn10-O-POSS90	34.72	11.97	18.08	16.2	0.089	4.9
CuZn20-O-POSS80	50.29	12.79	17.71	21.3	0.060	11.7
CuZn30-O-POSS70	59.63	28.65	23.75	53.7	0.242	27.4
D-POSS	58.52	-	-	0.4	0.001	5.9
CuZn10-D-POSS90	45.63	10.51	13.89	6.9	0.016	3.2
CuZn20-D-POSS80	62.77	26.22	28.28	5.6	0.033	29.4
CuZn30-D-POSS70	62.99	24.86	34.46	3.9	0.033	27.4
RGO	92.05	-	-	582.7	0.450	3.8
CuZn10-RGO90	60.96	11.36	11.89	154.7	0.220	3.8

[a] Determined by Scherrer's equation

To characterize the electronic properties of the samples, we conducted X-ray photoelectron spectroscopy (XPS) measurements of the neat POSS and the 10% loaded metal. Fig. A-3 (SI) shows the survey spectra for neat O-POSS and D-POSS and for CuZn10-O-POSS90 and CuZn10-D-POSS90. For both supports new peaks appeared after the impregnation, which are attributed to Cu^{2+} and Zn^{2+}. The % of O 1s rose from 19 to 23% and from 18 to 23% for O-POSS and D-POSS, respectively, after impregnation due to the incorporation of the oxides (Table 3-3). The weight % of Zn^{2+} is higher in the three supported catalysts than Cu^{2+} even though the XRF results showed a relative ratio 1:1. This phenomenon indicates CuO is deposited dispersedly on the ZnO particles, thus improving the active interfacial region or active sites [34,35] in agreement to the XRD grain size results.

Table 3-3 Elemental composition (weight %) of O-POSS, CuZn10-O-POSS90, D-POSS, and CuZn10-D-POSS calculated from XPS.

Sample	C 1s (%)	O 1s (%)	Si 2p (%)	Cu 2p (%)	Zn 2p (%)
O-POSS	53.89	19.28	26.83	-	-
CuZn10-O-POSS90	48.52	23.46	21.80	2.51	3.71
D-POSS	55.24	18.04	26.73	-	-
CuZn10-D-POSS90	47.76	23.20	22.98	1.01	5.06
RGO	22.86	77.86	-	-	-
CuZnO10-RGO90	76.08	18.48	-	0.84	4.60

Fig. 3-4a shows the high resolution spectra of Si 2p with two peaks about 103.3 and 102.6 eV, corresponding to the electron spin states Si 2p1/2 and Si 2p3/2, respectively [36]. The energy separation of the Si 2p1/2 and Si 2p3/2 was found to be 0.65 eV in good agreement with previous report [36]. However, the electron spin state energy separation for Si 2p1/2 and Si 2p3/2 CuZn10-O-POSS90 and CuZn10-D-POSS90 catalysts shifted to 0.56 and 0.71 eV, respectively, which might come from an atomic disorder at the surface or inside the crystal [37] as a result of metal oxide interactions with POSS, in agreement with the drastic changes in the crystallinity from the XRD results. Both, O-POSS and D-POSS, shows different trends as they have different molecular environment.

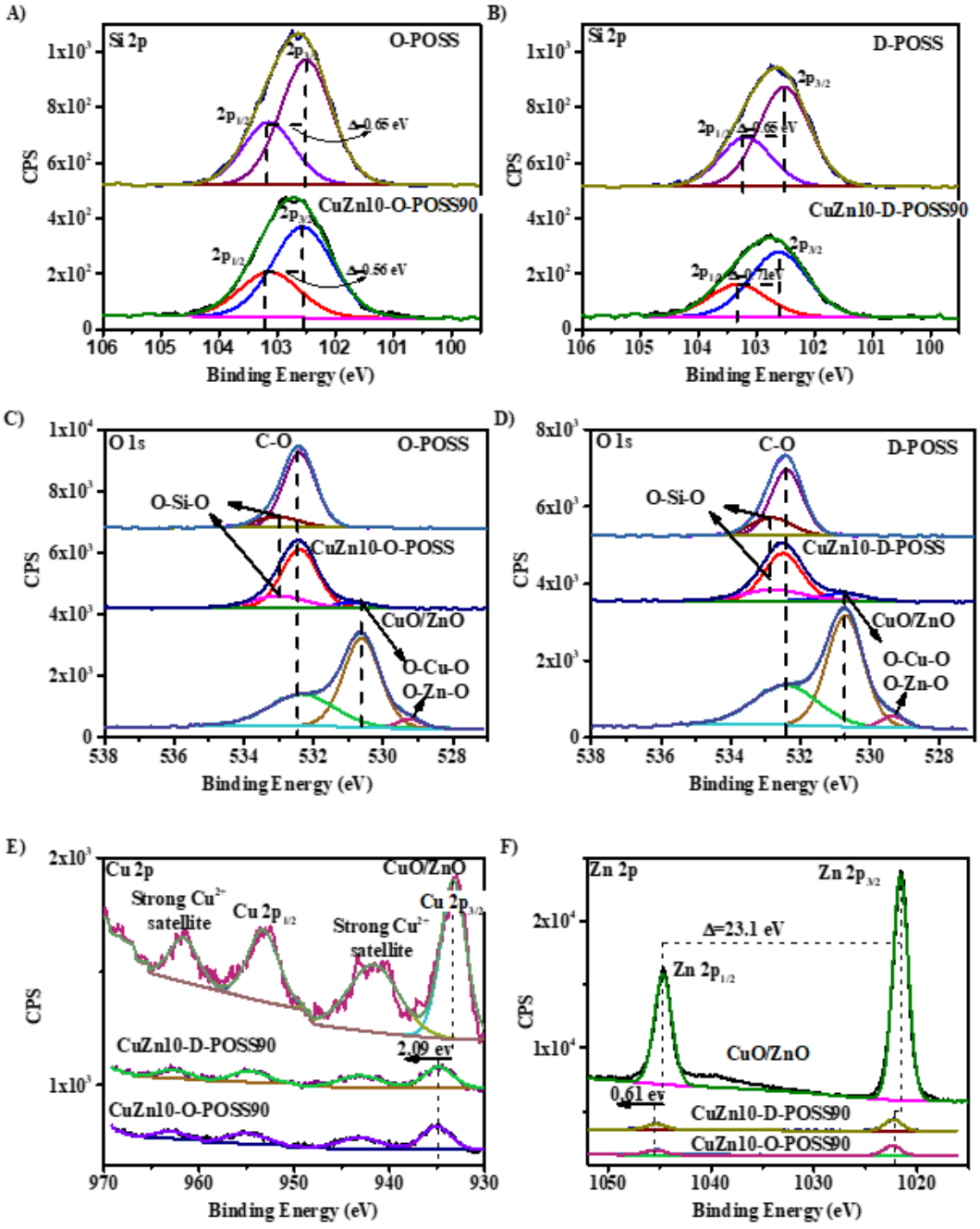

Figure 3-4 XPS high resolution spectra for: (**a**) Si 2p O-POSS, CuZn10-O-POSS90; (**b**) Si 2p D-POSS, CuZn10-O-POSS90; (**c**) O 1s O-POSS, CuZn10-O-POSS90, CuO/ZnO; (**d**) O 1s D-POSS, CuZn10-D-POSS90; CuO/ZnO; (**e**) Cu 2p CuO/ZnO, CuZn10-D-POSS90, CuZn10-O-POSS90; and (**f**) Zn 2p CuO/ZnO, CuZn10-D-POSS90, CuZn10-O-POSS90.

The high resolution spectra of C 1s spectra of O-POSS and D-POSS were deconvoluted about 284.5, 284.7, and 285.2 eV corresponding to C-Si, aromatic, C-O (adventitious carbon) and C-C/C-H, respectively. A resonance π–π* appears at 291 eV associated with the delocalization of the electrons of the phenyl groups (Fig. A-4, SI). Fig. 3-4c,d show O 1s spectra. The peaks 532.4 and 533.0 eV were assigned to Si-O and C-O for O-POSS and D-POSS, respectively. After the metals were impregnated in the supports, the O 1s peaks broaden out and a new peak was found at 530.8 eV, that matched the CuO/ZnO peak of the model compound.

Fig. 3-4e shows the high resolution spectra of Cu 2p for CuO/ZnO composite, CuZn10-O-POSS90, and CuZn10-D-POSS90.The calcination of the catalysts produced CuO as the Cu 2p showed a main peak at 934.8 eV and shake-up satellites as an indication of the presence of Cu (II) species. For the CuO/ZnO model compound, two peaks at 933.3 and 953.3 eV correspond to the Cu 2p3/2 and Cu 2p1/2, respectively. Additionally, there are two satellite peaks located at about 941.65 and 961.60 eV, as an indication of the 2^+ oxidation state of copper [38,39]. These shake-up satellites may occur when the outgoing photoelectron simultaneously interact with a valence electron and excites it to a higher-energy level. Furthermore, for the CuZn10-O-POSS90 and CuZn10-D-POSS90 the Cu 2p3/2 and Cu 2p1/2 and the satellite peaks show a positive shift of 2.09 eV, revealing that CuO acts as an electron donor [40]. Fig. 3-4f, the high-resolution XPS spectrum for Zn 2p of CuO/ZnO and the supported CuZn10-O-POSS90 and CuZn10-D-POSS90 are compared. For the CuO/ZnO, the significant split orbit Zn 2p1/2 and Zn 2p3/2 peaks are observed at 1021.6 and 1044.7 eV, respectively. The bonding energy difference between these two peaks is estimated about 23.1 eV, which is in agreement with other reports [41,42]. For the CuZn10-O-POSS90 and CuZn10-D-POSS90 catalysts, both the Zn 2p1/2 and Zn 2p3/2 peaks shift to the higher energies by 0.61 eV in comparison with those for the CuO/ZnO, revealing that ZnO acts as CuO as electron donor [43,44]. With CuO and ZnO as strong electron donors, the question is whether the phenyl groups, the siloxane cage, or both are acting as electron withdrawer. Zen et al. studied the electronic properties of the O-POSS and reported POSS silica core as a partially conjugated system that serves as electron acceptor, in agreement with the theoretical finding by Lin et al. [45,46].

The surface chemical composition of RGO and CuZn10-RGO90 were also evaluated via XPS as shown in Fig. A-5 (SI). The survey spectrum of CuZn10-RGO90 shows the carbon (C 1s) at 284.7 eV, the oxygen (O 1s) peak at 531.1 eV, a copper (Cu 2p) at 933.9 eV and zinc (Zn 2p) at 1021.50 eV [47]. Fig. A-6a (SI) shows the C 1s spectra of RGO and CuZn10-RGO90, the main difference between both is the disappearance of the C-O-C peak at 286.9 eV from RGO as and the appearance of the C-O-H peak at 285.4 eV as evidence of the hydrophilic character of the RGO. These changes in the surface of both materials are confirmed by the O1s spectra (Fig. A-6b, SI), where a new signal appeared at 532.7 corresponding to C-OH. It is noticeable the signal at 533. 7 eV in RGO assigned to moisture disappeared after impregnation/calcination of CuZn10-RGO90. Unlike the metal oxides supported on POSS, there is not shift in the Cu 2p and Zn 2p in contrast with the model compound CuO/ZnO.

To further investigate the interaction metal oxide – POSS, ATR FT-IR studies were conducted. Fig. 3-5 shows the spectra of the as-synthesized catalysts and their neat supports O-POSS and D-POSS in the region from 4000 to 400 cm^{-1}. The most intense peak around 1100 cm^{-1} corresponds to the asymmetrical stretching modes for inorganic core Si-O-Si of the molecule [48,49]. There is an intense peak from the wagging mode of the aromatic ring about 490 cm^{-1}. A group of peaks about 694 cm^{-1} corresponds to deformational bending of the phenyl rings. Some stretching modes for C-C bonds overlapped by C-H bond deformation are present in the range between 1400 and 1580 cm^{-1}. A group of peaks around 3100 cm^{-1} are assigned to the stretching modes for C-H bond in the phenyl ring [50]. There are no general differences in the spectra shape between the neat POSS and the supported catalysts other than a drop in the intensity of the asymmetrical stretching band ν_{as}Si-O-Si and νSi-C as the percentage of metals increase. This could be an indication of either endohedral and/or exohedral coordination complexes with the silicon/oxygen, which could impart rigidity to the siloxane cage causing a loss in symmetry [17]. These metal-Si interaction are energetically favored to ionic or electrostatic interaction. Interesting, they have shown to not been strong enough to open the cage when the metal ion interact with the molecule.

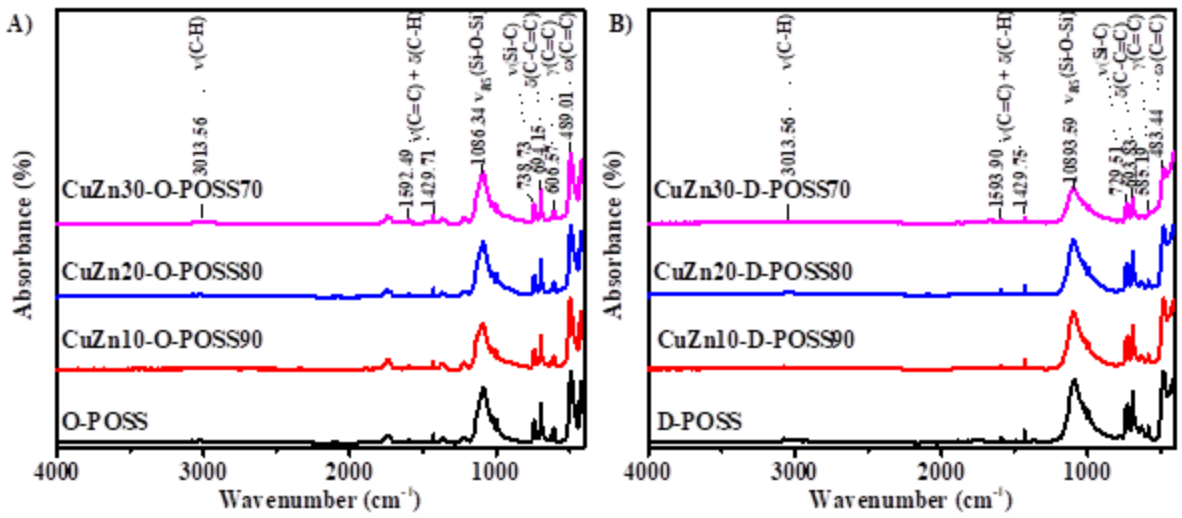

Figure 3-5 ATR FT-IR spectra of (**a**) O-POSS and CuZn-O-POSS catalysts; and (**b**) D-POSS and CuZn-D-POSS.

The FTIR spectrum of GO consists of vibrational groups of GO layer that includes carbonyl (C=O), aromatic (C=C)), carboxyl –(COOH), epoxy (C-O-C) and hydroxyl (OH) groups (Fig. A-7, SI). The spectrum shows a sharp peak about 3100 cm^{-1} corresponds to the hydroxyl groups due to the water molecules. The peak at 1736 cm^{-1} is due to carbonyls and/or carboxyls (C=O, COOH) and the main graphitic domain of the peak at 1618 cm^{-1} due to C=C in-plane stretching sp_2 hybridization [51]. The band at 1367 cm^{-1} reveals the C-O, 1216 cm^{-1} indicates about the C-O-C stretching of epoxy groups. The mode at 1044 cm^{-1} gives information about C-O-C stretching of alkoxy groups [30]. However, the intense signals associated to the oxygen groups are clearly diminished after the reduction of graphene oxide, after the metal oxides are supported on the RGO, some of those signals are visible to a minor extend, as a result of the tendency of RGO sheet to restack during the impregnation and calcination of the catalysts [52]. It is possible some of those hydrophilic groups get trap in the ordering of the layers. Furthermore, this could be the cause of the highly hydrophilic character of RGO and CuZn10-RGO90 that will be discussed later.

The BET Surface areas (S_{BET}), the average pore diameter, and pore volume of the catalysts and their neat supports are shown in Table 3-2. The surface area, calculated from the Brunauer-Emmett-Teller (BET) model derived from nitrogen adsorption was 1.7 and 0.4, and 582.7 m^2g^{-1} for O-POSS, D-POSS, and RGO respectively. Some authors reported high surface area of

phenylsilsesquioxane after functionalization to obtain highly cross-linked structures which are responsible for the porosity not the cages itself [9]. It is understandable that the higher surface area of RGO compared with O-POSS and D-POSS are due to the chemical oxidation and sonication of graphene oxide (GO) that produces sheet exfoliation of RGO [53]. The S_{BET} of the catalysts on O-POSS increases from 1.7 m^2g^{-1} to 16.2, 21.3, and 53.7 m^2g^{-1} as the percentage of CuO/ZnO increases 10, 20, and 30 %, respectively. Apparently, the metals create a more heterogeneous and rougher surface when are deposited on the surface of O-POSS. A different trend is observed when the metals are deposited on D-POSS, the surface area initially increases from 0.4 m^2g^{-1} to 6.9 m^2g^{-1} with a 10% CuO/ZnO, next the surface area decreases to 5.6% and 3.9% with 20 and 30 wt.% of CuO/ZnO, respectively due to pore blocking or clogging. The total pore volume follows in general the same trend as the S_{BET}. These results demonstrate that the pore structure of the supported catalysts can have a different behavior even though the similarity of the supports.

Both of the nitrogen adsorption-desorption isotherms for O-POSS and D-POSS show a reversible type II isotherm with essentially no adsorption as an indication of nonporous or microporous adsorbents (Fig. 3-6a,b) [54]. These results are corroborated with the SEM analysis (Fig. 3-8a,b), that show packed cubic crystals for O-POSS and D-POSS. Once the metals are dispersed on the POSS supports, the isotherms revealed a type IV(a) with H3 hysteresis loop, according to the IUPAC classification [54] that is a characteristic of slit-like pores [55]. The shape of the adsorption branches shows a small intake of gas until close to the saturation pressure showing no limiting absorption at high P/P_0 as a result of gas condensation in pores at a pressure less than the saturation pressure of the bulk fluid [56]. This is an indication of abundant mesoporous structure as shown in the pore size distribution on Fig. 3-7.

The adsorption-desorption isotherms of RGO and CuZn10-RGO90 showed a shape type IV (the IUPAC classification) with a H3 hysteresis loop, demonstrating the presence of mesoporous structure and slit-shaped pores (Fig. 3-6c). A considerable reduction on the hysteresis loop of CuZn10-RGO90 it is an evidence of metal oxides deposited between the RGO layers causing pore blockage. The adsorption isotherm has a lower gas uptake. All the desorption isotherms show a stepdown between 0.4 and 0.5 P/P_0 means the mechanism of desorption points out to cavitation, as an indication of ink-bottle pore shape.

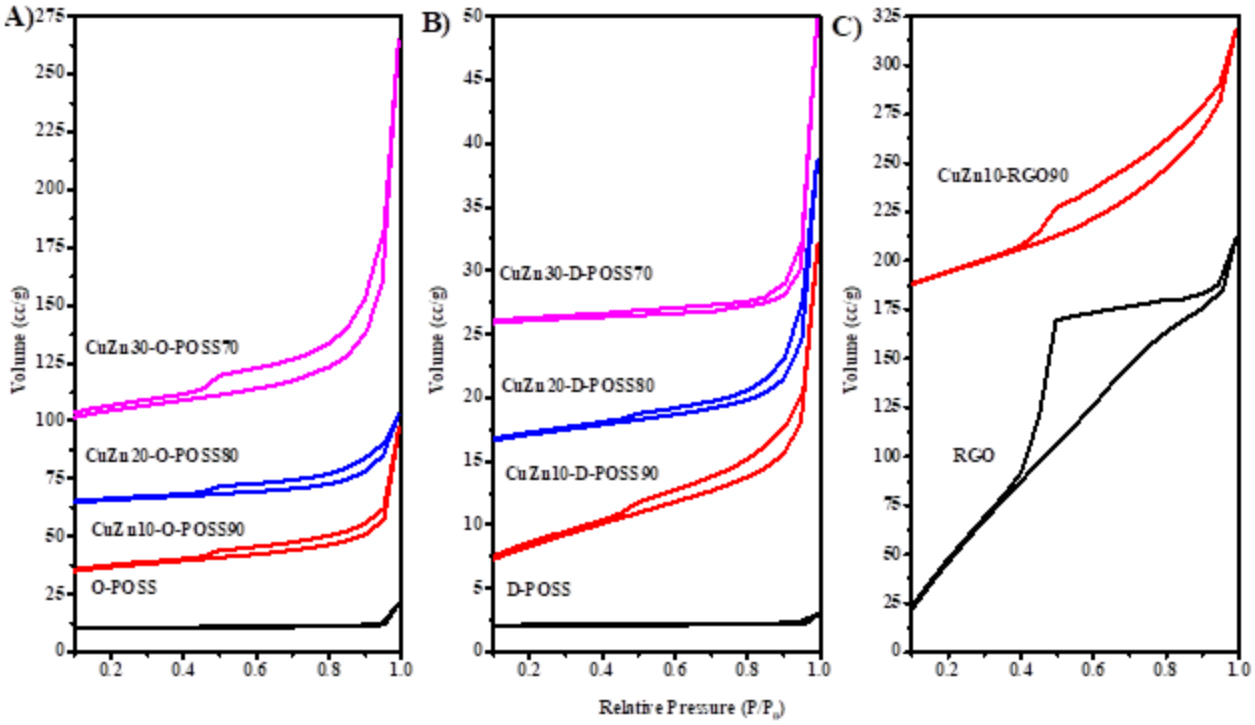

Figure 3-6 N_2 adsorption-desorption isotherms for (**a**) O-POSS and their catalysts; (**b**) D-POSS and their catalysts; and (**c**) RGO and CuZn10-RGO90.

The pore size distribution of O-POSS and D-POSS catalysts were estimated using nonlocal density functional theory (NLDFT) model using the silica cylindrical pore adsorption branch model [57]. The results indicated two main peaks for O-POSS (4 nm and 30 nm, Fig. 3-7a) and for D-POSS (5 nm and 33 nm, Fig. 3-7b). For the POSS supported catalysts, a wide peak distribution in the region from 4 nm to 45 nm which confirms the mesoporous character of the metal oxides/POSS materials. The pore size distribution of RGO and CuZn10-RGO90 were estimated using quenched solid density functional theory (QSDFT) model using the carbon slit/cylindrical pore adsorption branch model (Fig. A-8, SI) [58]. The calculations confirmed that on CuZn10-RGO90 there is a blockage on the mesopores after metal oxide impregnation, causing the reduction on the number of pores available and the reduction in the surface area.

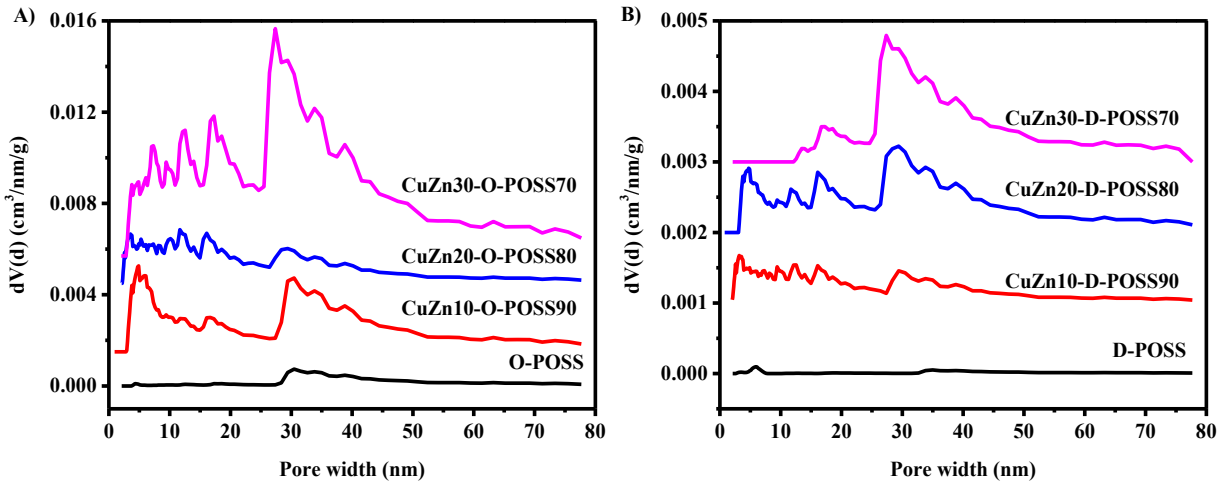

Figure 3-7 Pore size distribution of (**a**) O-POSS and its catalysts and (**b**) D-POSS and its catalysts.

SEM was employed to investigate the morphology of the supported catalysts (Fig. 3-8). The SEM micrographs of the catalysts supported on CuZn10-O-POSS90 and CuZn10-D-POSS90 show well defined cubic crystals in the range 2–7 μm and 80–180 μm, respectively (Fig. 3-8a, d). The cubic shape changed when the concentration of the metals increased, as a result the crystal size decreased to 1–2 μm and 0.2–1 μm for CuZn20-O-POSS80 and CuZn30-O-POSS70, respectively (Fig. 3-8b, c). Similar trend happens for the CuZn20-D-POSS80 and CuZn30-D-POSS70 (Fig. 3-8e, f), where the crystal particle sizes were reduced to 1–5 μm and 0.1–0.3 μm, respectively, with the difference that the particles preserved the cubic shape and with some evident fractures as an indication of the metal oxides deposition along the surface. Fig. 3-8g shows the packed structure of the graphene oxide and the exfoliation of the layers after chemical reduction of RGO in Fig. 3-8h. Fig. 3-8i confirmed the incorporation of the metal oxides in the RGO causes a shrinkage of the layers and pore blockage.

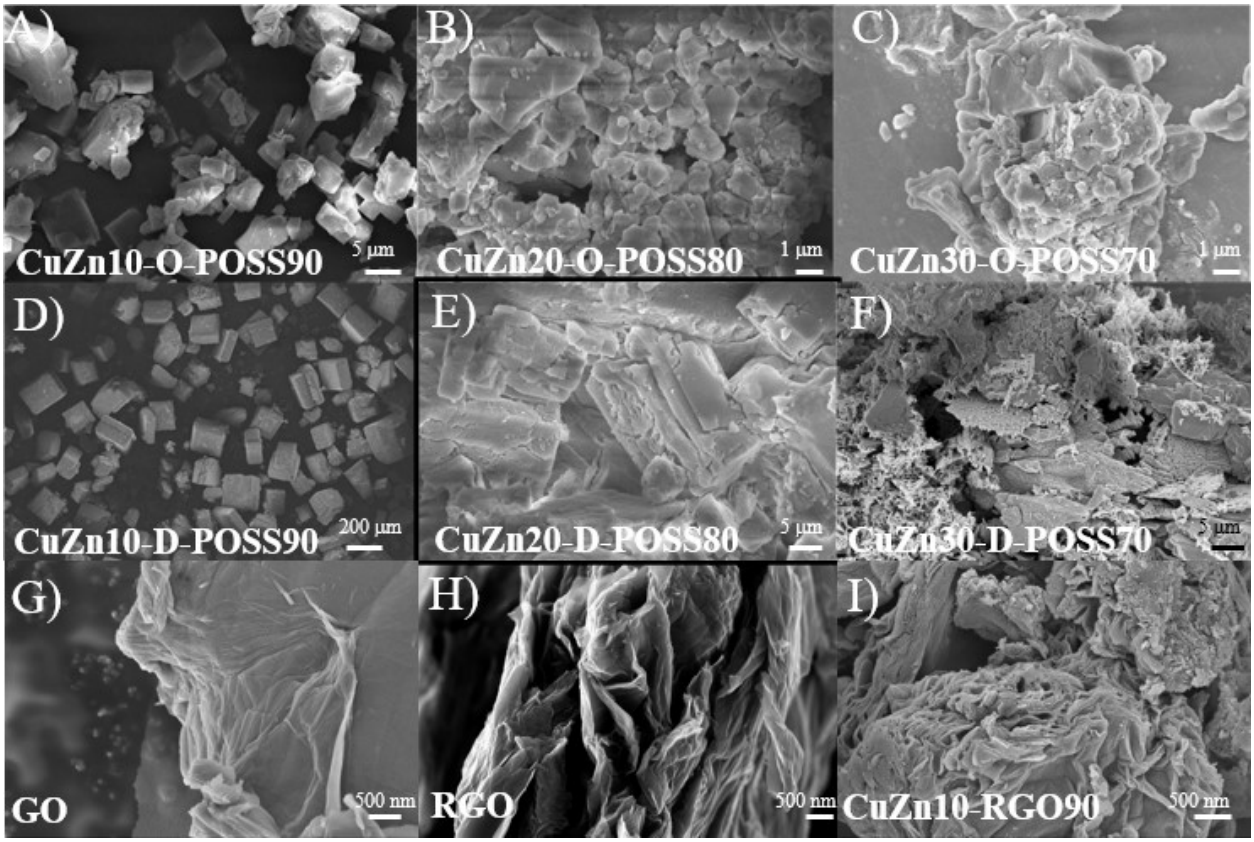

Figure 3-8 SEM of (**a**) CuZn10-O-POSS90; (**b**) CuZn20-O-POSS80; (**c**) CuZn30-O-POSS70; (**d**) CuZn10-D-POSS90; (**e**) CuZn20-D-POSS80; (**f**) CuZn30-D-POSS70; (**g**) Graphene Oxide (GO); (**h**) Reduced Graphene Oxide (RGO); and (**i**) CuZn10-RGO90.

TEM micrographs of neat O-POSS shows a platelike morphology (Fig. 3-9a), while the neat D-POSS (Fig. 3-9e) shows a well defined packed cubic shapes conforming previous report where this material can pack in a layer-by layer structure [29]. When the 10 wt.% of metals are supported O-POSS, the range of particle size goes from 3–16 nm with an average of 7 nm (Fig. 3-9b-d). The particle size on the D-POSS material range from 5–40 nm with an average of 15 nm (Fig. 3-9f-g). The CuZn10-D-POSS90 shows a lattice spacing of d=0.46 nm and d=0.33 nm in agreement with XRD results corresponding to the size of the body diagonal of the D-POSS cage and the distance between opposite Si_4O_4 faces of the silsesquioxane cube plane, respectively. A lattice space matching ZnO (d=0.28 nm) could be seen surrounding small particles of CuO

(d=0.23 nm). This interconnection between CuO and ZnO could benefit the synergy between Cu and ZnO during the CO_2 hydrogenation and prevent the sintering of the Cu particles [59].

Fig. 3-10 shows the EDX mapping images of the as-synthetize catalysts. Zn from O-POSS appears as the most intense element and Cu shows well disperse over Si and Zn. This is in agreement with the previous XRD results where ZnO tend to disperse CuO avoiding aggregation. This phenomenon is more visible over O-POSS, as the difference in the grain size between CuO ($D_{(-1\ 1\ 1)}$=11.97 nm) and ZnO ($D_{(1\ 0\ 0)}$=18.08 nm) is larger compared with the grain size of CuO ($D_{(-1\ 1\ 1)}$=10.51 nm) and ZnO ($D_{(1\ 0\ 0)}$=13.89 nm) over D-POSS (Table 3-2). Furthermore, average particle size over O-POSS is smaller compared with D-POSS. Cu and Zn reveal a homogeneous distribution over the layer of RGO Fig. 3-10c.

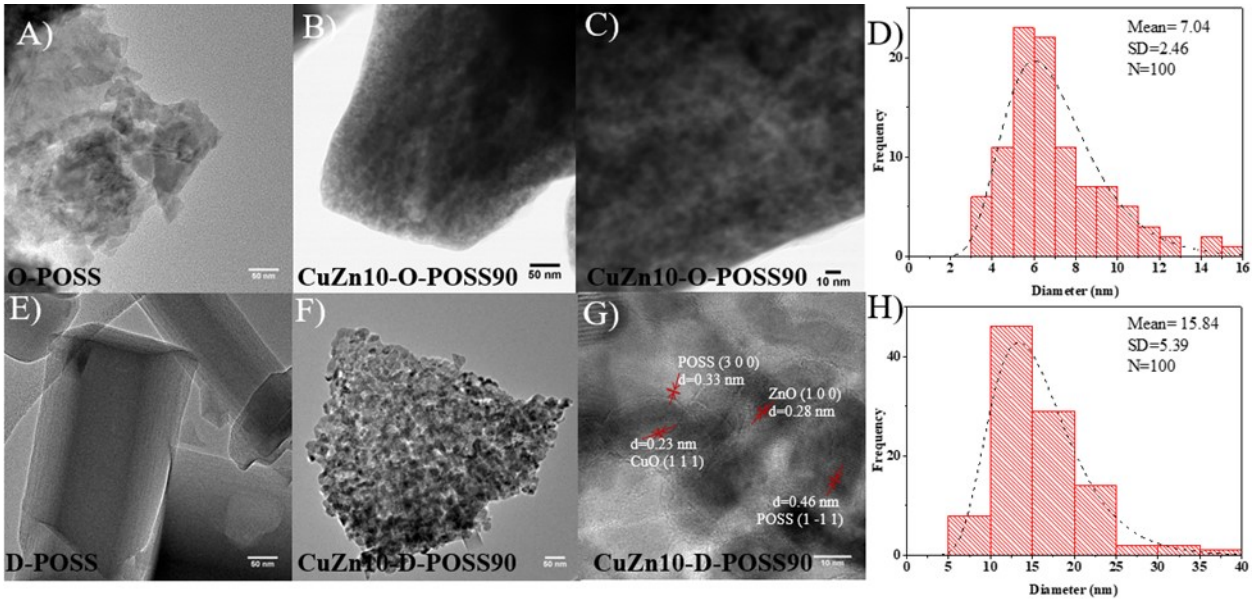

Figure 3-9 TEM of (**a**) O-POSS; (**b-c**) CuZn10-O-POSS90; (**d**) Particle size distribution of CuZn10-O-POSS90; (**e**) D-POSS; (**f-g**) CuZn10-D-POSS90; and (**h**) Particle size distribution of CuZn10-D-POSS90.

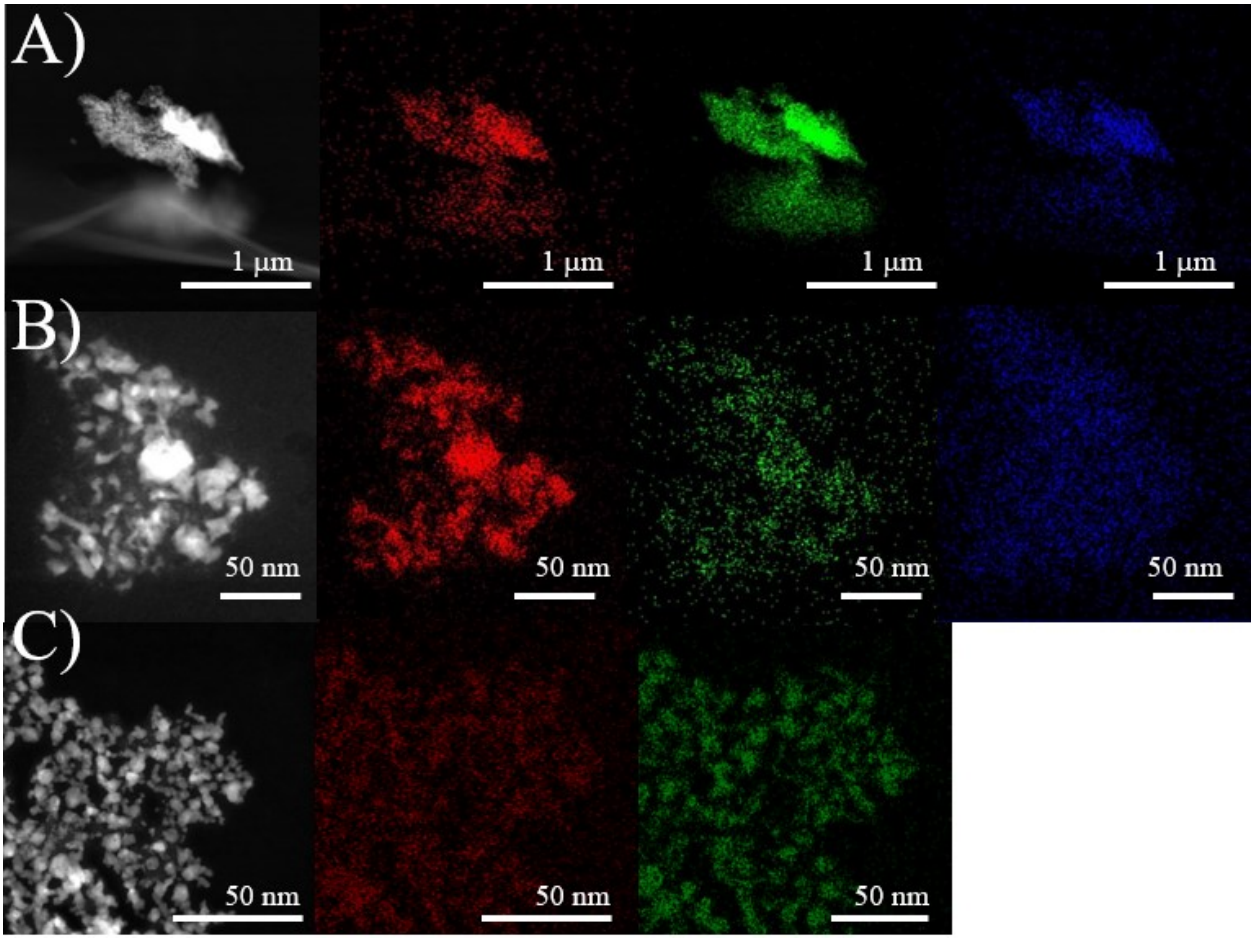

Figure 3-10 EDX of (**a**) 10Cu/ZnO-O-POSS; (**b**) 10Cu/Zn-D-POSS; (**c**) CuZn10-RGO90. Red-Copper; Green-Zinc; Blue-Silica.

3.3.2 Thermal Gravimetric Analyses

The thermal stability of the supports O-POSS and D-POSS and their catalysts are shown in Fig. 3-11. All the samples were degraded in a thermobalance in flowing nitrogen up to 900 °C. TGA profile of O-POSS and D-POSS implies that both supports are thermally stable in the reaction range (200 – 270 °C) with the first weight loss step at temperature onset of 440 °C and 481 °C, respectively. This weight loss is associated with the cleavage of Si-O-Si core rather than the cleavage of Si-C(aryl) [60]. A second thermal weight loss is observed for both POSS around 600 °C, producing around 70 wt.% stable black residue at 890 °C mostly associated to SiO_2 [61,62].

Metal loading from 10 to 30 wt.% on O-POSS and D-POSS did not affect the thermal stability of both supports in the desire reaction temperature (200 – 270 °C) except for the 10 wt.% loaded on O-POSS that reduces the onset temperature to 254 °C with initial weight loss of 2 wt.%. From Table A-2 (SI), it is obvious the metal loading reduces the thermal stability of the catalysts depending in the type of POSS. For 20 and 30 wt.% of metal loading on O-POSS, the onset temperature was reduced from 440 °C to 339 °C and 346 °C, respectively. For D-POSS, the onset temperature was reduced with a 10, 20 and 30 wt.% of metal loading to 459 °C, 458 °C, and 440 °C, respectively. When compared with the onset temperature of CuO/ZnO composite at 347 °C, the initial temperature drop of the catalyst is due to the portion of the metal oxide itself and not to a change in the physical chemical properties of POSS. The difference in temperature drop with O-POSS and D-POSS are presumed to be determined mainly by the degree of distortion of the Si-O-Si angle, as the number of phenyl groups increases, the molecules get bulkier, translated in increase rigidity [63].

Interestingly, O-POSS and D-POSS supports with a 10% of metal loading show the highest weight loss with maximum rates (571 °C and 521 °C, respectively). CuZn10-O-POSS90 shows the lower residue (16%) amount all catalysts prepared. In general, catalysts supported on D-POSS showed a higher residue at 890 °C compared with its counterpart O-POSS. Noted that for all the catalysts supported on POSS, there is <5% weight loss by the calcination temperature 270 °C employed to prepare the samples which implied that calcination at this temperature doesn't break the structure of the POSS supports. Despite this, we speculate that at temperature >400 °C CuO/ZnO may act as catalyst to accelerate either the sublimation or decomposition of POSS due to the lower residual left at 890 °C compared with the neat POSS.

The TGA patterns of RGO and CuZn10-RGO90 are shown in Fig. A-9 (SI). TGA profile of RGO and CuZn10-RGO90 show the onset temperature of both materials at 51 °C and 63 °C, respectively, associated with physisorbed water [7]. There is a residue of 74% for CuZn10-RGO90 at 890 °C. Since there is <5% of weight loss at the calcination temperature 350 °C, TGA can confirm that RGO was not destroyed by the calcination step of the supporting of the metals.

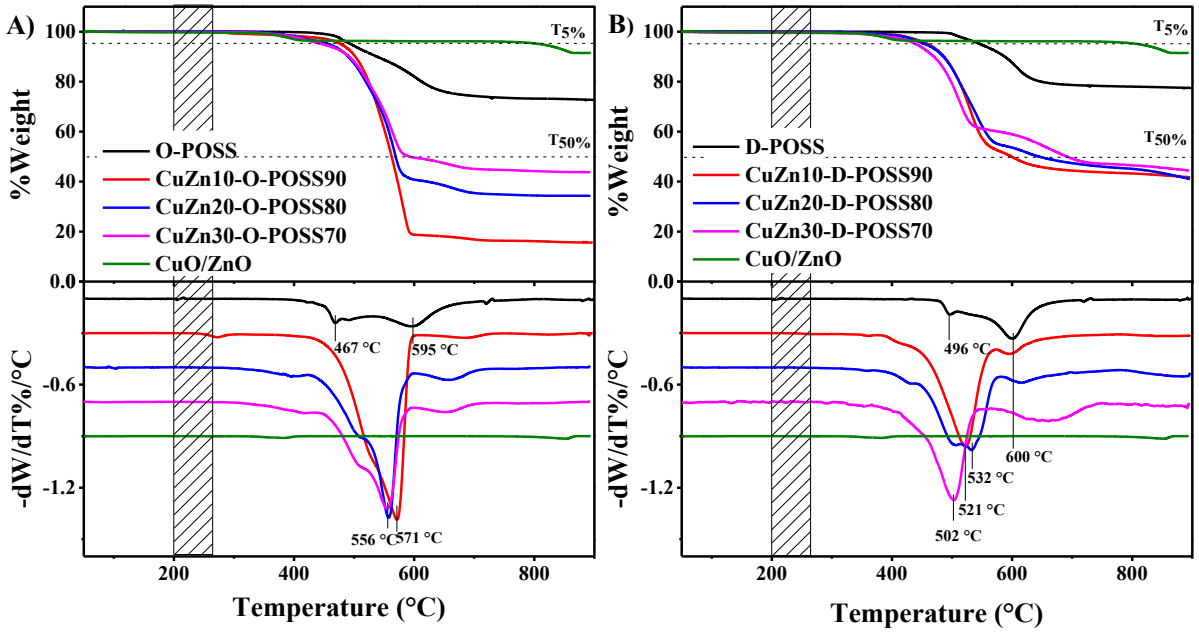

Figure 3-11 TGA and DTG profiles of (**a**) O-POSS, their catalysts, and CuO/ZnO and (**b**) D-POSS, their catalysts, and CuO/ZnO. Conditions 10 °C/min in N_2.

3.3.3 Effects of POSS as Hydrophobic Support

The hydrophobicity of the synthesized catalysts and the neat supports was evaluated with contact angle measurements (Fig. 3-12) using the sessile drop method. The catalysts supported on O-POSS and D-POSS showed a high degree of hydrophobicity compared with the catalyst supported on RGO. This result was expected as the O-POSS and D-POSS have eight and twelve phenyl ligands attached to the POSS cages, respectively; while RGO has some hydrophilic oxygen attached to the surface such as –OH, –COOH, and –CO–, which enhances its hydrophilic character. Phenyl groups have greater stability in comparison with the hydrophilic groups due to the unique properties of phenyl aromatic molecular orbitals. D-POSS has 12 phenyl groups attached to the siloxane core and a contact angle, θ=136.7 ± 0.2, larger than O-POSS, θ= 123.1 ± 1.1, that has eight phenyl groups. As the percentage of CuO/ZnO increases from 10 to 30 wt.%, the contact angle decreases too. As XPS analysis showed a new O 1s peak due to the oxides on the surface of the POSS supported catalysts that may form hydrogen bonds. As the

D-POSS is bulkier and the number of phenyl groups is less affine to bond with water, that gives a more hydrophobic character to the D-POSS catalysts. Despite the reduction of the contact angle of both supports, they still can be considered hydrophobic, as the θ≥ 90° [64].

RGO has a θ=40.6 ± 1.3 to be considered as hydrophilic material in agreement with the XPS results that shows C=O and physisorb water in the RGO surface even after the calcination step at 350 °C. Loading the 10 wt.% of metals on the surface of RGO, introduces the O1s corresponding to the oxide, but XPS analysis also shows the retention of -OH on the surface. The carbonyl, hydroxyl, and physisorb water present in RGO and CuZn10-RGO could have been a result of interlayer entrapment. The contact angle of CuZn10-RGO90 (θ≥ 0°) shows the great affinity for water for this material. Comparing catalysts supported on POSS and RGO, the first one shows a higher hydrophobic character that it is evident from the ability to repel water away from the active sites of a catalysts, hence, to reduce the opportunity water to Cu oxidation by water [65].

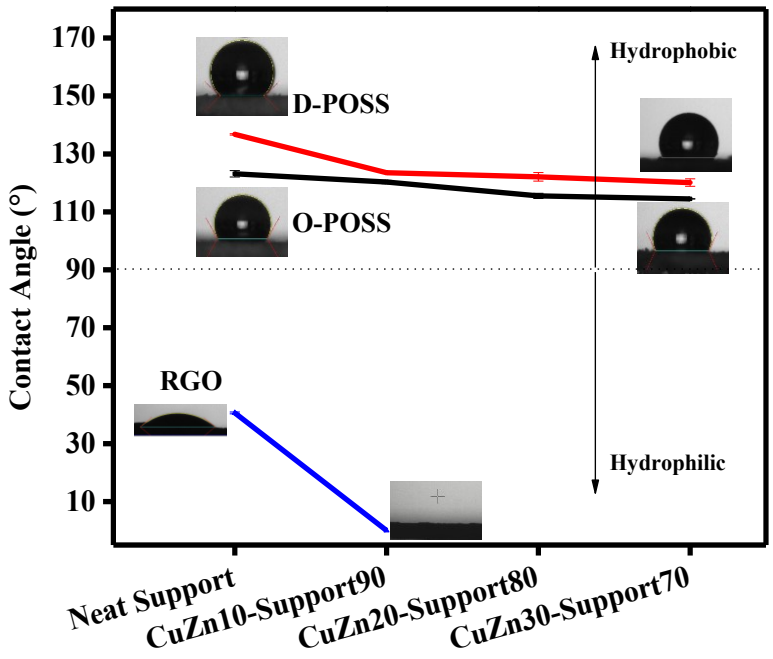

Figure 3-12 Contact angle of neat supports and their catalysts before reaction.

3.3.4 Catalytic Activity Evaluation

Firstly, the supported catalysts were reduced in H_2/N_2 (3:1) atmosphere at 220 °C for 30 min using a mini batch reactor. The procedure was repeated three times to remove impurities and water formed during catalysts activation. After flushed with N_2, the batch reactor was filled with the reaction mixture CO_2/H_2 (1:3) and thermally treated at 220 °C, 2 MPa and lasted for 18 h. The evaluation results of the catalysts are listed in Table 3-4.

The results show that the catalysts supported on POSS successfully favored the hydrogenation of CO_2 to methanol yield in the same order of magnitude. CuZn20-D-POSS80 shows the higher selectivity to methanol and less selectivity to CO. CuZn10-O-POSS90 shows the lower CO_2 conversion, and methanol yield although has the highest surface area among the POSS catalysts. It is interesting to observe that CuZn10-RGO90 even though has the highest surface area and highest CO_2 conversion rate compared with POSS catalysts, the selectivity to methanol is undetectable, meaning, under the reaction conditions, the hydrophobic character of POSS may be playing a decisive role on the stabilization and protection of the active species CuO and ZnO during the CO_2 hydrogenation, as it is reported the detrimental effect of the water content on the catalyst stability [66,67].

Table 3-4 The catalytic activity of CO_2 hydrogenation to methanol at 220 °C and 2 MPa after 18 h of reaction.

Sample	CO_2 conversion (%)	CH_3OH selectivity (%)	CO selectivity (%)	Other selectivity (%)	Yield of CH_3OH (%)
CuZn10-RGO90	81.1	-	87.5	12.5	-
CuZn10-O-POSS90	3.2	89.7	8.9	1.4	2.9
CuZn10-D-POSS90	4.4	87.5	11.6	0.9	3.8
CuZn20-D-POSS80	3.3	97.1	1.4	1.5	3.2
CuZn30-D-POSS70	5.3	72.0	28.0	0	3.8

The effect of hydrogenation temperature over the catalysts was explored on CuZn10-D-POSS90 as a model compound from 200 °C to 270 °C (Fig. 3-13). Typically, the conversion of CO_2 to methanol at equilibrium in gas phase is very low under ordinary reactions conditions, the use of a recycle reactor for unreacted gases is desired [68]. In this study, the micro-batch reactors were used for the purpose of initial screening of the catalysts and the equilibrium curve was calculated to reflect the experimental conditions.

Fig. 3-13 shows the yield of methanol to decrease when the reaction temperature increases from 220 °C to 270 °C in agreement with previous report [69]. Noted the outlier result at 200 °C although the experiments were repeated in triplicated. Despite the fact the CO_2 conversion did not reach the equilibrium, the methanol yield follows the equilibrium trend, a decrease in the methanol formation at higher temperature, as the equilibrium constant for methanol synthesis decreases with temperature [70]. Many studies have been dedicated to examining the mechanisms of CO_2 conversion and temperature correlation which can be summarized as follows: water gas shift reaction [71]; Cu particle sintering due to high reaction time [72]; carbon deposition [73]; and Cu and ZnO crystallization due to in-situ water generation [74]. It should be noted that even though the methanol yield and selectivity decreased with the temperature, the ATR-FTIR (Fig. A-10, SI) and thermal analysis (Fig. A-11, SI) of the spent catalyst showed stability on the internal structure of POSS as well as a similar thermal behaviour to the fresh catalyst. Our results imply that incipient wetness impregnation of CuO/ZnO on hydrophobic POSS results in highly dispersed active phase that promotes the CO_2 hydrogenation to methanol at low temperature. This work should be seen as an encouragement to further use n-phenyl POSS as hydrophobic systems that protect the active site from water deactivation. This hydrophobic system could be improved to further increase the surface area and more study on the deactivation mechanism from in-situ water generation should be encouraged.

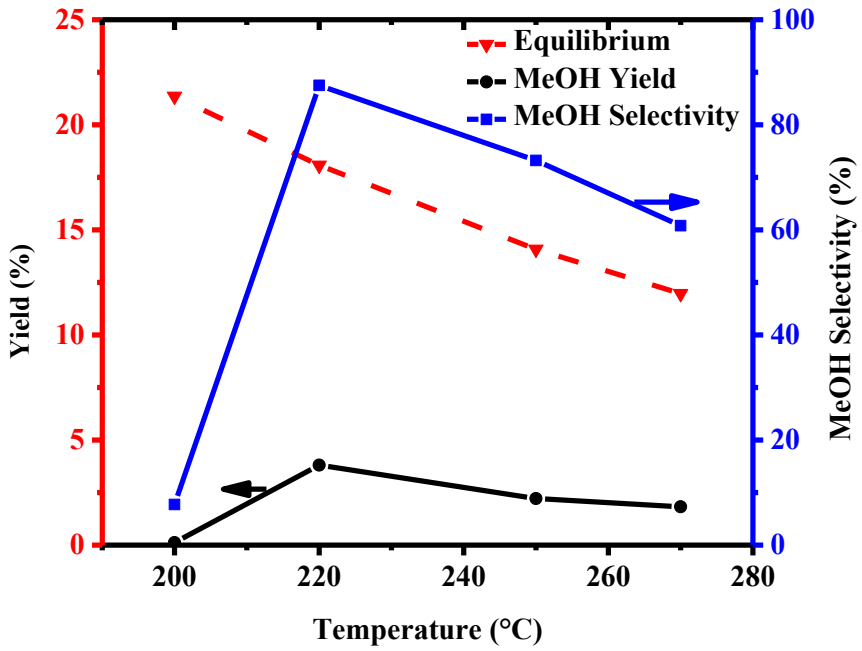

Figure 3-13 Conversion of CO_2 with CuZn10-D-POSS90. Conditions: CO_2:H_2 (1:3) at 2 MPa, 18 h. Catalysts activated at 0.8 MPa, 3 times with H_2/N_2 at 220 °C for 30 min.

3.4 Conclusions

CuZn-POSS catalysts were successfully prepared. The catalysts are thermally stable up to 400 °C and the integrity of the catalysts is preserved after one cycle of reaction. The metal oxides are homogeneously dispersed on the surface of the supports. The bulky phenyl groups around the silicon cages impart a hydrophobic character to the catalysts and play a hindrance role to repel the water produced in the reverse water gas shift reaction. The D-POSS with twelve phenyl groups results in a higher hydrophobic character than O-POSS, with eight phenyl groups, and RGO due to the bulky molecular structure and the higher contact angle. The hydrophobic character of the supports resulted in a more decisive factor than the surface area to influence the selectivity of CO_2 hydrogenation to methanol, as the catalysts supported on D-POSS have higher selectivity to methanol and higher conversion. Hence, POSS materials with hydrophobic properties have the potential to be efficiently used as support in catalytic reactions where active sites are sensible to water deactivation.

3.5 References

[1] Arena F, Barbera K, Italiano G, Bonura G, Spadaro L, Frusteri F. Synthesis, characterization and activity pattern of Cu–ZnO/ZrO2 catalysts in the hydrogenation of carbon dioxide to methanol. J Catal 2007;249:185–94.

[2] Joo O-S, Jung K-D, Moon I, Rozovskii AY, Lin GI, Han S-H, et al. Carbon dioxide hydrogenation to form methanol via a reverse-water-gas-shift reaction (the CAMERE process). Ind Eng Chem Res 1999;38:1808–12.

[3] Saito M, Murata K. Development of high performance Cu/ZnO-based catalysts for methanol synthesis and the water-gas shift reaction. Catal Surv from Asia 2004;8:285–94.

[4] Liaw BJ, Chen YZ. Liquid-phase synthesis of methanol from CO2/H2 over ultrafine CuB catalysts. Appl Catal A Gen 2001;206:245–56.

[5] Bagheri S, Julkapli NM, Yehye WA. Catalytic conversion of biodiesel derived raw glycerol to value added products. Renew Sustain Energy Rev 2015;41:113–27.

[6] Fan YJ, Wu SF. A graphene-supported copper-based catalyst for the hydrogenation of carbon dioxide to form methanol. J CO2 Util 2016;16:150–6.

[7] Deerattrakul V, Dittanet P, Sawangphruk M, Kongkachuichay P. CO2 hydrogenation to methanol using Cu-Zn catalyst supported on reduced graphene oxide nanosheets. J CO2 Util 2016;16:104–13.

[8] Wysokowski M, Materna K, Walter J, Petrenko I, Stelling AL, Bazhenov V V., et al. Solvothermal synthesis of hydrophobic chitin–polyhedral oligomeric silsesquioxane (POSS) nanocomposites. Int J Biol Macromol 2015;78:224–9.

[9] Laine RM, Roll MF. Polyhedral phenylsilsesquioxanes. Macromolecules 2011;44:1073–109.

[10] Liang F, Wang H, Liu G, Zhao J, Jin W. Designing highly selective and stable water transport channel through graphene oxide membranes functionalized with polyhedral

oligomeric silsesquioxane for ethanol dehydration. J Memb Sci 2021;638:119675.

[11] Kim K, Lichtenhan JD, Otaigbe JU. Facile route to nature inspired hydrophobic surface modification of phosphate glass using polyhedral oligomeric silsesquioxane with improved properties. Appl Surf Sci 2019;470:733–43.

[12] Deng Y, Han D, Deng YY, Zhang Q, Chen F, Fu Q. Facile one-step preparation of robust hydrophobic cotton fabrics by covalent bonding polyhedral oligomeric silsesquioxane for ultrafast oil/water separation. Chem Eng J 2020;379:122391.

[13] Létant SE, Herberg J, Dinh LN, Maxwell RS, Simpson RL, Saab AP. Structure and catalytic activity of POSS-stabilized Pd nanoparticles. Catal Commun 2007;8:2137–42.

[14] Zhou W, Wang J, Wang C, Du Y, Xu J, Yang P. A novel reusable platinum nanocatalyst. Mater Chem Phys 2010;122:10–4.

[15] Li X, Du Y, Dai J, Wang X, Yang P. Metal nanoparticles stabilized by cubic silsesquioxanes for catalytic hydrogenations. Catal Letters 2007;118:151–8.

[16] Liu Z, Ma S, Chen L, Xu J, Ou J, Ye M. Porous styryl-linked polyhedral oligomeric silsesquioxane (POSS) polymers used as a support for platinum catalysts. Mater Chem Front 2019;3:851–9.

[17] Hossain D, Pittman CU, Hagelberg F, Saebo S. Endohedral and exohedral complexes of T8-polyhedral oligomeric silsesquioxane (POSS) with transition metal atoms and ions. J Phys Chem C 2008;112:16070–7.

[18] Hossain D, Hagelberg F, Saebo S, Pittman CU. Structures, stabilities and electronic properties of endo- and exohedral dodecahedral silsesquioxane (T12-POSS) nanosized complexes with atomic and ionic species. J Inorg Organomet Polym Mater 2010;20:424–44.

[19] El Aziz Y, Taylor PG, Bassindale AR, Coles SJ, Pitak MB. Synthesis and Structures of Novel Molecular Ionic Compounds Based on Encapsulation of Anions and Cations. Organometallics 2016;35:4004–13.

[20] Bassindale AR, Pourny M, Taylor PG, Hursthouse MB, Light ME. Fluoride-ion encapsulation within a silsesquioxane cage. Angew Chemie - Int Ed 2003;42:3488–90.

[21] Unno M, Takada K, Matsumoto H. Synthesis, Structure, and Reaction of the Tetrahydroxycyclotetrasiloxane, [(i-Pr)(OH)SiO] $_4$. Chem Lett 1998;27:489–90.

[22] Harima Y, Komaguchi K, Oka K, Maruoka T, Imae I, Ooyama Y. Trapping of atomic hydrogens in cage-shaped silsesquioxanes by electric discharge. Chem Commun 2010;46:2076–8.

[23] Bonura G, Cordaro M, Cannilla C, Arena F, Frusteri F. The changing nature of the active site of Cu-Zn-Zr catalysts for the CO2 hydrogenation reaction to methanol. Appl Catal B Environ 2014;152–153:152–61.

[24] C. Marcano D, V. Kosynkin D, M. Berlin J, Sinitskii A, Sun Z, Slesarev A, et al. Improved Synthesis of Graphene Oxide. ACS Nano 2010;4:4806–14.

[25] Chau TT. A review of techniques for measurement of contact angles and their applicability on mineral surfaces. Miner Eng 2009;22:213–9.

[26] Chinnam PR, Gau MR, Schwab J, Zdilla MJ, Wunder SL. The polyoctahedral silsesquioxane (POSS) 1,3,5,7,9,11,13,15-octaphenylpentacyclo[9.5.1.13,9.15,15.17,13]-octasiloxane (octaphenyl-POSS). Acta Crystallogr Sect C Struct Chem 2014;70:971–4.

[27] Clegg BYW, Sheldrick GM, Vater N. Dodeea (phenylsilasesquioxane)* 1981:3162–4.

[28] Handke B, Jastrzebski W, Mozgawa W, Kowalewska A. Structural studies of crystalline octamethylsilsesquioxane (CH3)8Si8O12. J Mol Struct 2008;887:159–64.

[29] Kowalewska A. Self-assembling polyhedral silsesquioxanes - Structure and Properties. Curr Org Chem 2017;21:1243–64.

[30] Lesiak B, Trykowski G, Tóth J, Biniak S, Kövér L, Rangam N, et al. Chemical and structural properties of reduced graphene oxide—dependence on the reducing agent. J Mater Sci 2021;56:3738–54.

[31] Saito Y, Luo X, Zhao C, Pan W, Chen C, Gong J, et al. Filling the gaps between graphene oxide: a general strategy toward nanolayered oxides. Adv Funct Mater 2015;25:5683–90.

[32] Hu Y, Zhang Y, Du J, Li C, Wang K, Liu L, et al. The influence of composition on the functionality of hybrid CuO-ZnO-Al2O3/HZSM-5 for the synthesis of DME from CO2 hydrogenation. RSC Adv 2018;8:30387–95.

[33] Fujitani T, Nakamura J. The effect of ZnO in methanol synthesis catalysts on Cu dispersion and the specific activity. Catal Letters 1998;56:119–24.

[34] Zhang Y, Li D, Zhang S, Wang K, Wu J. CO 2 hydrogenation to dimethyl ether over CuO–ZnO–Al 2 O 3 /HZSM-5 prepared by combustion route. RSC Adv 2014;4:16391–6.

[35] Shimokawabe M, Asakawa H, Takezawa N. Characterization of copper/zirconia catalysts prepared by an impregnation method. Appl Catal 1990;59:45–58.

[36] O'Hare LA, Parbhoo B, Leadley SR. Development of a methodology for XPS curve-fitting of the Si 2p core level of siloxane materials. Surf Interface Anal 2004;36:1427–34.

[37] Cui YT, Kimura A, Miyamoto K, Sakamoto K, Xie T, Qiao S, et al. Electronic structures of Fe3 -x V x Si probed by photoemission spectroscopy. Phys Status Solidi 2006;203:2765–8.

[38] Moretti G, Fierro G, Lo Jacono M, Porta P. Characterization of CuO-ZnO catalysts by X-ray photoelectron spectroscopy: Precursors, calcined and reduced samples. Surf Interface Anal 1989;14:325–36.

[39] Biesinger MC. Advanced analysis of copper X-ray photoelectron spectra. Surf Interface Anal 2017;49:1325–34.

[40] Shao S, Li X, Gong Z, Fan B, Hu J, Peng J, et al. A new insight into the mechanism in Fe3O4@CuO/PMS system with low oxidant dosage. Chem Eng J 2022;438:135474.

[41] Al-Gaashani R, Radiman S, Daud AR, Tabet N, Al-Douri Y. XPS and optical studies of different morphologies of ZnO nanostructures prepared by microwave methods. Ceram Int

2013;39:2283–92.

[42] Biesinger MC, Lau LWM, Gerson AR, Smart RSC. Resolving surface chemical states in XPS analysis of first row transition metals, oxides and hydroxides: Sc, Ti, V, Cu and Zn. Appl Surf Sci 2010;257:887–98.

[43] CHANG C. Base catalyzed adsorption of toluene by zinc oxide. J Catal 1975;38:491–3.

[44] Zhu L, Li H, Liu Z, Xia P, Xie Y, Xiong D. Synthesis of the 0D/3D CuO/ZnO Heterojunction with Enhanced Photocatalytic Activity. J Phys Chem C 2018;122:9531–9.

[45] Lin T, He C, Xiao Y. Theoretical Studies of Monosubstituted and Higher Phenyl-Substituted Octahydrosilsesquioxanes. J Phys Chem B 2003;107:13788–92.

[46] Zhen CG, Becker U, Kieffer J. Tuning electronic properties of functionalized polyhedral oligomeric silsesquioxanes: A DFT and TDDFT study. J Phys Chem A 2009;113:9707–14.

[47] Fang H, Zhao L, Yue W, Wang Y, Jiang Y, Zhang Y. Facile and large-scale preparation of sandwich-structured graphene-metal oxide composites as anode materials for Li-ion batteries. Electrochim Acta 2015;186:397–403.

[48] Lee AS, Choi SS, Lee HS, Baek KY, Hwang SS. A new, higher yielding synthetic route towards dodecaphenyl cage silsesquioxanes: Synthesis and mechanistic insights. Dalt Trans 2012;41:10585–8.

[49] Monticelli O, Fina A, Ullah A, Waghmare P. Preparation, Characterization, and Properties of Novel PSMA-POSS Systems by Reactive Blending. Macromolecules 2009;42:6614–23.

[50] Handke B, Klita Ł, Nizioł J, Jastrze W, Adamczyk A. Studies of dodecaphenyl polyhedral oligomeric silsesquioxane thin films on Si (1 0 0) wafers q 2014;1066:248–53.

[51] Acik M, Mattevi C, Gong C, Lee G, Cho K, Chhowalla M, et al. The role of intercalated water in multilayered graphene oxide. ACS Nano 2010;4:5861–8.

[52] Zhou S, Kim S, Di Gennaro E, Hu Y, Gong C, Lu X, et al. Film structure of epitaxial graphene oxide on SiC: insight on the relationship between interlayer spacing, water

content, and intralayer structure. Adv Mater Interfaces 2014;1:1–8.

[53] Alam SN, Sharma N, Kumar L. Synthesis of Graphene Oxide (GO) by Modified Hummers Method and Its Thermal Reduction to Obtain Reduced Graphene Oxide (rGO)*. Graphene 2017;06:1–18.

[54] Thommes M, Kaneko K, Neimark A V., Olivier JP, Rodriguez-Reinoso F, Rouquerol J, et al. Physisorption of gases, with special reference to the evaluation of surface area and pore size distribution (IUPAC Technical Report). Pure Appl Chem 2015;87:1051–69.

[55] Condon JB. An Overview of Physisorption. Surf Area Porosity Determ by Physisorption 2006:1–27.

[56] Lowell S, Shields JE, Thomas MA, Thommes M. Surface Area Analysis from the Langmuir and BET Theories, 2004, p. 58–81.

[57] Peng Y, Ben T, Xu J, Xue M, Jing X, Deng F, et al. A covalently-linked microporous organic-inorganic hybrid framework containing polyhedral oligomeric silsesquioxane moieties. Dalt Trans 2011;40:2720–4.

[58] Gor GY, Thommes M, Cychosz KA, Neimark A V. Quenched solid density functional theory method for characterization of mesoporous carbons by nitrogen adsorption. Carbon N Y 2012;50:1583–90.

[59] Zhang F, Xu X, Qiu Z, Feng B, Liu Y, Xing A, et al. Improved methanol synthesis performance of Cu/ZnO/Al2O3 catalyst by controlling its precursor structure. Green Energy Environ 2022;7:772–81.

[60] Pakjamsai C, Kawakami Y. Study on effective synthesis and properties of ortho-alkyl-substituted phenyl octasilsesquioxane. Des Monomers Polym 2005;8:423–35.

[61] Fina A, Tabuani D, Carniato F, Frache A, Boccaleri E, Camino G. Polyhedral oligomeric silsesquioxanes (POSS) thermal degradation. Thermochim Acta 2006;440:36–42.

[62] Takahashi K, Sulaiman S, Katzenstein JM, Snoblen S, Laine RM. New

aminophenylsilsesquioxanes—Synthesis, properties, and epoxy nanocomposites. Aust J Chem 2006;59:564.

[63] Schubert US, Hüsing N, Laine RM. Materials syntheses. Vienna: Springer Vienna; 2008.

[64] Marmur A, Della Volpe C, Siboni S, Amirfazli A, Drelich JW. Contact angles and wettability: towards common and accurate terminology. Surf Innov 2017;5:3–8.

[65] Li C, Yuan X, Fujimoto K. Development of highly stable catalyst for methanol synthesis from carbon dioxide. Appl Catal A Gen 2014;469:306–11.

[66] Liang B, Ma J, Su X, Yang C, Duan H, Zhou H, et al. Investigation on Deactivation of Cu/ZnO/Al2O3 Catalyst for CO2 Hydrogenation to Methanol. Ind & Eng Chem Res 2019;58:9030–7.

[67] Fichtl MB, Schlereth D, Jacobsen N, Kasatkin I, Schumann J, Behrens M, et al. Kinetics of deactivation on Cu/ZnO/Al2O3 methanol synthesis catalysts. Appl Catal A Gen 2015;502:262–70.

[68] Saito M. R&D activities in Japan on methanol synthesis from CO2 and H2. Catal Surv from Asia 1998;2:175–84.

[69] Vu TTN, Desgagnés A, Iliuta MC. Efficient approaches to overcome challenges in material development for conventional and intensified CO2 catalytic hydrogenation to CO, methanol, and DME. Appl Catal A Gen 2021;617:118119.

[70] Chinchen GC, Denny PJ, Jennings JR, Spencer MS, Waugh KC. Synthesis of methanol. Appl Catal 1988;36:1–65.

[71] Spencer MS. The role of zinc oxide in Cu/ZnO catalysts for methanol synthesis and the water–gas shift reaction. Top Catal 1999;8:259.

[72] Sun JT, Metcalfe IS, Sahibzada M. Deactivation of Cu/ZnO/Al2O3 methanol synthesis catalyst by sintering. Ind Eng Chem Res 1999;38:3868–72.

[73] Zhai X, Shamoto J, Xie H, Tan Y, Han Y, Tsubaki N. Study on the deactivation phenomena

of Cu-based catalyst for methanol synthesis in slurry phase. Fuel 2008;87:430–4.

[74] Wu J, Saito M, Takeuchi M, Watanabe T. The stability of Cu/ZnO-based catalysts in methanol synthesis from a CO2-rich feed and from a CO-rich feed. Appl Catal A Gen 2001;218:235–40.

Chapter 4. Thermal Stability Study of Catalyst (CuO/ZnO) Supported on Phenyl Polyhedral Oligomeric Silsesquioxanes (POSS)

Abstract

The stability of heterogeneous catalytic systems is critical for the long-term use of the catalyst. Therefore, the thermal degradation behaviors of CuO/ZnO supported on polyhedral oligomeric octaphenyl silsesquioxane (O-POSS) and dodecaphenyl silsesquioxane (D-POSS) were investigated. The presence of the metal oxides does not interfere with the degradation mechanisms up to the temperature of 450 °C. After that temperature, the metal oxides accelerate the degradation rate of the supports. Irreversible thermal events, including molecular relaxation and crystal rearrangement, with low transition energy, were observed using differential scanning calorimetry. In all cases, the thermal analysis revealed complex behaviors. The crystal structure of both supports is destroyed in the oxidative atmosphere at 900 °C but partially destroyed in the nitrogen atmosphere. The vibrational frequencies of the residues in the inert and oxidative atmosphere showed after 500 °C the deformation of the Si-O peak due to intercage linkages formation.

Keyword: heterogeneous catalysis; POSS, thermal degradation; octaphenyl silsesquioxane; dodecaphenyl silsesquioxane

4.1 Introduction

Developing thermally stable heterogeneous catalysts that can endure elevated temperatures in corrosive and reductive environments is of great interest to industrial processes. Nevertheless, active metal sites tend to sinter or coalescence into larger particles under harsh conditions, especially at high temperatures, leading to catalyst [1]. Furthermore, support materials are used to produce a high surface area and carefully selected to tailor particular systems and thermal stability, as the support could accelerate the sintering through phase transformation or structural collapse of the support [2]. Even though the temperature is the primary parameter in the sintering process, reaction atmospheres can also impact the rate of catalyst deactivation. Water vapor, in particular, exacerbates the crystallization and structural modification of oxide supports [3]. Hence, it is vital to select a thermally stable support that is resistant to water deactivation, extending the catalytic system's productive life.

For example, the conversion of carbon dioxide to liquid fuels, including methanol, gasoline, jet fuel, diesel, ethanol, and other higher alcohols, requires highly active catalysts to decrease reaction barriers, as CO_2 is kinetically inert. In particular, Cu/ZnO is used as an active phase supported on gamma phase alumina (γ-Al_2O_3) to convert CO_2 to methanol. Nevertheless, the water formed in the reverse water gas shift reaction (RWGS) sticks to the surface of the active sites and promotes the formation of $ZnAl_2O_4$ poisoning the active sites, disrupting the synergistic effect of Cu/ZnO, and accelerating the Cu sintering [4,5]. Therefore, the reduced activity and short lifetime of this system limit its long-term industrial viability. Furthermore, more research is needed in the field on hydrophobic material with outstanding thermal stability. For instance, in this research, we studied phenyl oligomeric silsesquioxanes (POSS) as hydrophobic supports for CuO/ZnO for CO_2 hydrogenation.

Phenyl POSS is a type of hybrid inorganic/organic material with general formula $(RSiO_{1.5})n$, where phenyl groups are attached to the siloxane cage. POSS is prepared by sol-gel hydrolytic condensation of trifunctional monomers $RSiX_3$, where X may be a highly reactive substituent, such as Cl or alkoxy [6]. POSS molecules find applications in the preparation of polymer nanocomposites and hybrids to prepare multifunctional materials with organic/inorganic

properties and improve the thermal, oxidation, and mechanical properties as well as fire retardancy [7].

In the light of this background, a profound study on POSS thermal stability is required to tune the final properties and expand the applications of POSS as a thermally stable hydrophobic support in the heterogenous catalysis field. Fina *et al.* studied the thermal degradation of octaphenyl POSS, which showed higher thermal stability than saturated aliphatic POSS and reduced volatility [8]. In addition, they found POSS at high temperatures yields ceramic products. Blanco *et al.* studied the thermal degradation of various hetero-substituted POSS with a cyclopentyl group. The study showed different behaviours when inert and oxidative atmospheres were used [9].

Mantz *et al.* studied the thermal degradation of fully and partially condensed POSS. They analyzed the gases via TGA-FTIR and mass spectrometry. They reported that monomers such as $Cy_8Si_8O_{11}(OH)_2$, which contain silanol groups, initially decomposed through the loss of T-type silanol silicon environment, presumably through the elimination of H_2O. Decomposition continues through the loss of the organic substituents and after 450 °C results in the formation of SiO_xC_y chars [10].

Fan *et al.* studied the thermal degradation of polyhedral oligomeric octaphenyl silsesquioxane, octa(nitrophenyl)silsesquioxane, and octa(aminophenyl) silsesquioxane [11]. They found that —NO_2 and —NH_2 substituents on the phenyl group affected the mechanism of the POSS thermal degradation. In addition, the presence of amino groups reduced the thermal stability of the POSS core.

This work aimed to investigate the thermostability of the metal supported on POSS composites CuZn/O-POSS and CuZn/D-POSS to determine whether or not the presence of the metal oxides accelerate the POSS degradation in an inert or oxidative atmosphere to use these systems as heterogeneous catalytic material further. Unfortunately, there appeared to be no data on the thermal behaviour of these systems, such data was available only for the supports but not for the composites [8,11].

A secondary objective was to compare the thermal stability of the composites supported on O-POSS and D-POSS and whether the number of phenyl groups and the cage size have a weight

in the thermal properties. Any generalization would be helpful in future work to enable inferences to be drawn from data for the support to be selected according to the reaction type and the thermal conditions.

4.2 Material and Methods

4.2.1 Materials

Octaphenyl silsesquioxane (O-POSS, MS0840) and dodecaphenyl silsesquioxane (D-POSS, MS0802) were purchased from Hybrid Plastics Inc., USA. Copper nitrate trihydrate (99.5%, $Cu(NO_3)_2 \cdot 3H_2O$, Sigma-Aldrich), zinc nitrate hexahydrate (98%, $Zn(NO_3)_2 \cdot 6H_2O$, Sigma-Aldrich), and anhydrous ethyl alcohol (≥99.5%, CH_3CH_2OH, Supelco) were used as received.

4.2.2 Synthesis of CuO/ZnO/POSS

The CuO/ZnO/POSS composites were prepared with 10, 20, and 30% Cu-Zn metals, with equivalent Cu:Zn molar ratio using POSS as support via incipient wetness impregnation. Anhydrous ethyl alcohol was used as solvent. The composites were dried at 50 °C for 24 hours followed by calcination in a muffle at 270 °C for 7 h at a heating rate of 2 $°C min^{-1}$. The composites were coded based on the % of POSS used. Catalysts supported on octaphenyl POSS and dodecaphenyl POSS were labelled O-POSS and D-POSS, respectively. Herein, catalysts loaded with 10, 20, and 30% are denoted as follows: CuZnX-Y-POSSZ, where X is the weight percentage of CuZn, Y is the type of POSS, and Z is the % weight of POSS.

4.2.3 Equipment and Methods

Attenuated Total Reflectance - Fourier-transform infrared spectroscopy (ATR-FTIR) was used in the analysis of the products obtained after thermal analysis. Infrared spectra were collected using a Bruker Alpha Fourier Transform Infrared spectrophotometer (Bruker Optics, Esslingen, Germany) with OPUS software (version 7.0). The spectrometer was equipped with a single-bounce diamond reflection attenuated total reflectance (ATR) crystal plate. Spectra were recorded in triplicate at room temperature in the region of 400-4000 cm^{-1} using an average of 24 scans and a

resolution of 4 cm^{-1}. The manipulations of the spectra and baseline corrections were done using Nicolet Omnic software (version 8).

The thermal behaviour of the supports and the composites was studied through thermogravimetric analysis (TGA) (TGA/DSC1, Mettler Toledo, Switzerland) with MX5 microbalance, and GC 10 gas controller was employed in a nitrogen environment with 50 $mLmin^{-1}$. The thermal degradation experiments were performed in air flow 50 $mLmin^{-1}$ with nitrogen as purge gas at 50 $mLmin^{-1}$. Approximately 10 mg of sample was placed in an alumina crucible (70 μL) and heated from 25 °C to 900 °C at a heating rate of 10 $ºCmin^{-1}$ in N_2 or air. The residues were collected and studied by ATR FTIR.

The samples were investigated through differential scanning calorimetry (DSC) using a DSC 1 STAR^e System, Mettler Toledo, Switzerland. Around 4 mg of sample was placed in a sealed aluminum crucible. The analyses were conducted in a nitrogen atmosphere at a flow rate of 50 $mLmin^{-1}$ in triplicate. Initially, the heat flow of the sample was explored in a run from 25 to 500 °C at a heating rate of 10 $°Cmin^{-1}$. Then, the reversibility of each event was investigated by heating the sample just past the observed transition followed by cooling down below the event and heating up again [12]. Each heating segment employed a heating rate of 10 $°Cmin^{-1}$ while the cooling segments employed a cooling rate of -10 $°Cmin^{-1}$ [13]. The residues of the samples were collected at each step to study the vibrational changes of the composites. The temperature and heat flow calibration of the DSC was regularly checked, measuring the melting enthalpy and onset temperature of indium. The temperature measurements were accurate within 0.5 °C and the enthalpy measurements were accurate within 3.3% respect to the values reported in the literature for the standard indium (156.6 °C and 28.6 Jg^{-1}) [14].

The phase structure and crystalline features of the materials were evaluated with *in situ* powder X-ray diffraction (XRD) recorded on Bruker D8 Discover instrument using Cu-Kα radiation (40 kV, 30 mA, λ=0.154059 nm) equipped with LynxEYE 1- dimensional detector. A step size of 0.02° was used to measure spectra in the 2θ range of 5-80°. The powder samples were spread on a silicon wafer and placed on the sample heating stage. The samples were heated from room temperature to 600 °C under a nitrogen atmosphere. Interpretation of the data was performed using JADE 9.5 software.

4.2.4 Calculations

Results from the thermal analysis are reported following the format described by Eq. 4.1, where $\bar{x}$ corresponds to the average value (Eq. 4.2) of N independent measures of the quantity x, and $s(x_k)$ corresponds to the experimental standard deviation (Eq. 4.3) used as a measure of the uncertainty of the experimental data.

$$x = \bar{x} \pm s(x_k) \quad \text{Eq. 4.1}$$

$$\bar{x} = \frac{1}{N}\sum_{k=1}^{N} x_k \quad \text{Eq. 4.2}$$

$$s(x_k) = \sqrt{\frac{1}{N-1}\sum_{i=1}^{N}(x_i - \bar{x})^2} \quad \text{Eq. 4.3}$$

4.3 Results and Discussion

4.3.1 Thermal Degradation of Octaphenyl POSS and their Composites in Inert Atmosphere

Thermogravimetric analysis of O-POSS and their composites over the temperature range of 25 to 900 °C resulted in weight loss that could be classified into four regions labeled I to IV. Fig. 4-1 shows the TGA of O-POSS and their composites in nitrogen and their corresponding smooth first derivative (DTG). The differential scanning calorimetry calorigrams are also shown in Fig. 4-1, where the thermal events are labeled *i* to *v*. For the TGA curves of O-POSS and their composites, the temperature range related to each region and their weight loss are listed in Table 4-1. Likewise, for the calorigrams, the onset, endpoint, peak temperatures, and energy associated with each thermal event are listed in Table 4-2.

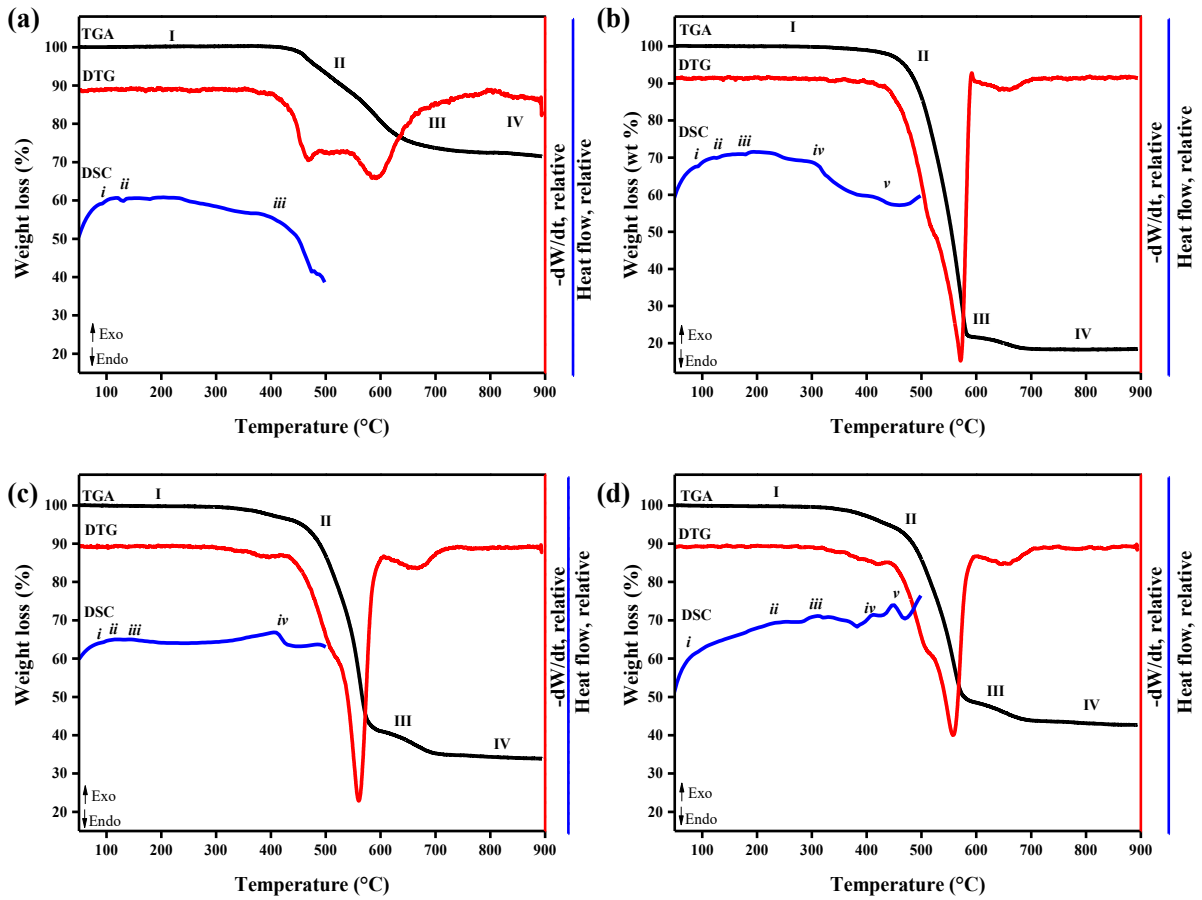

Figure 4-1 TGA (black), DTG (red), and DSC (blue) of (**a**) O-POSS, (**b**) CuZn10-O-POSS90, (**c**) CuZn20-O-POSS80, and (**d**) CuZn30-O-POSS70 in nitrogen flow (50 $mLmin^{-1}$).

Table 4-1 Thermal decomposition and weight loss profile of O-POSS and their composites studied by TGA analysis in nitrogen atmosphere of 50 $mLmin^{-1}$.

Composite	Region[a]	Temperature		Weight loss	Δwt/ΔT
		T_{onset} (°C)	T_{endset} (°C)	(wt%)[b]	(Δ(wt.%)C^{-1})
O-POSS	I	30.9 ± 0.6	439.0 ± 0.0	0.8 ± 0.2	0.0
	II	439.0 ± 0.0	491.2 ± 0.1	5.0 ± 0.2	0.1
	III	561.4 ± 0.0	648.4 ± 0.0	10.8 ± 0.0	0.1
	IV	648.4 ± 0.0	894.9 ± 0.0	9.0 ± 6.7	0.0
CuZn10-O-POSS90	I	31.5 ± 0.0	471.6 ± 0.1	5.5 ± 0.0	0.0
	II	471.6 ± 0.1	512.7 ± 0.0	13.9 ± 1.1	0.3
	III	561.9 ± 0.1	585.4 ± 0.0	22.1 ± 1.5	0.9
	IV	580.3 ±0.1	894.7 ± 0.2	3.7 ± 0.3	0.0
CuZn20-O-POSS80	I	31.5 ± 0.0	458.8 ± 0.0	5.7 ± 0.7	0.0
	II	458.8 ± 0.0	509.7 ± 0.0	12.4 ± 1.6	0.2
	III	556.5 ± 0.0	573.8 ± 0.0	16.7 ± 0.3	1.0
	IV	585.4 ± 0.0	894.7 ± 0.2	14.3 ± 0.0	0.0
CuZn30-O-POSS70	I	31.5 ± 0.0	455.6 ± 0.1	6.2 ± 0.2	0.0
	II	455.6 ± 0.1	506.1 ± 0.0	10.4 ± 0.4	0.2
	III	541.5 ± 0.0	572.2 ± 0.1	17.3 ± 1.0	0.6
	IV	572.2 ± 0.1	892.9 ± 0.0	8.1 ± 1.0	0.0

[a] All experiments were performed in nitrogen atmosphere with a flow rate of 50 $mLmin^{-1}$ at atmospheric pressure (~0.1 MPa).

[b] Weight loss profile of POSS and their composites were defined considering the temperature regions containing the main thermal events.

Table 4-2 Thermal decomposition of O-POSS and their composites studied by DSC analysis.

Composite	Transition[a,b]	Onset temperature (°C)	Endset temperature (°C)	Peak temperature (°C)	Enthalpy of transition[c] ($kJkg^{-1}$)
O-POSS	*i*	87.5 ± 0.3	100.0 ± 3.8	93.7 ± 0.1	-0.6 ± 0.0
	ii	124.7 ± 1.5	132.6 ± 0.2	126.7 ± 1.4	-4.2 ± 1.0
	iii	436.3 ± 0.3	—	—	—
CuZn10-O-POSS90	*i*	86.5 ± 3.9	99.8 ± 2.3	93.7 ± 0.3	-0.6 ± 0.3
	ii	124.2 ± 0.3	133.0 ± 0.6	129.1 ± 0.2	-0.7 ± 0.0
	iii	173.9 ± 7.4	184.9 ± 0.6	179.6 ± 0.4	-1.2 ± 0.9
	iv	266.0 ± 4.7	311.6 ± 4.7	308.1 ± 0.6	48.3 ± 6.0
	v	392.2 ± 2.9	441.3 ± 1.2	416.3 ± 0.5	8.0 ± 4.3
CuZn20-O-POSS80	*i*	88.0 ± 1.3	100.4 ± 2.4	93.6 ± 0.2	-0.2 ± 0.0
	ii	124.1 ± 0.9	132.2 ± 0.9	127.2 ± 0.7	-0.1 ± 0.0
	iii	165.9 ± 3.6	184.4 ± 1.0	175.5 ± 1.0	-1.0 ± 0.2
	iv	295.0 ± 3.1	445.4 ± 2.9	407.2 ± 1.0	87.0 ± 24.6
CuZn30-O-POSS70	*i*	86.1 ± 1.0	96.3 ± 4.9	92.4 ± 3.1	-0.3 ± 0.2
	ii	180.9 ± 2.3	249.3 ± 1.0	227.8 ± 2.8	22.0 ± 1.0
	iii	290.6 ± 3.0	336.8 ± 9.3	316.5 ± 5.3	35.1 ± 5.5
	iv	383.3 ± 0.7	426.1 ± 4.9	410.9 ± 2.3	7.8 ± 1.1
	v	438.0 ± 5.0	466.6 ± 18.7	452.0 ± 3.5	20.3 ± 6.3

[a] All experiments were performed in nitrogen atmosphere with a flow rate of 50 $mLmin^{-1}$ at atmospheric pressure (~0.1 MPa).

[b] All transitions observed by DSC analysis were irreversible upon dynamic cooling.

[c] Endothermic values are negative, and exothermic values are positive.

O-POSS is a thermally stable material up to 439.0 ± 0.0 °C with only a 0.8 ± 0.0 °C mass loss in region I. The calorigram shows that up to that temperature, two small endothermic transitions happened with energy changes lower than 4.5 $kJkg^{-1}$ (transitions *i* and *ii*) that could be related to molecular relaxation [15]. The biggest event in the calorigram started at 436.3 ± 0.3 °C (transition *iii*), which is related to the initial degradation of O-POSS. The TGA curve shows a continuous mass loss from 439.0 ± 0.0 °C to 648.4 ± 0.0 °C with a constant rate of weight loss of 0.1 $g°C^{-1}$ classified as region II and III. Furthermore, Fig. 4-2 shows in the FTIR analysis of the DSC residue at 500 °C a significant broadening of the peak at 1089 cm^{-1} associated with the formation of stretched intercage linkages of Si-O-Si at 500 °C [11,16]. A new peak appears at 778 cm^{-1} related to the vibration to intercage formation Si-O bond. The stretching vibration of the phenyl rings at 739 and 694 cm^{-1} decreased, shifted to a lower wavenumber at 500 °C and, completely disappeared at 900 °C.

Four regions characterize the TGA curve of O-POSS composites. Region I corresponds to the initial segment up to the onset temperature, where the first mass loss is registered. Region II represents the first considerable change in the mass loss of the composite. Even though the onset temperature moves to a higher range compared to O-POSS, the incorporation of the 10%, 20%, and 30% of metal oxides had a significant influence accelerating the weight loss of the composites, which changes from 0.8 ± 0.2% (O-POSS) to 5.5 ± 0.0%, 5.7 ± 0.7%, and 6.2 ± 0.2%, respectively. Table 4-1 shows an increase in the rate of weight loss to 0.3, 0.2, and 0.2 $g°C^{-1}$ in this region.

Region III has the highest weight loss for the three composites. A big peak in the DTG curve in this region indicates the biggest event in the thermal evaluation. The weight loss % increases from 10.8 ± 0.0% on O-POSS to 22.1 ± 1.5%, 16.7 ± 0.3%, and 17.3 ± 1.0% of the 10, 20, 30% metal loading, respectively. The presence of the metals accelerate the mass loss from 0.1 $g°C^{-1}$ in O-POSS to 0.9, 1.0, and 0.6 $g°C^{-1}$ of the 10%, 20%, and 30% metal oxide composites in this region. The lower mass loss rate at 30 % may be associated with the metal oxides covering the siloxane cages, protecting them from degradation. Region IV shows the last thermal degradation event in the studied temperature range. The O-POSS and the composites show a steady mass loss with a loss rate lower than 0.1 $g°C^{-1}$ [11].

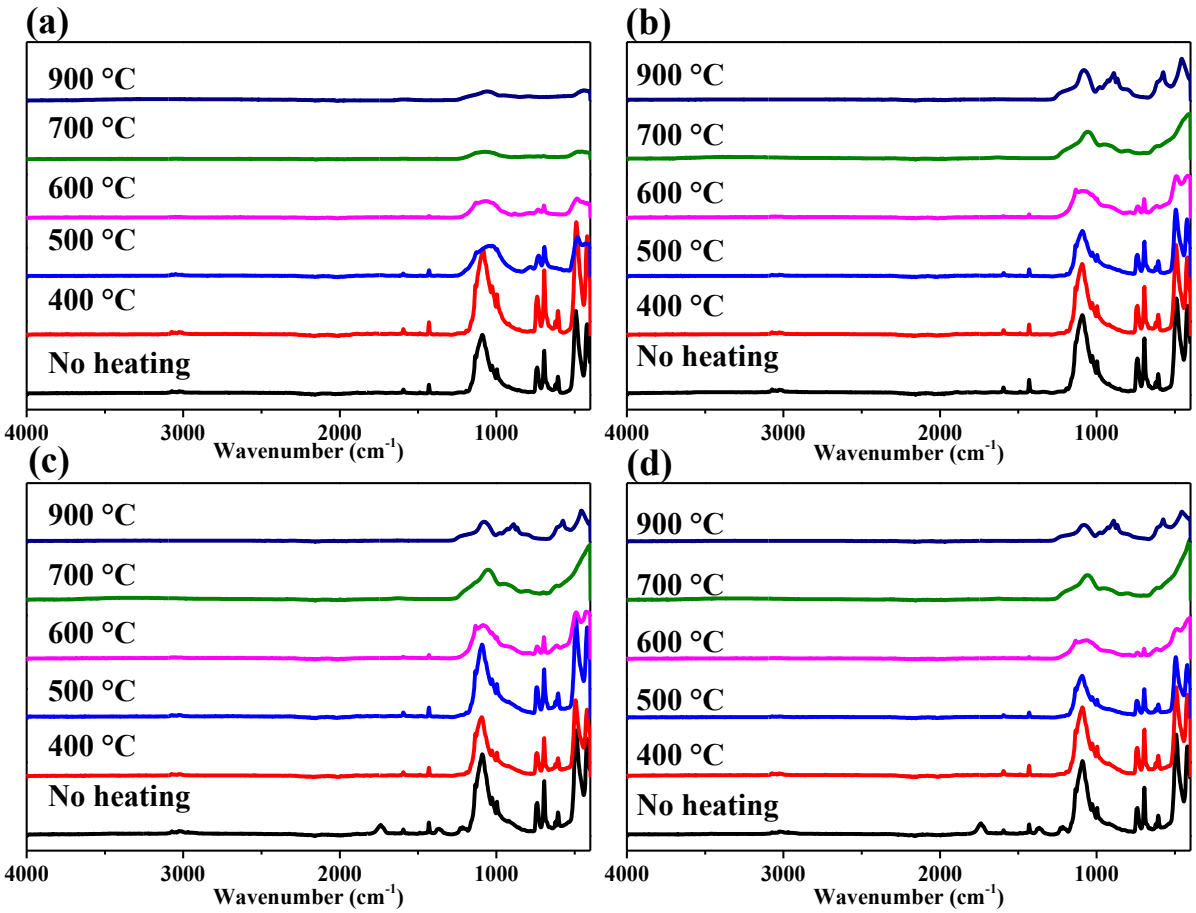

Figure 4-2 ATR FTIR of the residues of (**a**) O-POSS, (**b**) CuZn10-O-POSS90, (**c**) CuZn20-O-POSS80, and (**d**) CuZn30-O-POSS70 in nitrogen flow of 50 $mLmin^{-1}$.

The calorigram of CuZn10-O-POSS90 and CuZn20-O-POSS80 shows the same endothermic transitions *i* and *ii* present in O-POSS related to molecular relaxation associated with POSS. CuZn30-O-POSS70 calorigram shows a complex behaviour with four exothermic events from 180 °C up to 500 °C. These events were replicated in the analyses performed in triplicate.

There is steep mass loss from the range 450 °C to 570 °C. In this region, O-POSS showed two separate events (Fig. 4-1b); in the metal composites, those events overlap in one broad peak. As the percentage of the metals on O-POSS increases from 10 to 30%, the rate of weight loss double causing an acceleration in the degradation of the support.

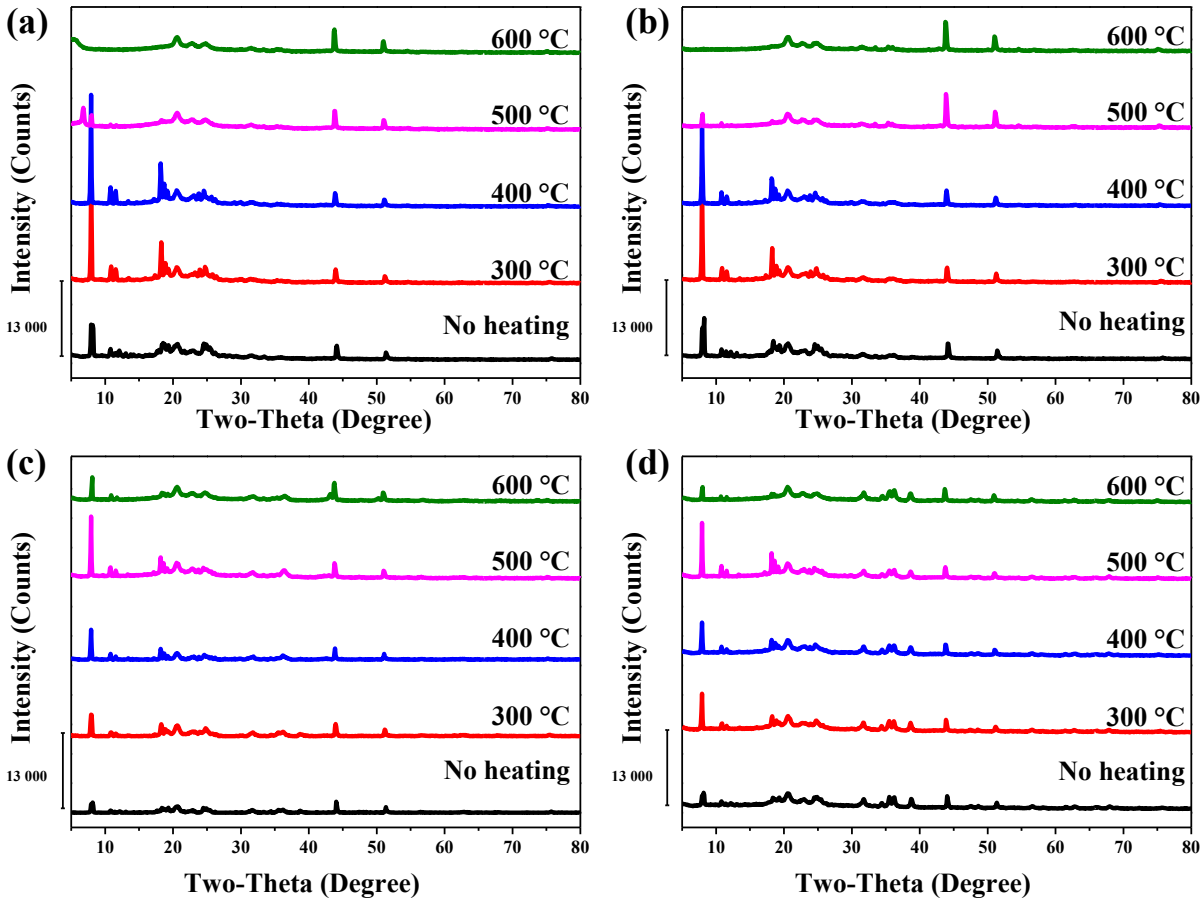

Figure 4-3 XRD profiles of samples heated at different temperatures (**a**) O-POSS, (**b**) CuZn10-O-POSS90, (**c**) CuZn20-O-POSS80, and (**d**) CuZn30-O-POSS70 in nitrogen flow of 50 $mLmin^{-1}$.

Fig. 4-3 shows the XRD diffraction of the O-POSS and O-POSS composites. O-POSS has three characteristic peaks at 8.0° (d=1.1 nm), 18.5° (d=0.48 nm), and 24.4° (d=0.36 nm) associated with the overall size of POSS molecules, diagonal of the POSS cage, and the distance between opposite Si_4O_4 faces of the cage, respectively. From 300 °C to 500 °C the definition of the peaks previously mentioned increases, as a confirmation of the stability of the crystal structure of the POSS cage when temperature is increased. On the other hand, the broadening of the signal Si-O at 500 °C in the FTIR spectra may have been related to the increase of the 8.0° signal in the diffractogram. At 600 °C, the diffractogram of O-POSS shows the disappearance of the peak at 8.0°, presumably for the complete degradation of the siloxane cage by heat treatment.

A similar trend is followed by CuZn10-O-POSS90, where at 600 °C, the peaks associated with the siloxane cage are destroyed. Interestingly, as the CuO/ZnO ratio to O-POSS increases, the peak at 8.0° is preserved in the composites even though the intensity was reduced compared to the intensity at 500 °C. Presumably, the metal oxides bonded to the siloxane cage protect it from heat degradation at that temperature. While the support is affected at temperatures higher than 500 °C, the composites' diffractograms show how the metal oxides' crystal features are preserved in the temperature range.

4.3.2 Thermal Degradation of Octaphenyl POSS and Their Composites in Oxidative Atmosphere

Thermogravimetric analysis of O-POSS and their composites in an oxidative atmosphere were investigated in the temperature range of 25 to 900 °C. Fig. 4-4 shows the TGA and DTG curves as well as the main thermal events, classified from I to V. For the TGA curves the temperature onset, endpoint, mass loss, rate of mass loss, and mass of residue are listed in Table 4-3.

Initially, O-POSS has a similar thermal trend in an oxidative atmosphere as in the inert atmosphere. In air, O-POSS is a stable material to about 445.1 ± 0.0 °C with a weight loss of 1.0 ± 0.0% (Fig. 4-4a), region I). The FTIR of the residues at 400 °C shows no change in the vibrational spectrum compared with the sample without any heat treatment (Fig. 4-5a). Next, three consecutive regions of mass loss together correspond to the larger mass loss event of O-POSS (Fig. 4-4a region II, III, IV). The series of events goes from 445.1 ± 0.0 °C to 646.4 ± 0.6 °C with a total mass loss of 43.6 ± 0.1 %. The FTIR of the residues at 600 °C shows broadening of the signal at 1100 cm^{-1} corresponding to the Si-O framework, and the peaks related to the phenyl group out-of-plane deformation (697, 746 cm^{-1}) almost disappeared, indicating that the phenyl groups have been removed from the silicon cage, which is in agreement with previous studies [11].

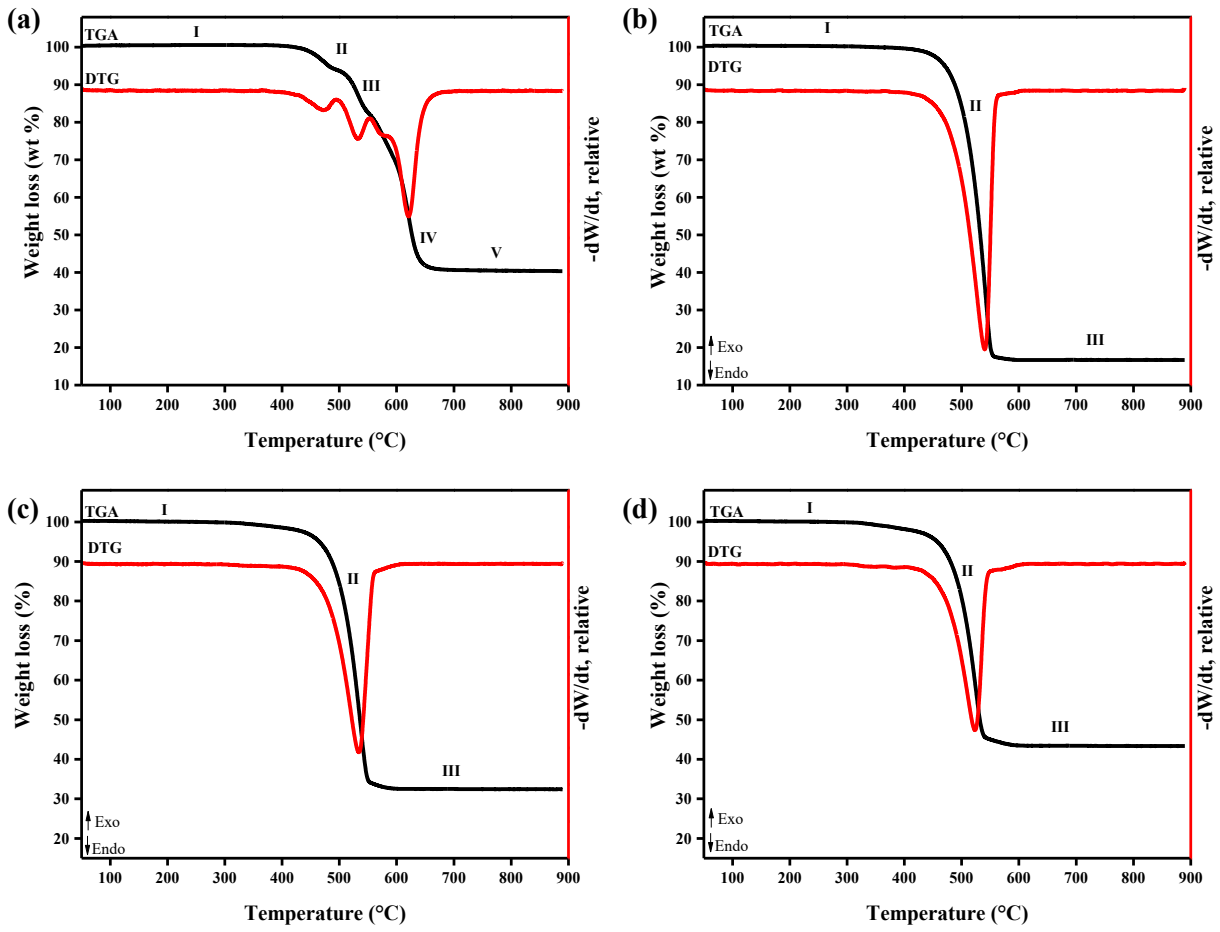

Figure 4-4 TGA and DTG of (**a**) O-POSS, (**b**) CuZn10-O-POSS90, (**c**) CuZn20-O-POSS80, and (**d**) CuZn30-O-POSS70 in an airflow of 50 $mLmin^{-1}$.

The last region of the O-POSS thermogram is a stable segment with only a mass loss of 1.9 ± 0.1 %. The char residues at 889 °C were 40.4±0.0 %. The FTIR of the residues from 600 °C and forward barely changed, in agreement with the mass loss that remained constant. The XRD analysis of the char at 900 °C revealed that the crystal structure was destroyed (Fig. 4-6).

Table 4-3 Thermal decomposition and weight loss profile of O-POSS and their composites studied by TGA in airflow of 50 $mLmin^{-1}$.

Composite	Region[a]	Temperature		Weight loss	Δwt/ΔT	Residue
		T_{onset} (°C)	T_{endset} (°C)	(wt%)[b]	(Δ(wt.%)C^{-1})	(wt%)[c]
O-POSS	I	31.2 ± 0.0	445.1 ± 0.0	1.0 ± 0.0	0.0	40.4 ± 0.0
	II	445.1 ± 0.0	491.7 ± 0.4	4.9 ± 0.0	0.1	
	III	524.1 ± 0.2	554.8 ± 0.5	8.2 ± 0.0	0.3	
	IV	587.5 ± 0.2	646.4 ± 0.6	30.5 ± 0.1	0.5	
	V	646.4 ± 0.6	889.2 ± 0.1	1.9 ± 0.1	0.0	
CuZn10-O-POSS90	I	31.2 ± 0.0	505.0 ± 0.2	19.1 ± 0.2	0.0	17.0 ± 0.5
	II	505.0 ± 0.2	562.2 ± 0.4	63.6 ± 0.2	1.1	
	III	562.2 ± 0.4	889.4 ± 0.1	0.7 ± 0.0	0.0	
CuZn20-O-POSS80	I	31.3 ± 0.0	507.4 ± 0.6	20.1 ± 0.4	0.0	32.4 ± 0.0
	II	507.4 ± 0.6	555.2 ± 0.7	45.9 ± 0.4	1.0	
	III	555.2 ± 0.7	889.5 ± 0.1	1.6 ± 0.1	0.0	
CuZn30-O-POSS70	I	31.3 ± 0.0	487.6 ± 0.5	12.7 ± 0.2	0.0	43.4 ± 0.0
	II	487.6 ± 0.5	546.6 ± 0.4	42.1 ± 0.2	0.7	
	III	546.6 ± 0.4	889.6 ± 0.1	1.8 ± 0.0	0.0	

[a] All experiments were performed in air atmosphere with a flow rate of 50 $mLmin^{-1}$ at atmospheric pressure (~0.1 MPa).

[b] Weight loss profile of POSS and their composites were defined considering the temperature regions containing the main thermal events.

[c] Residue represents the weight % of the mass after the heating cycle.

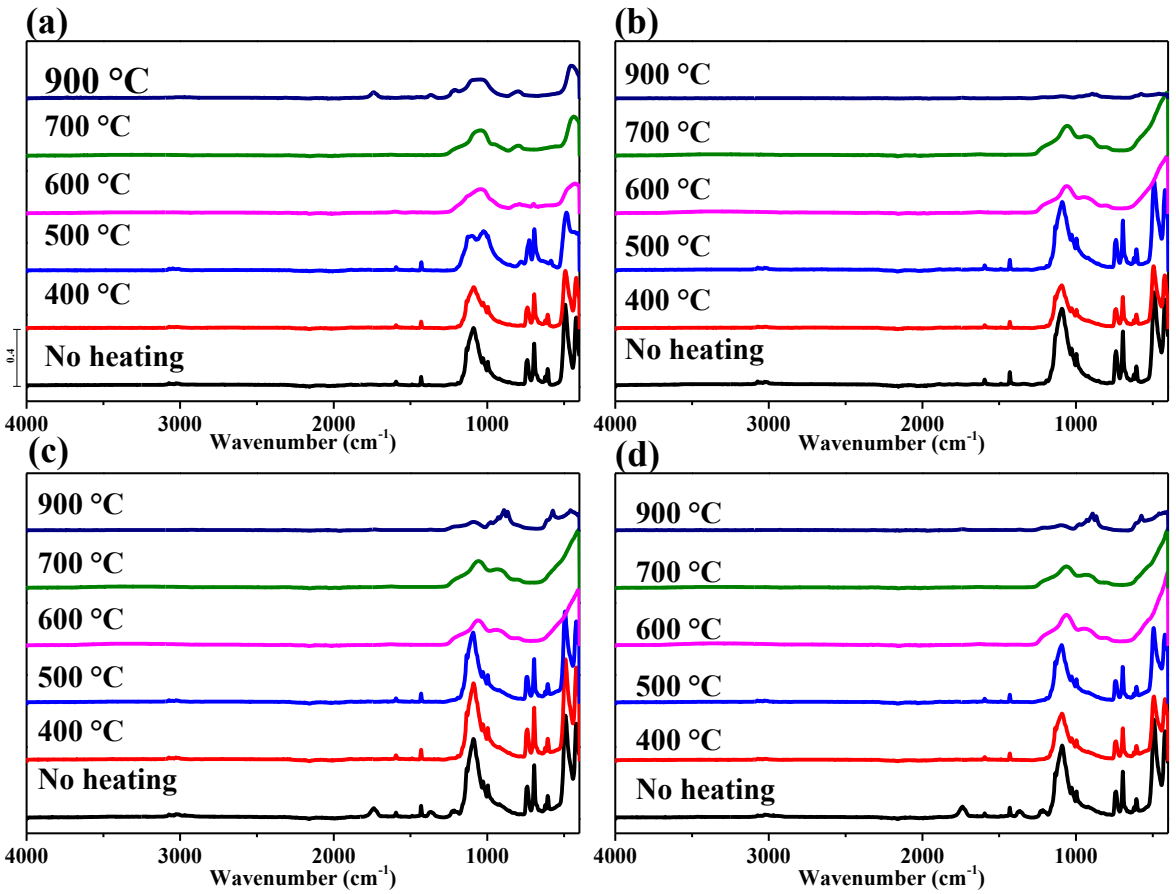

Figure 4-5 ATR FTIR of the residues (**a**) O-POSS, (**b**) CuZn10-O-POSS90, (**c**) CuZn20-O-POSS80, and (**d**) CuZn30-O-POSS70 in an airflow of 50 $mLmin^{-1}$.

The thermograms of the composites CuZn/O-POSS in the oxidative atmosphere show a similar trend with three main regions, I, II, and III. The presence of the metal oxides accelerates the mass loss of the composites when compared with the neat O-POSS. When region I of the composites is compared with the region I and II of O-POSS, the mass loss increased four folds for CuZn10-O-POSS90 and CuZn20-O-POSS80 and doubled for CuZn30-D-POSS70. Presumably, the presence of the metal oxides reacts with the support catalyzing the degradation of the silsesquioxane in an oxidative atmosphere, despite this the spectra of the residues of the composites show similar spectra to the non-heated O-POSS up to 500 °C. After 600 °C, the composites' molecules vibrate in a similar pattern to that of the neat O-POSS, presenting a broad and deformed peak at 1099 cm^{-1} and the complete disappearance of phenyl peaks (697, 746 cm^{-1}).

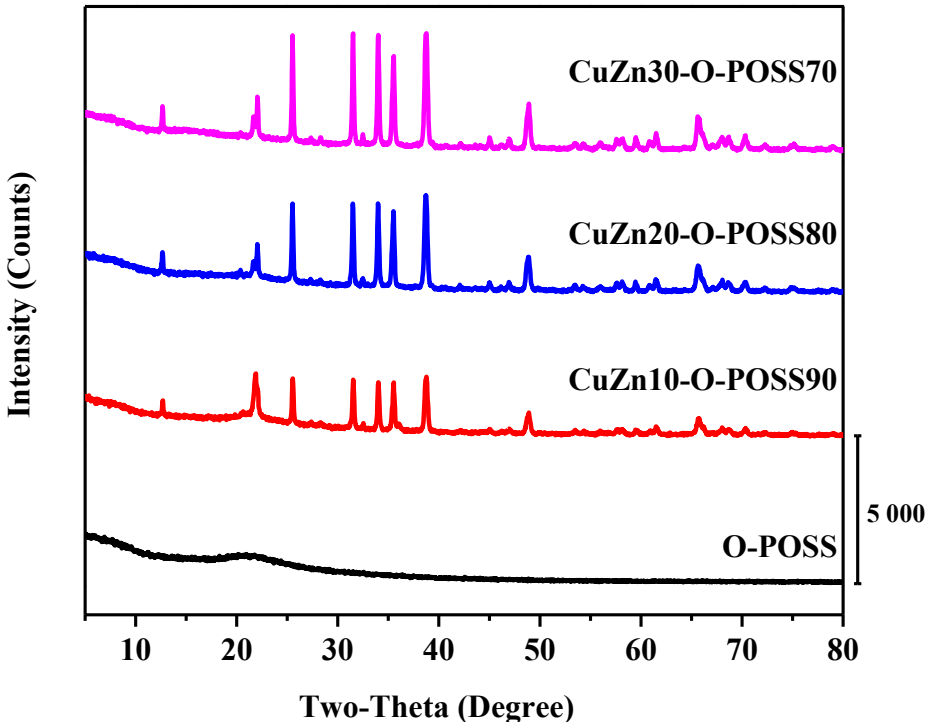

Figure 4-6 XRD of the residues of O-POSS and the composites of TGA at 900 °C in an airflow at 50 $mLmin^{-1}$.

The XRD of the char of the composites shows the diffraction peaks associated with CuO/ZnO. The crystal structure of O-POSS was destroyed with the heating treatment in the air atmosphere at 900 °C.

4.3.3 Thermal Degradation of Dodecaphenyl POSS and Their Composites in Inert Atmosphere

Thermogravimetric analysis of D-POSS and the D-POSS composites over the temperature range 25 to 900 °C resulted in a mass loss that could be classified into four regions labeled I to IV (Fig. 4-7). The calorigram obtained by differential scanning calorimetry of D-POSS and the composites are also shown in Fig. 4-7, and thermal events are labeled *i* to i*v*. For the TGA curve, the mass loss, the onset, and endpoint temperature are listed in Table 4-4. Similarly, for the calorigram, the onset, endpoint, peak temperatures of the thermal events, and energy change associated with each event are listed in Table 4-5.

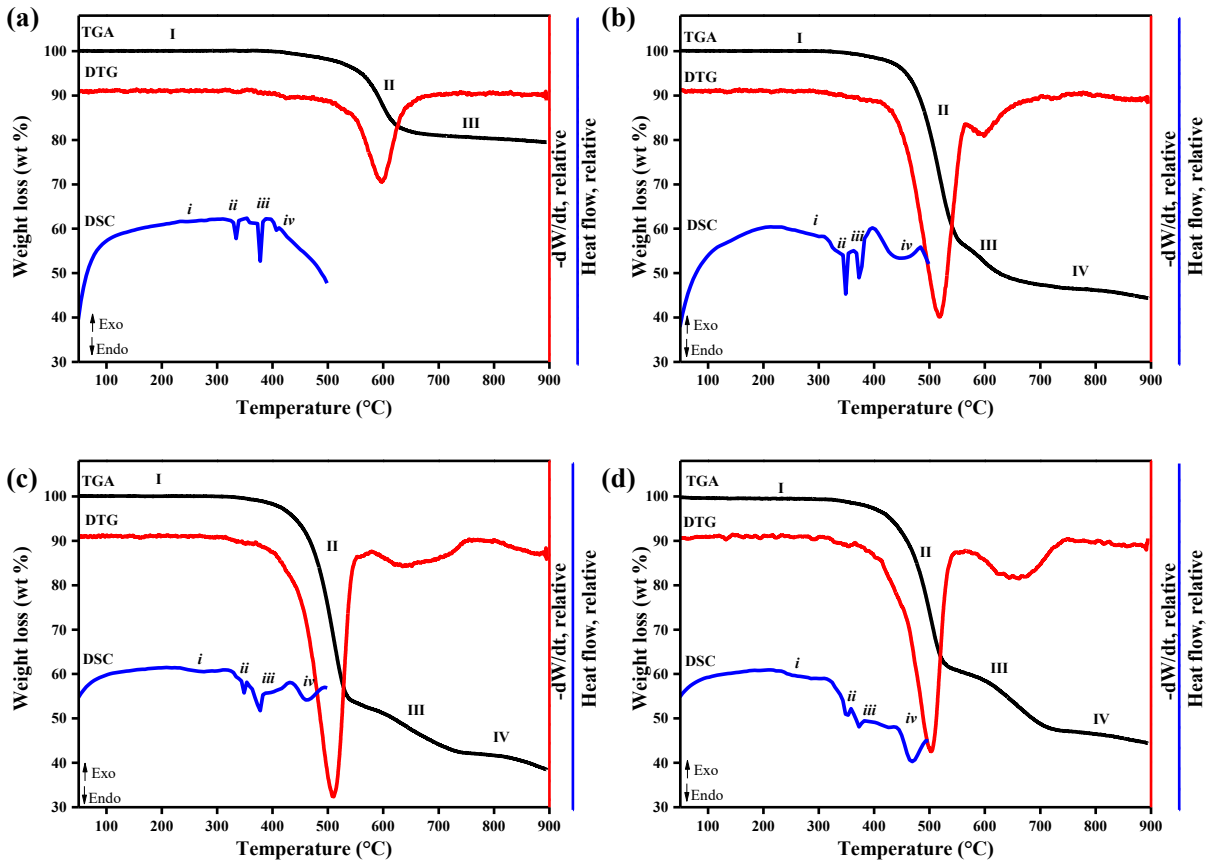

Figure 4-7 TGA (black), DTG (red), and DSC (blue) of (**a**) D-POSS, (**b**) CuZn10-D-POSS90, (**c**) CuZn20-D-POSS80, and (**d**) CuZn30-D-POSS70 in nitrogen flow of 50 $mLmin^{-1}$.

Table 4-4 Thermal decomposition and weight loss profile of D-POSS and their composites studied by TGA analysis in nitrogen atmosphere of 50 $mLmin^{-1}$.

Composite	Region[a]	Temperature		Weight loss	Δwt/ΔT
		T_{onset} (°C)	T_{endset} (°C)	(wt%)[b]	(Δ(wt.%)C^{-1})
D-POSS	I	31.3 ± 0.1	547.8 ± 0.1	4.0 ± 0.0	0.0
	II	547.8 ± 0.1	624.6 ± 0.0	12.7 ± 0.0	0.2
	III	624.6 ± 0.0	892.1 ± 0.0	7.1 ± 0.0	0.0
CuZn10-D-POSS90	I	31.3 ± 0.0	471.1 ± 0.0	8.0 ± 0.8	0.0
	II	471.1 ± 0.0	540.9 ± 0.0	33.0 ± 1.1	0.5
	III	548.2 ± 0.0	641.1 ± 0.0	9.3 ± 0.3	0.1
	IV	641.1 ± 0.0	892.3 0.1	4.4 ± 4.2	0.0
CuZn20-D-POSS80	I	31.3 ± 0.0	460.8 ± 0.0	7.7 ± 1.0	0.0
	II	460.8 ± 0.0	528.9 ± 0.0	33.8 ± 1.4	0.5
	III	595.4 ± 0.1	728.8 ± 0.1	7.2 ± 2.1	0.0
	IV	728.8 ± 0.1	892.5 ± 0.0	4.7 ± 0.7	0.0
CuZn30-D-POSS70	I	31.0 ± 0.1	454.5 ± 0.0	10.1 ± 1.5	0.0
	II	454.5 ± 0.0	519.5 ± 0.1	22.4 ± 6.4	0.3
	III	599.1 ± 0.0	715.1 ± 0.1	12.9 ± 3.2	0.1
	IV	715.1 ± 0.1	892.1 ± 0.0	2.4 ± 1.4	0.0

[a] All experiments were performed in nitrogen atmosphere with a flow rate of 50 $mLmin^{-1}$ at atmospheric pressure (~0.1 MPa).

[b] Weight loss profile of POSS and their composites were defined considering the temperature regions containing the main thermal events.

Table 4-5 Thermal decomposition of D-POSS and their composites studied by DSC analysis.

Composite	Transition[a,b]	Onset temperature (°C)	Endset temperature (°C)	Peak temperature (°C)	Enthalpy of transition[c] ($kJkg^{-1}$)
D-POSS	*i*	269 ± 0.4	285.0 ± 0.9	278.2 ± 1.2	-0.7 ± 0.3
	ii	330.3 ± 0.1	338.4 ± 0.4	334.3 ± 0.2	-10.9 ± 2.6
	iii	376.2 ± 0.7	380.7 ± 0.5	378.4 ± 0.7	-25.5 ± 1.0
	iv	400.8 ± 2.2	410.0 ± 1.6	405.3 ± 1.9	-4.1 ± 0.4
CuZn10-D-POSS90	*i*	235.1 ± 4.7	256.7 ± 2.1	—	—
	ii	345.8 ± 0.2	352.1 ± 0.3	349.3 ± 0.4	-11.5 ± 0.3
	iii	372.9 ± 0.3	378.9 ± 0.4	376.9 ± 0.6	-18.1 ± 0.7
	iv	408.2 ± 5.8	484.0 ± 2.2	439.3 ± 1.6	-52.3 ± 9.0
CuZn20-D-POSS80	*i*	233.7 ± 1.2	258.5 ± 1.0	—	—
	ii	347.4 ± 0.4	353.7 ± 0.2	351.2 ± 0.2	-14.9 ± 5.5
	iii	373.6 ± 0.4	381.9 ± 0.2	378.6 ± 0.1	-89.3 ± 8.7
	iv	439.4 ± 0.1	488.9 ± 0.1	459.6 ± 0.4	-42.7 ± 0.8
CuZn30-D-POSS70	*i*	228.3 ± 0.4	244.59 ± 0.2	—	—
	ii	342.7 ± 5.8	356.1 ± 2.9	350.8 ± 0.8	-12.5 ± 1.1
	iii	370.6 ± 6.8	386.0 ± 11.7	380.8 ± 8.7	-14.3 ± 0.4
	iv	449.5 ± 1.6	493.1 ± 0.9	467.3 ± 1.7	-57.1 ± 8.6

[a] All experiments were performed in nitrogen atmosphere with a flow rate of 50 $mLmin^{-1}$ at atmospheric pressure (~0.1 MPa).

[b] All transitions observed by DSC analysis were irreversible upon dynamic cooling.

[c] Endothermic values are negative, and exothermic values are positive

The TGA curve of D-POSS shows a stable material classified as region I up to 547 °C, where the most critical mass loss event started. The composites are also thermally stable in Region I, with a mass loss of ≤ 10%. The CuZn10-D-POSS90, CuZn20-D-POSS80, and CuZn30-D-POSS70 are sturdy materials up to 471, 460, and 454 °C, respectively. As the concentration of the CuZn increases, the endset temperature of region I moves to a lower temperature, and the average mass loss increases (Table 4-4). The calorigrams of D-POSS and the composites show a small endothermic event (*i*) around 230 °C (Fig. 4-4). For D-POSS event *i* appears as a small peak with an energy change of -0.7±0.3. For the composites, event *i* shows as a drop in energy with no defined peak. The D-POSS and its composites show two significant endothermic transitions (events ii and iii) carried forward from the support D-POSS. The TGA mass loss curves confirm that these endothermic transitions are not associated with mass loss, so it is assumed that these may be due to physical changes or molecular rearrangement in the structure. The FT IR spectra of samples show no major change in the fingerprint of the vibrational transitions of the residues of 400 °C (Fig. 4-8).

Region II in the TGA curve was carefully selected to show the most prominent weight loss event in the D-POSS and its composites. In this region, D-POSS has a mass loss of 12.7±0.0 % while CuZn10-D-POSS90, Cu20-D-POSS80, and CuZn30-D-POSS70 have a steady mass loss of 33.0 ± 1.1, 33.8 ± 1.4, and 22.4 ± 6.4%, respectively. The onset and endpoint temperature in this region for D-POSS and the composites shifted to lower temperatures as the CuZn concentration increased. The calorigram of the samples showed the event *iv* above 400 °C. In D-POSS, this event appeared as a negative slope. In contrast, this event in the composites appeared as a broad endothermic peak associated with the sample's mass loss, which started around the same temperature in both analyses. The FT-IR spectra show a loss of the typical fingerprint of the materials above 500 °C. The Si-O-Si vibration at 1099 cm^{-1} gets broader and smaller (Fig. 4-8).

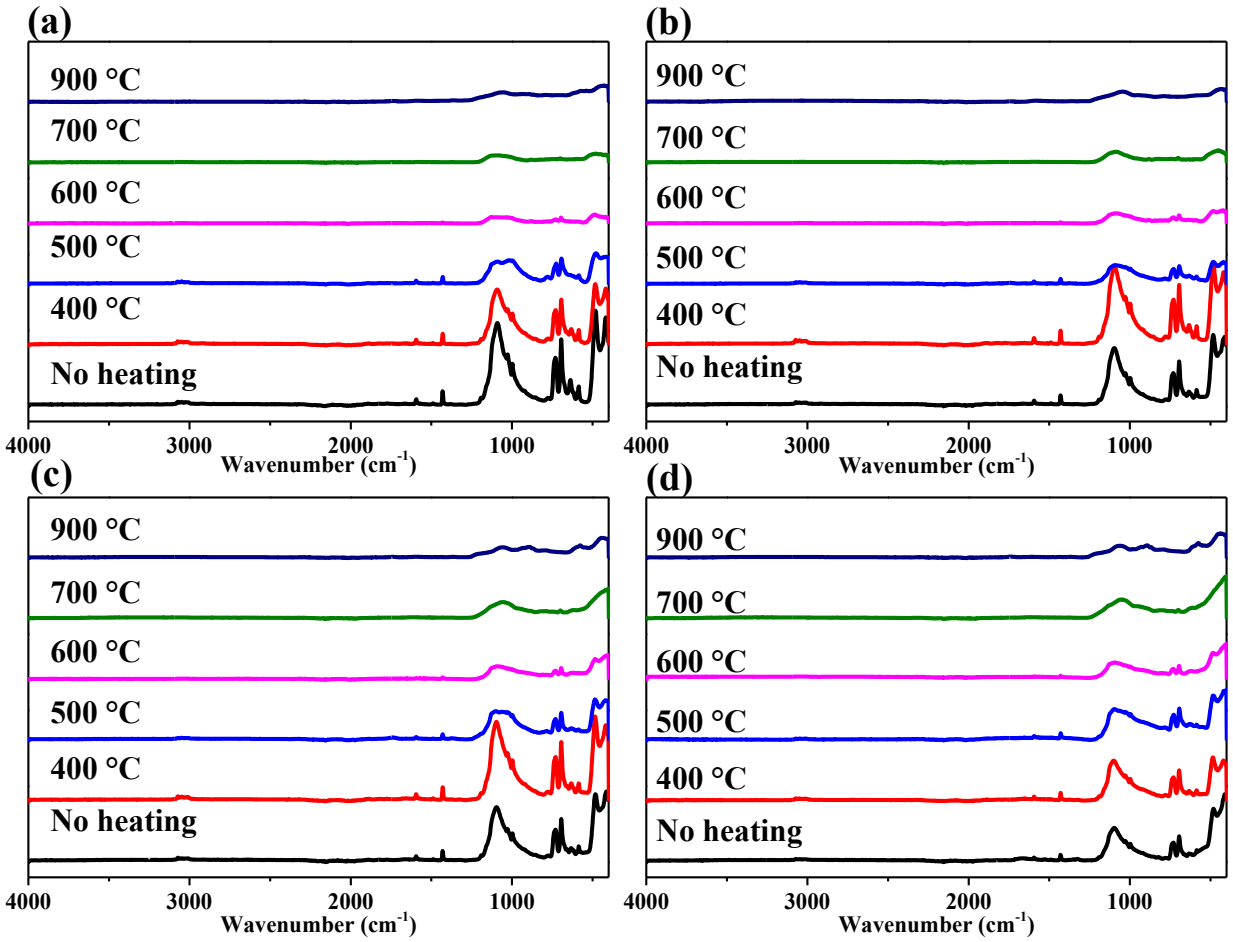

Figure 4-8 ATR FTIR of the residues of (**a**) D-POSS, (**b**) CuZn10-D-POSS90, (**c**) CuZn20-D-POSS80, and (**d**) CuZn30-D-POSS70 in nitrogen flow of 50 $mLmin^{-1}$.

Region III is the last mass loss event of D-POSS, this region has a 7.1±0.0 % mass loss and is considered as the formation of ceramic [8]. For the composites, region III has another step of mass loss identified as the second peak of the DTG curve. For CuZn10-D-POSS90 the mas loss looks like a small and sharp peak with 9.3±0.3 mass loss, while for CuZn20-D-POSS80 and CuZn30-D-POSS70 is a broad event with 7.2 ±2.1 and 12.9 ±3.2 % mass loss, respectively.

Region IV of the composites resembles region III of D-POSS with constable mass loss to yield the final residue of the samples. The FT IR of the residues at 900 °C shows the destruction of the D-POSS. The most characteristic peak is shown at 1050 cm^{-1} as a broad signal.

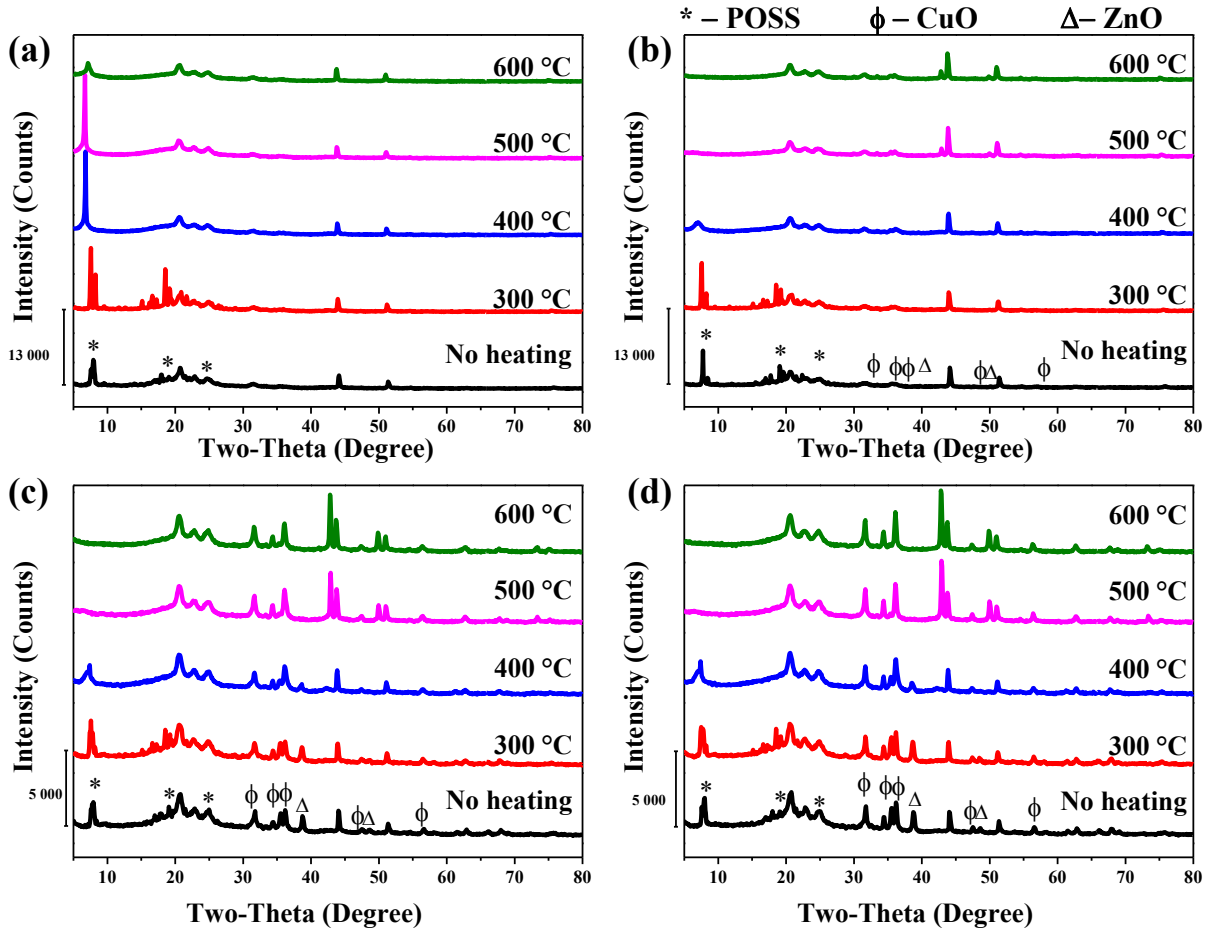

Figure 4-9 Heating profile of XRD of (**a**) D-POSS, (**b**) CuZn10-D-POSS90, (**c**) CuZn20-D-POSS80, and (**d**) CuZn30-D-POSS70 in nitrogen flow of 50 $mLmin^{-1}$.

Fig. 4-9 shows the XRD diffraction of the D-POSS and its composites. D-POSS has three characteristic peaks at 8.0° (d=1.1 nm), 17.9° (d=0.49 nm), and 24.7° (d=0.36 nm) at room temperature representing the overall dimension of POSS molecules, body diagonal of the POSS cage, and the distance between opposite Si_4O_4 faces of the silsesquioxane cube plane, respectively. When D-POSS is heated up to 300 °C, these peaks increase the intensity and look well-defined and sharp. As the temperature continues to 400 °C, the sample appears to change from a crystalline form to an amorphous state. The peak at 7.9°associated with the overall dimension of POSS shifts to lower 2θ (6.7°), and the crystal lattice distance (d) increases to 1.3 nm as an indication of either one or both the expansion and deformation in the shape of the core of silicon cage.

XRD diffractograms of the metal oxide composites (Fig. 4-9) at room temperature and 300 °C shows the crystalline phases of D-POSS, CuO, and ZnO. At 400 °C, the shape of the peak 7.9° gets broader, and the intensity is reduced. At 500 °C, this peak completely disappears from the composites. This indicates that the silicon cage has lost its crystallinity and is probably opened. The FT IR spectra at 500 °C still show the peak 1099 cm^{-1} associated with the Si-O-Si, even though it is broader, deformed, and less intense.

4.3.4 Thermal Degradation of Dodecaphenyl POSS and Their Composites in an Oxidative Atmosphere

The thermal degradation of D-POSS and their composites were evaluated using TGA, FTIR, and XRD for the residues at 900 °C. Fig. 4-10 shows the TGA and DTG of D-POSS and their composites. TGA mass loss curves of D-POSS and its composites were divided into four regions I, II, III, and IV. Temperature onset, endpoint, weight loss, and residues are listed in Table 4-6. The first region corresponded to the thermally stable area up to the temperature onset of region II. Similar to O-POSS, the thermal stability of D-POSS is affected by the presence of CuO/ZnO. As Table 4-6 shows, the temperature onset of the composites shifted to lower temperatures, and the mass loss increased around ten times at a similar temperature range of D-POSS (around 550 °C). A thermal examination of CuO/ZnO shows no degradation of the sample up to 900 °C in air.

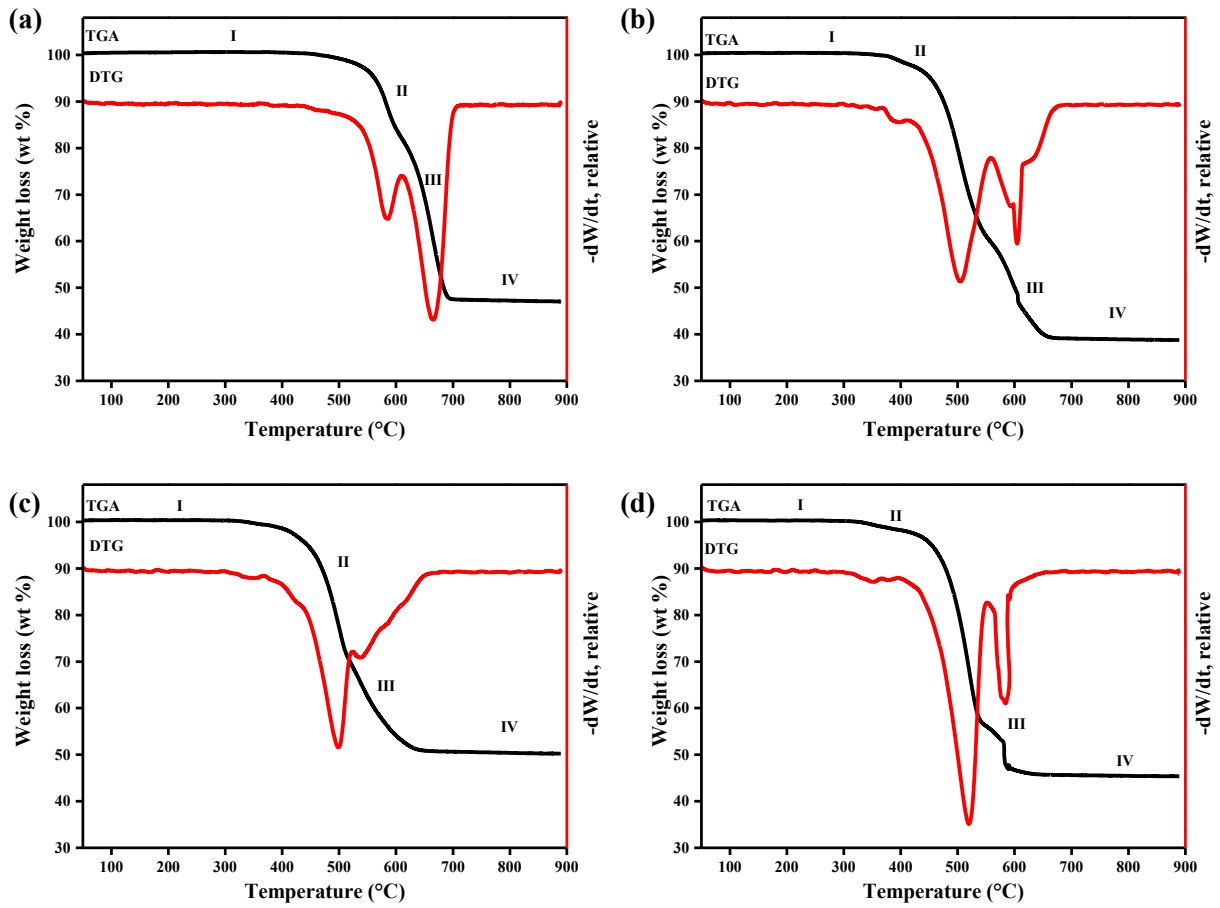

Figure 4-10 TGA and DTG of (**a**) D-POSS, (**b**) CuZn10-D-POSS90, (**c**) CuZn20-D-POSS80, and (**d**) CuZn30-D-POSS70 air flow of 50 $mLmin^{-1}$.

Table 4-6 Thermal decomposition and weight loss profile of D-POSS and their composites studied by TGA in airflow of 50 $mLmin^{-1}$.

Composite	Region[a]	Temperature		Weight loss	Δwt/ΔT	Residue
		T_{onset} (°C)	T_{endset} (°C)	(wt%)[b]	(Δ(wt.%)C^{-1})	(wt%)[c]
D-POSS	I	31.2 ± 0.0	550.0 ± 0.1	3.3 ± 0.0	0.0	47.0 ± 0.0
	II	550.0 ± 0.1	593.1 ± 0.1	14.0 ± 0.0	0.3	
	III	639.3 ± 1.0	683.5 ± 0.2	24.2 ± 0.3	0.5	
	IV	683.5 ± 0.2	889.4 ± 0.1	3.1 ± 0.1	0.0	
CuZn10-D-POSS90	I	31.3 ± 0.0	379.4 ± 0.6	0.3 ± 0.0	0.0	38.8 ± 0.0
	II	379.4 ± 0.6	410.4 ± 0.5	1.5 ± 0.0	0.0	
	III	477.1 ± 0.5	540.2 ± 0.4	26.4 ± 0.1	0.4	
	IV	573.1 ± 0.3	643.4 ± 0.7	16.5 ± 0.0	0.2	
	V	643.4 ± 0.7	889.3 ± 0.1	2.0 ± 0.1	0.0	
CuZn20-D-POSS80	I	31.3 ± 0.0	461.1 ± 0.4	7.8 ± 0.1	0.0	50.2 ± 0.0
	II	461.1 ± 0.4	513.7 ± 0.5	20.9± 0.2	0.4	
	III	520.0 ± 0.2	598.1 ± 0.2	15.4 ± 0.1	0.2	
	IV	598.1 ± 0.2	889.4 ± 0.1	4.1 ± 0.7	0.0	
CuZn30-D-POSS70	I	31.1 ± 0.0	315.2 ± 0.1	0.0 ± 0.0	0.0	45.4 ± 0.0
	II	315.2 ± 0.1	424.2 ± 0.3	2.5 ± 0.0	0.0	
	III	489.9 ± 0.2	542.0 ± 0.4	29.1 ± 0.2	0.6	
	IV	577.4 ± 0.9	596.2 ± 0.1	6.2 ± 0.1	0.3	
	V	596.2 ± 0.1	889.2 ± 0.1	1.5 ± 0.0	0.0	

[a] All experiments were performed in air atmosphere with a flow rate of 50 $mLmin^{-1}$ at atmospheric pressure (~0.1 MPa).

[b] Weight loss profile of POSS and their composites were defined considering the temperature regions containing the main thermal events.

[c] Residue represents the weight % of the mass after the heating cycle.

The FTIR of the residues of D-POSS and the composites at 400, 500, 600, 700, and 900 °C are shown in Fig. 4-11. Interesting to note that when the metals are not present in the sample, at 400 °C the peak at 1099 cm^{-1} associated with the silicon framework (Si-O) gets broadened and deformed while the composites preserve the shape and intensity of the same peak when the metal oxides are present in the samples. In our previous work on CuZn/POSS, we proposed the metal oxides were either inside the silicon cage or protecting the cage, this may support that theory.

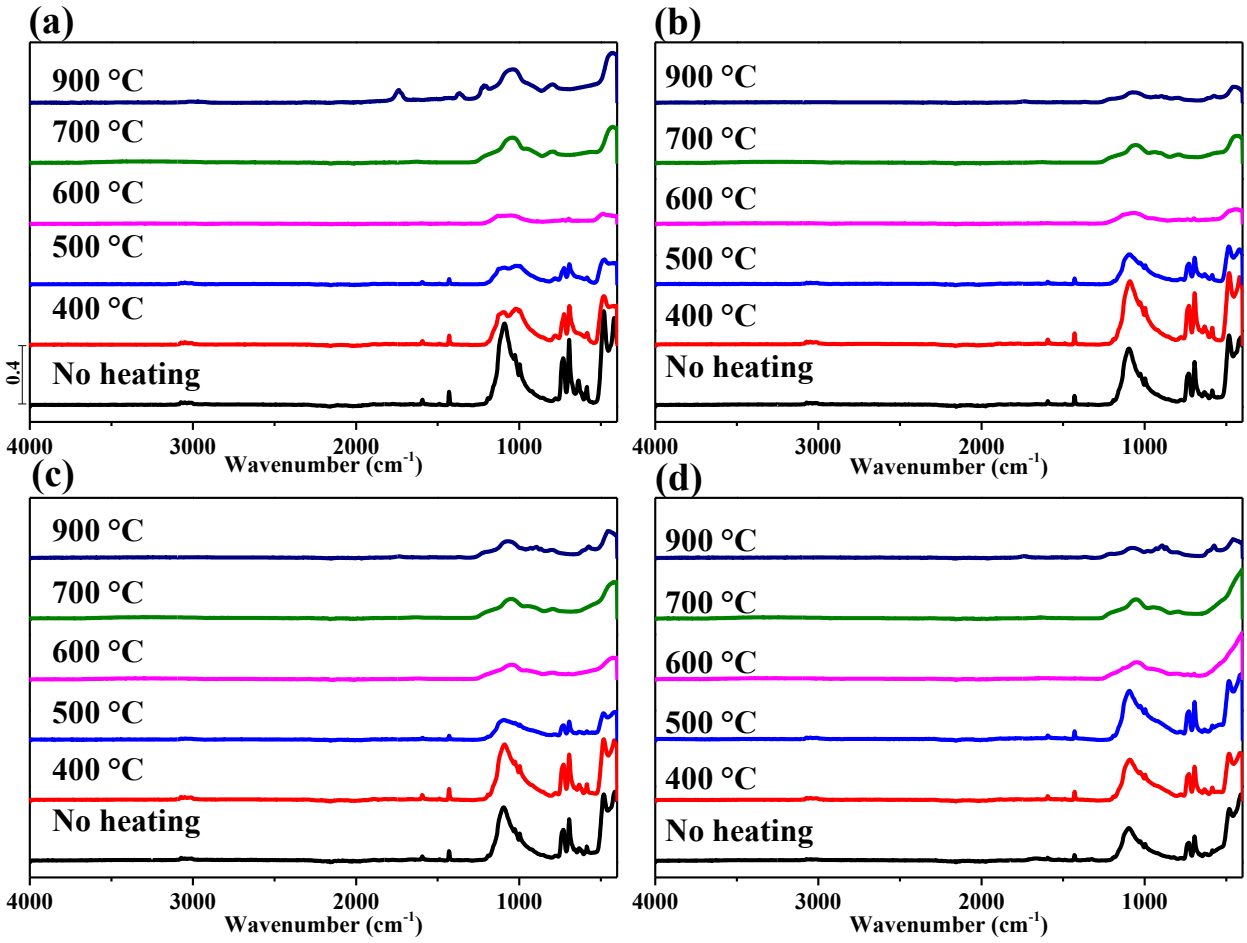

Figure 4-11 ATR FTIR of the residues of (**a**) D-POSS, (**b**) CuZn10-D-POSS90, (**c**) CuZn20-D-POSS80, and (**d**) CuZn30-D-POSS70 air flow 50 $mLmin^{-1}$.

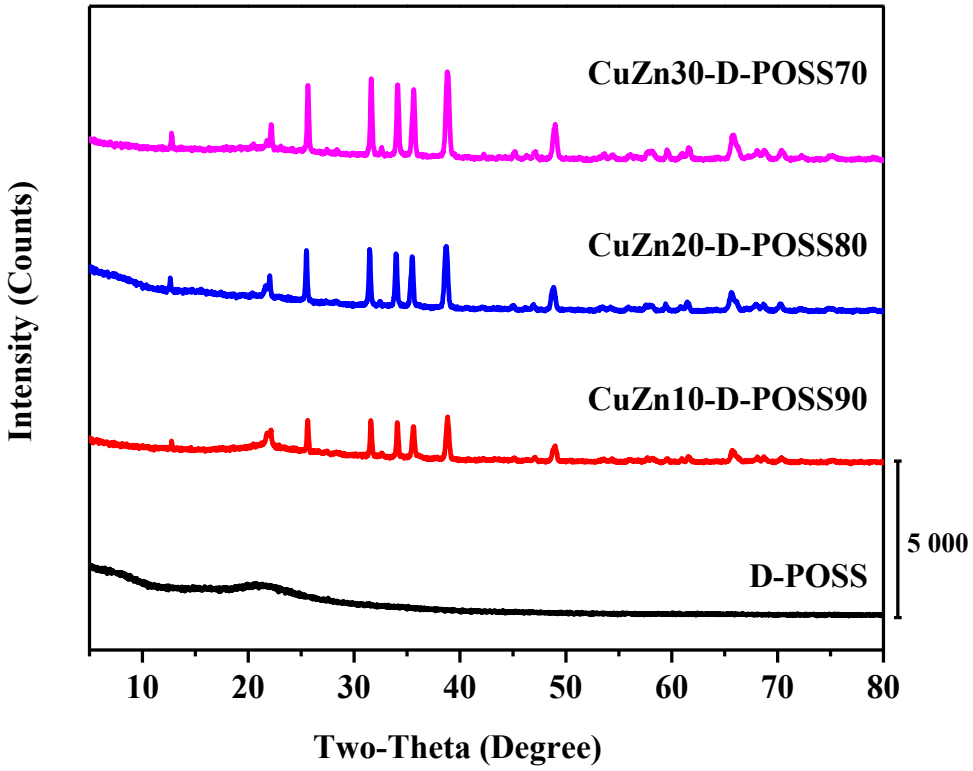

Figure 4-12 XRD of the residues of D-POSS and the composites of TGA at 900 °C in air flow at 50 $mLmin^{-1}$.

At 600 °C, 700 °C, and 900 °C, the vibrational spectra of the D-POSS and the composites are entirely different from the initial samples. In addition, the phenyl group out-of-plane (697, 746 cm^{-1}) peak disappeared in all composites. As previously reported, the phenyl were decomposed in carbon dioxide (CO_2) and cyclobutadiene [11]. The diffraction patterns of the char at 900 °C show destruction of the crystal structure of D-POSS (Fig. 4-12). Similar to the O-POSS composites, the D-POSS composites preserved the crystal properties of CuO/ZnO even at high temperature (900 °C).

4.3.5 Generalization of O-POSS and D-POSS as Thermal Stable Supports

The search for thermally stable supports for catalytic systems has been the subject of considerable research [17,18]. The use of mesoporous materials [19], cellulose nanocrystal/graphene hybrids [20], graphene [21], carbon nanotubes [22], and Al_2O_3 [23] are some of the supports employed to improve the thermal stability of active phases in catalytic reactions. However, hydrophobic supports that are thermally stable are rare to find [24]. POSS materials are easy to synthesize, and the structure could be tailored according to the application, but its use as thermally stable support in catalytic applications is still premature.

O-POSS and D-POSS have the same elements and follow similar degradation patterns; the main difference is the size of their cages and the number of pendant phenyl groups. After this study, we could say both materials are thermally stable and follow similar thermal behaviour. In both cases, the presence of metal oxides, CuO/ZnO, doesn't affect the vibrational fingerprint and the thermal stability of the silsesquioxane until about 450 °C. After this temperature, the oxides accelerate the degradation of the supports. In the case of O-POSS, the presence of the metal oxide preserve part of the siloxane cage even at 600 °C. On the other hand, both supports have a series of low-energy irreversible thermal transitions associated with molecular relaxation and crystal rearrangement up to 400 °C that are not involved with mass loss.

The findings of this work partially match previous reports on the thermal behaviour of oligomeric silsesquioxane. Herein, we look at how the presence of active sides like metal oxides could also contribute to the stability or early degradation of the support. Furthermore, the use of different atmospheres, such as inert or oxidative, are factors to consider when a system is selected for a specific reaction.

4.4 Conclusions and Future Perspectives

The thermochemistry of CuO/ZnO supported on octaphenyl silsesquioxane (O-POSS) and dodecaphenyl silsesquioxane (D-POSS) was investigated to evaluate the suitability of these materials as potential supports for metal oxides in catalytic reactions. Both materials are thermally stable to about 450 °C. Furthermore, the CuO/ZnO/POSS composites of these silsesquioxanes are also thermally stable to almost the same temperature, but the presence of the metal oxides

accelerates the degradation of the supports and increases the mass loss compared with the support. The crystal structures of both POSS molecules are thermally stable to about 500 °C, above this temperature, the siloxane cage is destroyed. The composites of O-POSS, with a ratio of 20 % and above, protect the crystalline features of the cage. Finally, as the composites have high thermal stability in an inert and oxidative atmosphere to around 450 °C, these supports could be extended to other catalytic systems that require hydrophobic and thermally stable supports.

4.5 References

[1] Argyle MD, Bartholomew CH. Heterogeneous catalyst deactivation and regeneration: a review. Catalysts 2015;5:145–269.

[2] Trimm DL. Thermal stability of catalyst supports. Stud. Surf. Sci. Catal., Elsevier; 1991, p. 29–51.

[3] Dalai AK, Davis BH. Fischer–Tropsch synthesis: A review of water effects on the performances of unsupported and supported Co catalysts. Appl Catal A Gen 2008;348:1–15.

[4] Zhang X, Zhang G, Liu W, Yuan F, Wang J, Zhu J, et al. Reaction-driven surface reconstruction of ZnAl2O4 boosts the methanol selectivity in CO2 catalytic hydrogenation. Appl Catal B Environ 2021;284:119700.

[5] Kurtz M, Strunk J, Hinrichsen O, Muhler M, Fink K, Meyer B, et al. Active sites on oxide surfaces: ZnO-catalyzed synthesis of methanol from CO and H2. Angew Chemie Int Ed 2005;44:2790–4.

[6] Laine RM, Roll MF. Polyhedral phenylsilsesquioxanes. Macromolecules 2011;44:1073–109.

[7] Zhang W, Camino G, Yang R. Polymer/polyhedral oligomeric silsesquioxane (POSS) nanocomposites: An overview of fire retardance. Prog Polym Sci 2017;67:77–125.

[8] Fina A, Tabuani D, Carniato F, Frache A, Boccaleri E, Camino G. Polyhedral oligomeric

silsesquioxanes (POSS) thermal degradation. Thermochim Acta 2006;440:36–42.

[9] Blanco I, Abate L, Bottino FA, Bottino P, Chiacchio MA. Thermal degradation of differently substituted Cyclopentyl Polyhedral Oligomeric Silsesquioxane (CP-POSS) nanoparticles. J Therm Anal Calorim 2012;107:1083–91.

[10] Mantz RA, Jones PF, Chaffee KP, Lichtenhan JD, Gilman JW, Ismail IMK, et al. Thermolysis of polyhedral oligomeric silsesquioxane (POSS) macromers and POSS−siloxane copolymers. Chem Mater 1996;8:1250–9.

[11] Fan H, Yang R. Thermal decomposition of polyhedral oligomeric octaphenyl, octa(nitrophenyl), and octa(aminophenyl) silsesquioxanes. J Therm Anal Calorim 2014;116:349–57.

[12] Bohmer N, Roussiere T, Kuba M, A Schunk S. Valorisation of glycerol as renewable feedstock: comparison of the exploration of chemical transformation methods aided by high hroughput Experimentation. Comb Chem High Throughput Screen 2012;15:123–35.

[13] Montoya Sánchez N, de Klerk A. Oxidative ring-opening of aromatics: Thermochemistry of sodium, potassium and magnesium biphenyl carboxylates. Thermochim Acta 2016;645:31–42.

[14] Höhne GWH, Hemminger WF, Flammersheim H-J. Theoretical fundamentals of differential scanning calorimeters. Differ. Scanning Calorim., Berlin, Heidelberg: Springer Berlin Heidelberg; 2003, p. 31–63.

[15] Siew YK, Sarkar G, Hu X, Hui J, See A, Chua CT. Thermal curing of hydrogen silsesquioxane. J Electrochem Soc 2000;147:335.

[16] Toivola Y, Thurn J, Cook RF. Structural, electrical, and mechanical properties development during curing of low-k hydrogen silsesquioxane films. J Electrochem Soc 2002;149:F9.

[17] Fu N, Liang X, Li Z, Li Y. Single-atom site catalysts based on high specific surface area supports. Phys Chem Chem Phys 2022;24:17417–38.

[18] Takashima H, Karches M, Kanno Y. Catalytic decomposition of trichloroethylene over Pt-

/Ni-catalyst under microwave heating. Appl Surf Sci 2008;254:2023–30.

[19] Sun J, Bao X. Textural manipulation of mesoporous materials for hosting of metallic nanocatalysts. Chem - A Eur J 2008;14:7478–88.

[20] Trache D, Thakur VK, Boukherroub R. Cellulose nanocrystals/graphene hybrids—A promising new class of materials for advanced applications. Nanomaterials 2020;10:1523.

[21] Li M, Wang Y, Gao H, Wang J, Sun B. Thermally stable microstructure and mechanical properties of graphene reinforced aluminum matrix composites at elevated temperature. J Mater Res Technol 2020;9:13230–8.

[22] Sun Z, Zhang H, Zhao Y, Huang C, Tao R, Liu Z, et al. Thermal-stable carbon nanotube-supported metal nanocatalysts by mesoporous silica coating. Langmuir 2011;27:6244–51.

[23] Fu W, Li Z, Xu W, Wang Y, Sun Y, Dai Y. Exceptionally thermal-stable Al2O3/TiO2 nanofibers by depressing surface-initiated grain growth as new supports for anti-sintering Pt nanoparticles. Mater Today Nano 2020;11:100088.

[24] Vidal K, Gómez E, Goitandia AM, Angulo-Ibáñez A, Aranzabe E. The synthesis of a superhydrophobic and thermal stable silica coating via sol-gel process. Coatings 2019;9:627.

Chapter 5. Rapid, Metal-Free, Catalytic Conversion of Glycerol to Allyl Monomers and Polymers

Abstract[7]

With expanding biodiesel and oleochemical industries, glycerol is produced as main co/byproduct. The expansion of glycerol applications is of foremost importance especially selective conversion methods using low energy consumption, shorter times, and high yield are of great interest. Here, we report the rapid and selective conversion of glycerol to allyl alcohol in a single step using microwave (MW) irradiation through a formic acid-mediated metal-free deoxydehydration reaction. First, a three-factor Box−Behnken response surface design was used to assess the influence of three independent variables including time, temperature, and molar ratio of formic acid/glycerol on the allyl alcohol yield. Then, under optimized conditions, about 84% glycerol conversion to allyl alcohol (~56%) was achieved in 10 min at 260 °C using a glycerol to formic acid ratio of 1:1.57. Furthermore, the allyl alcohol was converted to allyl formate, allyl phthalate, and their correspondent polymers. The synthesized monomers and polymers were characterized by proton nuclear magnetic resonance spectroscopy (^{1}H NMR), attenuated total reflectance-Fourier transform infrared spectroscopy (ATR-FTIR). The polymers were further characterized by differential scanning calorimetry (DSC), thermal gravimetric analysis (TGA), and size exclusion chromatography (SEC).

Keywords: alcohols, alkenes, allyl alcohol, formic acid, glycerol, microwave, polymers

[7] This work was published as Herrero YR, Ullah A. Rapid, metal-free, catalytic conversion of glycerol to allyl monomers and polymers. ACS Sustainable Chemistry & Engineering. 2021 Jul 2;9(28):9474-85.

5.1 Introduction

The abundance of glycerol (**1**, Scheme 5-1) is rapidly increasing due to the growing biodiesel industry, which generates this polyol as the prime byproduct (~10 wt %). Its chemical structure, rich in oxygen, makes it useful for a wide range of chemical reactions as oxidation [1–3], reduction [4,5], esterification [6], dehydration [7,8], and hydrogenolysis [9], with numerous applications in food [10], energy [11], pharmaceutical [12,13], and cosmetic [14] industries. Chemical transformation of glycerol, in general, employs solid catalysts [15] to convert glycerol into more valuable compounds such as hydrogen [16–18], dihydroxyacetone [19–21], propanediol [22,23], acrolein [24–26], glycerol carbonate [27,28], or epichlorohydrin [29,30]. However, the conversion of glycerol to allyl alcohol (**3,** Scheme 5-1) [31] has been less intensively studied despite having immense utility. Allyl alcohol (**3**) is the precursor of value-added products such as acrylic acid, allyl monomers, thermoplastic and thermosetting polymers, and the feedstock for a large variety of specialized chemicals like butanediol. **3** is also commercially used in flame-resistant materials, drying oils, and plasticizers.

The commercial production of **3** is sustained on fossil fuel derivatives through the hydrogenation of propylene-derived acrolein, propylene oxide isomerization, or the catalyzed acetoxylation of propylene over noble metal catalysts [32]. Unfortunately, these processes have many drawbacks including unsustainable processes, non-renewable raw material, and multistep synthesis. These limitations have motivated scientists to investigate novel green routes for the synthesis of allyl alcohol from the biogenerated glycerol.

According to some reports, glycerol could be converted to **3** by gas-phase transfer hydrogenation [33,34], using rhenium complex −catalyzed deoxydehydration (DODH) [35] reaction. However, these methods lead to rapid catalyst deactivation by coke deposition as a result of elevated reaction temperatures [36]. Furthermore, rhenium is one of the rarest elements on earth with continuously increasing prices. An attractive metal-free route for glycerol conversion to **3** has been reported using formic acid (**2**, Scheme 5-1) as a DODH agent. Formic acid is a green and inexpensive feedstock that can be produced from renewable sources like biomass [37] or carbon dioxide (CO_2) [38]. The formic acid-assisted DODH was first reported by Kamm and Marvel with an allyl alcohol yield of about 45−47% at 195−260 °C [39]. Later, Ellman's group improved the

method by performing the same reaction under nitrogen atmosphere and using a narrower temperature range (230−240 °C) improving the yield of alcohol up to 80% [40]. Later on, Zhang's group adopted Kam and Marvel procedure for a continuous distillation for ~2 h at 235 °C to synthesis allyl alcohol as an intermediate to produce acrylic acid [31]. The main drawback of the formic acid-assisted DODH is related to the thermal stability of the acid itself requiring large excess or multiple additions. Monbaliu's group attended the same method under continuous flow conditions to 56% yield of allyl alcohol and 6% yield of allyl formate starting from a feed solution of glycerol and formic acid (2.5 equiv) [41]. The main difficulty found was the high viscosity of the glycerol, see Table B-6 in the electronic Supporting Information (SI) for comparison of literature reported using DODH.

The use of the conventional distillation to produce **3** from glycerol (**1**) not only requires large amounts or multiple addition of acid or its salt but is also considered time consuming and therefore makes it difficult to extend the current methodologies to industrial processes. Hence, less energy intensive, highly effective, and rapid methodologies are required to utilize glycerol from the biodiesel industry to add value and enhance its sustainability.

Microwave (MW) chemistry is known for assisting ionic compounds and polar molecules by dielectric heating with short reaction time, high reaction rate, and yield. Conventional heating techniques such as hot plates and oil/sand baths take longer times to reach the desired temperature by convection, leading to a thermal gradient throughout the reaction mixture with nonuniform reactions [42], which may create undesired byproducts. Microwaves have been reported from 1.5 to 100 times more energy efficient compared to conventional technologies [43]. The microwaves are electromagnetic radiations with both electric and magnetic components. Dramatic rate accelerations using microwaves could be due to thermal effects, specific thermal microwave effects, and nonthermal microwave effects [44]. More recent investigations suggest that the dramatic rate accelerations of reactions, enhanced product selectivity, reduced energy costs of reactions, and control of materials properties are more likely due to the dielectric relaxation phenomenon [45,46]. We compared the energy consumption in a three-sequential addition of **2** to **1** using conventional heating and microwave heating. The microwave heating was >16 times more energy efficient compared to conventional heating (see Table B-1, SI).

Herein, we report formic acid-assisted DODH of glycerol under microwave heating without using any other solvent. Both reagents are polar molecules with a high dielectric constant (glycerol, ε = 42.5; formic acid, ε = 57.2) [47], which makes them suitable to be rapidly heated by the microwave (MW) electromagnetic radiation. This microwave-assisted method leads to efficient conversion with rapid production of allyl alcohol (56% yield in 10 min). We further envisioned using allyl alcohol (**3**) as an intermediate to prepare allyl formate (**4**), diallyl phthalate 1(**6**), poly(allyl alcohol) (**8**), poly(allyl formate) (**9**), and poly(diallyl phthalate) (**10**) via microwave dielectric heating (Scheme 5-1). The conversions of glycerol under solvent-free conditions and using microwave irradiation, as safer energy transfer, are efficient and sustainable in terms of energy consumption, toxicity, substrate, and solvent use.

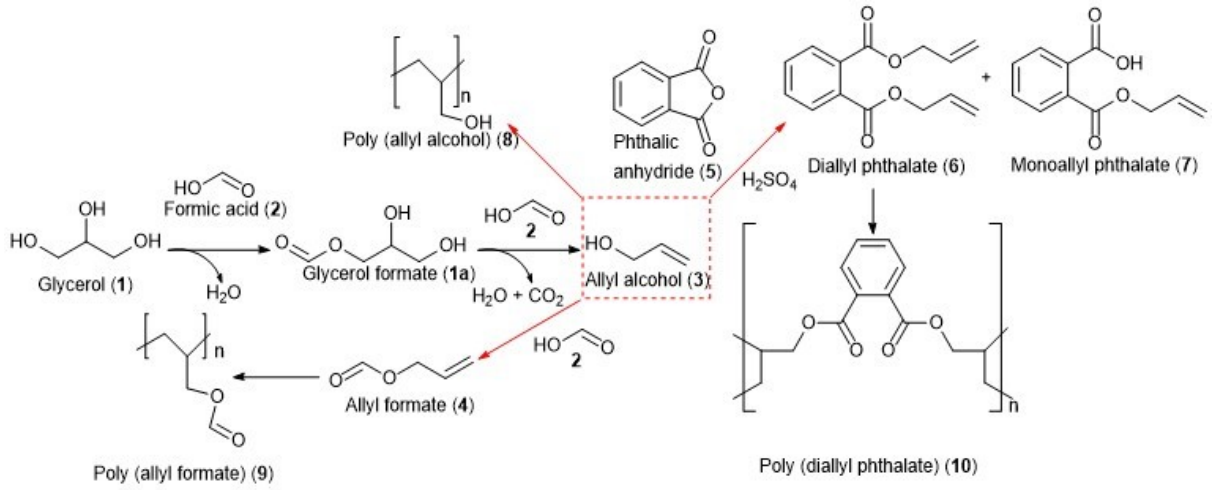

Scheme 5-1 Glycerol DODH to allyl alcohol (**3**) and further conversion to allyl monomers and polymers.

5.2 Experimental Section

5.2.1 Materials

Glycerol (**1**, Sigma-Aldrich, 99.5%), formic acid (**2**, Sigma-Aldrich, ≥98%), allyl alcohol (**3**, Sigma-Aldrich, ≥99%), 3- (trimethylsilyl)-1-propanesulfonic acid sodium salt (DSS, Sigma-Aldrich, 97%), deuterium oxide (D_2O, Sigma-Aldrich, "100%", 99.96 atom % D), dimethyl sulfoxide-d6 (DMSO-d_6, Sigma-Aldrich "100%," 99.96 atom % D), chloroform-d_3 ($CDCl_3$, Sigma-Aldrich, "100%," 99.96 atom % D), methanol-d_4 (CD_3OD, Sigma-Aldrich, "100%," 99.8

atom % D), acetone-d_6 (CD_3COCD_3, Sigma-Aldrich, "100%," 99.96 atom % D), sulfuric acid (H_2SO_4, Sigma-Aldrich, 95−98%), phthalic anhydride (**5**, Sigma-Aldrich ≥99%), ethyl acetate (anhydrous, Sigma-Aldrich, 99.8%), hexane (anhydrous, Sigma-Aldrich, ≥99%), methanol (anhydrous, Sigma-Aldrich, 99.8%), tetrahydrofuran (THF, Sigma-Aldrich 99%), tert-butyl hydroperoxide solution (TBHP, Sigma-Aldrich 70 wt % in H_2O), benzoyl peroxide (BPO, Sigma-Aldrich, ≥98%), and silica gel for chromatography (Whatman, 60 Å, Supelco, 70−230 mesh) were used as received. Optical borosilicate glasses were purchased from Fisher Scientific.

5.2.2 Microwave-Assisted Glycerol Conversion to Allyl Alcohol

Reactions were carried out in the DiscoverTM System (CEM Corporation) with a 50 mL round bottom vessel (Pyrex glass) connected to a fractional column, reflux condenser, and four collection vessels. A typical reaction consisted of 32.2 g of **1** (350 mmol, 99.5%) and 7.8, 15.6, 23.4 mL of **2** (207, 414, and 620 mmol, ≥98%), respectively. All reactions were performed at maximum stirring speed using a magnetic bar and a microwave power of 200 W. Reaction temperatures were measured by an infrared temperature sensor. Samples were collected after cooling the reaction, quenched with solvent, and stored in a freezer until nuclear magnetic resonance (NMR) analysis was carried out the same day (Fig. B-1, SI). DSS in DMSO-d_6 was used as an internal standard in NMR analysis. The yield of the allyl alcohol was calculated by the following equation

$$Yield\ \% = 100 \times \frac{\left(\frac{N_{std} \times I_{AA} \times nH_{std}}{I_{std} \times nH_{AA}}\right)}{N_{gly}} \qquad \text{Eq. 5.1}$$

where

N_{std} = moles of internal standard (DSS)
I_{AA} = proton integral area of the signal at 4.99 ppm on allyl alcohol
nH$_{std}$ = number of hydrogens associated with the standard peak
I_{std} = proton integral area of the signal at 0.00 ppm on DSS
nH$_{AA}$ = number of hydrogens associated with the allyl alcohol peak
N_{gly} = initial moles of glycerol.

5.2.3 Microwave-Assisted Glycerol Conversion to Allyl Formate

Twenty milliliters of **3** (294 mmol, ≥99%) and 11.2 mL of **2** (297 mmol, ≥98%) were placed in a 50 mL round bottom flask in the microwave reactor. The flask was connected to a reflux system. The reaction was carried out at 60 °C for 30 min using 200 W MW power. After the reaction, water was added and two layers were formed, which were separated with a separation funnel.

5.2.4 Microwave-Assisted Allyl Alcohol Conversion to Diallyl Phthalate

In a round bottom flask, 24.6 g of **5** (100 mmol, ≥99%), 15.3 mL of **3** (225 mmol, ≥99%), and 0.25 mL of 1% H_2SO_4 were added. The flask was then placed inside the microwave reactor, connected to a reflux system, and the reaction was carried out at 95 °C for 20 min using a MW power of 200 W. After the reaction, the reaction mixture turned orange, the water was then added, and two layers were separated. The organic layer containing diallyl phthalate was neutralized with $NaHCO_3$. Diallyl phthalate (**6**) was then purified by column chromatography using ethyl acetate/hexane (20:80 v/v) mixture as eluent with a progressive increase in the ethyl acetate ratio of 1 to 20 v/v %.

5.2.5 Microwave-Assisted Poly(Allyl Alcohol) Synthesis

In a 10 mL MW glass vial equipped with a magnetic stir bar, 4 mL of **3** (60 mmol, ≥99%) and 4 mmol of TBHP (0.75 mL, 70 wt % in H_2O) were added. The resulting solution was purged with nitrogen for 20 min (10 min inside the solution and 10 min in the reaction vessel's head space) and the reaction vial was then placed in the cavity of the microwave instrument, and the temperature was programmed to 130 °C for 10 min using a MW power of 200 W. After 10 min, the polymerization was quenched by ceasing microwave irradiation, removing the vial from the instrument, cooling and exposing the reaction solution to air. The polymer was then purified via vacuum distillation.

5.2.6 Microwave-Assisted Poly(Diallyl Phthalate) Synthesis

In a 10 mL microwave reaction vessel, 1 mL of **6** (4.55 mmol) and 0.04 g of BPO (0.15 mmol, ≥98%) were mixed. The vessel was sealed and purged with nitrogen for 20 min. The reaction was carried out at 100 °C for 5 min using a MW power of 200 W. A yellow polymer was obtained, which was washed with methanol and dried in an oven at 80 °C for 24 h before testing.

5.2.7 Instrumentation

5.2.7.1 Attenuated Total Reflectance-Fourier Transform Infrared Spectroscopy (ATR-FTIR)

Absorbance spectra were recorded at room temperature in the region of 400−4000 cm^{-1} at 16 scans and a resolution of 4 cm^{-1} with a Bruker α FTIR spectrophotometer (Bruker Optics, Esslingen, Germany) equipped with a single-bounce diamond ATR crystal. The samples of **3** and **4** were collected and analyzed immediately. The samples were covered with an optical borosilicate glass cover to avoid early evaporation. The reaction between **2** and **3** was followed at room temperature for 1 h at different concentrations covered with an optical borosilicate glass. Corresponding spectra of the optical borosilicate glass were measured and subtracted from the spectra of the samples. Baseline correction was applied to the subtracted spectra. In the case of the study of the **3** and **4** reactions at room temperature, a Norris Gap Derivatives method [48] was employed with segments of 3 and a gap of 2 between segments. The manipulation of the spectra was done using Nicolet Omnic software (version 8).

5.2.7.2 Differential Scanning Calorimetry (DSC)

The thermal properties of polymers were investigated by differential scanning calorimeter using a 2920 Modulated DSC, TA instrument, United States in a nitrogen environment. The calibration of the instrument was performed with indium as a standard sample. All samples were tested in a temperature range of -25 to 300 °C at a heating rate of 10 °Cmin^{-1}. The samples were analyzed in sealed aluminum pans previously weighed (5−10 mg). All of the DSC measurements were performed following the ASTM E1356-08 (2014) standard procedure.

5.2.7.3 Thermogravimetric Analysis (TGA)

The thermal stability of polymers was studied by thermogravimetric analysis TGA Q50 (TA instrument) under a nitrogen flow of 100 mL min^{-1} according to the ASTM D3850-12 (2012) standard. The temperature range was from 25 to 600 °C at a heating rate of 10 °Cmin^{-1}. The sample was weighed (10−12 mg) and loaded into an aluminum pan. The weight loss of the sample was measured as a function of temperature.

5.2.7.4 Proton Nucleic Magnetic Resonance (^{1}H NMR)

Spectra were collected using a Varian Inova spectrometer (Varian, CA) at 400 MHz and 26.9 °C. Samples were prepared by adding 50 mg of sample in 0.75 mL of D_2O, DMSO-d_6, CD_3OD, CD_3COCD_3, or $CDCl_3$-*d*. Quantitative analysis was performed with 5 mg of DSS as an internal standard in DMSO-d_6.

5.2.7.5 Gel Permeation Chromatography (GPC)

The molecular weights of allyl polymers were determined using a GPC system with Styragel HR5E GPC column (300 × 7.8 mm i.d., particle size = 5 μm, Waters Corporation). The instrument used an isocratic Agilent 1100 pump (Agilent Technologies; CA) with an evaporative light scattering detector (Alltech ELSD 2000, Mandel Scientific Company, Canada). THF was used as an eluent at a rate of 1 mLmin^{-1}, sample concentrations 0.5 mgmL^{-1}, and injection volumes were 10 μL. The Agilent Polystyrene EasiVial PS-H standard kit with known molecular weight in the range of 770−113 300 g mol−1 and the polydispersity ≤1 was used to generate the calibration curve by the Agilent GPC-Addon Rev. B. 01.01 software.

5.2.7.6 Electrospray Ionization Mass Spectrometry (ESI-MS)

The analysis of **6** and **7** was conducted on Agilent Technologies 6220 oaTOF (Santa Clara California) mass spectrometer (see Figs. B-2 and B-3, Supporting information (SI)).

5.2.8 Experimental Design for Optimization of the DODH of Glycerol Using MW

The response surface methodology (RSM) was used to optimize the conditions for the DODH of glycerol using MW irradiation. The experimental design and statistical analysis were carried out using the Design Expert software (11.1.1.0, Stat-Ease, Inc.). The experimental plan was based on the Box−Behnken Design (BBD), which has been used to achieve the maximum efficacy for an RSM involving three variables at three different levels. In the present study, the effects of the three independent variables at three levels (A, temperatures of 200, 230, 260 °C; B, molar ratio FA/Gly of 0.6, 1.2, 1.8; C, irradiation time of 10, 20, 30 min) was investigated.

The number of experiments designed was 17 with five center points to allow calculations of the response function at intermediate levels. The experimental design and results are shown in Table 5-1. The conversion of **1**, selectivity of **3** and **4**, and formic acid recovered after the reaction are recorded in Table B-2 (SI).

To study the mathematic relationship between the three independent variables and the responses, a quadratic polynomial equation was used (Eq. 5.2). A multiple regression analysis was performed to obtain the coefficients and solved the equations to predict the responses.

$$Y = \beta_0 + \beta_1 X_1 + \beta_2 X_2 + \beta_3 X_3 + \beta_{12} X_1 X_2 + \beta_{13} X_1 X_3 + \beta_{23} X_2 X_{3+} \beta_{11} X_1^2 + \beta_{22} X_2^2 + \beta_{33} X_3^2 \quad \text{Eq. 5.2}$$

where

Y predicted yield percent

β_0 constant

β_1, β_2, β_3 linear coefficients

β_{12}, β_{13}, β_{23} interaction coefficients between the three factors

β_{11}, β_{22}, β_{33} quadratic coefficients

Table 5-1 Box-Behnken design matrix for coded values and experimental and predicted values for allyl alcohol (3) and allyl formate (4).

Code	*A* *[°C]*	*B* *[FA:Gly]*	*C* *[min]*	**3** Yield Exp. [%][a]	**3** Yield Predicted [%]	**4** Yield Exp. [%][a]	**4** Yield Predicted [%]
1	260	1.8	20	48.93	49.21	2.34	2.34
2	230	1.2	20	43.39	43.29	2.01	2.00
3	200	1.2	10	33.49	33.52	2.14	2.12
4	230	1.2	20	43.34	43.29	2.01	2.00
5	230	1.8	10	47.62	47.29	2.55	2.55
6	200	1.8	20	35.20	35.49	2.67	2.69
7	260	1.2	30	39.93	39.89	1.95	1.97
8	230	0.6	30	35.59	35.92	1.24	1.24
9	230	1.2	20	43.24	43.29	2.00	2.00
10	200	0.6	20	31.75	31.47	1.18	1.19
11	200	1.2	30	42.41	42.36	2.24	2.24
12	260	1.2	10	54.52	54.57	5.47	5.04
13	230	0.6	10	35.86	36.10	1.7	2.04
14	230	1.8	30	41.87	41.63	6.77	6.43
15	230	1.2	20	43.56	43.29	3.77	4.04
16	260	0.6	20	36.62	36.32	1.86	1.95
17	230	1.2	20	42.94	43.29	3.71	4.04

[a] Determined by ^{1}H-NMR using DSS as internal standard in DMSO-d_6.

5.3 Results and Discussion

5.3.1 Ambient Temperature Interactions of Glycerol with Formic Acid and MW Conversion of Glycerol to Allyl Alcohol

The DODH of alcohols (diols and triols) can be carried out using formic acid when heated above 200 °C, and the reaction is reported to proceed via cyclic carbocation intermediate formation, (40) as illustrated in Scheme 5-2.

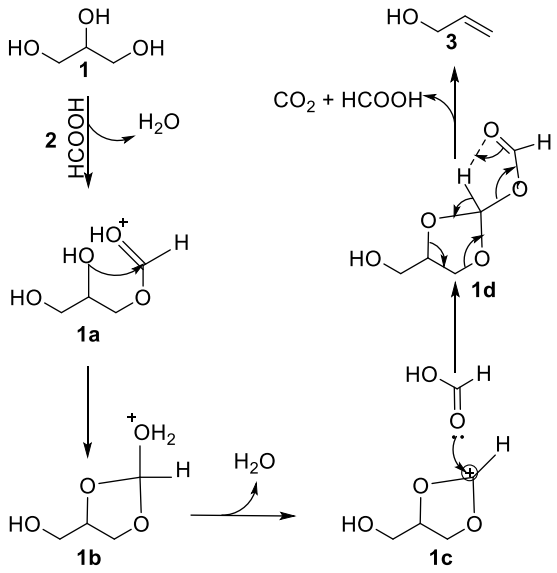

Scheme 5-2 Schematic mechanism for the assisted-formic acid (**2**) deoxydehydration of glycerol (**1**).

Initially, the mixture of **1** and **2** undergoes an equilibrium reaction with the removal of one molecule of water to produce glycerol formate (**1a**, Scheme 5-2). This mixture was studied at room temperature under nitrogen. Samples were withdrawn at 5, 10, 15, and 20 min, and ^{1}H NMR analyses were performed (Fig. 5-1a). The spectra of total correlation spectroscopy (TOCSY) (Fig. B-4, SI) and heteronuclear single-quantum coherence adiabatic (gHSQCAD) (Fig. B-5, SI) showed the presence of new peaks at 3.63, 3.95, 4.12, and 8.19 ppm as a function of time. The TOCSY spectrum demonstrated correlations between H27 with H24 up to H29 when the proton at 3.63 ppm in the crude sample was excited. TOCSY confirmed one molecule of formic acid-assisted dehydration of glycerol from a terminal hydroxyl group even before heating the sample.

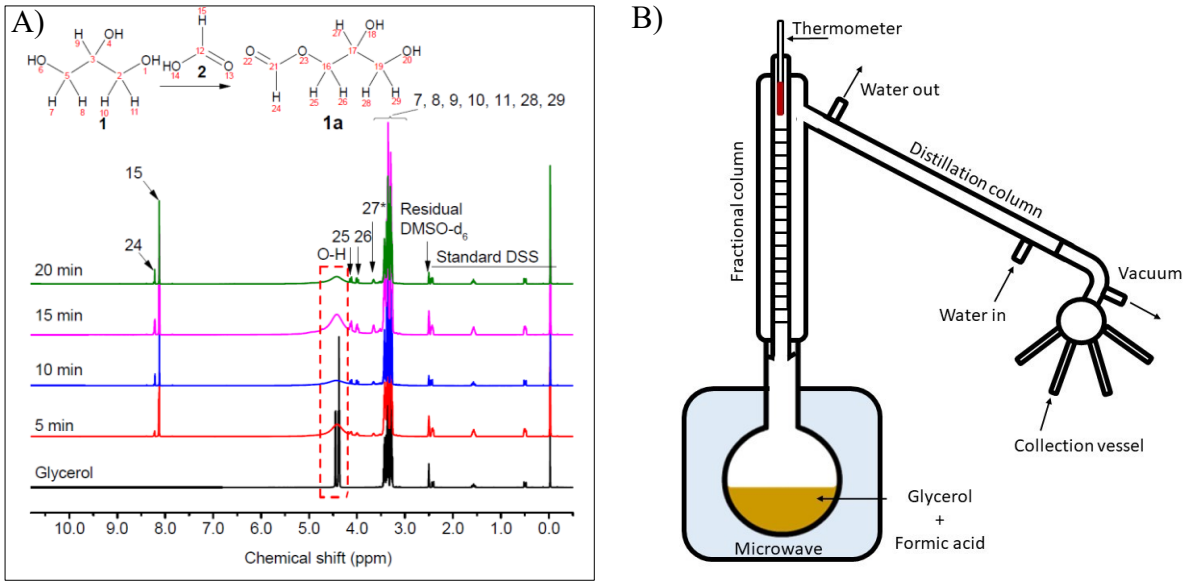

Figure 5-1 (**a**) ^{1}H-NMR of pre-mixture of FA:Gly in DMSO-d_6 under nitrogen at room temperature at different mixing times. (**b**) Microwave reactor setup.

Later, trials were performed with **1** and **2** using a distillation column attached to a reflux system using the microwave as a heating source (T = 200 °C, t = 20 min, FA/Gly = 0.6). The distillation products were a mixture of **1a** (12.1%), **3** (17.6%), and **4** (2.5%) (Fig. 5-1b) Even though **3** has the highest percentage in the mixture, the presence of **1a** in the distillation products is aligned with previous studies that require temperatures of 230–240 °C to favor the second dehydration leading to carbocation and then attacked by the carbonyl oxygen of the second formic acid molecule to provide a 2-acyloxy-1,3-dioxolane (**3d**, Scheme 5-2) which is further transformed to **3** and one molecule of **2** is regenerated.

Another set of trials was performed using a fractional column connected to the distillation system. Although the condensation of the mixture of water, **2**, and **3** affected the stability of the temperature and the microwave power during the refluxing, the % yield of components **3** and **4** increased to 31.9 and 3.2%, respectively, leaving only traces of **1a**. The cooling and condensation of the upflowing vapors in the fractional column allowed the reaction mixture to carry out the DODH of **1** with a minimal loss of reactants.

5.3.2 Optimization of Glycerol Conversion

Inspired by these results, we proceeded to optimize the DODH of **1** using the microwave-assisted fractional column. Furthermore, we studied the interaction between three independent variables, which are critical in the DODH of **1** such as temperature, FA/Gly, and time. A response surface methodology (RSM) was employed. The experimental plan was based on Box–Behnken design (BBD) which has been used to achieve the maximum efficacy for an RSM involving three variables at three different levels (*A*, temperatures of 200, 230, 260 °C; *B*, molar ratio FA/Gly of 0.6, 1.2, 1.8; and C, irradiation time of 10, 20, 30 min).

5.3.3 Model Comparison Table

The experimental data was fitted in linear, two-factor interaction, quadratic, and cubic models to evaluate the best model that led to logical and consistent results. Table 5-2 shows the comparison among the different models and their comparison between three different tests: sequential model sum of squares, lack of fit tests, and model summary statistics. Based on the results of R^2, adjusted R^2, predicted R^2, and the standard deviation, the quadratic model was the best model fitted for % yield of allyl alcohol.

The model was evaluated based on the experimental data to check if the estimated model would provide logical results.

Table 5-2 Sequential model fitting for yield percent of allyl alcohol (3).

Sequential Model Sum of Squares						
Source	Sum of Squares	DF	Mean Square	F-value	*p*-value	Remarks
Mean	28843.92	1	28843.92			
Linear	332.53	3	110.84	6.07	0.0082	
2FI	165.38	3	55.13	7.65	0.0060	
Quadratic	**71.14**	**3**	**23.71**	**188.41**	**< 0.0001**	**Suggested**
Cubic	0.6672	3	0.2224	4.16	0.1011	Aliased
Residual	0.2138	4	0.0535			
Total	29413.85	17	1730.23			
Lack of Fit Tests						
Source	Sum of Squares	DF	Mean Square	F-value	*p*-value	Remarks
Linear	237.18	9	26.35	492.95	< 0.0001	
2FI	71.81	6	11.97	223.86	< 0.0001	
Quadratic	**0.6672**	**3**	**0.2224**	**4.16**	**0.1011**	**Suggested**
Cubic	0.0000	0				Aliased
Pure Error	0.2138	4	0.0535			
Model Summary Statistics						
Source	Std. Dev.	R^2	Adjusted R^2	Predicted R^2	Press	Remarks
Linear	4.27	0.5835	0.4873	0.1658	475.44	
2FI	2.68	0.8736	0.7978	0.5075	280.68	
Quadratic	**0.35**	**0.9985**	**0.9965**	**0.9807**	**11.01**	**Suggested**
Cubic	0.23	0.9996	0.9985	–		Aliased

[a] Bold values show the higher significance.

5.3.4 Fitting of the Second-Order Polynomial Equation for Allyl Alcohol % Yield

When the response ratio is greater than 10, usually a transformation is required; in the case of **3**, the response ratio was only 1.72, where no transformation was required. After fitting the data to the quadratic model, the equation explained the relationship among independent variables and their significance in the system.

A, B, C, AB, AC, BC, A^2, B^2, C^2 as all of the *p*-value are < 0.0001, means the model is significant, as well all of the model terms.

$$Y(AA) = -154.46807 + 1.11870 * T + 8.34504 * r + 4.35326 * t + 0.123183 * T * r - 0.019593 * T * t - 0.228414 * r * t - 0.001565 * T^2 - 10.44331 * r^2 + 0.007031 * t^2 \quad \text{Eq. 5.3}$$

5.3.5 Fitting of the Second-Order Polynomial Equation For Allyl Formate % Yield

The ratio response of **4** % yield is 5.14. When the initial model is fitted without any transformation and the analysis of variances (ANOVA) is applied, the Box-Cox test suggest applying a square root with a $\lambda = 0.5$, being the final equation fitting quadratic the equation below.

$$SqrtY(AF) = +0.585221 - 0.013008 * T + 3.68161 * r + 0.027713 * t - 0.007615 * T * r - 0.000328 * T * t + 0.006876 * r * t + 0.000060 * T^2 - 0.436331 * r^2 + 0.000881 * t^2 \quad \text{Eq. 5.4}$$

5.3.6 Statistical Analysis

After the model was selected based on the fitting of the experimental data, an analysis of variances (ANOVA) was applied to evaluate the model and the significance of each model term based on the p-value. The p-values of both model equations for 5.3 and 5.4, shown in Tables B-3 and B-4 (SI), respectively, indicate that linear, quadratic, and interactive coefficients are significant terms in the models.

In the case of a 3% yield, the model *F*-value of 502.36 indicates that the model is significant. The lack of fit *F*-value of 4.16 and the correspondent p-value of 0.1011 was not significant as it was smaller than the pure error of 0.2138. The determination coefficient (R^2), adjusted determination coefficient (R_α^2), and the predicted determination coefficient (R_p^2) were also considered to evaluate the fitting of the model. As can be seen in Table 5-3, the $R^2 = 0.9985$ of the quadratic model indicates that the model has a good fit. The adjusted determination coefficient (R_α^2) and the predicted determination coefficient (R_p^2) are also in agreement; as is suggested, both should be within 0.20 of each other; otherwise, there may be a problem with either the data or the model.

In the case of the model **4**, the determination coefficient has a value of 0.9985. The difference between the adjusted and predicted determination coefficient for the allyl formate model is also <0.2, suggesting an adequate agreement between the model and the data.

Table 5-3 The determination coefficient (R^2), adjusted determination coefficient ($R\alpha^2$), and the predicted determination coefficient (Rp^2) for % yield of allyl alcohol (**3**) and allyl formate (**4**).

	R^2	Adjusted $R\alpha^2$	Predicted Rp^2	Mean ± SD	CV, %	Adequate precision
Allyl alcohol	0.9985	0.9965	0.9807	41.19	0.8613	84.8902
Allyl formate	0.9997	0.9993	0.9963	1.99	0.6195	158.1618

5.3.7 Diagnostic of Model Adequacy

The obtained model underwent further analysis to confirm its validity. The normal % probability plot of residuals, the Box-Cox, the predicted versus actual values, the residual versus predicted values, the residual versus run values, the externally studentized residual versus factor plots, and Cook's distance plots were analyzed to estimate the adequacy of the models. The normal % probability versus the studentized residual plot is linear indicating the normality of the residuals (Fig. 5-2a) for **3**. Fig. 5-2b shows a random distribution of the predicted values versus internally studentized residuals to get a satisfactory model. The Cook's distance was checked for influential values (Fig. 5-2c). There were two influential points out of the limits (runs 5 and 8) for **3**. In the case of **4**, there were no points out of the limits, but four values were close to 1, indicating the high influence of these points if they are removed from the model. The Box-Cox analysis indicates that no transformation was required for the **3** model. In the case of **4**, it indicates that the best results for normality were reached with Lambda values between 0.46 and 0.85 after power transformation with the best value of Lambda equals to 0.66.

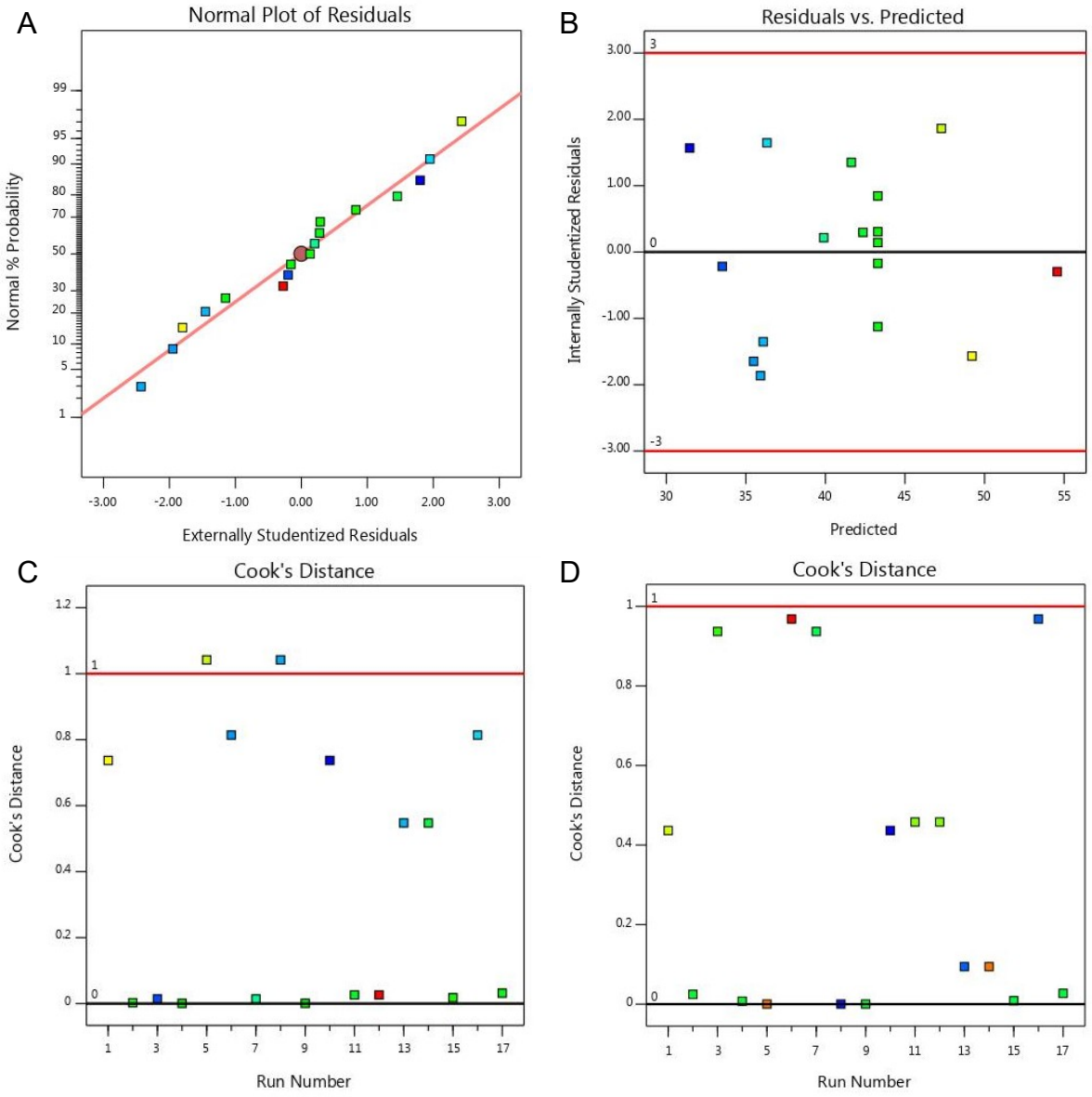

Figure 5-2 (**a**) Normal plot of residuals of allyl alcohol (**3**); (**b**) Internally studentized residuals vs run for allyl alcohol (**3**); (**c**) Cook's distance for allyl alcohol (**3**); (**d**) Cook's distance for allyl formate (**4**).

5.3.8 Effect of the model Terms on the % Yield Of Allyl Alcohol

The three-dimensional (3D) response surface plots obtained for the calculated models were used to analyze the interaction of the independent variables. These plots were drawn by keeping one variable constant and investigating the other two factors in their range. Fig. 5-3 shows that all relations among the variables are nonlinear as previously shown in Eqs 5-2 and 5-3. The surface plots demonstrate that the yield of **3** increases with the increase of temperature in the range studied. When the molar ratio increases, the yield of **3** increases too, but when the molar ratios are above the optimal level, the yield of **3** decreases. This behavior is aligned with the relationship between the molar ratio and the yield of **4**. When the concentration of **2** increases, the yield of **4** increases, reducing the yield of **3**. This suggests that a higher molar concentration of **2** in the collection vessel will displace the equilibrium to favor the formation of **4**. Interestingly, the temperature is a factor that does not affect the yield of **4**, as allyl formate is produced at room temperature in the collection vessel. On other hand, time is a factor with a low influence on the yield of **3** and **4**. This fact was observed during experiments; it was noticed that the distillation stopped at around 10 min once the temperature reached 260 °C. The use of the microwave as a heating source improves the DODH of glycerol by reducing the reaction time to 10 min compared to the previously reported reaction time of 2 h in a continuous flow or up to 6 h with multisequential additions of **2** [31].

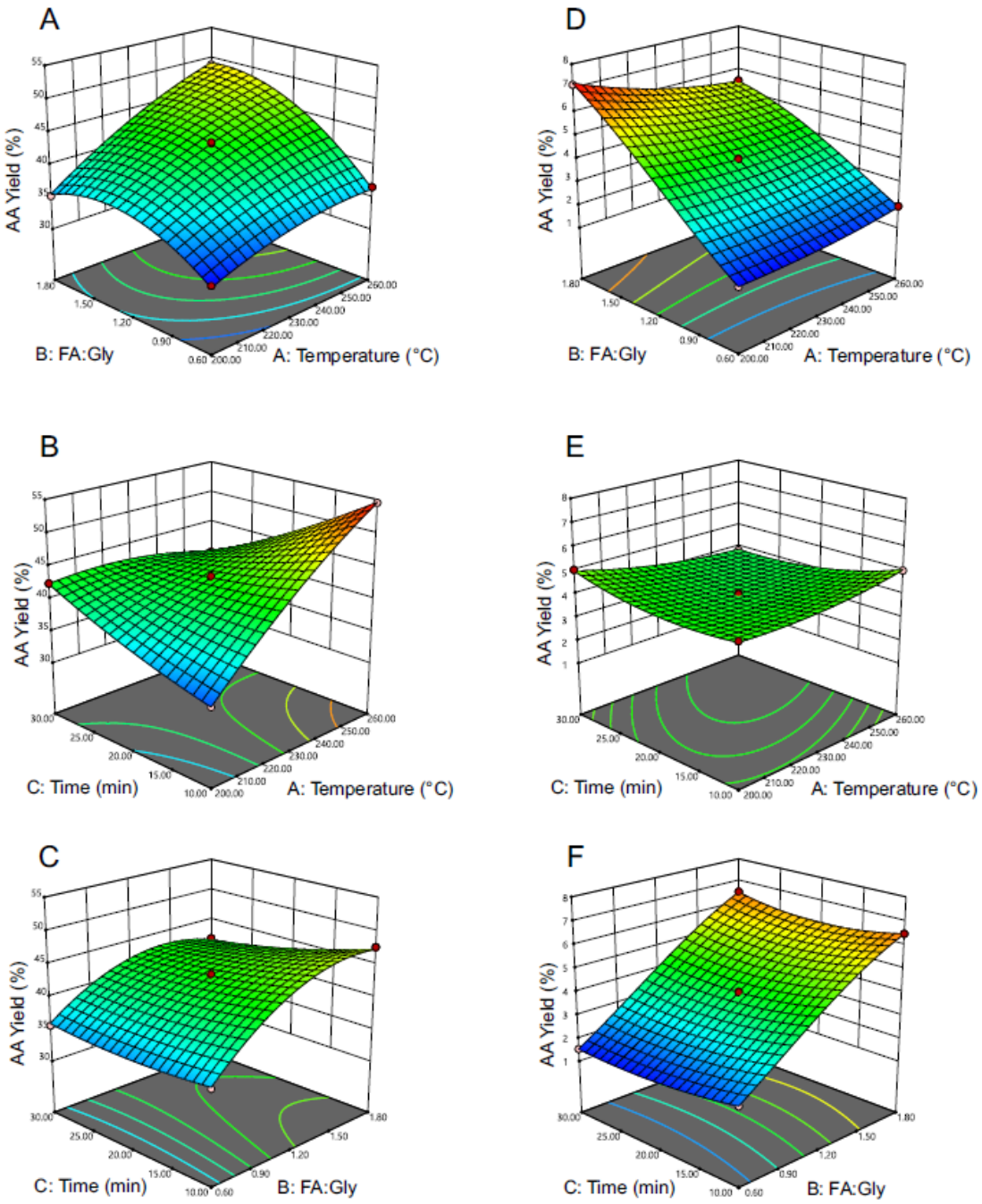

Figure 5-3 Response surface plots for two-factor interaction for % yield of allyl alcohol (**3**) (**a-c**) and allyl formate (**4**) (**d-f**) during microwave-assisted DODH of glycerol with formic acid.

5.3.9 Optimization and Verification of the Model

The regression equation was used to confirm the validity of the model and to calculate the optimum conditions to increase the yield of **3** on Design Expert software. The optimal conditions were 259.84 °C, 10.84 min, and FA/Gly = 1:1.57. The predicted value of **3** under these conditions was 57.08%. The experimental yield of **3** was 56.19 ± 0.35%, which was within the 95% confidence interval (Table 5-4). Consequently, the outcomes obtained by BBD were accurate and reliable, and had practical implementation.

Table 5-4 Confirmation of the validity of the model at three different locations in triplicate.

Temperature (°C)	FA:Gly ratio	Time (min)	Response % Yield	Predicted Mean	Std Dev	95% PI low	Experimental Data*	95% PI high
259.84	1.57	10.84	AA	57.08	0.35477	56.19	56.43	57.98
			AF	5.89	0.05998	5.74	5.75	6.04
			Total	62.84	0.37469	61.90	62.04	63.79
250.00	1.61	10.27	AA	54.71	0.35477	53.90	54.17	55.53
			AF	5.97	0.06036	5.83	5.86	6.11
			Total	60.58	0.37469	59.72	60.01	61.44
233.79	1.67	10.00	AA	49.061	0.35477	48.27	49.38	49.85
			AF Yield	6.13	0.06120	6.00	6.096	6.27
			Total	55.14	0.37469	54.30	55.47	55.97

Note: For convenience, temperatures and times were rounded off to the nearest whole number during experiments.

5.3.10 Microwave-Assisted Conversion of Allyl Alcohol to Allyl Formate

Hence, the formation of **4** from **3** and **2** was investigated in situ using ATR-FTIR at room temperature for 55 min (Fig. 5-4). The evolution of acyl vibration band of **4** (ν_{C-O-C} = 1273 cm^{-1}) verified the formation of **4** at room temperature over a period of 55 min. This fact explains the formation of allyl formate in the collection vessel at room temperature when allyl alcohol is prepared from glycerol using excess formic acid. The excess of recovered formic acid in the collection vessel reacts with the alcohol to produce the ester. This is contrary to the findings of the previous report [49], where **3** is produced from glycerol in excess of formic acid through glycerol diformate.

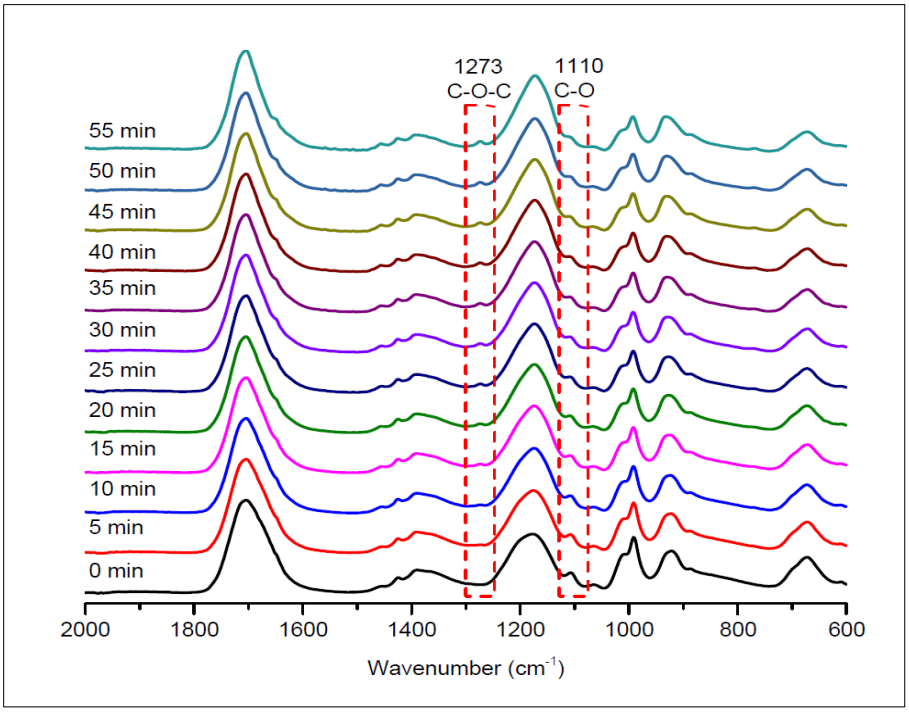

Figure 5-4 ATR FT-IR of allyl formate (**4**) from allyl alcohol (**3**) and formic acid (**2**) at room temperature.

Further, the reaction between **3** and **2** was studied under conventional heating (60 °C, 30 min). Samples were taken every 5 min and analyzed immediately. After 20 min, a higher yield of **4** and a reduction in the intensity of the characteristic band of **3** (ν_{C-O} = 1110 cm^{-1}) was observed. As the reaction evolved, the equilibrium of the reaction was constantly shifting between **4** and **3** and vice versa. This phenomenon prompted to use **3** as a precursor for the synthesis of **4**, which is used as a solvent in sprays lacquers, varnishes, and latex paints [50].

Further, we explored the esterification of **3** to **4** using the microwave-assisted open-vessel reaction under reflux (60 °C, 30 min). Water was added to the mixture after the reaction and two layers were formed. The top layer was **4** and the bottom layer contained unreacted reagents. ATR-FTIR (Fig. 5-5) analysis confirmed the formation of **4** with the peaks at 1720, 1648, and 1273 cm^{-1}. The O–H band of **3** (3307 cm^{-1}) disappeared after the two layers separation and recovery of **4**.

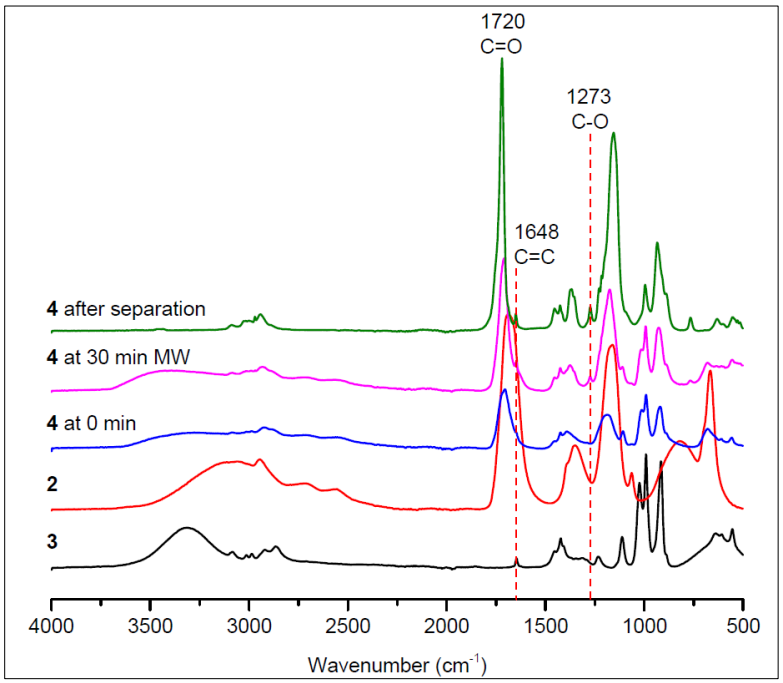

Figure 5-5 ATR FT-IR of allyl alcohol (**3**), formic acid (**2**), and allyl formate (**4**) at 0 min, 30 min after microwave treatment, and after separation. (200 W; 30 min; reflux).

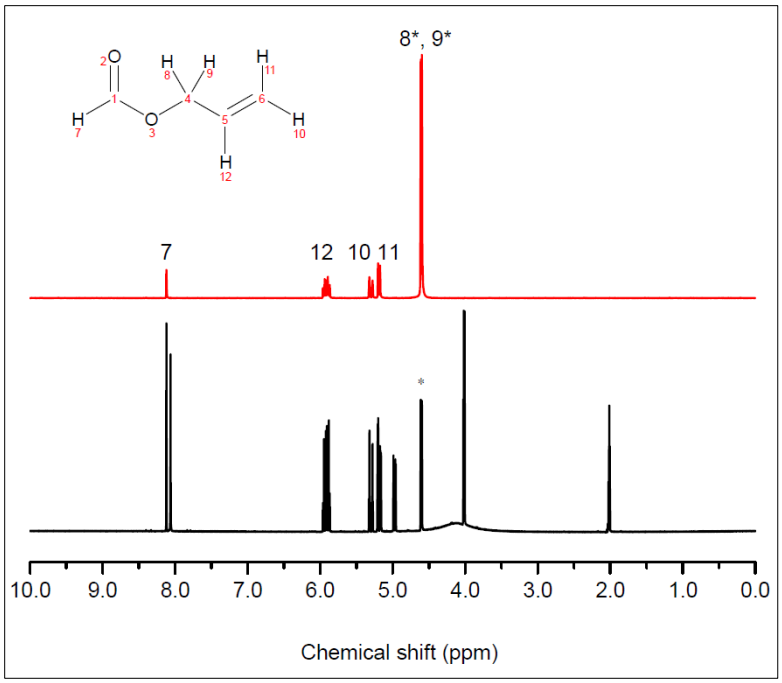

Figure 5-6 ^{1}H NMR of raw product (bottom) and TOCSY of excited proton at 4.61 corresponding to allyl formate (**4**) (top).

The ^{1}H NMR analysis was performed to characterize the final product, as shown in Fig. 5-6. As the spectra of **3** and **4** have overlapping peaks, an excitation of the proton at 4.61 was performed to identify the coupling protons corresponding to **4**.

5.3.11 Microwave-Assisted Polymerization of Allylic Monomers

The polymerization of allyl monomers is a challenging task as it has been previously reported that the chain transfer between the allyl monomer and the growing chain can terminate the growing polymer and the kinetic chain [51]. The polymerization of **3**, **4**, and **6** into poly(allyl alcohol) (**8**), poly(allyl formate) (**9**), and poly(diallyl phthalate) (**10**) were performed in a microwave reactor under solvent-free conditions using a radical initiator. Results are summarized in Table 5-5.

Table 5-5 Polymerization of allyl alcohol (**3**), allyl formate (**4**), and diallyl phthalate (**6**) initiated by tert-butyl hydroperoxide (TBHP) or benzoyl peroxide (BPO).

Entry	Monomer	Initiator	M/I	Condition	Temperature [°C]	Time [min]	M_w [g/mol]
1[a]	**3**	TBHP	100/6	N_2	130	480	941
2[b]	**3**	TBHP	100/6	N_2	130	10	2531
3[b]	**3**	TBHP	100/6	N_2	130	10	1155
4[b]	**3**	TBHP	100/6	N_2	130	20	1169
5[b]	**3**	BPO	100/4	N_2	130	20	906
6[b]	**3**	TBHP	100/6	N_2	60	30	806
					100	15	-
7[b]	**4**	TBHP	100/8	N_2	130	20	1201
8[b]	**7**	BPO	100/3	N_2	100	5	37576

[a] Oil bath

[b] Microwave, CEM DiscoverTM, 300 W maximum magnetron output power

The polymerization of allyl alcohol was carried out at 130 °C under nitrogen in a sealed tube using tert-butyl hydroperoxide or benzoyl peroxide as an initiator (Fig. B-6, SI). The characteristic band of unsaturation in the IR spectra at 1644 cm^{-1} generally disappeared but was only observed in some polymers indicating traces of monomer left in the mixture after polymerization (Fig. 5-7). A typical ^1H NMR spectrum of the synthesized polymer is presented in Fig. 5-8. The spectrum shows the peaks at 1.18, 1.51, 3.36, and 3.54 ppm for the methylene and methyl moieties of the main chain and the hydroxyl and the methylene moiety of the side chain, respectively.

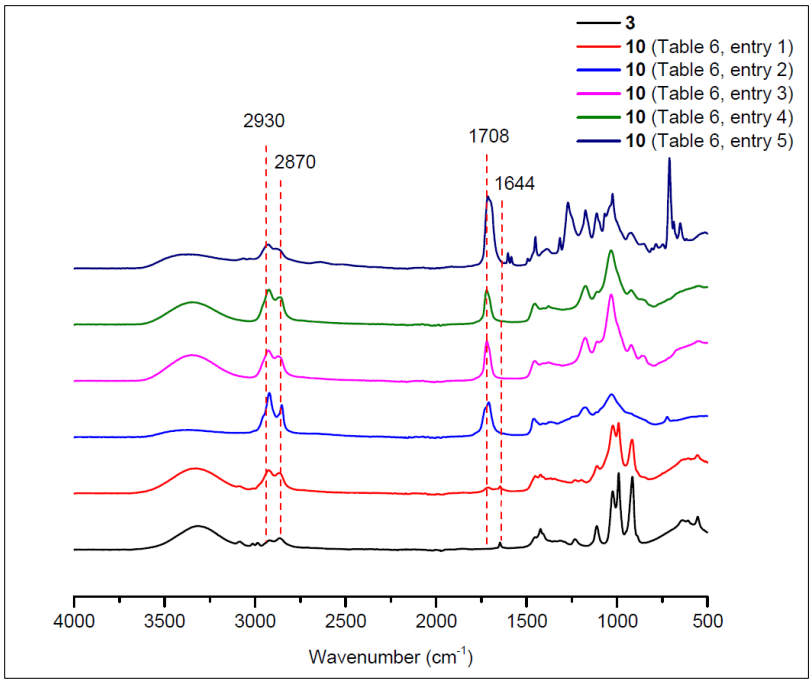

Figure 5-7 ATR FT-IR comparison of allyl alcohol (**3**) and poly (allyl alcohol) (**8**) (Table 5-5, entry 1, entry 2, entry 3, entry 4, and entry 5).

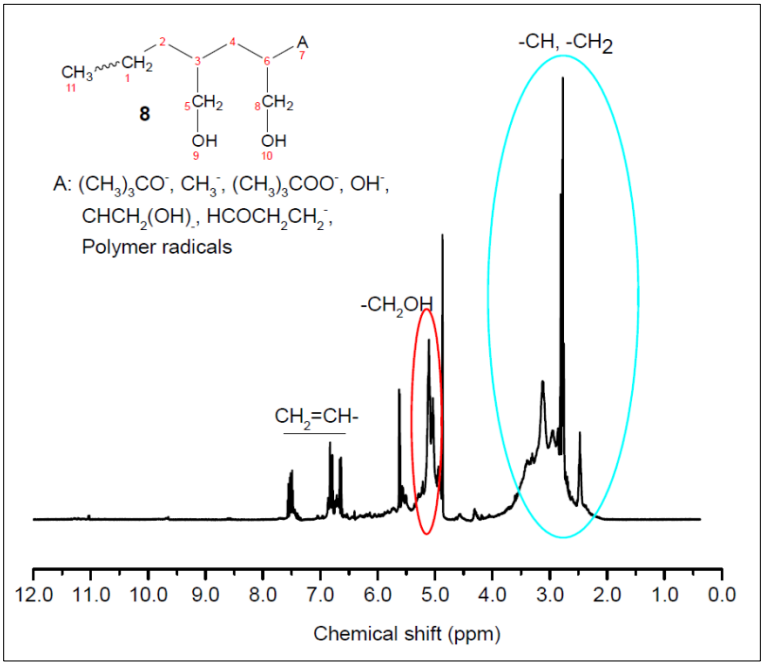

Figure 5-8 ^{1}H-NMR poly (allyl alcohol) (**8**) (Table 5-5, entry 2) in CD_3OD.

After preparing allyl alcohol polymers via microwave heating and conventional heating, it was a notable difference in the molecular weight (Table 5-5, entry 1 versus entry 2) of the polymers prepared with both methods (Fig. B-7, SI). The microwave-assisted polymer had 2.7 times higher molecular weight than the polymer prepared using an oil bath and MW polymerization took a fraction of time (ca. 48%) of the oil bath polymerization reaction.

Allyl formate (**4**) was polymerized with tert-butyl hydroperoxide (Table 5-5, entry 7). The FT-IR analysis confirmed the polymerization after the band corresponding to the alkenyl stretch at 1646 cm^{-1} disappeared in the polymer and the carbonyl stretching band at 1710 cm^{-1} increased in intensity (Fig. B-8, SI). ^{1}H NMR was performed to corroborate the polymerization of **4**. Fig. B-9 (SI) shows the disappearance of allylic hydrogen at 5.80 ppm, which agrees with ATR-FTIR data where C═C disappeared. The new peak at 4.13 ppm which is associated with the polymeric methylene group further confirmed polymerization. The molecular weight of the polymer was investigated by GPC (Fig. B-10, SI), showing the molecular weight of the **9** (M_w = 1201 g mol^{-1}) in the same order as the **3** polymers previously discussed.

The synthesis and characterization of poly(allyl phthalate) was also carried out using MW heating. The discussion and characterization are provided in the Supplementary Information (please see Figs. B-11–B-15, SI). The thermal transitions and degradation behaviors of all synthesized polymers were determined using DSC and TGA. Please see the Supplementary Information for discussion and thermograms (Figs. B-16 and B-17, SI).

5.4 Conclusions

In summary, this work presents a rapid, metal-free, microwave-assisted deoxydehydration of glycerol to allyl alcohol using single addition of formic acid as a hydrogen transfer agent without any additional solvent. The DODH reaction of glycerol was optimized using a three-factor, three-level Box–Behnken design and successfully completed within 10 min at 259 °C with an allyl alcohol yield of 56%, a substantially short time with a high yield and >16 times less energy consumption. The conversion of glycerol and yield of allyl alcohol depends on reaction conditions, such as temperature and molar ratio of formic acid to glycerol. The time of the reaction did not

play a significant role in the DODH reaction hence suggesting a more energy-efficient process for allyl alcohol production using a shorter time.

Furthermore, microwave heating was applied to accelerate the synthesis of allyl derivates like allyl formate, diallyl phthalate, and their polymerizations into corresponding polymers such as poly(allyl alcohol), poly(allyl formate), and poly(diallyl phthalate) with short reaction times (<30 min). These results prove that glycerol being inexpensive, abundantly available, and renewable represents a great opportunity for an efficient and rapid production of allyl alcohol and its derivates, which can be converted to polymers using microwaves as an alternative heating source. The rapid, sustainable, and effective conversion of glycerol to monomers and polymers may open new routes and opportunities for industrial applications of this promising biorenewable feedstock.

5.5 References

[1] Dou J, Zhang B, Liu H, Hong J, Yin S, Huang Y, et al. Carbon supported Pt9Sn1 nanoparticles as an efficient nanocatalyst for glycerol oxidation. Appl Catal B Environ 2016;180:78–85.

[2] Dodekatos G, Schünemann S, Tüysüz H. Recent advances in thermo-, photo-, and electrocatalytic glycerol oxidation. ACS Catal 2018;8:6301–33.

[3] Villa A, Dimitratos N, Chan-Thaw CE, Hammond C, Prati L, Hutchings GJ. Glycerol oxidation using gold-containing catalysts. Acc Chem Res 2015;48:1403–12.

[4] Nakagawa Y, Tamura M, Tomishige K. Perspective on catalyst development for glycerol reduction to C3 chemicals with molecular hydrogen. Res Chem Intermed 2018;44:3879–903.

[5] Sun Y-Q, Shen J-T, Yan L, Zhou J-J, Jiang L-L, Chen Y, et al. Advances in bioconversion of glycerol to 1, 3-propanediol: prospects and challenges. Process Biochem 2018;71:134–6.

[6] Cai Z-Z, Wang Y, Teng Y-L, Chong K-M, Wang J-W, Zhang J-W, et al. A two-step biodiesel production process from waste cooking oil via recycling crude glycerol esterification catalyzed by alkali catalyst. Fuel Process Technol 2015;137:186–93.

[7] Katryniok B, Paul S, Capron M, Lancelot C, Belliere-Baca V, Rey P, et al. A long-life catalyst for glycerol dehydration to acrolein. Green Chem 2010;12:1922–5.

[8] Ott L, Bicker M, Vogel H. Catalytic dehydration of glycerol in sub-and supercritical water: a new chemical process for acrolein production. Green Chem 2006;8:214–20.

[9] Balaraju M, Rekha V, Raju N, Lingaiah N. Hydrogenolysis of glycerol: comparison of continuous and batch mode reactions over Ni-ZnO catalysts. Catal Green Chem Eng 2018;1:13–26.

[10] Liu F, Chiou B-S, Avena-Bustillos RJ, Zhang Y, Li Y, McHugh TH, et al. Study of combined effects of glycerol and transglutaminase on properties of gelatin films. Food Hydrocoll 2017;65:1–9.

[11] Gupta M, Kumar N. Scope and opportunities of using glycerol as an energy source. Renew Sustain Energy Rev 2012;16:4551–6.

[12] Behr A, Eilting J, Irawadi K, Leschinski J, Lindner F. Improved utilisation of renewable resources: new important derivatives of glycerol. Green Chem 2008;10:13–30.

[13] Corma A, Iborra S, Velty A. Chemical routes for the transformation of biomass into chemicals. Chem Rev 2007;107:2411–502.

[14] Bagheri S, Julkapli NM, Yehye WA. Catalytic conversion of biodiesel derived raw glycerol to value added products. Renew Sustain Energy Rev 2015;41:113–27.

[15] Sánchez G, Dlugogorski BZ, Kennedy EM, Stockenhuber M. Zeolite-supported iron catalysts for allyl alcohol synthesis from glycerol. Appl Catal A Gen 2016;509:130–42.

[16] Adhikari S, Fernando S, Gwaltney SR, To SDF, Bricka RM, Steele PH, et al. A thermodynamic analysis of hydrogen production by steam reforming of glycerol. Int J

Hydrogen Energy 2007;32:2875–80.

[17] Lin Y-C. Catalytic valorization of glycerol to hydrogen and syngas. Int J Hydrogen Energy 2013;38:2678–700.

[18] Schwengber CA, Alves HJ, Schaffner RA, da Silva FA, Sequinel R, Bach VR, et al. Overview of glycerol reforming for hydrogen production. Renew Sustain Energy Rev 2016;58:259–66.

[19] Painter RM, Pearson DM, Waymouth RM. Selective catalytic oxidation of glycerol to dihydroxyacetone. Angew Chemie Int Ed 2010;49:9456–9.

[20] Duan X, Zhang Y, Pan M, Dong H, Chen B, Ma Y, et al. SbOx-promoted pt nanoparticles supported on CNTs as catalysts for base-free oxidation of glycerol to dihydroxyacetone. AIChE J 2018;64:3979–87.

[21] Ulgheri F, Spanu P. An efficient chemical conversion of glycerol to dihydroxyacetone. ChemistrySelect 2018;3:11569–72.

[22] Wang Y, Zhou J, Guo X. Catalytic hydrogenolysis of glycerol to propanediols: a review. RSC Adv 2015;5:74611–28.

[23] García-Fernández S, Gandarias I, Requies J, Soulimani F, Arias PL, Weckhuysen BM. The role of tungsten oxide in the selective hydrogenolysis of glycerol to 1, 3-propanediol over Pt/WOx/Al2O3. Appl Catal B Environ 2017;204:260–72.

[24] Estevez R, Lopez-Pedrajas S, Blanco-Bonilla F, Luna D, Bautista FM. Production of acrolein from glycerol in liquid phase on heterogeneous catalysts. Chem Eng J 2015;282:179–86.

[25] Feng X, Yao Y, Su Q, Zhao L, Jiang W, Ji W, et al. Vanadium pyrophosphate oxides: the role of preparation chemistry in determining renewable acrolein production from glycerol dehydration. Appl Catal B Environ 2015;164:31–9.

[26] Beerthuis R, Huang L, Shiju NR, Rothenberg G, Shen W, Xu H. Facile synthesis of a novel

hierarchical ZSM-5 zeolite: a stable acid catalyst for dehydrating glycerol to acrolein. ChemCatChem 2018;10:211–21.

[27] Teng WK, Ngoh GC, Yusoff R, Aroua MK. Microwave-assisted transesterification of industrial grade crude glycerol for the production of glycerol carbonate. Chem Eng J 2016;284:469–77.

[28] Li H, Jiao X, Li L, Zhao N, Xiao F, Wei W, et al. Synthesis of glycerol carbonate by direct carbonylation of glycerol with CO 2 over solid catalysts derived from Zn/Al/La and Zn/Al/La/M (M= Li, Mg and Zr) hydrotalcites. Catal Sci Technol 2015;5:989–1005.

[29] Lari GM, Pastore G, Mondelli C, Pérez-Ramírez J. Towards sustainable manufacture of epichlorohydrin from glycerol using hydrotalcite-derived basic oxides. Green Chem 2018;20:148–59.

[30] Almena A, Martín M. Technoeconomic analysis of the production of epichlorohydrin from glycerol. Ind Eng Chem Res 2015;55:3226–38.

[31] Li X, Zhang Y. Highly efficient process for the conversion of glycerol to acrylic acid via gas phase catalytic oxidation of an allyl alcohol intermediate. ACS Catal 2016;1:143–50.

[32] Speight JG. Chemical process and design handbook. McGraw-Hill Education; 2002.

[33] Lan H, Yao Q, Zhou Y, Zhang B, Jiang Y. Direct conversion of gas-glycerol to Allyl alcohol over V, Ti or Nb modified MoFe/KIT-6 oxide catalysts. Mol Catal 2020;498:111279.

[34] Kostyniuk A, Bajec D, Djinović P, Likozar B. Allyl alcohol production by gas phase conversion reactions of glycerol over bifunctional hierarchical zeolite-supported bi-and tri-metallic catalysts. Chem Eng J 2020;397:125430.

[35] Tshibalonza NN, Monbaliu J-CM. The deoxydehydration (DODH) reaction: a versatile technology for accessing olefins from bio-based polyols. Green Chem 2020;22:4801–48.

[36] Wu ST, She QM, Tesser R, Serio M Di, Zhou CH. Catalytic glycerol dehydration-oxidation to acrylic acid. Catal Rev 2020;62:481–523.

[37] Zunita M, Wahyuningrum D, Bundjali B, Wenten IG, Boopathy R. The performance of 1, 3-dipropyl-2-(2-propoxyphenyl)-4, 5-diphenylimidazolium iodide based ionic liquid for biomass conversion into levulinic acid and formic acid. Bioresour Technol 2020;315:123864.

[38] Chen X, Liu Y, Wu J. Sustainable production of formic acid from biomass and carbon dioxide. Mol Catal 2020;483:110716.

[39] Kamm O, Marvel CS. Synthesis of allyl alcohol. Org Synth 1921;1:15–7.

[40] Arceo E, Marsden P, Bergman RG, Ellman JA. An efficient didehydroxylation method for the biomass-derived polyols glycerol and erythritol. Mechanistic studies of a formic acid-mediated deoxygenation. Chem Commun 2009:3357–9.

[41] Tshibalonza NN, Monbaliu J-CM. Revisiting the deoxydehydration of glycerol towards allyl alcohol under continuous-flow conditions. Green Chem 2017;19:3006–13.

[42] Kappe CO. Controlled microwave heating in modern organic synthesis. Angew Chemie Int Ed 2004;43:6250–84.

[43] Hoogenboom R, Wilms TFA, Erdmenger T, Schubert US. Microwave-assisted chemistry: a closer look at heating efficiency. Aust J Chem 2009;62:236–43.

[44] Priecel P, Lopez-Sanchez JA. Advantages and limitations of microwave reactors: from chemical synthesis to the catalytic valorization of biobased chemicals. ACS Sustain Chem Eng 2019;7:3–21.

[45] Ullah A, Arshad M. Remarkably efficient microwave-assisted cross-metathesis of lipids under solvent-free conditions. ChemSusChem 2017;10:2167–74.

[46] Dudley GB, Richert R, Stiegman AE. On the existence of and mechanism for microwave-specific reaction rate enhancement. Chem Sci 2015;6:2144–52.

[47] Ullah A, Herrero YR. Methods for converting glycerol to allyl compounds. CANADA Patent US 10,633,316 B22020, 2020.

[48] Hopkins DW. What is a Norris derivative? NIR News 2001;12:3–5.

[49] Kim DS, Lee WJ, Myungjin K, Choe Y, Nam H. Method for preparing allyl alcohol. US Patent US9,120,718B12015, 2015.

[50] Sawant SP, Parihar HS, Mehendale HM. Allyl alcohol. In: Wexler P, editor. Encycl. Toxicol. 3er ed., Oxford: Elsevier; 2014, p. 146–8.

[51] Shigetomi Y, Kojima T, Ono N. Allylic polymers. I. Copolymerization of allyl esters with vinyl acetate. J Polym Sci Part A Polym Chem 1990;28:3317–25.

Chapter 6. Conclusions and Future Directions

6.1 General Conclusions

Given the heavy dependence on fossil fuels and their depleting outlook, together with the contribution of CO_2 to the atmosphere, new sources of energy, feedstock, and fuels are required. Biomass is one of the most promising substitutes as it is readily available, renewable, and an organic carbon source to produce fuels and chemicals. Even though this sustainable feedstock accounts for 9.4% of the global energy supply [1], industry and academia are researching to adapt current technologies and develop new approaches for efficient biomass valorization.

This research investigated two methods for utilizing renewable feedstocks, carbon dioxide and glycerol, produced as byproducts of established processes. The thesis developed one chapter as a literature review and three data chapters. Below, we highlight our work's key observations and findings of scientific value.

The literature review, divided into two sessions, exposed the opportunities and challenges of the target materials. The research on CO_2 revealed that the gap in the research field and the industry reducing CO_2 to methanol lies in the lack of an active, selective, and stable catalytic system [2]. For instance, the water produced as a byproduct in the hydrogenation process caused catalyst deactivation and shortened the active sites' life [3,4]. On the other hand, new methods are required to convert the abundant glycerol to valuable chemicals, as current technologies are becoming obsolete and expensive to process the crude product [5].

In Chapter Three, a hydrophobic catalytic system was developed to improve CO_2 hydrogenation to methanol. The structural results unveiled that CuO/ZnO behaves as an electron donor in the presence of POSS, whereas we could not confirm whether the metal oxides were endohedral or exohedral even though computational studies reported exohedral complexes as more stable [6]. The comparison between a hydrophilic material with a high surface area (reduced graphene oxide) and a hydrophobic material with a low surface area (POSS) confirmed that the hydrophobic character of the support plays a decisive role in driving this reaction to completion. The phenyl ligands attached to the siloxane cages are responsible for repelling the water formed as a byproduct. Thus, the metal oxides supported on D-POSS with twelve phenyls resulted in a

higher hydrophobic character, CO_2 conversion, and methanol yield than the silsesquioxane with eight phenyl ligands.

Typically, heterogeneous catalysts towards CO_2 hydrogenation to methanol are evaluated in continuous flow reactors over a wide range of temperature, time, and pressure for rapid route to scale-up, convenient products evaluation, and safer reactions involving gas evolution. Nevertheless, the initial capital cost of continuous flow reactors is one of the main drawbacks on this field. Through our catalytic evaluation in Chapter Three, we demonstrated the use of batch reactor are a useful alternative for a quick catalyst screening. As in the continuous flow reactors, in batch reactor mass transfer should be avoided, reaction conditions should be replicated and monitored to guaranteed reliable results.

In order to understand how the presence of metal oxides affected the stability of the hydrophobic supports oligomeric silsesquioxanes, Chapter Four investigated the thermal degradation of the new catalytic systems. In summary, the impregnation of the metal oxides CuO/ZnO does not affect the crystal structure or the vibrational fingerprint of the supports up to 450 °C. However, the degradation rate is accelerated after this temperature, as showed TGA results. The contrasting results between TGA (inert atmosphere) and FTIR/XRD for the thermostability evaluation between O-POSS and D-POSS after metal impregnations, suggest metal oxides had different interaction with the supports. While the metal oxides accelerate the degradation of both POSS, the cage of O-POSS is not completely loss after 500 °C. One hypothesis is the metal oxide are exohedral linked to the O-POSS while on D-POSS, metal oxides are inside the cages resulting in cage deformation. On both supports, metal oxides could be decorating de phenyl groups favoring the formation of an intercage network.

In the third study (Chapter 5), glycerol was used as a feedstock to synthesize allyl monomers and polymers. The use of a metal-free, microwave-assisted method was explored. This work confirmed that microwaves could effectively accelerate reactions with polar compounds and be more energy efficient than conventional heating methods. Using ^1H NMR confirmed that the glycerol converts to allyl alcohol through a deoxydehydration with allyl formate as the main byproduct. We demonstrated the formation of glycerol formate as an initial intermediate at room temperature, so reaching temperatures between 230-240 °C is required for higher allyl alcohol yield. Furthermore, the optimization of the method proved that temperature and reagents ratio influenced the reaction, whereas the reaction time effect was null. We proved with a simple

esterification procedure the formation of two layers to separate allyl alcohol and allyl formate. The synthesis of microwave-assisted soluble allyl polymers was performed in a short time. The novelty of these approaches resulted in a patent to be used at an industrial scale.

In conclusion, this work established that waste products are suitable for synthesizing fine chemicals and fuels. The conversion of CO_2 to methanol provides an opportunity to use a readily available feedstock as long as the catalytic system is selective, active, and stable. Using phenyl oligomeric silsesquioxanes as hydrophobic supports for Cu/ZnO provides a unique and promising opportunity, not only for the hydrogenation of CO_2 to methanol but for other industrial processes where water hinders the catalytic properties of the system. The environmentally friendly conversion of glycerol to allyl monomers and polymers provides a rapid and green approach to the synthesis of value-added chemicals.

6.2 Recommended Work

6.2.1 Future Work on CO_2 Conversion to Methanol

(a) Results from the CO_2 hydrogenation to methanol highlighted that the reactions did not get even close to reaching the equilibrium of reaction, so the use of a different type of reactor, e.g., packed-bed reactor, to investigate the effect of water vapor as co-feed on the catalytic system is suggested.

(b) The use of a flow reactor system will also help investigate the recyclability of the heterogenous catalysis and the conversion data and product selectivity.

(c) The design of the catalysts in this study was limited to equimolar amounts of Cu:Zn. The variation of the ratio of both metals supported on the oligomeric silsesquioxanes will give more insights into the reaction mechanism.

(d) Various mechanisms have been proposed for Cu/ZnO with different supports, but the synergistic effect between these two species is being mentioned as responsible for methanol selectivity. It is still unknown whether the metals are inside or outside the cage. This gap in our fundamental understanding between the metal oxide and support interaction remains and presents an opportunity for future fundamental study.

(e) The metal oxide—support interaction accelerates the weight loss of the supports, an in-situ evaluation with FTIR and Mass Spectroscopy of the new volatize products will bring light to the mechanist question of the thermal stability change in the vibrational and crystalline change on the POSS pattern.

(f) Using POSS as hydrophobic supports with other metals such as Fe, Co, and Ni will offer new opportunities to other industrial reactions hinder by water. These studies with in-situ spectroscopy such as XAS, XANES, XPS will open a new area of research and expand the applications of these novel materials in the catalytic field.

(g) Computational studies are required to support experimental results on nanoparticles Metal/POSS formations, as well as the tendency for quickly aggregation of the support, support degradation mechanism, and water/metal oxide/support interactions.

(f) Comparing different nanocomposites synthesis strategies such as incipient wetness impregnation, co-precipitation, grafting, drop casting, vapor chemical deposition will develop a better sense of to tune particle size, dispersion, surface area, catalytic efficiency, and selectivity.

(h) Exploring other type of hydrophobic POSS molecules and combine them with synthesis methods to increase hydrophobicity and surface area at the same time will be the great interest towards methanol synthesis from CO_2 hydrogenation and any other type of synthesis reaction affected by water and thermal deactivation.

6.2.2 Future Work on Glycerol Conversion

(a) Testing of the glycerol conversion method studied in this work using an industrial feed material is recommended. Nevertheless, this research should be carefully approached. Glycerol feed from the industry is contaminated with soap, catalyst, and sodium hydroxide. In addition, industrial feeds add new complexities that may cause problems to the microwave operation, which are not necessarily related to the actual glycerol conversion. For instance, the presence of a spent catalyst in the feed may change the reaction mechanism. As a result, the yield and selectivity of allyl alcohol will be negatively affected.

(b) Typically, the synthesis of allyl polymers yields low molecular weight, hence we recommend the preparation of co-polymers using allyl alcohol and allyl formate as precursors to improve solubility to challenging materials.

6.3 Presentations

A list of the publications and presentations in conferences related to the work developed in the current research project is presented in the following:

- 6th International Conference and Postgraduate Colloquium for Environmental Research 2022. University of Nottingham. Oral Presentation: "Polyhedral oligomeric silsesquioxane as hydrophobic support for heterogeneous catalysis: CO_2 hydrogenation to methanol" (June 2022, Malaysia)
- ALES Graduate Research Symposium. University of Alberta. Oral Presentation: "POSS as hydrophobic support for heterogeneous catalysis for carbon dioxide hydrogenation" (March 2019, Canada)
- Faculty of Engineering Graduate Research Symposium |University of Alberta Poster Presentation: "Hydrogenation of carbon dioxide to methanol assisted by Cu/Zn catalyst prepared under microwave irradiation" (July 2018, Canada)
- SPARK 2017 Conference. SHAW Conference Center, Alberta. Poster Presentation: "Microwave-assisted rapid conversion of glycerol to monomers" (November 2017, Canada)
- 5th World Bioenergy Congress and Expo. Hotel Melia America Conference Center. Poster Presentation: "Microwave-assisted deoxydehydration of glycerol to allyl alcohol" (June 2017, Spain)
- ALES Graduate Research Symposium. University of Alberta. Poster Presentation: "Glycerol conversion to acrylic acid assisted by microwave heating" (March 2017, Canada)

6.4 Publications

A list of the publications related to the work developed in the current research project is presented in the following:

- Rodriguez Herrero, Yanet*, and Aman Ullah. "Rapid, metal-free, catalytic conversion of glycerol to allyl monomers and polymers." ACS Sustainable Chemistry & Engineering 9.28 (2021): 9474-9485.
- Rodriguez Herrero, Yanet*, and Aman Ullah. "Metal oxide powder technologies in catalysis." Metal Oxide Powder Technologies. Elsevier, 2020. 279-297
- Ullah, Aman, and Rodriguez Herrero, Yanet*(2018) Methods for Converting Glycerol to Allyl Compounds. USP Patent Appl. (62691308) CAD Patent Appl. (2017059/CA)
- Rodriguez Herrero, Yanet* and Ullah, Aman (2017) Microwave-assisted deoxydehydration of glycerol to allyl alcohol. J Fundam Renewable Energy Appl. (Volume 7, Issue 4, page 80)

6.5 References

[1] Key World Energy Statistics 2021. https://www.iea.org/reports/key-world-energy-statistics-2021 (accessed October 14, 2022).

[2] Liang B, Ma J, Su X, Yang C, Duan H, Zhou H, et al. Investigation on deactivation of Cu/ZnO/Al2O3 catalyst for CO2 hydrogenation to methanol. Ind Eng Chem Res 2019;58:9030–7.

[3] Fichtl MB, Schlereth D, Jacobsen N, Kasatkin I, Schumann J, Behrens M, et al. Kinetics of deactivation on Cu/ZnO/Al2O3 methanol synthesis catalysts. Appl Catal A Gen 2015;502:262–70.

[4] Li C, Yuan X, Fujimoto K. Development of highly stable catalyst for methanol synthesis from carbon dioxide. Appl Catal A Gen 2014;469:306–11.

[5] Al-Mashhadani HAM, Capareda SC, Lacey RE, Fernando SD. Catalytic valorization of

glycerol for producing biodiesel-compatible biofuel blends. Biofuels 2017:1–15.

[6] Hossain D, Pittman CU, Hagelberg F, Saebo S. Endohedral and exohedral complexes of T8-polyhedral oligomeric silsesquioxane (POSS) with transition metal atoms and ions. J Phys Chem C 2008;112:16070–7.

References

About Renewable Energy. n.d. https://www.nrcan.gc.ca/our-natural-resources/energy-sources-distribution/renewable-energy/about-renewable-energy/7295.

Abreu AP, Morais RC, Teixeira JA, Nunes J. A comparison between microalgal autotrophic growth and metabolite accumulation with heterotrophic, mixotrophic and photoheterotrophic cultivation modes. Renew Sustain Energy Rev 2022;159:112247.

Acik M, Mattevi C, Gong C, Lee G, Cho K, Chhowalla M, et al. The role of intercalated water in multilayered graphene oxide. ACS Nano 2010;4:5861–8.

Adhikari S, Fernando S, Gwaltney SR, To SDF, Bricka RM, Steele PH, et al. A thermodynamic analysis of hydrogen production by steam reforming of glycerol. Int J Hydrogen Energy 2007;32:2875–80.

Agrafiotis C, von Storch H, Roeb M, Sattler C. Hydrogen production by solar thermal methane reforming. Transit. to Renew. Energy Syst., Weinheim, Germany: Wiley-VCH Verlag GmbH & Co. KGaA; 2013, p. 451–82.

Aiba S. Growth kinetics of photosynthetic microorganisms. Microb. React., Berlin, Heidelberg: Springer Berlin Heidelberg; 1982, p. 85–156.

Al-Gaashani R, Radiman S, Daud AR, Tabet N, Al-Douri Y. XPS and optical studies of different morphologies of ZnO nanostructures prepared by microwave methods. Ceram Int 2013;39:2283–92.

Al-Mashhadani HAM, Capareda SC, Lacey RE, Fernando SD. Catalytic valorization of glycerol for producing biodiesel-compatible biofuel blends. Biofuels 2017:1–15.

Alam SN, Sharma N, Kumar L. Synthesis of Graphene Oxide (GO) by Modified Hummers Method and Its Thermal Reduction to Obtain Reduced Graphene Oxide (rGO)*. Graphene 2017;06:1–18.

Almena A, Martín M. Technoeconomic analysis of the production of epichlorohydrin from glycerol. Ind Eng Chem Res 2015;55:3226–38.

Amouroux J, Siffert P. Carbon dioxide: a raw material and a future chemical fuel for a sustainable energy industry. IOP Conf. Ser. Mater. Sci. Eng., vol. 19, 2011, p. 012001.

Anitha M, Kamarudin SK, Kofli NT. The potential of glycerol as a value-added commodity. Chem Eng J 2016;295:119–30.

Arceo E, Marsden P, Bergman RG, Ellman JA. An efficient didehydroxylation method for the biomass-derived polyols glycerol and erythritol. Mechanistic studies of a formic acid-mediated deoxygenation. Chem Commun 2009:3357–9.

Archer D, Eby M, Brovkin V, Ridgwell A, Cao L, Mikolajewicz U, et al. Atmospheric lifetime of fossil fuel carbon dioxide. Annu Rev Earth Planet Sci 2009;37:117–34.

Arena F, Barbera K, Italiano G, Bonura G, Spadaro L, Frusteri F. Synthesis, characterization and activity pattern of Cu–ZnO/ZrO2 catalysts in the hydrogenation of carbon dioxide to methanol. J Catal 2007;249:185–94.

Aresta M, Dibenedetto A, Angelini A. The changing paradigm in CO2 utilization. J CO2 Util 2013;3:65–73.

Argyle MD, Bartholomew CH. Heterogeneous catalyst deactivation and regeneration: a review. Catalysts 2015;5:145–269.

Arneth A, Sitch S, Pongratz J, Stocker BD, Ciais P, Poulter B, et al. Historical carbon dioxide emissions caused by land-use changes are possibly larger than assumed. Nat Geosci 2017;10:79–84.

von der Assen N, Müller LJ, Steingrube A, Voll P, Bardow A. Selecting CO2 sources for CO2 utilization by environmental-Merit-Order curves. Environ Sci Technol 2016;50:1093–101.

El Aziz Y, Taylor PG, Bassindale AR, Coles SJ, Pitak MB. Synthesis and Structures of Novel Molecular Ionic Compounds Based on Encapsulation of Anions and Cations. Organometallics 2016;35:4004–13.

Bagheri S, Julkapli NM, Yehye WA. Catalytic conversion of biodiesel derived raw glycerol to value added products. Renew Sustain Energy Rev 2015;41:113–27.

Bailera M, Lisbona P, Romeo LM, Espatolero S. Power to gas projects review: lab, pilot and demo plants for storing renewable energy and CO2. Renew Sustain Energy Rev 2017;69:292–312.

Bains P, Psarras P, Wilcox J. CO2 capture from the industry sector. Prog Energy Combust Sci 2017;63:146–72.

Baker RW. Membrane technology and applications. John Wiley & Sons; 2012.

Balaraju M, Rekha V, Raju N, Lingaiah N. Hydrogenolysis of glycerol: comparison of continuous and batch mode reactions over Ni-ZnO catalysts. Catal Green Chem Eng 2018;1:13–26.

Barchas R, Davis R. The Kerr-McGee/ABB Lummus Crest technology for the recovery of CO2 from stack gases. Energy Convers Manag 1992;33:333–40.

Bassindale AR, Pourny M, Taylor PG, Hursthouse MB, Light ME. Fluoride-ion encapsulation within a silsesquioxane cage. Angew Chemie - Int Ed 2003;42:3488–90.

BCC Research, Report Code CHM062E, Published January 2019. 2019.

BCC Research, Report Code EGY171A, Published March 2020. 2020.

Beerthuis R, Huang L, Shiju NR, Rothenberg G, Shen W, Xu H. Facile synthesis of a novel hierarchical ZSM-5 zeolite: a stable acid catalyst for dehydrating glycerol to acrolein. ChemCatChem 2018;10:211–21.

Behr A, Eilting J, Irawadi K, Leschinski J, Lindner F. Improved utilisation of renewable resources: new important derivatives of glycerol. Green Chem 2008;10:13–30.

Bertau M, Offermanns H, Plass L, Schmidt F, Wernicke H-J. Methanol: the basic chemical and energy feedstock of the future. Springer; 2014.

Biesinger MC. Advanced analysis of copper X-ray photoelectron spectra. Surf Interface Anal 2017;49:1325–34.

Biesinger MC, Lau LWM, Gerson AR, Smart RSC. Resolving surface chemical states in XPS analysis of first row transition metals, oxides and hydroxides: Sc, Ti, V, Cu and Zn. Appl Surf Sci 2010;257:887–98.

Blanco I, Abate L, Bottino FA, Bottino P, Chiacchio MA. Thermal degradation of differently substituted Cyclopentyl Polyhedral Oligomeric Silsesquioxane (CP-POSS) nanoparticles. J Therm Anal Calorim 2012;107:1083–91.

Bohmer N, Roussiere T, Kuba M, A Schunk S. Valorisation of glycerol as renewable feedstock: comparison of the exploration of chemical transformation methods aided by high hroughput Experimentation. Comb Chem High Throughput Screen 2012;15:123–35.

Bonura G, Cordaro M, Cannilla C, Arena F, Frusteri F. The changing nature of the active site of Cu-Zn-Zr catalysts for the CO2 hydrogenation reaction to methanol. Appl Catal B Environ 2014;152–153:152–61.

Boretti A, Banik BK. Advances in hydrogen production from natural gas reforming. Adv Energy Sustain Res 2021;2:2100097.

Budzianowski WM. Negative carbon intensity of renewable energy technologies involving biomass or carbon dioxide as inputs. Renew Sustain Energy Rev 2012;16:6507–21.

Butburee T, Chakthranont P, Phawa C, Faungnawakij K. Beyond artificial photosynthesis: prospects on photobiorefinery. ChemCatChem 2020;12:1873–90.

C. Marcano D, V. Kosynkin D, M. Berlin J, Sinitskii A, Sun Z, Slesarev A, et al. Improved Synthesis of Graphene Oxide. ACS Nano 2010;4:4806–14.

Cai Z-Z, Wang Y, Teng Y-L, Chong K-M, Wang J-W, Zhang J-W, et al. A two-step biodiesel production process from waste cooking oil via recycling crude glycerol esterification catalyzed by alkali catalyst. Fuel Process Technol 2015;137:186–93.

Callam CS, Singer SJ, Lowary TL, Hadad CM. Computational analysis of the potential energy surfaces of glycerol in the gas and aqueous phases: effects of level of theory, basis set, and solvation on strongly intramolecularly hydrogen-bonded systems. J Am Chem Soc 2001;123:11743–54.

Carlson CG, Hall JE, Huang YY, Kotila S, Rauk A, Tavares DF. The preparation of esters of formic acid using boron oxide. Can J Chem 1987;65:2461–3.

Carmona M, Valverde JL, Pérez A, Warchol J, Rodriguez JF. Purification of glycerol/water solutions from biodiesel synthesis by ion exchange: sodium removal Part I. J Chem Technol Biotechnol 2009;84:738–44.

Carvalho VB, Leite RF, Almeida MTC, Paschoaloto JR, Carvalho EB, Lanna DPD, et al. Carcass characteristics and meat quality of lambs fed high concentrations of crude glycerin in low-starch diets. Meat Sci 2015;110:285–92.

CHANG C. Base catalyzed adsorption of toluene by zinc oxide. J Catal 1975;38:491–3.

Chase MW, (US) NISO. NIST-JANAF thermochemical tables. American Chemical Society Washington, DC; 1998.

Chau TT. A review of techniques for measurement of contact angles and their applicability on mineral surfaces. Miner Eng 2009;22:213–9.

Chelli R, Procacci P, Cardini G, Della Valle RG, Califano S. Glycerol condensed phases Part I. A molecular dynamics study. Phys Chem Chem Phys 1999;1:871–7.

Chen X, Liu Y, Wu J. Sustainable production of formic acid from biomass and carbon dioxide. Mol Catal 2020;483:110716.

Chilakamarry CR, Sakinah AMM, Zularisam AW, Sirohi R, Khilji IA, Reddy VJ, et al. Bioconversion of glycerol into biofuels—Opportunities and challenges. BioEnergy Res 2022;15:46–61.

Chinchen GC, Denny PJ, Jennings JR, Spencer MS, Waugh KC. Synthesis of methanol. Appl Catal 1988;36:1–65.

Chinnam PR, Gau MR, Schwab J, Zdilla MJ, Wunder SL. The polyoctahedral silsesquioxane (POSS) 1,3,5,7,9,11,13,15-octaphenylpentacyclo[9.5.1.13,9.15,15.17,13]-octasiloxane (octaphenyl-POSS). Acta Crystallogr Sect C Struct Chem 2014;70:971–4.

Chisti Y. Biodiesel from microalgae. Biotechnol Adv 2007;25:294–306.

Chongkhong S, Tongurai C, Chetpattananondh P. Continuous esterification for biodiesel production from palm fatty acid distillate using economical process. Renew Energy

2009;34:1059–63.

Ciriminna R, Pina C Della, Rossi M, Pagliaro M. Understanding the glycerol market. Eur J Lipid Sci Technol 2014;116:1432–9.

Clegg BYW, Sheldrick GM, Vater N. Dodeea (phenylsilasesquioxane)* 1981:3162–4.

Condon JB. An Overview of Physisorption. Surf Area Porosity Determ by Physisorption 2006:1–27.

Corma A, Iborra S, Velty A. Chemical routes for the transformation of biomass into chemicals. Chem Rev 2007;107:2411–502.

Costa JAV, Linde GA, Atala DIP, Mibielli GM, Krüger RT. Modelling of growth conditions for cyanobacterium Spirulina platensis in microcosms. World J Microbiol Biotechnol 2000;16:15–8.

Crabtree GW, Dresselhaus MS, Buchanan M V. The hydrogen economy. Phys Today 2004;57:39–44.

Cuellar-Bermudez SP, Garcia-Perez JS, Rittmann BE, Parra-Saldivar R. Photosynthetic bioenergy utilizing CO2: an approach on flue gases utilization for third generation biofuels. J Clean Prod 2015;98:53–65.

Cui YT, Kimura A, Miyamoto K, Sakamoto K, Xie T, Qiao S, et al. Electronic structures of Fe3 - x V x Si probed by photoemission spectroscopy. Phys Status Solidi 2006;203:2765–8.

Dalai AK, Davis BH. Fischer–Tropsch synthesis: A review of water effects on the performances of unsupported and supported Co catalysts. Appl Catal A Gen 2008;348:1–15.

Dalena F, Senatore A, Marino A, Gordano A, Basile M, Basile A. Methanol production and applications: an overview. Methanol, Elsevier; 2018, p. 3–28.

Daneshvar E, Wicker RJ, Show P-L, Bhatnagar A. Biologically-mediated carbon capture and utilization by microalgae towards sustainable CO2 biofixation and biomass valorization – A review. Chem Eng J 2022;427:130884.

Deerattrakul V, Dittanet P, Sawangphruk M, Kongkachuichay P. CO2 hydrogenation to methanol

using Cu-Zn catalyst supported on reduced graphene oxide nanosheets. J CO2 Util 2016;16:104–13.

Deka TJ, Osman AI, Baruah DC, Rooney DW. Methanol fuel production, utilization, and techno-economy: a review. Environ Chem Lett 2022.

Deng Y, Han D, Deng YY, Zhang Q, Chen F, Fu Q. Facile one-step preparation of robust hydrophobic cotton fabrics by covalent bonding polyhedral oligomeric silsesquioxane for ultrafast oil/water separation. Chem Eng J 2020;379:122391.

Dhabhai R, Ahmadifeijani E, Dalai AK, Reaney M. Purification of crude glycerol using a sequential physico-chemical treatment, membrane filtration, and activated charcoal adsorption. Sep Purif Technol 2016;168:101–6.

Dobrowolski A, Mituła P, Rymowicz W, Mirończuk AM. Efficient conversion of crude glycerol from various industrial wastes into single cell oil by yeast Yarrowia lipolytica. Bioresour Technol 2016;207:237–43.

Dodekatos G, Schünemann S, Tüysüz H. Recent advances in thermo-, photo-, and electrocatalytic glycerol oxidation. ACS Catal 2018;8:6301–33.

Dou J, Zhang B, Liu H, Hong J, Yin S, Huang Y, et al. Carbon supported Pt9Sn1 nanoparticles as an efficient nanocatalyst for glycerol oxidation. Appl Catal B Environ 2016;180:78–85.

Duan X, Zhang Y, Pan M, Dong H, Chen B, Ma Y, et al. SbOx-promoted pt nanoparticles supported on CNTs as catalysts for base-free oxidation of glycerol to dihydroxyacetone. AIChE J 2018;64:3979–87.

Dudley GB, Richert R, Stiegman AE. On the existence of and mechanism for microwave-specific reaction rate enhancement. Chem Sci 2015;6:2144–52.

E2550. Standard Test Method for Thermal Stability by Thermogravimetry. ASTM Int 2017;11:1–5.

Eisenbart FJ, Angermeier N, Ulrich J. Production of highly dry glycerol by solvent-aided melt layer crystallization. J Cryst Growth 2017;469:191–6.

Enzmann F, Mayer F, Rother M, Holtmann D. Methanogens: biochemical background and biotechnological applications. AMB Express 2018;8:1.

Estevez R, Lopez-Pedrajas S, Blanco-Bonilla F, Luna D, Bautista FM. Production of acrolein from glycerol in liquid phase on heterogeneous catalysts. Chem Eng J 2015;282:179–86.

Fagorite VI, Onyekuru SO, Opara AI, Oguzie EE. The major techniques, advantages, and pitfalls of various methods used in geological carbon sequestration. Int J Environ Sci Technol 2022:1–30.

Fan H, Yang R. Thermal decomposition of polyhedral oligomeric octaphenyl, octa(nitrophenyl), and octa(aminophenyl) silsesquioxanes. J Therm Anal Calorim 2014;116:349–57.

Fan YJ, Wu SF. A graphene-supported copper-based catalyst for the hydrogenation of carbon dioxide to form methanol. J CO2 Util 2016;16:150–6.

Fang H, Zhao L, Yue W, Wang Y, Jiang Y, Zhang Y. Facile and large-scale preparation of sandwich-structured graphene-metal oxide composites as anode materials for Li-ion batteries. Electrochim Acta 2015;186:397–403.

Farrelly DJ, Everard CD, Fagan CC, McDonnell KP. Carbon sequestration and the role of biological carbon mitigation: A review. Renew Sustain Energy Rev 2013;21:712–27.

Feng X, Yao Y, Su Q, Zhao L, Jiang W, Ji W, et al. Vanadium pyrophosphate oxides: the role of preparation chemistry in determining renewable acrolein production from glycerol dehydration. Appl Catal B Environ 2015;164:31–9.

Fichtl MB, Schlereth D, Jacobsen N, Kasatkin I, Schumann J, Behrens M, et al. Kinetics of deactivation on Cu/ZnO/Al2O3 methanol synthesis catalysts. Appl Catal A Gen 2015;502:262–70.

Fina A, Tabuani D, Carniato F, Frache A, Boccaleri E, Camino G. Polyhedral oligomeric silsesquioxanes (POSS) thermal degradation. Thermochim Acta 2006;440:36–42.

Friedlingstein P, O'Sullivan M, Jones MW, Andrew RM, Hauck J, Olsen A, et al. Global carbon budget 2020. Earth Syst Sci Data 2020;12:3269–340.

Frontera P, Macario A, Ferraro M, Antonucci P. Supported catalysts for CO2 methanation: a

review. Catalysts 2017;7:59.

Fu N, Liang X, Li Z, Li Y. Single-atom site catalysts based on high specific surface area supports. Phys Chem Chem Phys 2022;24:17417–38.

Fu W, Li Z, Xu W, Wang Y, Sun Y, Dai Y. Exceptionally thermal-stable Al2O3/TiO2 nanofibers by depressing surface-initiated grain growth as new supports for anti-sintering Pt nanoparticles. Mater Today Nano 2020;11:100088.

Fujishima A, Honda K. Electrochemical photolysis of water at a semiconductor electrode. Nature 1972;238:37–8.

Fujitani T, Nakamura I, Uchijima T, Nakamura J. The kinetics and mechanism of methanol synthesis by hydrogenation of CO2 over a Zn-deposited Cu (111) surface. Surf Sci 1997;383:285–98.

Fujitani T, Nakamura J. The effect of ZnO in methanol synthesis catalysts on Cu dispersion and the specific activity. Catal Letters 1998;56:119–24.

Gadikota G. Carbon mineralization pathways for carbon capture, storage and utilization. Commun Chem 2021;4:1–5.

Galindo Cifre P, Badr O. Renewable hydrogen utilisation for the production of methanol. Energy Convers Manag 2007;48:519–27.

Ganesh I. Conversion of carbon dioxide into methanol – a potential liquid fuel: Fundamental challenges and opportunities (a review). Renew Sustain Energy Rev 2014;31:221–57.

García-Fernández S, Gandarias I, Requies J, Soulimani F, Arias PL, Weckhuysen BM. The role of tungsten oxide in the selective hydrogenolysis of glycerol to 1, 3-propanediol over Pt/WOx/Al2O3. Appl Catal B Environ 2017;204:260–72.

Gerdemann SJ, O'Connor WK, Dahlin DC, Penner LR, Rush H. Ex situ aqueous mineral carbonation. Environ Sci Technol 2007;41:2587–93.

Van Gerpen J. Biodiesel processing and production. Fuel Process Technol 2005;86:1097–107.

Gerssen-Gondelach SJ, Saygin D, Wicke B, Patel MK, Faaij APC. Competing uses of biomass: Assessment and comparison of the performance of bio-based heat, power, fuels and materials. Renew Sustain Energy Rev 2014;40:964–98.

Gholami Z, Abdullah AZ, Lee KT. Dealing with the surplus of glycerol production from biodiesel industry through catalytic upgrading to polyglycerols and other value-added products. Renew Sustain Energy Rev 2014;39:327–41.

Glycerol Market Size, Share & Trends Analysis Report By Source (Biodiesel, Fatty Alcohol, Fatty Acids, Soaps), By Type (Crude, Refined), By End Use, By Region, And Segment Forecasts, 2021 - 2027. n.d. https://www.grandviewresearch.com/industry-analysis/glycerol-market# (accessed July 5, 2022).

González-Castaño M, Dorneanu B, Arellano-García H. The reverse water gas shift reaction: a process systems engineering perspective. React Chem Eng 2021;6:954–76.

Gonzalez-Meler MA. Plant respiration and elevated atmospheric CO2 concentration: cellular responses and global significance. Ann Bot 2004;94:647–56.

Gor GY, Thommes M, Cychosz KA, Neimark A V. Quenched solid density functional theory method for characterization of mesoporous carbons by nitrogen adsorption. Carbon N Y 2012;50:1583–90.

Götz M, Lefebvre J, Mörs F, McDaniel Koch A, Graf F, Bajohr S, et al. Renewable Power-to-Gas: A technological and economic review. Renew Energy 2016;85:1371–90.

Gregory SR. Physical properties of glycerine. Glycerine, CRC Press; 2018, p. 113–56.

Guo B, Ghalambor A. Dehydration. Nat Gas Eng Handb 2005:143–71.

Gupta M, Kumar N. Scope and opportunities of using glycerol as an energy source. Renew Sustain Energy Rev 2012;16:4551–6.

Hájek M, Skopal F. Treatment of glycerol phase formed by biodiesel production. Bioresour Technol 2010;101:3242–5.

Handke B, Jastrzebski W, Mozgawa W, Kowalewska A. Structural studies of crystalline

octamethylsilsesquioxane (CH3)8Si8O12. J Mol Struct 2008;887:159–64.

Handke B, Klita Ł, Nizioł J, Jastrzębski W, Adamczyk A. Studies of dodecaphenyl polyhedral oligomeric silsesquioxane thin films on Si(1 0 0) wafers. J Mol Struct 2014;1065–1066:248–53.

Harima Y, Komaguchi K, Oka K, Maruoka T, Imae I, Ooyama Y. Trapping of atomic hydrogens in cage-shaped silsesquioxanes by electric discharge. Chem Commun 2010;46:2076–8.

Hass H, Patterson J. Purification of glycerol by crystallization. Ind Eng Chem 1941;33:615–6.

Höhne GWH, Hemminger WF, Flammersheim H-J. Theoretical fundamentals of differential scanning calorimeters. Differ. Scanning Calorim., Berlin, Heidelberg: Springer Berlin Heidelberg; 2003, p. 31–63.

Holechek JL, Geli HME, Sawalhah MN, Valdez R. A global assessment: can renewable energy replace fossil fuels by 2050? Sustainability 2022;14:4792.

Hong A-A, Cheng K-K, Peng F, Zhou S, Sun Y, Liu C-M, et al. Strain isolation and optimization of process parameters for bioconversion of glycerol to lactic acid. J Chem Technol Biotechnol 2009;84:1576–81.

Hoogenboom R, Wilms TFA, Erdmenger T, Schubert US. Microwave-assisted chemistry: a closer look at heating efficiency. Aust J Chem 2009;62:236–43.

Hopkins DW. What is a Norris derivative? NIR News 2001;12:3–5.

Höppener RH, Doesburg EBM, Scholten JJF. Preparation and characterization of stable copper/zinc oxide/alumina catalysts for methanol systhesis. Appl Catal 1986;25:109–19.

Hossain D, Hagelberg F, Saebo S, Pittman CU. Structures, stabilities and electronic properties of endo- and exohedral dodecahedral silsesquioxane (T12-POSS) nanosized complexes with atomic and ionic species. J Inorg Organomet Polym Mater 2010;20:424–44.

Hossain D, Pittman CU, Hagelberg F, Saebo S. Endohedral and exohedral complexes of T8-polyhedral oligomeric silsesquioxane (POSS) with transition metal atoms and ions. J Phys Chem C 2008;112:16070–7.

Hou S, Dong J, Zhao B. Formation of C-X Bonds in CO2 chemical fixation catalyzed by metal−organic frameworks. Adv Mater 2020;32:1806163.

Hu Y, Zhang Y, Du J, Li C, Wang Kangjun, Liu L, et al. The influence of composition on the functionality of hybrid CuO-ZnO-Al2O3/HZSM-5 for the synthesis of DME from CO2 hydrogenation. RSC Adv 2018;8:30387–95.

IEA. Global Energy Review: CO2 Emissions in 2021. https://www.iea.org/reports/global-energy-review-co2-emissions-in-2021-2.

IEA (2020). Renewables 2020, IEA, Paris 2020. https://www.iea.org/reports/renewables-2020 (accessed October 17, 2022).

IEA (2021), Greenhouse Gas Emissions from Energy Data Explorer, IEA, Paris. 2021. https://www.iea.org/data-and-statistics/data-tools/greenhouse-gas-emissions-from-energy-data-explorer (accessed October 27, 2022).

IEA (2022), Global energy review: CO2 emissions in 2021, IEA, Paris. 2022.

Inoue T, Fujishima A, Konishi S, Honda K. Photoelectrocatalytic reduction of carbon dioxide in aqueous suspensions of semiconductor powders. Nature 1979;277:637–8.

Isahak WNRW, Ismail M, Yarmo MA, Jahim JM, Salimon J. Purification of crude glycerol from transesterification RBD palm oil over homogeneous and heterogeneous catalysts for the biolubricant preparation. J Appl Sci 2010;10:2590–5.

Isahak WNRW, Ramli ZAC, Ismail M, Jahim JM, Yarmo MA. Recovery and Purification of Crude Glycerol from Vegetable Oil Transesterification. Sep \& Purif Rev 2015;44:250–67.

Ito T, Nakashimada Y, Senba K, Matsui T, Nishio N. Hydrogen and ethanol production from glycerol-containing wastes discharged after biodiesel manufacturing process. J Biosci Bioeng 2005;100:260–5.

Jansen D, Gazzani M, Manzolini G, Dijk E van, Carbo M. Pre-combustion CO2 capture. Int J Greenh Gas Control 2015;40:167–87.

Javani A, Hasheminejad M, Tahvildari K, Tabatabaei M. High quality potassium phosphate

production through step-by-step glycerol purification: A strategy to economize biodiesel production. Bioresour Technol 2012;104:788–90.

Joo O-S, Jung K-D, Moon I, Rozovskii AY, Lin GI, Han S-H, et al. Carbon dioxide hydrogenation to form methanol via a reverse-water-gas-shift reaction (the CAMERE process). Ind Eng Chem Res 1999;38:1808–12.

Kamm O, Marvel CS. Synthesis of allyl alcohol. Org Synth 1921;1:15–7.

Kappe CO. Controlled microwave heating in modern organic synthesis. Angew Chemie Int Ed 2004;43:6250–84.

Katada N, Iseki Y, Shichi A, Fujita N, Ishino I, Osaki K, et al. Production of ethanol by vapor phase hydration of ethene over tungsta monolayer catalyst loaded on titania. Appl Catal A Gen 2008;349:55–61.

Katryniok B, Paul S, Capron M, Lancelot C, Belliere-Baca V, Rey P, et al. A long-life catalyst for glycerol dehydration to acrolein. Green Chem 2010;12:1922–5.

Kaur L, Gupta GD. A review on microwave assisted grafting of polymers. Int J Pharm Sci Res 2017;8:422.

Keller N, Rebmann G, Keller V. Catalysts, mechanisms and industrial processes for the dimethylcarbonate synthesis. J Mol Catal A Chem 2010;317:1–18.

Key World Energy Statistics. 2021. https://www.iea.org/reports/key-world-energy-statistics-2021 (accessed October 14, 2022).

Kim DS, Lee WJ, Myungjin K, Choe Y, Nam H. Method for preparing allyl alcohol. US Patent US9,120,718B12015, 2015.

Kim K, Lichtenhan JD, Otaigbe JU. Facile route to nature inspired hydrophobic surface modification of phosphate glass using polyhedral oligomeric silsesquioxane with improved properties. Appl Surf Sci 2019;470:733–43.

de Klerk A, Maitlis PM. Greener Fischer-Tropsch processes for fuels and feedstocks. Wiley; 2013.

Kodera M, Moriya Y, Katayama M, Hisatomi T, Minegishi T, Domen K. Investigation on nitridation processes of Sr2Nb2O7 and SrNbO3 to SrNbO2N for photoelectrochemical water splitting. Sci Rep 2018;8:15849.

Kongjao S, Damronglerd S, Hunsom M. Purification of crude glycerol derived from waste used-oil methyl ester plant. Korean J Chem Eng 2010;27:944–9.

Kostyniuk A, Bajec D, Djinović P, Likozar B. Allyl alcohol production by gas phase conversion reactions of glycerol over bifunctional hierarchical zeolite-supported bi-and tri-metallic catalysts. Chem Eng J 2020;397:125430.

Kou J, Gao J, Li Z, Yu H, Zhou Y, Zou Z. Construction of visible-light-responsive SrTiO3 with enhanced CO2 adsorption ability: highly efficient photocatalysts for artifical photosynthesis. Catal Letters 2015;145:640–6.

Kourkoumpas DS, Papadimou E, Atsonios K, Karellas S, Grammelis P, Kakaras E. Implementation of the power to methanol concept by using CO2 from lignite power plants: Techno-economic investigation. Int J Hydrogen Energy 2016;41:16674–87.

Kowalewska A. Self-assembling polyhedral silsesquioxanes - Structure and Properties. Curr Org Chem 2017;21:1243–64.

Krylova AY. Products of the Fischer-Tropsch synthesis (A Review). Solid Fuel Chem 2014;48:22–35.

Kumar A, Madden DG, Lusi M, Chen K, Daniels EA, Curtin T, et al. Direct air capture of CO2 by physisorbent materials. Angew Chemie Int Ed 2015;54:14372–7.

Kumar LR, Kaur R, Tyagi RD, Drogui P. Identifying economical route for crude glycerol valorization: Biodiesel versus polyhydroxy-butyrate (PHB). Bioresour Technol 2021;323:124565.

Kumar LR, Yellapu SK, Tyagi RD, Zhang X. A review on variation in crude glycerol composition, bio-valorization of crude and purified glycerol as carbon source for lipid production. Bioresour Technol 2019;293:122155.

Kurtz M, Strunk J, Hinrichsen O, Muhler M, Fink K, Meyer B, et al. Active sites on oxide surfaces:

ZnO-catalyzed synthesis of methanol from CO and H2. Angew Chemie Int Ed 2005;44:2790–4.

Laine RM, Roll MF. Polyhedral phenylsilsesquioxanes. Macromolecules 2011;44:1073–109.

Lan H, Yao Q, Zhou Y, Zhang B, Jiang Y. Direct conversion of gas-glycerol to Allyl alcohol over V, Ti or Nb modified MoFe/KIT-6 oxide catalysts. Mol Catal 2020;498:111279.

Lange J-P. Methanol synthesis: a short review of technology improvements. Catal Today 2001;64:3–8.

Lari GM, Pastore G, Mondelli C, Pérez-Ramírez J. Towards sustainable manufacture of epichlorohydrin from glycerol using hydrotalcite-derived basic oxides. Green Chem 2018;20:148–59.

Lee AS, Choi SS, Lee HS, Baek KY, Hwang SS. A new, higher yielding synthetic route towards dodecaphenyl cage silsesquioxanes: Synthesis and mechanistic insights. Dalt Trans 2012;41:10585–8.

Leffingwell G, Lesser MA. Glycerin, its industrial and commercial applications. Chemical publishing, New York; 1945.

Leng L, Yuan X, Zeng G, Chen X, Wang H, Li H, et al. Rhamnolipid based glycerol-in-diesel microemulsion fuel: formation and characterization. Fuel 2015;147:76–81.

Lesiak B, Trykowski G, Tóth J, Biniak S, Kövér L, Rangam N, et al. Chemical and structural properties of reduced graphene oxide—dependence on the reducing agent. J Mater Sci 2021;56:3738–54.

Létant SE, Herberg J, Dinh LN, Maxwell RS, Simpson RL, Saab AP. Structure and catalytic activity of POSS-stabilized Pd nanoparticles. Catal Commun 2007;8:2137–42.

Li C, Yuan X, Fujimoto K. Development of highly stable catalyst for methanol synthesis from carbon dioxide. Appl Catal A Gen 2014;469:306–11.

Li H, Jiao X, Li L, Zhao N, Xiao F, Wei W, et al. Synthesis of glycerol carbonate by direct carbonylation of glycerol with CO 2 over solid catalysts derived from Zn/Al/La and Zn/Al/La/M (M= Li, Mg and Zr) hydrotalcites. Catal Sci Technol 2015;5:989–1005.

Li M, Wang Y, Gao H, Wang J, Sun B. Thermally stable microstructure and mechanical properties of graphene reinforced aluminum matrix composites at elevated temperature. J Mater Res Technol 2020;9:13230–8.

Li X, Du Y, Dai J, Wang X, Yang P. Metal nanoparticles stabilized by cubic silsesquioxanes for catalytic hydrogenations. Catal Letters 2007;118:151–8.

Li X, Sun Y, Xu J, Shao Y, Wu J, Xu X, et al. Selective visible-light-driven photocatalytic CO2 reduction to CH4 mediated by atomically thin CuIn5S8 layers. Nat Energy 2019;4:690–9.

Li X, Zhang Y. Highly efficient process for the conversion of glycerol to acrylic acid via gas phase catalytic oxidation of an allyl alcohol intermediate. ACS Catal 2016;1:143–50.

Liang B, Ma J, Su X, Yang C, Duan H, Zhou H, et al. Investigation on Deactivation of Cu/ZnO/Al2O3 Catalyst for CO2 Hydrogenation to Methanol. Ind & Eng Chem Res 2019a;58:9030–7.

Liang B, Ma J, Su X, Yang C, Duan H, Zhou H, et al. Investigation on deactivation of Cu/ZnO/Al2O3 catalyst for CO2 hydrogenation to methanol. Ind Eng Chem Res 2019b;58:9030–7.

Liang F, Wang H, Liu G, Zhao J, Jin W. Designing highly selective and stable water transport channel through graphene oxide membranes functionalized with polyhedral oligomeric silsesquioxane for ethanol dehydration. J Memb Sci 2021;638:119675.

Liaw BJ, Chen YZ. Liquid-phase synthesis of methanol from CO 2/H 2 over ultrafine CuB catalysts. Appl Catal A Gen 2001;206:245–56.

Lin T, He C, Xiao Y. Theoretical Studies of Monosubstituted and Higher Phenyl-Substituted Octahydrosilsesquioxanes The electronic and structural properties of molecules (octahydrosilsesquioxane, H 8 Si 8 O 12), the monosubstituted and higher phenyl-substituted octahydrosilsesquioxanes (2003.

Lin Y-C. Catalytic valorization of glycerol to hydrogen and syngas. Int J Hydrogen Energy 2013;38:2678–700.

Liu F, Chiou B-S, Avena-Bustillos RJ, Zhang Y, Li Y, McHugh TH, et al. Study of combined effects of glycerol and transglutaminase on properties of gelatin films. Food Hydrocoll 2017;65:1–9.

Liu X-M, Lu GQ, Yan Z-F, Beltramini J. Recent advances in catalysts for methanol synthesis via hydrogenation of CO and CO2. Ind Eng Chem Res 2003;42:6518–30.

Liu X, Elgowainy A, Wang M. Life cycle energy use and greenhouse gas emissions of ammonia production from renewable resources and industrial by-products. Green Chem 2020;22:5751–61.

Liu Z, Ma S, Chen L, Xu J, Ou J, Ye M. Porous styryl-linked polyhedral oligomeric silsesquioxane (POSS) polymers used as a support for platinum catalysts. Mater Chem Front 2019;3:851–9.

Lloyd L. Hanbook of industrial catalysts. Springer Science & Business Media; 2011.

Lowell S, Shields JE, Thomas MA, Thommes M. Surface Area Analysis from the Langmuir and BET Theories, 2004, p. 58–81.

Lu J, Wang P, Wang Q, Wang Y, Jiang M. Validated 1H and 13C nuclear magnetic resonance methods for the quantitative determination of glycerol in drug injections. Molecules 2018;23:1177.

Luo X, Ge X, Cui S, Li Y. Value-added processing of crude glycerol into chemicals and polymers. Bioresour Technol 2016;215:144–54.

Lyngfelt A. Chemical looping combustion: status and development challenges. Energy & Fuels 2020;34:9077–93.

Maltsev Y, Maltseva K. Fatty acids of microalgae: diversity and applications. Rev Environ Sci Bio/Technology 2021;20:515–47.

Manosak R, Limpattayanate S, Hunsom M. Sequential-refining of crude glycerol derived from waste used-oil methyl ester plant via a combined process of chemical and adsorption. Fuel Process Technol 2011;92:92–9.

Mantz RA, Jones PF, Chaffee KP, Lichtenhan JD, Gilman JW, Ismail IMK, et al. Thermolysis of polyhedral oligomeric silsesquioxane (POSS) macromers and POSS−siloxane copolymers. Chem Mater 1996;8:1250–9.

Marmur A, Della Volpe C, Siboni S, Amirfazli A, Drelich JW. Contact angles and wettability: towards common and accurate terminology. Surf Innov 2017;5:3–8.

Martin A, Richter M. Oligomerization of glycerol –A critical review. Eur J Lipid Sci Technol 2011;113:100–17.

Meenan PA, Anderson SR, Klug DL. The influence of impurities and solvents on crystallization. Handb Ind Cryst 2002:67–100.

Mekhilef S, Saidur R, Safari A. Comparative study of different fuel cell technologies. Renew Sustain Energy Rev 2012;16:981–9.

Metz, B., Davidson, O. De Coninck, H.C. Loos, M., Meyer L. IPCC special report on carbon dioxide capture and storage. 2005.

Metz, Bert and Davidson, Ogunlade and De Coninck, H and Loos, M and Meyer L. Intergovernmental panel on climate change special report on carbon dioxide capture and storage. Cambridge, UK New York, USA 2005.

Mhadmhan S, Ngamcharussrivichai C, Hinchiranan N, Kuchonthara P, Li Y, Wang S, et al. Direct biogas upgrading via CO2 methanation to high-quality biomethane over NiMg/CNT-SiO2 fiber catalysts. Fuel 2022;310:122289.

Miller BG. Carbon dioxide emissions reduction and storage. Clean Coal Eng. Technol., Elsevier; 2017, p. 609–68.

Moghaddam MB, Goharshadi EK, Moosavi F. Glycerol revisited molecular dynamic simulations of structural, dynamical, and thermodynamic properties. J Iran Chem Soc 2017;14:1–7.

Monticelli O, Fina A, Ullah A, Waghmare P. Preparation, Characterization, and Properties of Novel PSMA-POSS Systems by Reactive Blending. Macromolecules 2009;42:6614–23.

Montoya Sánchez N, de Klerk A. Oxidative ring-opening of aromatics: Thermochemistry of sodium, potassium and magnesium biphenyl carboxylates. Thermochim Acta 2016;645:31–42.

Montoya Sánchez N, Link F, Chauhan G, Halmenschlager C, El-Sayed HEM, Sehdev R, et al. Conversion of waste to sustainable aviation fuel via Fischer–Tropsch synthesis: front-end design

decisions. Energy Sci Eng 2022;10:1763–89.

Mora JR, Perez CD, Maldonado A, Loroño M, Córdova T, Chuchani G. Theoretical study on thermal decomposition kinetics of allyl formates in the gas phase. Comput Theor Chem 2013;1019:48–54.

Moretti G, Fierro G, Lo Jacono M, Porta P. Characterization of CuO-ZnO catalysts by X-ray photoelectron spectroscopy: Precursors, calcined and reduced samples. Surf Interface Anal 1989;14:325–36.

Muniru OS, Ezeanyanaso CS, Akubueze EU, Igwe CC, Elemo GN. Review of different purification techniques for crude glycerol from biodiesel production. J Energy Res Rev 2018;2:1–6.

Murdoch K, Goldblatt L, Carrasquillo R, Harris D. Sabatier methanation reactor for space exploration. 1st Sp. Explor. Conf. Contin. Voyag. Discov., Reston, Virigina: American Institute of Aeronautics and Astronautics; 2005.

Nakagawa Y, Tamura M, Tomishige K. Perspective on catalyst development for glycerol reduction to C3 chemicals with molecular hydrogen. Res Chem Intermed 2018;44:3879–903.

Nanda, MR and Yuan, Z and Qin, W and Poirier, MA and Chunbao X. Purification of crude glycerol using acidification: effects of acid types and product characterization. Austin J Chem Eng 2014;1:1–7.

Nandy A, Loha C, Gu S, Sarkar P, Karmakar MK, Chatterjee PK. Present status and overview of chemical looping combustion technology. Renew Sustain Energy Rev 2016;59:597–619.

Neeraj, Yadav S. Carbon storage by mineral carbonation and industrial applications of CO2. Mater Sci Energy Technol 2020;3:494–500.

Nemitallah MA, Habib MA, Badr HM, Said SA, Jamal A, Ben-Mansour R, et al. Oxy-fuel combustion technology: current status, applications, and trends. Int J Energy Res 2017;41:1670–708.

Nutting JE, Gerken JB, Stamoulis AG, Bruns DL, Stahl SS. “How should I think about voltage?

What is overpotential?": Establishing an Organic Chemistry intuition for Electrochemistry. J Org Chem 2021;86:15875–85.

Nzihou A. Toward the valorization of waste and biomass. Waste and Biomass Valorization 2010;1:3–7.

O'Hare LA, Parbhoo B, Leadley SR. Development of a methodology for XPS curve-fitting of the Si 2p core level of siloxane materials. Surf Interface Anal 2004;36:1427–34.

O'Neill BC, Tebaldi C, van Vuuren DP, Eyring V, Friedlingstein P, Hurtt G, et al. The scenario model intercomparison project (scenario MIP) for CMIP6. Geosci Model Dev 2016;9:3461–82.

Okoye PU, Abdullah AZ, Hameed BH. Synthesis of oxygenated fuel additives via glycerol esterification with acetic acid over bio-derived carbon catalyst. Fuel 2017;209:538–44.

Olabi AG, Obaideen K, Elsaid K, Wilberforce T, Sayed ET, Maghrabie HM, et al. Assessment of the pre-combustion carbon capture contribution into sustainable development goals SDGs using novel indicators. Renew Sustain Energy Rev 2022;153:111710.

Olah GA. Beyond oil and gas: the methanol economy. Angew Chemie Int Ed 2005;44:2636–9.

Ooi T, Yong K, Dzulkefly K, Wan Yunus W, Hazimah A. Crude glycerine recovery from glycerol residue waste from a palm kernel oil methyl ester plant. J Oil Palm Res 2001;13:16–22.

Ott L, Bicker M, Vogel H. Catalytic dehydration of glycerol in sub-and supercritical water: a new chemical process for acrolein production. Green Chem 2006;8:214–20.

Pagliaro M. Glycerol: the renewable platform chemical. Elsevier; 2017.

Pagliaro M, Ciriminna R, Kimura H, Rossi M, Della Pina C. From glycerol to value-added products. Angew Chemie Int Ed 2007;46:4434–40.

Pagliaro M, Rossi M. The future of glycerol. 2008.

Painter RM, Pearson DM, Waymouth RM. Selective catalytic oxidation of glycerol to dihydroxyacetone. Angew Chemie Int Ed 2010;49:9456–9.

Pakjamsai C, Kawakami Y. Study on effective synthesis and properties of ortho-alkyl-substituted

phenyl octasilsesquioxane. Des Monomers Polym 2005;8:423–35.

Pastor-Pérez L, Baibars F, Le Sache E, Arellano-García H, Gu S, Reina TR. CO2 valorisation via Reverse Water-Gas Shift reaction using advanced Cs doped Fe-Cu/Al2O3 catalysts. J CO2 Util 2017;21:423–8.

Peng Y, Ben T, Xu J, Xue M, Jing X, Deng F, et al. A covalently-linked microporous organic-inorganic hybrid framework containing polyhedral oligomeric silsesquioxane moieties. Dalt Trans 2011;40:2720–4.

Perez M, Perez R. Update 2022 – A fundamental look at supply side energy reserves for the planet. Sol Energy Adv 2022;2:100014.

Pham Minh D, Siang TJ, Vo D-VN, Phan TS, Ridart C, Nzihou A, et al. Hydrogen production from biogas reforming: an overview of steam reforming, dry reforming, dual reforming, and tri-reforming of methane. Hydrog. Supply Chain., Elsevier; 2018, p. 111–66.

Popp J, Kovács S, Oláh J, Divéki Z, Balázs E. Bioeconomy: biomass and biomass-based energy supply and demand. N Biotechnol 2021;60:76–84.

Potthast R, Chung CP, Mathur I. Purification of glycerin obtained as a bioproduct from the transesterification of triglycerides in the synthesis of biofuel. US Patent 7,718,833, 2010.

Prabu SL, Suriya Prakash TNK, Thirumurugan R. Cleaning validation and its regulatory aspects in the pharmaceutical industry. Dev Surf Contam Clean 2015:129–86.

Priecel P, Lopez-Sanchez JA. Advantages and limitations of microwave reactors: from chemical synthesis to the catalytic valorization of biobased chemicals. ACS Sustain Chem Eng 2019;7:3–21.

Pruess K. Leakage of CO2 from geologic storage: Role of secondary accumulation at shallow depth. Int J Greenh Gas Control 2008;2:37–46.

Raman A, Abdul A, Tan HW, Buthiyappan A. Two-step purification of glycerol as a value added by product from the biodiesel production process. Front Chem 2019;7:774.

Räuchle K, Plass L, Wernicke H-J, Bertau M. Methanol for renewable energy storage and

utilization. Energy Technol 2016;4:193–200.

Razzaq T, Kappe CO. On the energy efficiency of microwave-assisted organic reactions. ChemSusChem Chem Sustain Energy Mater 2008;1:123–32.

Riedel T, Claeys M, Schulz H, Schaub G, Nam S-S, Jun K-W, et al. Comparative study of Fischer–Tropsch synthesis with H2/CO and H2/CO2 syngas using Fe- and Co-based catalysts. Appl Catal A Gen 1999;186:201–13.

Rochelle GT. Amine scrubbing for CO2 capture. Science (80-) 2009;325:1652–4.

Rodriguez Herrero Y, Ullah A. Rapid, Metal-Free, Catalytic Conversion of Glycerol to Allyl Monomers and Polymers. ACS Sustain Chem Eng n.d.;9:9474–85.

Rogerson PL. Imperial chemical industries' low pressure methanol plant. Proc. Chem. Eng. Prog. Symp. Ser., vol. 66, 1970, p. 28–34.

Rönsch S, Schneider J, Matthischke S, Schlüter M, Götz M, Lefebvre J, et al. Review on methanation – From fundamentals to current projects. Fuel 2016;166:276–96.

Roode-Gutzmer QI, Kaiser D, Bertau M. Renewable methanol synthesis. ChemBioEng Rev 2019;6:209–36.

Saha BC, Nichols NN, Qureshi N, Kennedy GJ, Iten LB, Cotta MA. Pilot scale conversion of wheat straw to ethanol via simultaneous saccharification and fermentation. Bioresour Technol 2015;175:17–22.

Sahibzada M, Metcalfe IS, Chadwick D. Methanol synthesis from CO/CO2/H2 over Cu/ZnO/Al2O3 at differential and finite conversions. J Catal 1998;174:111–8.

Saito M. R&D activities in Japan on methanol synthesis from CO2 and H2. Catal Surv from Asia 1998;2:175–84.

Saito M, Murata K. Development of high performance Cu/ZnO-based catalysts for methanol synthesis and the water-gas shift reaction. Catal Surv from Asia 2004;8:285–94.

Saito M, Takeuchi M, Fujitani T, Toyir J, Luo S, Wu J, et al. Advances in joint research between

NIRE and RITE for developing a novel technology for methanol synthesis from CO2 and H2. Appl Organomet Chem 2000;14:763–72.

Saito Y, Luo X, Zhao C, Pan W, Chen C, Gong J, et al. Filling the gaps between graphene oxide: a general strategy toward nanolayered oxides. Adv Funct Mater 2015;25:5683–90.

Sánchez G, Dlugogorski BZ, Kennedy EM, Stockenhuber M. Zeolite-supported iron catalysts for allyl alcohol synthesis from glycerol. Appl Catal A Gen 2016;509:130–42.

Sawant SP, Parihar HS, Mehendale HM. Allyl alcohol. In: Wexler P, editor. Encycl. Toxicol. 3er ed., Oxford: Elsevier; 2014, p. 146–8.

Saygin D, Gielen DJ, Draeck M, Worrell E, Patel MK. Assessment of the technical and economic potentials of biomass use for the production of steam, chemicals and polymers. Renew Sustain Energy Rev 2014;40:1153–67.

Schubert US, Hüsing N, Laine RM. Materials syntheses. Vienna: Springer Vienna; 2008.

Schwengber CA, Alves HJ, Schaffner RA, da Silva FA, Sequinel R, Bach VR, et al. Overview of glycerol reforming for hydrogen production. Renew Sustain Energy Rev 2016;58:259–66.

Sdrula N. A study using classical or membrane separation in the biodiesel process. Desalination 2010;250:1070–2.

Shao S, Li X, Gong Z, Fan B, Hu J, Peng J, et al. A new insight into the mechanism in Fe3O4@CuO/PMS system with low oxidant dosage. Chem Eng J 2022;438:135474.

Shigetomi Y, Kojima T, Ono N. Allylic polymers. I. Copolymerization of allyl esters with vinyl acetate. J Polym Sci Part A Polym Chem 1990;28:3317–25.

Shimokawabe M, Asakawa H, Takezawa N. Characterization of copper/zirconia catalysts prepared by an impregnation method. Appl Catal 1990;59:45–58.

Siew YK, Sarkar G, Hu X, Hui J, See A, Chua CT. Thermal curing of hydrogen silsesquioxane. J Electrochem Soc 2000;147:335.

Simon Araya S, Liso V, Cui X, Li N, Zhu J, Sahlin SL, et al. A review of the methanol economy:

the fuel cell route. Energies 2020;13.

Soeder DJ. Fossil fuels and climate change. Fracking Environ. A Sci. Assess. Environ. risks from Hydraul. Fract. Foss. fuels, Cham: Springer International Publishing; 2021, p. 155–85.

Speight JG. Chemical process and design handbook. McGraw-Hill Education; 2002.

Spencer MS. The role of zinc oxide in Cu/ZnO catalysts for methanol synthesis and the water–gas shift reaction. Top Catal 1999;8:259.

Spurr RA, Hanking BM, Rowen JW. The polymerization of diallyl phthalate, an investigation by infrared spectroscopy. J Polym Sci 1959;37:431–40.

Stanger R, Wall T, Spörl R, Paneru M, Grathwohl S, Weidmann M, et al. Oxyfuel combustion for CO2 capture in power plants. Int J Greenh Gas Control 2015;40:55–125.

Stocker TF, Qin D, Plattner G-K, Tignor M, Allen SK, Boschung J, et al. Climate change 2013: the physical science basis. Contribution of working group I to the fifth assessment report of the Intergovernmental Panel on climate change. Cambridge University Press, Cambridge, United Kingdom and New York, NY, USA: 2013.

Strucks P, Failing L, Kaluza S. A short review on Ni-catalyzed methanation of CO2: reaction mechanism, catalyst deactivation, dynamic operation. Chemie Ing Tech 2021;93:1526–36.

Sun J, Bao X. Textural manipulation of mesoporous materials for hosting of metallic nanocatalysts. Chem - A Eur J 2008;14:7478–88.

Sun JT, Metcalfe IS, Sahibzada M. Deactivation of Cu/ZnO/Al2O3 methanol synthesis catalyst by sintering. Ind Eng Chem Res 1999;38:3868–72.

Sun Y-Q, Shen J-T, Yan L, Zhou J-J, Jiang L-L, Chen Y, et al. Advances in bioconversion of glycerol to 1, 3-propanediol: prospects and challenges. Process Biochem 2018;71:134–6.

Sun Z, Zhang H, Zhao Y, Huang C, Tao R, Liu Z, et al. Thermal-stable carbon nanotube-supported metal nanocatalysts by mesoporous silica coating. Langmuir 2011;27:6244–51.

Takahashi K, Sulaiman S, Katzenstein JM, Snoblen S, Laine RM. New

aminophenylsilsesquioxanes—Synthesis, properties, and epoxy nanocomposites. Aust J Chem 2006;59:564.

Takashima H, Karches M, Kanno Y. Catalytic decomposition of trichloroethylene over Pt-/Ni-catalyst under microwave heating. Appl Surf Sci 2008;254:2023–30.

Tan HW, Abdul Aziz AR, Aroua MK. Glycerol production and its applications as a raw material: A review. Renew Sustain Energy Rev 2013;27:118–27.

Teng WK, Ngoh GC, Yusoff R, Aroua MK. Microwave-assisted transesterification of industrial grade crude glycerol for the production of glycerol carbonate. Chem Eng J 2016;284:469–77.

Thommes M, Kaneko K, Neimark A V., Olivier JP, Rodriguez-Reinoso F, Rouquerol J, et al. Physisorption of gases, with special reference to the evaluation of surface area and pore size distribution (IUPAC Technical Report). Pure Appl Chem 2015;87:1051–69.

Thonemann N, Zacharopoulos L, Fromme F, Nühlen J. Environmental impacts of carbon capture and utilization by mineral carbonation: A systematic literature review and meta life cycle assessment. J Clean Prod 2022;332:130067.

Tian P, Wei Y, Ye M, Liu Z. Methanol to olefins (MTO): from fundamentals to commercialization. ACS Catal 2015;5:1922–38.

Toivola Y, Thurn J, Cook RF. Structural, electrical, and mechanical properties development during curing of low-k hydrogen silsesquioxane films. J Electrochem Soc 2002;149:F9.

Toyir J, Miloua R, Elkadri NE, Nawdali M, Toufik H, Miloua F, et al. Sustainable process for the production of methanol from CO2 and H2 using Cu/ZnO-based multicomponent catalyst. Phys Procedia 2009;2:1075–9.

Trache D, Thakur VK, Boukherroub R. Cellulose nanocrystals/graphene hybrids—A promising new class of materials for advanced applications. Nanomaterials 2020;10:1523.

Trimm DL. Thermal stability of catalyst supports. Stud. Surf. Sci. Catal., Elsevier; 1991, p. 29–51.

Tshibalonza NN, Monbaliu J-CM. The deoxydehydration (DODH) reaction: a versatile technology

for accessing olefins from bio-based polyols. Green Chem 2020;22:4801–48.

Tshibalonza NN, Monbaliu J-CM. Revisiting the deoxydehydration of glycerol towards allyl alcohol under continuous-flow conditions. Green Chem 2017;19:3006–13.

Ulgheri F, Spanu P. An efficient chemical conversion of glycerol to dihydroxyacetone. ChemistrySelect 2018;3:11569–72.

Ullah A, Arshad M. Remarkably efficient microwave-assisted cross-metathesis of lipids under solvent-free conditions. ChemSusChem 2017;10:2167–74.

Ullah A, Herrero YR. Methods for converting glycerol to allyl compounds. CANADA Patent US 10,633,316 B22020, 2020.

Unno M, Takada K, Matsumoto H. Synthesis, Structure, and Reaction of the Tetrahydroxycyclotetrasiloxane, [(i-Pr)(OH)SiO] $_4$. Chem Lett 1998;27:489–90.

US EPA. Sources of greenhouse gas emissions 2022. https://www.epa.gov/ghgemissions/sources-greenhouse-gas-emissions (accessed October 16, 2022).

Ushikoshi K, Mori K, Kubota T, Watanabe T, Saito M. Methanol synthesis from CO2 and H2 in a bench-scale test plant. Appl Organomet Chem 2000;14:819–25.

Vannucci JA, Gatti MN, Cardaci N, Nichio NN. Economic feasibility of a solketal production process from glycerol at small industrial scale. Renew Energy 2022;190:540–7.

Vidal K, Gómez E, Goitandia AM, Angulo-Ibáñez A, Aranzabe E. The synthesis of a superhydrophobic and thermal stable silica coating via sol-gel process. Coatings 2019;9:627.

Villa A, Dimitratos N, Chan-Thaw CE, Hammond C, Prati L, Hutchings GJ. Glycerol oxidation using gold-containing catalysts. Acc Chem Res 2015;48:1403–12.

Vogt C, Monai M, Kramer GJ, Weckhuysen BM. The renaissance of the Sabatier reaction and its applications on Earth and in space. Nat Catal 2019;2:188–97.

Vu TTN, Desgagnés A, Iliuta MC. Efficient approaches to overcome challenges in material development for conventional and intensified CO2 catalytic hydrogenation to CO, methanol, and

DME. Appl Catal A Gen 2021;617:118119.

Wang F, Ouyang D, Zhou Z, Page SJ, Liu D, Zhao X. Lignocellulosic biomass as sustainable feedstock and materials for power generation and energy storage. J Energy Chem 2021;57:247–80.

Wang Y, Zhou J, Guo X. Catalytic hydrogenolysis of glycerol to propanediols: a review. RSC Adv 2015;5:74611–28.

Williams CL, Westover TL, Emerson RM, Tumuluru JS, Li C. Sources of biomass feedstock variability and the potential impact on biofuels production. BioEnergy Res 2016;9:1–14.

Wu J, Saito M, Takeuchi M, Watanabe T. The stability of Cu/ZnO-based catalysts in methanol synthesis from a CO2-rich feed and from a CO-rich feed. Appl Catal A Gen 2001;218:235–40.

Wu ST, She QM, Tesser R, Serio M Di, Zhou CH. Catalytic glycerol dehydration-oxidation to acrylic acid. Catal Rev 2020;62:481–523.

Wurzel T, Malcus S, Mleczko L. Reaction engineering investigations of CO2 reforming in a fluidized-bed reactor. Chem Eng Sci 2000;55:3955–66.

Wysokowski M, Materna K, Walter J, Petrenko I, Stelling AL, Bazhenov V V., et al. Solvothermal synthesis of hydrophobic chitin–polyhedral oligomeric silsesquioxane (POSS) nanocomposites. Int J Biol Macromol 2015;78:224–9.

Xie X, Economides MJ. The impact of carbon geological sequestration. All Days, SPE Americas E&P Envrironmenatl and Safety Conference; 2009.

Xu J, Banerjee A, Pan SH, Li ZJ. Galactose can be an inducer for production of therapeutic proteins by auto-induction using E. coli BL21 strains. Protein Expr Purif 2012;83:30–6.

Xu S-A, He M, Shi Q-F, Jin G-C, Yao J-Q, Yu R-B, et al. Effect of ultrasonic separation on the structure and properties of diallyl phthalate prepolymer. Ultrason Sonochem 2008;15:364–9.

Yan S, He Z, Zhou G, Yu Y, Cao Y. Hexagonal Zn2SnO4 nanoplates self-doped with Sn4+ ions towards efficient photoreduction of CO2 into CH4. Mater Sci Semicond Process 2021;130:105818.

Yan S, Wang J, Gao H, Wang N, Yu H, Li Z, et al. Zinc gallogermanate solid solution: a novel photocatalyst for efficiently converting CO2 into solar fuels. Adv Funct Mater 2013;23:1839–45.

Yang F, Hanna MA, Sun R. Value-added uses for crude glycerol--a byproduct of biodiesel production. Biotechnol Biofuels 2012;5:13.

Yang M, Fan D, Wei Y, Tian P, Liu Z. Recent progress in methanol-to-olefins (MTO) catalysts. Adv Mater 2019;31:1902181.

Yogalakshmi KN, Poornima Devi T, Sivashanmugam P, Kavitha S, Yukesh Kannah R, Varjani S, et al. Lignocellulosic biomass-based pyrolysis: a comprehensive review. Chemosphere 2022;286:131824.

Zarli A. Oleochemicals: all time players of green chemistry, 2020, p. 77–95.

Zhai X, Shamoto J, Xie H, Tan Y, Han Y, Tsubaki N. Study on the deactivation phenomena of Cu-based catalyst for methanol synthesis in slurry phase. Fuel 2008;87:430–4.

Zhang D, Song J. Mechanisms for geological carbon sequestration. Procedia IUTAM 2014;10:319–27.

Zhang F, Xu X, Qiu Z, Feng B, Liu Y, Xing A, et al. Improved methanol synthesis performance of Cu/ZnO/Al2O3 catalyst by controlling its precursor structure. Green Energy Environ 2022;7:772–81.

Zhang Jianlu, Xie Z, Zhang Jiujun, Tang Y, Song C, Navessin T, et al. High temperature PEM fuel cells. J Power Sources 2006;160:872–91.

Zhang Q, Cheng K, Kang J, Deng W, Wang Y. Fischer-Tropsch catalysts for the production of hydrocarbon fuels with high selectivity. ChemSusChem 2014;7:1251–64.

Zhang W, Camino G, Yang R. Polymer/polyhedral oligomeric silsesquioxane (POSS) nanocomposites: An overview of fire retardance. Prog Polym Sci 2017;67:77–125.

Zhang X, Zhang G, Liu W, Yuan F, Wang J, Zhu J, et al. Reaction-driven surface reconstruction of ZnAl2O4 boosts the methanol selectivity in CO2 catalytic hydrogenation. Appl Catal B Environ 2021;284:119700.

Zhang Y, Li D, Zhang S, Wang K, Wu J. CO 2 hydrogenation to dimethyl ether over CuO–ZnO–Al 2 O 3 /HZSM-5 prepared by combustion route. RSC Adv 2014;4:16391–6.

Zhen CG, Becker U, Kieffer J. Tuning electronic properties of functionalized polyhedral oligomeric silsesquioxanes: A DFT and TDDFT study. J Phys Chem A 2009;113:9707–14.

Zhou S, Kim S, Di Gennaro E, Hu Y, Gong C, Lu X, et al. Film structure of epitaxial graphene oxide on SiC: insight on the relationship between interlayer spacing, water content, and intralayer structure. Adv Mater Interfaces 2014;1:1–8.

Zhou W, Wang J, Wang C, Du Y, Xu J, Yang P. A novel reusable platinum nanocatalyst. Mater Chem Phys 2010;122:10–4.

Zhu L, Li H, Liu Z, Xia P, Xie Y, Xiong D. Synthesis of the 0D/3D CuO/ZnO Heterojunction with Enhanced Photocatalytic Activity. J Phys Chem C 2018;122:9531–9.

Ziyang Z, Hidajat K, Ray AK. Determination of adsorption and kinetic parameters for methyl tert-butyl ether synthesis from tert-butyl alcohol and methanol. J Catal 2001;200:209–21.

Zunita M, Wahyuningrum D, Bundjali B, Wenten IG, Boopathy R. The performance of 1, 3-dipropyl-2-(2-propoxyphenyl)-4, 5-diphenylimidazolium iodide based ionic liquid for biomass conversion into levulinic acid and formic acid. Bioresour Technol 2020;315:123864.

Appendix A. Chapter 3

Supporting information for Hydrophobic Polyhedral Oligomeric Silsesquioxane Support Enhanced Methanol Production from CO_2 Hydrogenation

A.1 Supporting Results

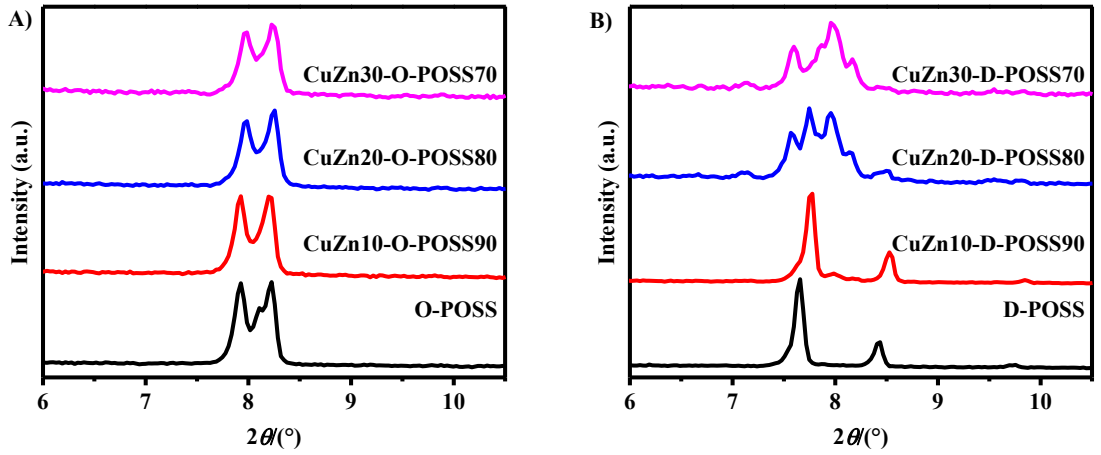

Figure A-1 XRD patterns of (**a**) O-POSS and their supported catalysts; and (**b**) D-POSS and their supported catalysts in the region 6° to 10.5°.

Table A-1 Dimension of POSS size over the different concentrations of metal oxide loading after calcination.

Sample	**Overall dimension of POSS molecule**		**Body diagonal of the POSS cage**		**Distance between opposite Si_4O_4 faces of the silsesquioxane cube plane**	
	2θ (°)	***d* (nm)**	**2θ (°)**	***d* (nm)**	**2θ (°)**	***d* (nm)**
O-POSS	8.2	1.1	18.5	0.48	24.5	0.36
CuZn10-O-POSS90	8.2	1.1	18.4	0.48	24.5	0.36
CuZn20-O-POSS80	8.2	1.1	18.4	0.48	24.5	0.36
CuZn30-O-POSS70	8.2	1.1	18.4	0.48	24.5	0.36
D-POSS	7.7	1.2	18.9	0.47	24.6	0.36
CuZn10-D-POSS90	7.8	1.1	19.1	0.46	24.7	0.36
CuZn20-D-POSS80	8.0	1.1	19.1	0.46	24.6	0.36
CuZn30-D-POSS70	8.0	1.1	19.1	0.46	23.9	0.37

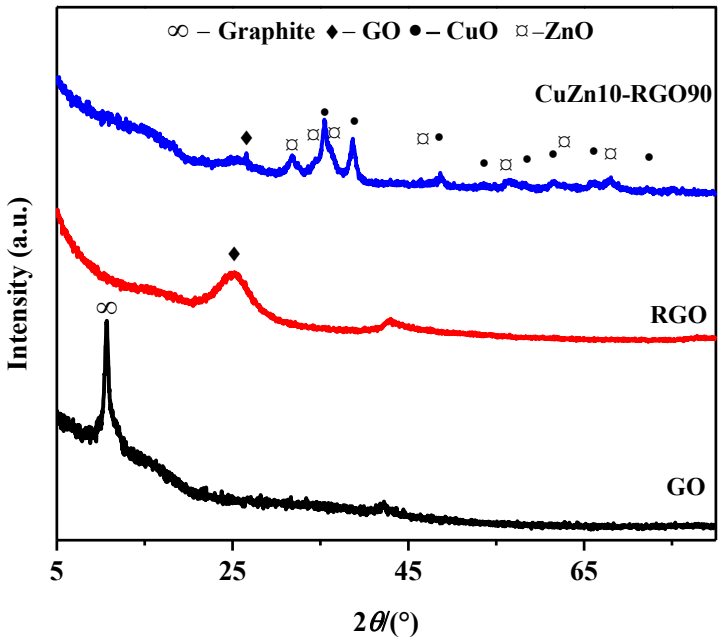

Figure A-2 XRD patterns of the CuZn10-RGO catalyst, graphene oxide (GO), and reduced graphene oxide (RGO).

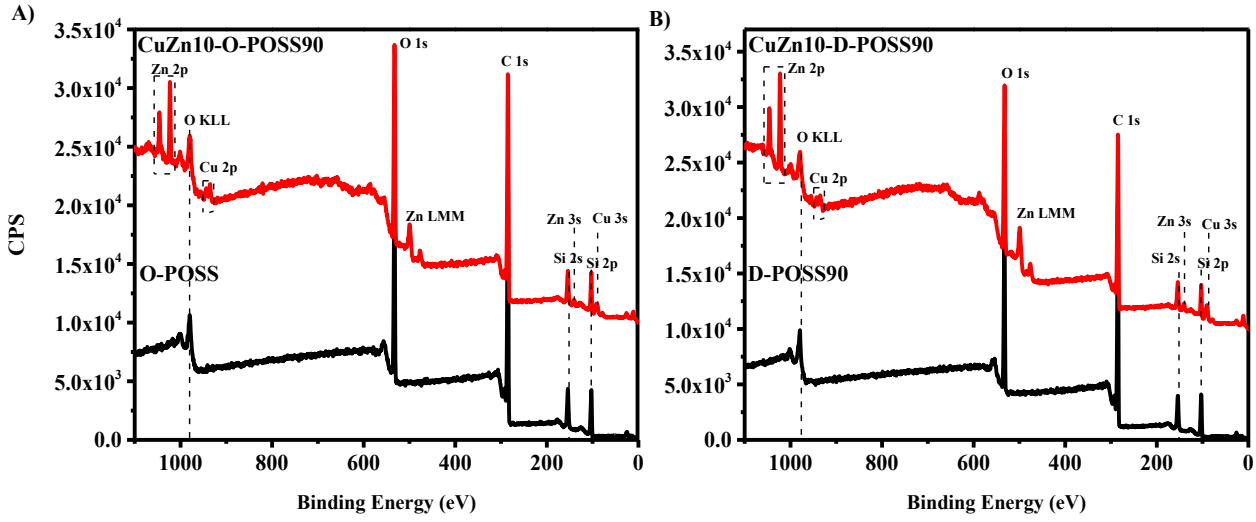

Figure A-3 XPS survey spectra (**a**) O-POSS and CuZn10-O-POSS90; (**b**) D-POSS and CuZn10-D-POSS90.

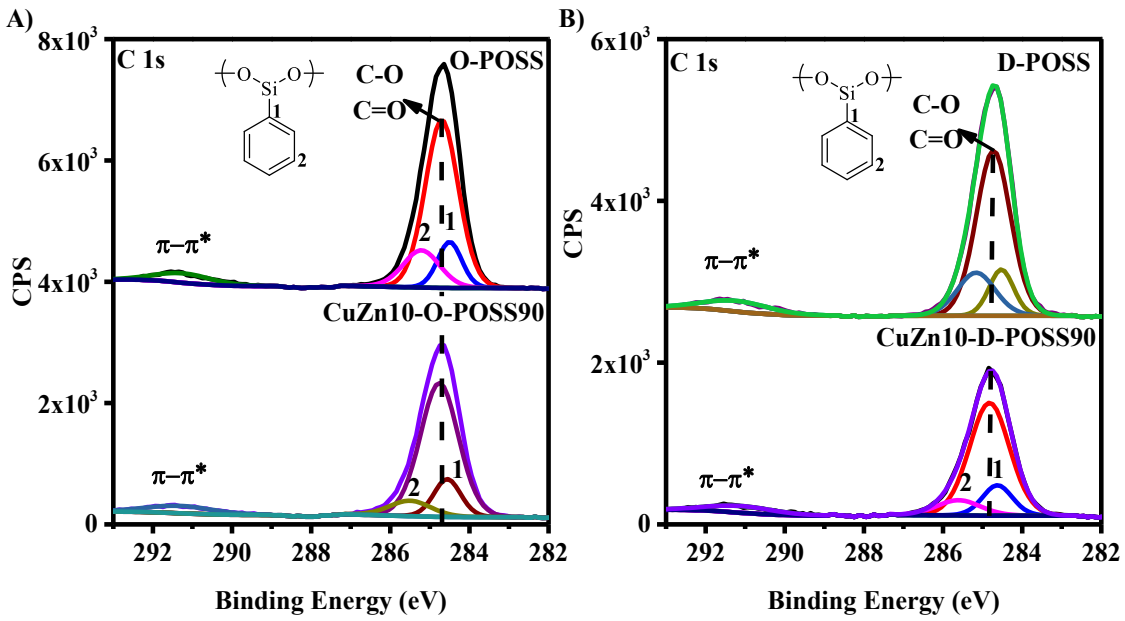

Figure A-4 XPS High resolution spectra for C 1s (**a**) O-POSS, CuZn10-O-POSS90; (**b**) D-POSS, CuZn10-O-POSS90.

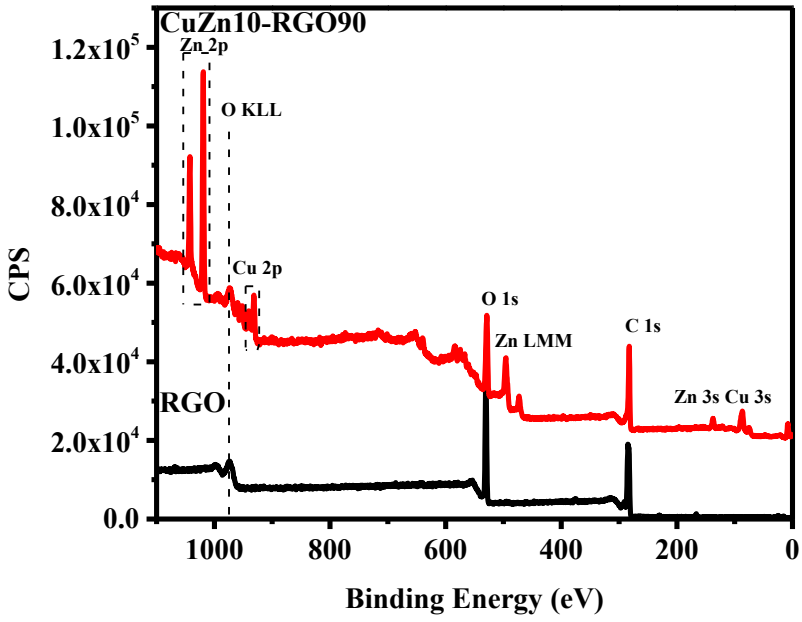

Figure A-5 XPS survey spectra of Reduced Graphene Oxide (RGO) and CuZn10-RGO90.

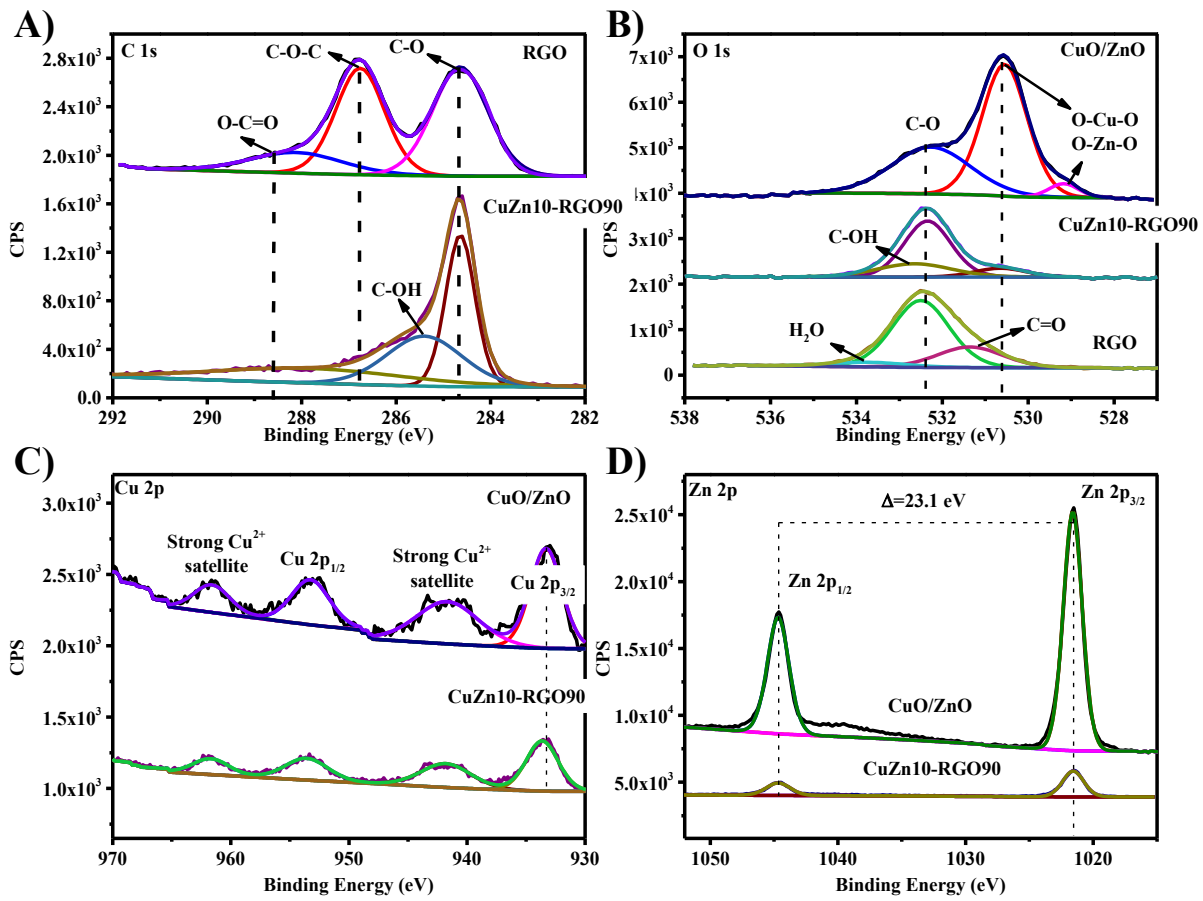

Figure A-6 XPS high resolution spectra for (**a**) C 1s for Reduced Graphene Oxide (RGO) and CuZnO10-RGO90; (**b**) O 1s for Reduced Graphene Oxide (RGO), CuZnO10-RGO90, and CuO/ZnO; (**c**) Cu 2p CuZnO10-RGO90, and CuO/ZnO; and (**d**) Zn 2p CuZnO10-RGO90, and CuO/ZnO.

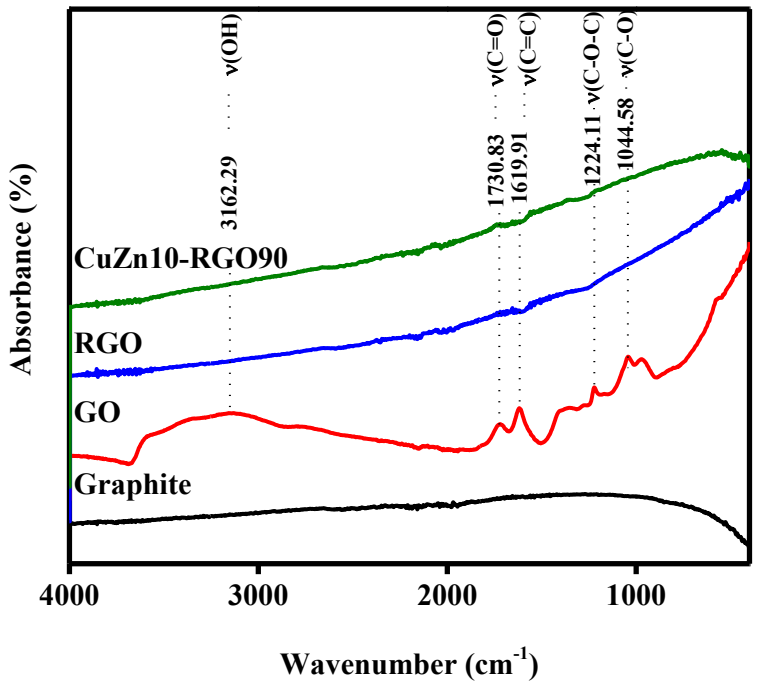

Figure A-7 ATR FT-IR spectra of Graphite, Graphite Oxide (GO), Reduced Graphene Oxide (RGO), and CuZn10-RGO90.

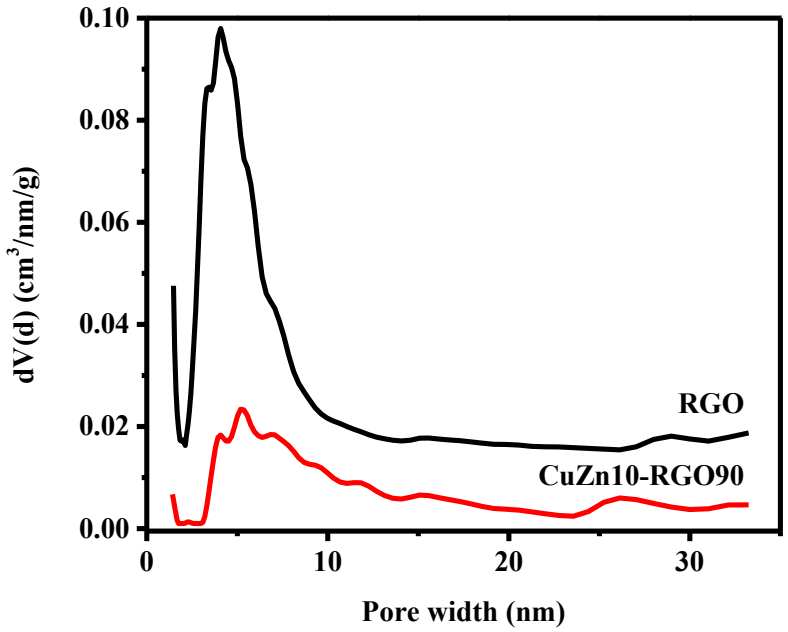

Figure A-8 Pore size distribution of reduced graphene oxide (RGO) and CuZn10-RGO90.

Table A-2 Temperature at which supports and catalysts loss 5%, 50%, and the wt% residue at 890 °C from TGA analysis.

Catalyst	**T_{onset} (°C)[a]**	**T_5 (5% mass loss, °C)**	**T_{50} (50% mass loss, °C)**	**Residues at 890 °C (wt%)**
O-POSS	440	484	-	72.7
CuZn10-O-POSS90	254	468	554	15.6
CuZn20-O-POSS80	339	447	561	34.3
CuZn30-O-POSS70	346	436	585	43.8
D-POSS	481	531	-	77.3
CuZn10-D-POSS90	463	449	592	41.8
CuZn20-D-POSS80	460	445	638	41.1
CuZn30-D-POSS70	440	431	685	44.3
RGO	51	429	-	81.4
CuZn10-RGO90	63	392	-	74.4
CuO/ZnO	347	808	-	91.5

[a]: ASTM E2550 – 21 "point in the TGA curve where a deflection is first observed from the established baseline prior to the thermal event" [1].

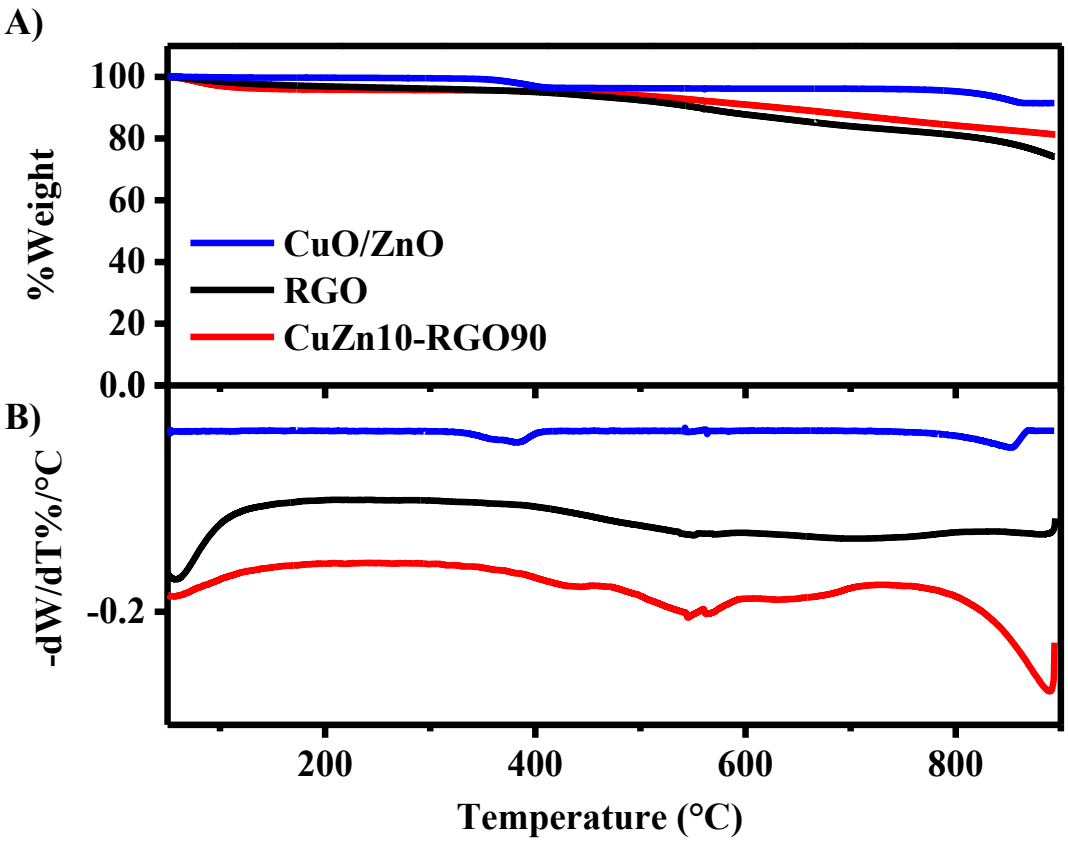

Figure A-9 (**a**) TGA and (**b**) DTG profile for CuO/ZnO, reduced graphene oxide (RGO), and CuZn10-RGO90.

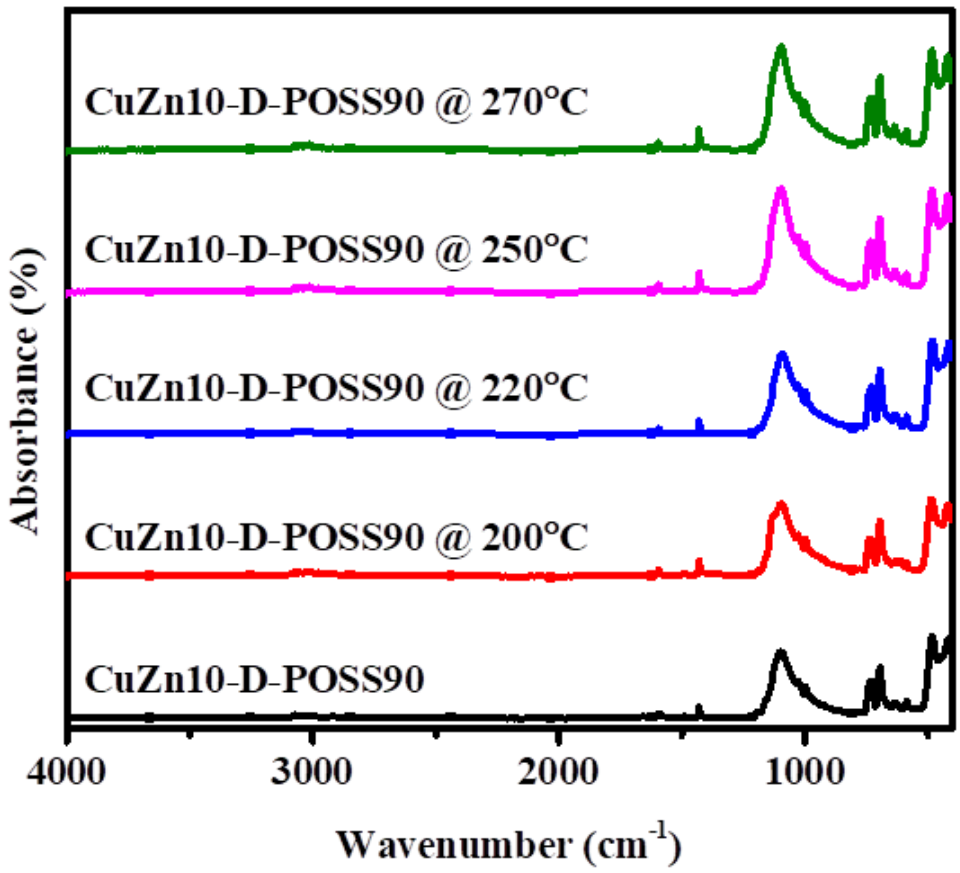

Figure A-10 ATR-FTIR profile of the spent CuZn10-D-POSS90 after one cycle of reaction.

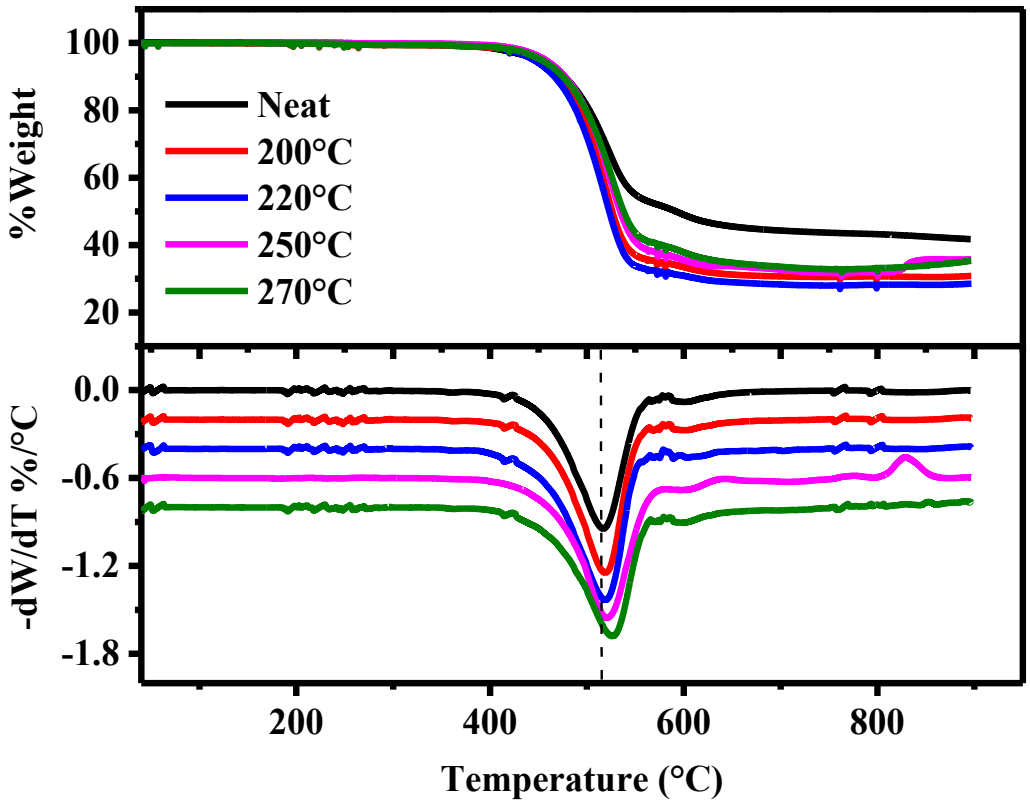

Figure A-11 TGA and DTG profile of the spent CuZn10-D-POSS90 after one cycle of reaction.

A.2 References

[1] E2550. Standard Test Method for Thermal Stability by Thermogravimetry. ASTM Int 2017;11:1–5.

Appendix B. Chapter 5

Supplementary information for Rapid, Metal-free, Catalytic Conversion of Glycerol to Allyl Monomers and Polymers

B.1 Supporting Results

B.1.1 Energy Efficiency Study

DODH of glycerol was carried out in a microwave-assisted distillation, and in a sand bath and energy efficiency comparison was carried out [1]. At first, glycerol 40 g (0.4 mol, 99.5%) and formic acid 9.8 mL (0.26, mol 98%) were charged into a 50 mL round bottom flask and placed in a microwave vessel, connected to a distillation system (Table B-1, Entry 1). The microwave was rapidly ramped (10 s) to 240 °C and hold for 25 minutes with continuous removal of AA from the reaction mixture through distillation. A second addition of formic acid was performed after the system was cooled down through sequential additions of formic acid (0.26, mol 98%) with a distillation time of 15 minutes. The procedure was repeated for a third formic acid addition and the distillation happened for 10 minutes.

Further, glycerol 36.4 g (0.4 mol, 99.5%) and formic acid 5.7 mL (0.15, mol 98%) were charged into a 50 mL round bottom flask and connect to distillation system in a preheated sand bath at 210 °C (Table B-1, Entry 2). Two more additions of formic acid were performed during the distillation. The procedure required several hours to reach completion.

To compare energy balance for both processes, we used a commercial domestic electricity meter ("Watt-hour meter") to measure the consumed energy in kWh and $kWhmol^{-1}$ [2].

Table B-1 Comparison of the energy consumed by sand bath and microwave for the DODH of glycerol [1].

Entry	Heating method	Glycerol [mol]	Formic acid [mol]	Yield [%][a]	$t_{\Delta total}$ [min][b]	Energy [kWh][c]	Energy [kWhmol^{-1}]
1	MW[d]	0.4	0.5	61	54	0.342	1.417
2	Sand bath	0.4	0.5	45	1819	5.672	31.857

[a] AA yield determined by ^{1}H-NMR

[b] Total heating time. For microwave analysis, this includes the ramp time and reaction time at the specified temperature. For sand bath analysis, this include the time required for heating the bath to the specified temperature and the reaction time

[c] Energy consumption as measured by the Wattmeter for the total heating time ($t_{\Delta total}$)

[d] Microwave, CEM DiscoverTM, 300 W maximum magnetron output power

As can be observed from the Table B-1 the microwave heating experiment required only a fraction (ca. 22%) of the energy needed for the traditional sand bath per mol prepared of AA. Our results were not surprising after comparing the striking difference in the total heating time (54 min versus 1819 min), moreover to the fact that the hot plate and the sand bath itself need to be heated before the temperature of the reaction mixture is increased [2]. Conversely, microwave dielectric heating affects direct molecular heating of the reaction mixture itself over a relative microwave-transparent reaction vessel (Pyrex glass).

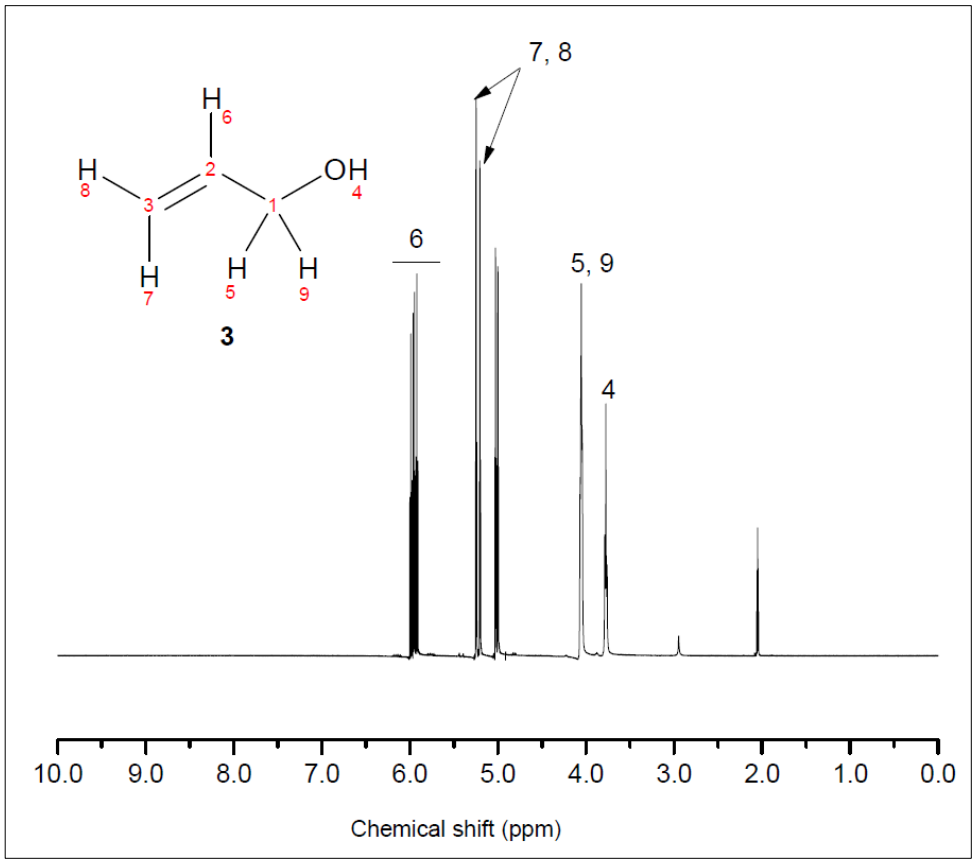

Figure B-1 1H-NMR of allyl alcohol (**3**) in acetone-d_6.

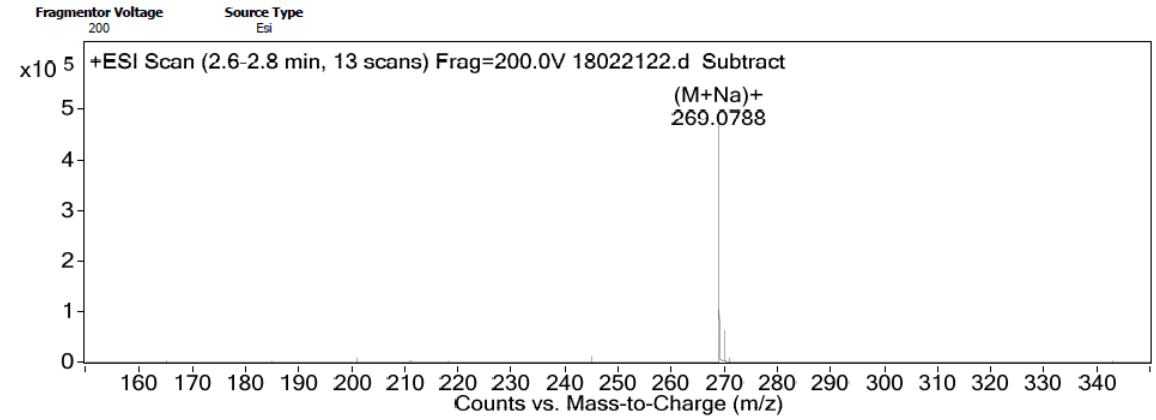

Formula Calculator Results

Formula	Ion Species	Mass	Calc. Mass	m/z	Calc. m/z	Diff (mDa)	Diff (ppm)	DBE	Ion	Score
C14 H14 O4	C14 H14 Na O4	246.0896	246.0892	269.0788	269.0784	-0.34	-1.27	8	(M+Na)+	89.8

Figure B-2 ESI-MS of diallyl phthalate (**6**) after purification.

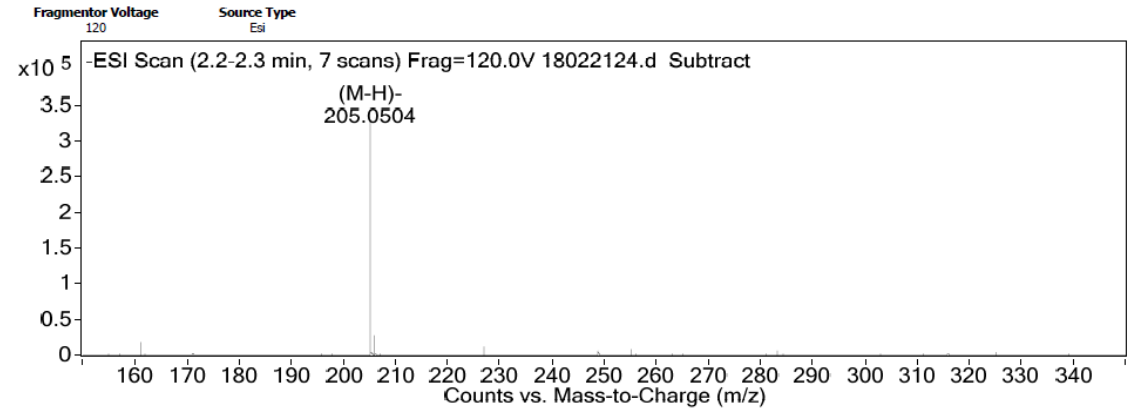

Formula Calculator Results

Formula	Ion Species	Mass	Calc. Mass	m/z	Calc. m/z	Diff (mDa)	Diff (ppm)	DBE	Ion	Score
C11 H10 O4	C11 H9 O4	206.0577	206.0579	205.0504	205.0506	0.19	0.9	7	(M-H)-	71.58

Figure B-3 ESI-MS of monoallyl phthalate (**7**) after purification.

Table B-2 Deoxydehydration (DODH) of glycerol to allyl alcohol (3) by formic acid (2).

Code	***A***	***B***	***C***	**Conversion**[a]	**Selectivity**[b]	**Selectivity**[b]	**Formic acid Recovered**
	[°C]	*[FA:Gly]*	*[min]*	[%]	AA [%]	AF [%]	**[%]**
1	260	1.8	20	36.65	95.4	4.6	84.2
2	230	1.2	20	74.53	95.6	4.4	45.2
3	200	1.2	10	64.60	94.0	6.0	40.2
4	230	1.2	20	70.19	95.6	4.4	39.3
5	230	1.8	10	57.76	94.9	5.1	68.1
6	200	1.8	20	64.29	92.9	7.1	46.3
7	260	1.2	30	52.80	95.3	4.7	43.2
8	230	0.6	30	55.90	96.6	3.4	17.5
9	230	1.2	20	43.79	95.6	4.4	43.4
10	200	0.6	20	60.87	96.4	3.6	16.7
11	200	1.2	30	36.65	95.0	5.0	33.6
12	260	1.2	10	55.90	90.9	9.1	41.2
13	230	0.6	10	46.58	95.5	4.5	9.5
14	230	1.8	30	65.22	86.1	13.9	54.5
15	230	1.2	20	63.98	92.0	8.0	41.9
16	260	0.6	20	45.34	95.2	4.8	20.4
17	230	1.2	20	64.29	92.0	8.0	40.2

[a] Conversion and selectivity determined by ^{1}H-NMR

[b] Selectivity calculated by the total yield of allyl alcohol + allyl formate in the liquid phase

Table B-3 ANOVA of RSM of %yield of allyl alcohol (**3**).

Source	Sum of squares	Mean square	F value	*p*-value
Model	569.05	63.23	502.36	< 0.0001
A	172.55	172.55	1370.95	< 0.0001
B	142.94	142.94	1135.65	< 0.0001
C	17.04	17.04	135.42	< 0.0001
A B	19.67	19.67	156.25	< 0.0001
A C	138.20	138.20	1098.01	< 0.0001
B C	7.51	7.51	59.69	0.0001
A^2	8.35	8.35	66.36	< 0.0001
B^2	59.51	59.51	472.85	< 0.0001
C^2	2.08	2.08	16.54	0.0048
Residual	0.8810	0.1259		
Lack of fit	0.6672	0.2224	4.16	0.1011
Pure error	0.2138	0.0535		
Cor Total	569.93			

Table B-4 ANOVA of RSM of %yield of allyl formate (**4**).

Source	Sum of squares	Mean square	F value	*p*-value
Model	3.29	0.3651	2392.20	< 0.0001
A	0.0113	0.0113	74.23	< 0.0001
B	3.00	3.00	19646.78	< 0.0001
C	0.0141	0.0141	92.10	< 0.0001
AB	0.0752	0.0752	492.47	< 0.0001
AC	0.0387	0.0387	253.50	< 0.0001
BC	0.0068	0.0068	44.61	0.0003
A^2	0.0121	0.0121	79.56	< 0.0001
B^2	0.1039	0.1039	680.69	< 0.0001
C^2	0.0327	0.0327	214.18	< 0.0001
Residual	0.0011	0.0002		
Lack of fit	0.0007	0.0002	2.96	0.1612
Pure error	0.0003	0.0001		
Cor Total	3.29			

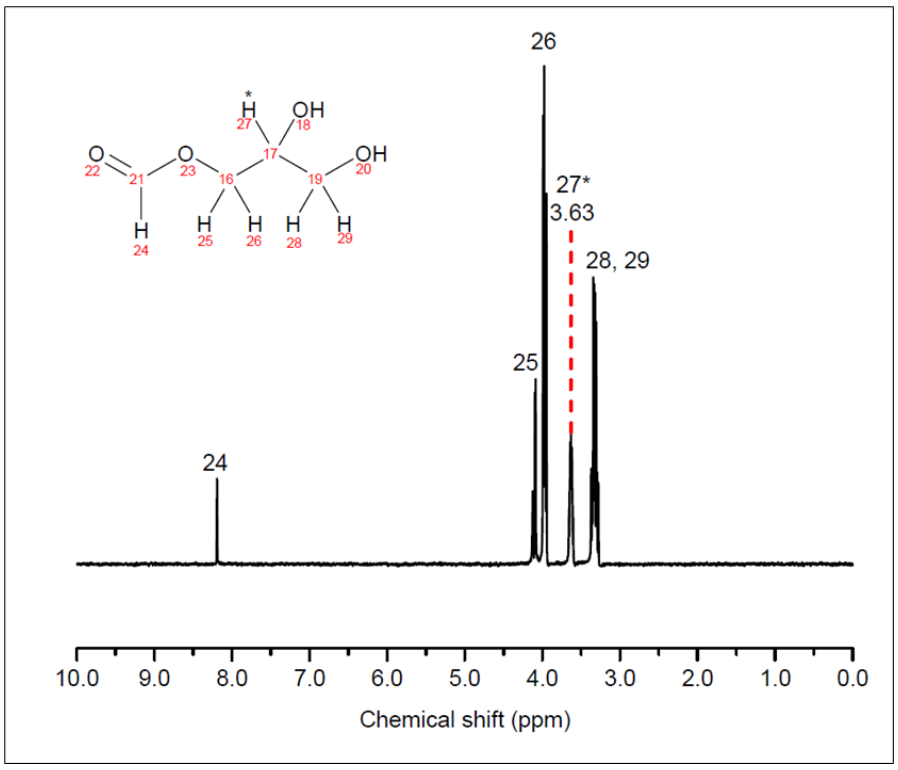

Figure B-4 1D-TOCSY with selective excitation of proton at 3.63 ppm of the FA:Gly mixture in DMSO-d_6 at 15 min.

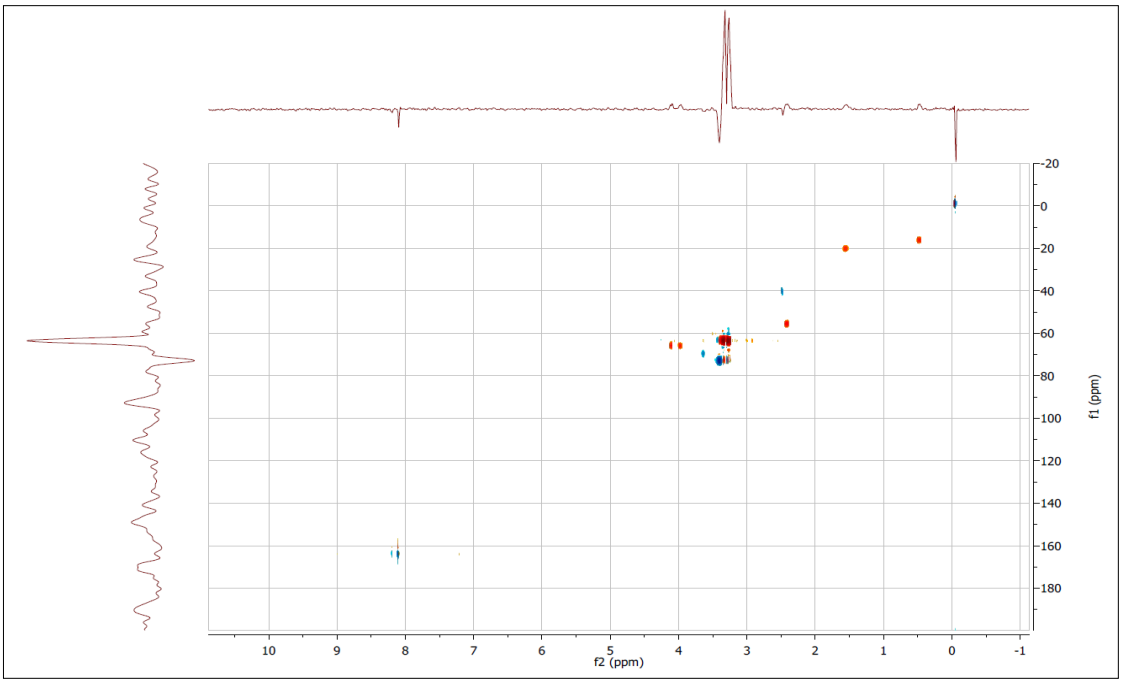

Figure B-5 gHSQCAD of raw mixture of the FA:Gly mixture in DMSO-d_6 at 15 min.

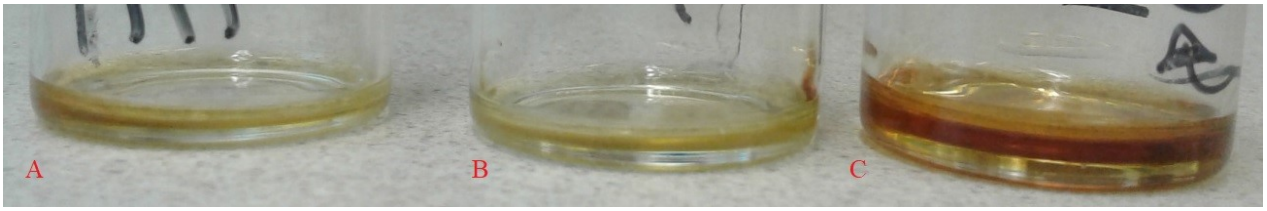

Figure B-6 PAA after drying, Table 5-5, entry 2, 3, and 4 from left to right (**a**, **b**, and **c**), respectively.

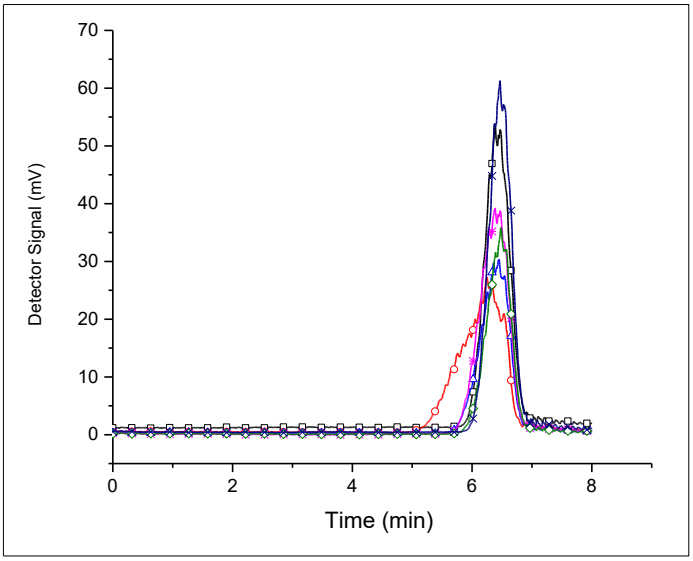

Figure B-7 GPC of poly (allyl alcohol) (**8**) (**Table 5-5,** entry 1 (□), entry 2 (○), entry 3 (Δ), entry 4 (*), entry 5 (◊), entry 6 (×)) in THF.

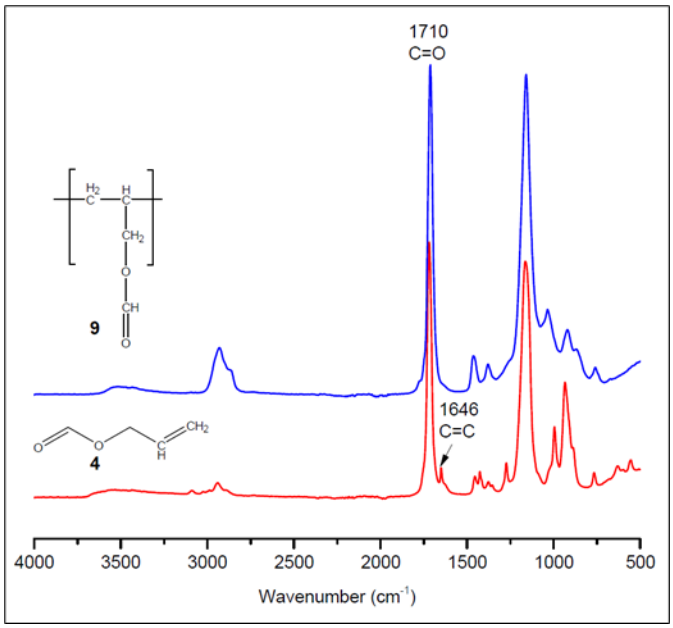

Figure B-8 ATR FT-IR of the allyl formate (**4**) and poly (allyl formate) (**9**) (**Table 5-5**, entry 7).

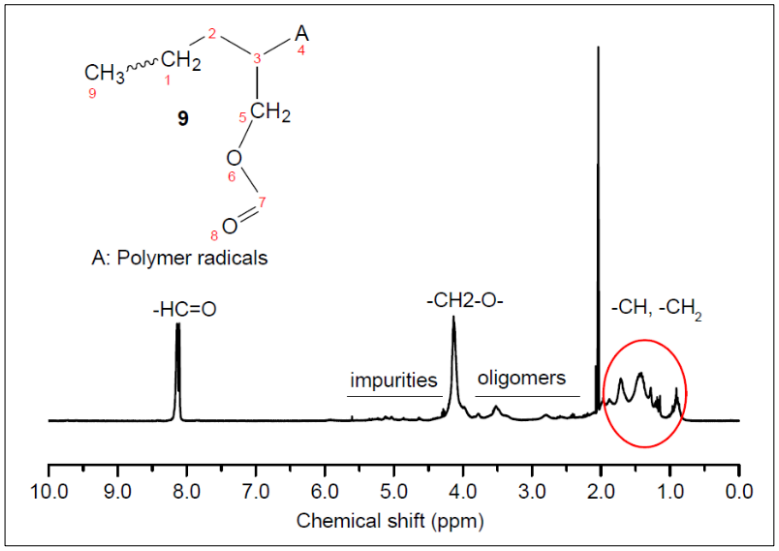

Figure B-9 ^{1}H-NMR of poly (allyl formate) (**9**) (Table 5-5, entry 7) in acetone-d_6.

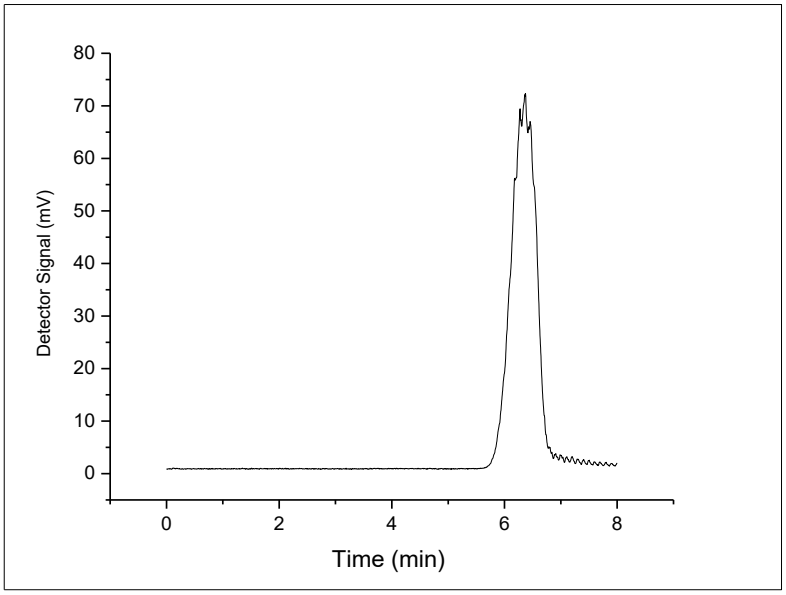

Figure B-10 GPC of poly (allyl formate) (**9**) (Table 5-5, entry 7) in THF.

B.1.2 Microwave-Assisted Conversion of Allyl Alcohol (3) to Diallyl Phthalate (6)

Diallyl phthalate (**6**) was prepared from **3** using microwave open-vessel reactor under reflux (95 °C, 20 min) using sulfuric acid as catalyst. Using quick TLC test, two new compounds were found in the raw mixture. In order to identify the products, a column separation was performed. The products were analyzed using ATR-FTIR (Fig. B-11). Diallyl phthalate shows a broad peak at 1720 cm^{-1} associated to the C=O stretching. The allyl C=C stretch peak is located at 1648 cm^{-1}, which appeared after the purification of the product. For the phthalate group, the more notable bands are located at 1266 and 1600 cm^{-1} which are associated to the C-O-C and aromatic vibration frequency [3], respectively. The allyl bands corresponding to C=C stretching are identified at 3076 and 1648 cm^{-1} for the mono- and diallyl alcohol. For the monoallyl alcohol, the carbonyl (C=O) broad peaks of carboxylic acid are observed at 2500-2700 cm^{-1} and 2700-3300 cm^{-1}. Additionally, the carbonyl peak of carboxylic acid at 1695 cm^{-1} appears as a split peak with the carbonyl peak attached to the allyl group at 1720 cm^{-1}.

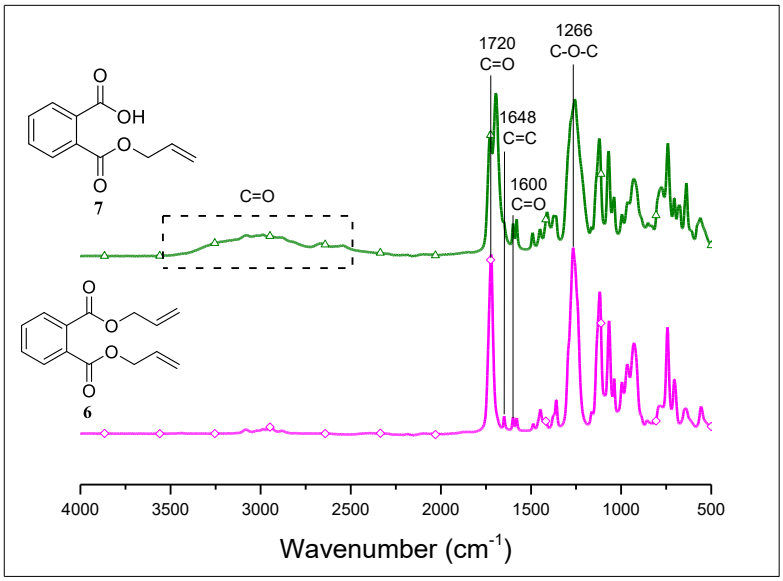

Figure B-11 ATR-FT IR of diallyl phthalate (**6**) (◊) and monoallyl phthalate (**7**) (Δ) after purification.

^{1}H NMR analysis of monoallyl and diallyl phthalate was carried out to confirm their chemical structures (Fig. B-12). Two peaks (7.54 and 7.75 ppm) are associated to the benzene ring in the diallyl phthalate and three are associated to the monoallyl alcohol (7.59, 7.71, 7.92). The integration of the peaks located at 6.00 ppm corresponding to allyl protons of monoallyl and diallyl phthalate indicates one proton for the "mono' and two for the "diallyl".

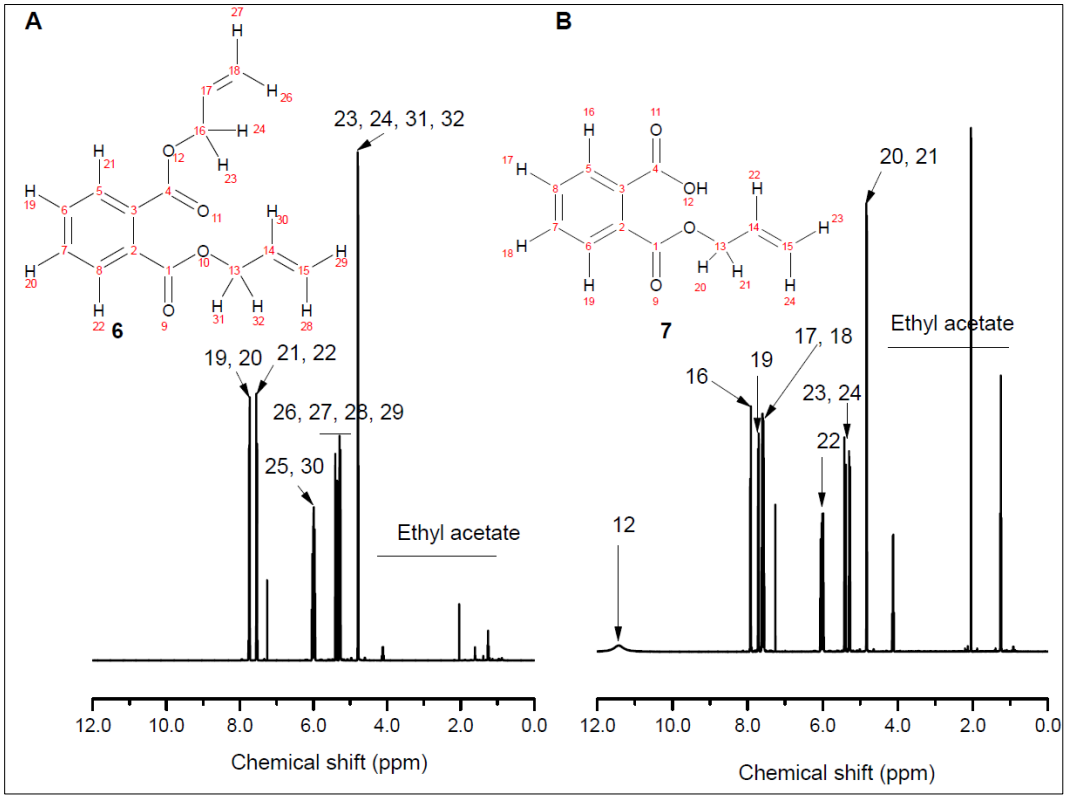

Figure B-12 ^{1}H-NMR of (**a**) diallyl phthalate (**6**) and (**b**) monoallyl phthalate (**7**) in $CDCl_3$ after purification.

The microwave-assisted polymerization of diallyl phthalate was confirmed by the appearance of a white-yellow solid after microwave reaction as seen in Fig. B-13a. The product was characterized by ATR-FT IR (Fig. B-14). The notable bands for phthalate group are located at 1720, 1264, and 1118 cm^{-1} and are associated to the C=O and C-O-C stretching vibrations [4]. These bands are also the predominant ones in the polymer. The molecular weight of the polymer was 37576 g/mol. A high value of polydispersity (6.62) indicates that the polymer is composed of different units of varying chain lengths (Fig. B-15).

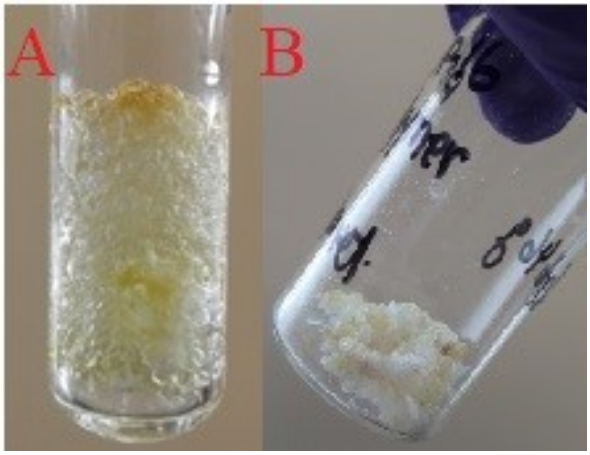

Figure B-13 (**a**) Raw poly (diallyl phthalate) (**10**) after microwave polymerization of diallyl phthalate (**7**) in the presence of benzoyl peroxide. (**b**) Poly (diallyl phthalate) (**10**) after washing with methanol and dried at 80 °C.

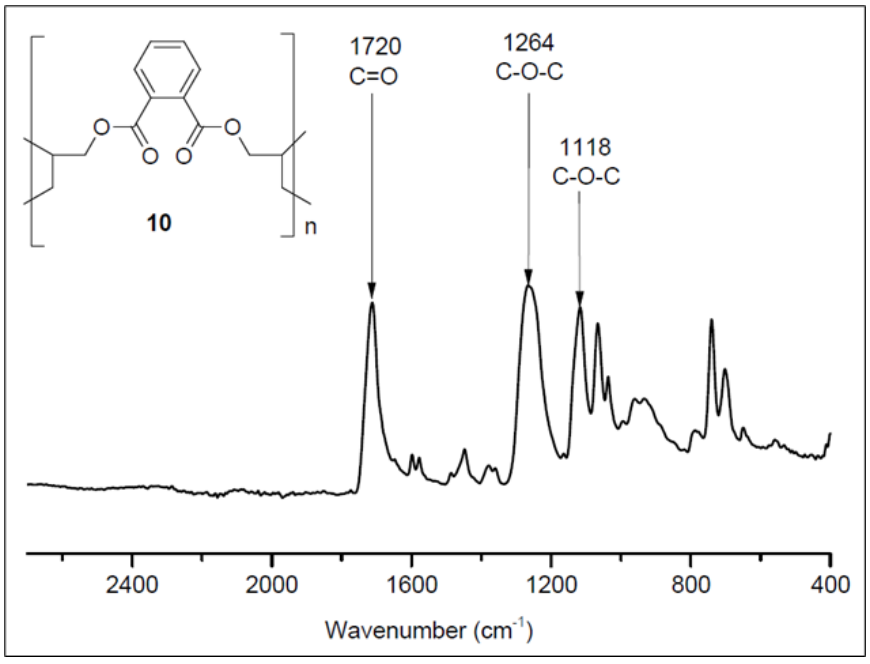

Figure B-14 ATR-FT IR of poly (diallyl phthalate) (**10**) (Table 5-5, entry 8) after MW polymerization.

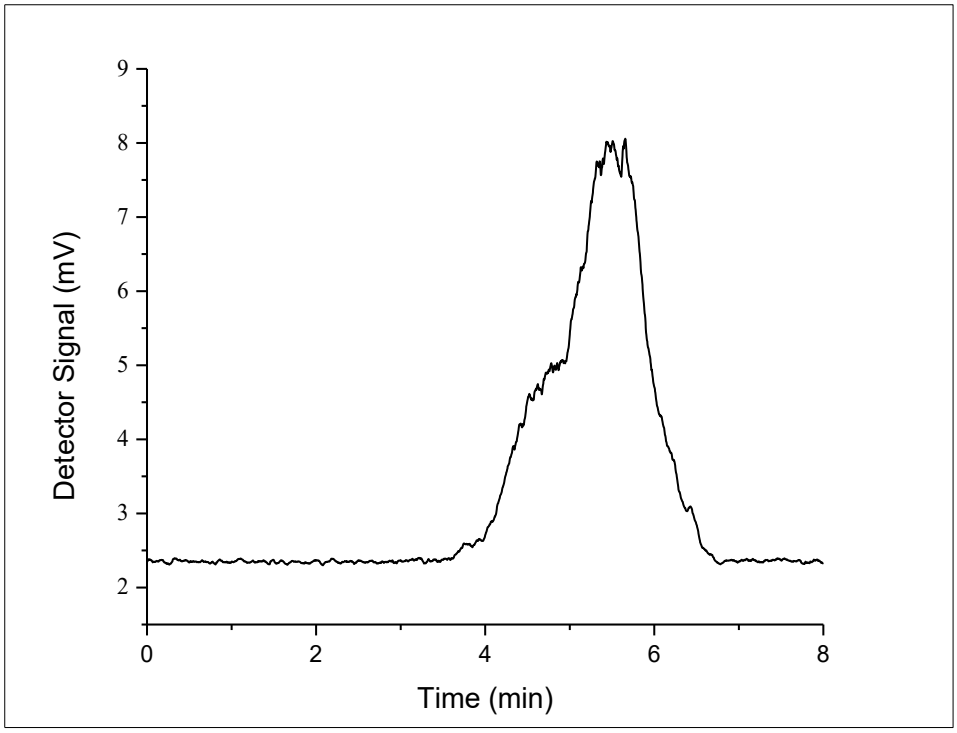

Figure B-15 GPC of poly (diallyl phthalate) (**10**) (Table 5-5, entry 8) in THF.

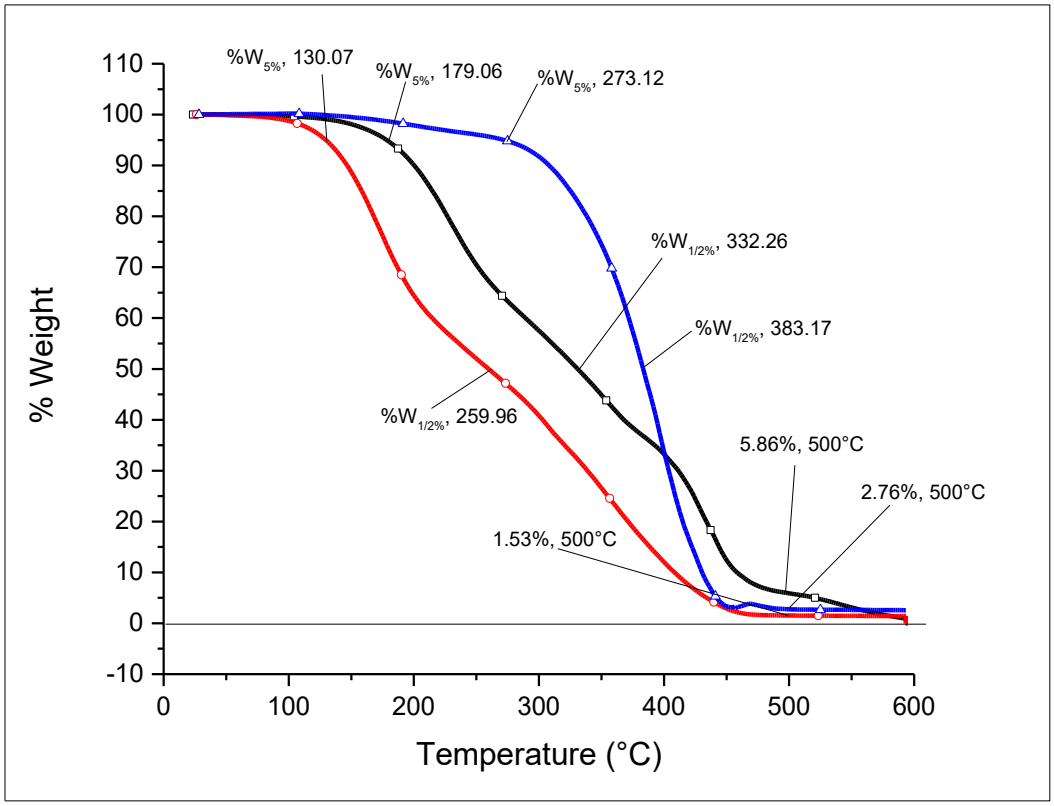

Figure B-16 TGA of poly (allyl alcohol) **8** (□) (Table 5-5, entry 2), poly (allyl formate) **9** (○) (Table 5-5, entry 7), and poly (diallyl phthalate) **10** (Δ) (Table 5-5, entry 8).

10 showed highest thermal stability with 5% and 50% weight loss at about 273 and 383 °C, respectively followed by **8** with 5% and 50% weight loss at about 179 and 332 °C, respectively. **9** showed least thermal stability compared to both **10** and **8** with 5% and 50% weight loss at ~130 and 260 °C, respectively. The earlier onset of degradation of **9** could be due to loss of CO_2 similar to decomposition of **4** [5].

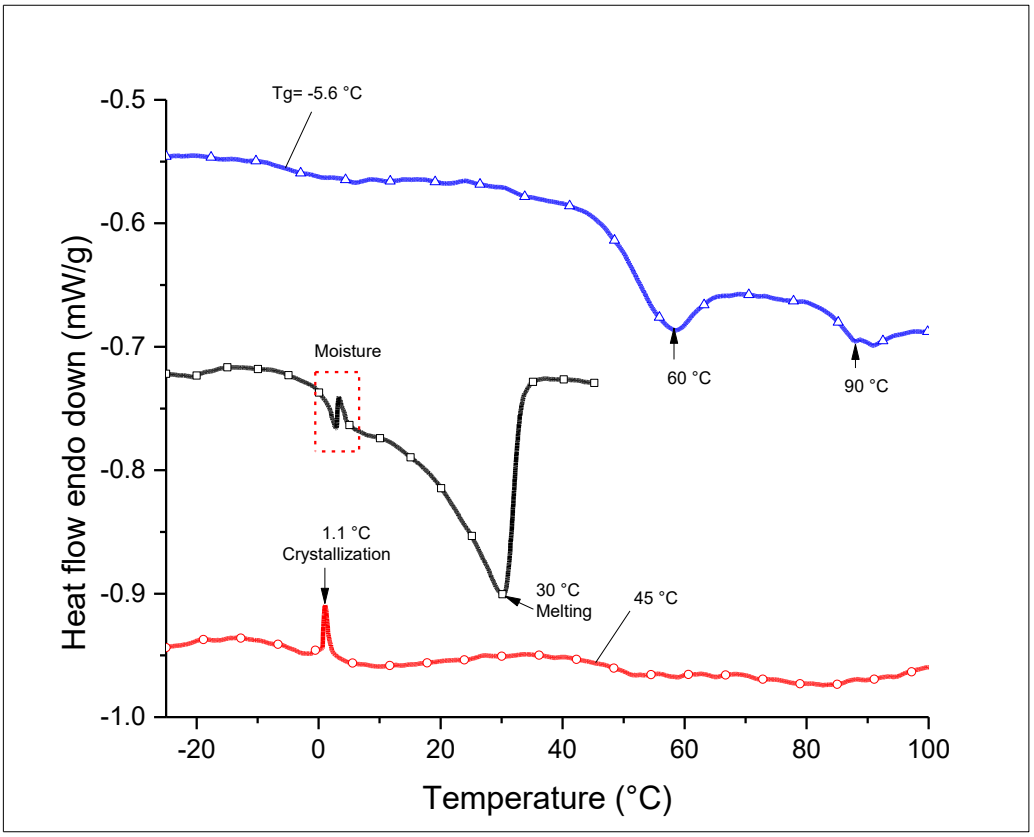

Figure B-17 DSC thermograms of poly (allyl alcohol) **8** (□) (Table 5-5, entry 2), poly (allyl formate) **9** (○) (Table 5-5, entry 7), and poly (diallyl phthalate) **10** (Δ) (Table 5-5, entry 8).

Table B-5 Mass balance for some representative samples.

Entry	Conditions [ºC, min]	Glycerol [mmole]	Total Initial sample [g]	Sample collected after DODH [g]	Total % Yield	Theoretical mass after DODH[a] [g]	ΔM[b] [%]
1	230, 20	350	51.26	22.60	45.40	23.30	2.83
2	200, 20	350	60.78	22.80	37.87	23.00	0.74
3	260, 10	350	51.26	30.40	59.99	30.70	1.13

[a] Expected theoretical mass of non-gaseous products for the corresponding % yield of allyl alcohol + allyl formate.

[b] Deviation between the theoretical mass and the experimental mass.

Table B-6 Summary of metal-free DODH of glycerol by formic acid (2) to synthesize allyl alcohol (3).

Entry	2 [equiv]	T [°C]	Time [h]	Process	Yield [%]	Ref.
1	1.44	195-260	<24	3 cycles of distillation / cooling (CH) [a]	45-47[c]	[39]
2	1.44	230-240	<1.5	3 cycles of distillation/ cooling (CH) [a]	80[d]	[40]
3	1.80	235	6	Batch distillation / 3 additions of formic acid (CH) [a]	99[e]	[31]
4	1.80	235	2	Continuous distillation (CH) [a]	99[e]	[31]
5	2.50	315	0.1	Continuous-flow microfluidic reactor, 250 psi (CH) [a]	56[f]	[41]
6	1.57	260	0.2	Batch distillation (MW)[b]	56[g]	This work

[a] CH: conventional heating

[b] MW: Microwave, CEM DiscoverTM, 300 W maximum magnetron output power

[c] Per cent yield of allyl alcohol of the theoretical amount

[d] The reported yield is referred as allyl alcohol

[e] The reported yield is a combination of allyl alcohol, water and unreacted formic acid

[f] The reported yield is referred as allyl alcohol after optimization

[g] The reported yield refers to allyl alcohol collected during distillation

B.1.3 NMR Data and Spectra of Compounds

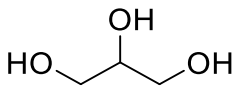

Scheme B--1 Glycerol (**1**).

^{1}H NMR (400 MHz, D_2O, 25.5 °C, TMS) δ_H 3.78 – 3.66 (1 H, m), 3.59 (2 H, dd, *J* 11.7, 4.4), 3.50 (2 H, dd, *J* 11.7, 6.5). ^{13}C NMR (101 MHz, D_2O, 25 °C, TMS): δ=73.2, 62.5 ppm. Spectral data are consistent with those reported in the literature [6].

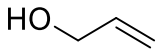

Scheme B-2 Allyl alcohol (**2**).

^{1}H NMR (400 MHz, D_2O, 25°C, TMS): δ=6.06 – 5.85 (m, 1H), 5.23 (ddd, J =4.06 Hz, 1H), 5.14 (ddd, J =10.0 Hz, 1H), 4.72 (s, 1H), 4.06 ppm (d, J= 5.3 Hz, 2H); ^{13}C NMR (101 MHz, D_2O, 25 °C, TMS): δ=137.54, 116.44, 63.45 ppm. Spectral data are consistent with those reported in the literature [7].

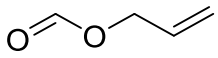

Scheme B-3 Allyl formate (**4**).

^{1}H NMR (400 MHz, D_2O, 25.5 °C, TMS): δ=8.14 (1 H, s), 5.95 (1 H, dddd, *J* 24.3, 10.8, 6.6, 5.5), 5.36 (1 H, q, *J* 1.5), 5.30 (1 H, dq, *J* 13.6, 1.4), 4.67 (d, *J* 5.6 Hz, 2H); ^{13}C NMR (101 MHz, D_2O, 25 °C, TMS): δ=160.72, 131.72, 118.76, 64.49 ppm. Spectral data are consistent with those reported in the literature [8].

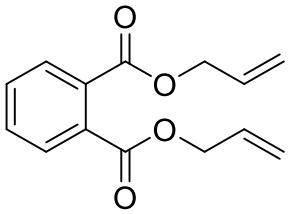

Scheme B-4 Diallyl phthalate (**6**).

^{1}H NMR (400 MHz, $CDCl_3$, 25.5 °C, TMS): δ= 7.82 – 7.66 (m, 2H), 7.61 – 7.44 (m, 2H), 6.09 – 5.90 (m, 2H), 5.47 – 5.32 (m, 2H), 5.33 – 5.19 (m, 1H), 4.79 (dt, *J* 5.8, 1.2, 4H). ^{13}C NMR (101 MHz, D_2O, 25.5 °C, TMS): δ= 167.15, 132.01, 131.85, 131.11, 128.92, 118.54, 66.20 ppm.

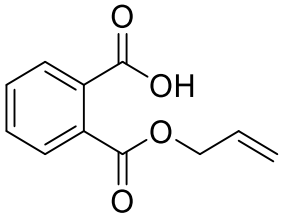

Scheme B-5 Monoallyl phthalate (**7**).

^{1}H NMR (400 MHz, $CDCl_3$, 25.5 °C, TMS) δ= 7.97 – 7.86 (m, 1H), 7.76 – 7.66 (1 H, m), 7.66 – 7.52 (2 H, m), 6.10 – 5.94 (m, 1H), 5.40 (dq, *J* 17.2, 1.5, 1H), 5.28 (dq, *J* 10.4, 1.2, 1H), 4.83 (dt, *J* 5.9, 1.3, 2H). ^{13}C NMR (101 MHz, D_2O, 25.5 °C, TMS): δ= 167.41, 165.52, 133.71, 132.87, 128.35, 128.01, 118.18, 67.02 ppm.

B.2 References

[1] Ullah A, Herrero YR. Methods for converting glycerol to allyl compounds. CANADA Patent US 10,633,316 B22020, 2020.

[2] Razzaq T, Kappe CO. On the energy efficiency of microwave-assisted organic reactions. ChemSusChem Chem Sustain Energy Mater 2008;1:123–32.

[3] Xu S-A, He M, Shi Q-F, Jin G-C, Yao J-Q, Yu R-B, et al. Effect of ultrasonic separation on the structure and properties of diallyl phthalate prepolymer. Ultrason Sonochem 2008;15:364–9.

[4] Spurr RA, Hanking BM, Rowen JW. The polymerization of diallyl phthalate, an investigation by infrared spectroscopy. J Polym Sci 1959;37:431–40.

[5] Mora JR, Perez CD, Maldonado A, Loroño M, Córdova T, Chuchani G. Theoretical study on thermal decomposition kinetics of allyl formates in the gas phase. Comput Theor Chem 2013;1019:48–54.

[6] Lu J, Wang P, Wang Q, Wang Y, Jiang M. Validated 1H and 13C nuclear magnetic resonance methods for the quantitative determination of glycerol in drug injections. Molecules 2018;23:1177.

[7] Arceo E, Marsden P, Bergman RG, Ellman JA. An efficient didehydroxylation method for the biomass-derived polyols glycerol and erythritol. Mechanistic studies of a formic acid-mediated deoxygenation. Chem Commun 2009:3357–9.

[8] Carlson CG, Hall JE, Huang YY, Kotila S, Rauk A, Tavares DF. The preparation of esters of formic acid using boron oxide. Can J Chem 1987;65:2461–3.